

CO_x Katalyse über CeO₂ und In₂O₃ basierten Katalysatoren: Kombination von *operando* Spektroskopie und DFT

CO_x catalysis over CeO₂ and In₂O₃ based catalysts: Combining *operando* spectroscopy and DFT

Zur Erlangung des Grades eines Doktors der Naturwissenschaften (Dr. rer. nat.)

Genehmigte Dissertation von Marc Niklas Ziemba aus Frankfurt am Main

Tag der Einreichung: 08. September 2022, Tag der Prüfung: 07. November 2022

1. Gutachten: Prof. Dr. Christian Hess
2. Gutachten: Prof. Dr. Rolf Schäfer
3. Gutachten: Prof. Dr. Rolf Jürgen Behm
Darmstadt 2022



TECHNISCHE
UNIVERSITÄT
DARMSTADT

Fachbereich Chemie
Eduard-Zintl-Institut für
anorganische und
physikalische Chemie
Arbeitsgruppe Prof. Hess

CO_x Katalyse über CeO₂ und In₂O₃ basierten Katalysatoren: Kombination von *operando* Spektroskopie und DFT

CO_x catalysis over CeO₂ and In₂O₃ based catalysts: Combining *operando* spectroscopy and DFT

Genehmigte Dissertation von Marc Niklas Ziemba

1. Gutachten: Prof. Dr. Christian Hess
2. Gutachten: Prof. Dr. Rolf Schäfer
3. Gutachten: Prof. Dr. Rolf Jürgen Behm

Tag der Einreichung: 08. September 2022

Tag der Prüfung: 07. November 2022

Darmstadt 2022

Bitte zitieren Sie dieses Dokument als:

URN: urn:nbn:de:tuda-tuprints-228699

URL: <http://tuprints.ulb.tu-darmstadt.de/22869>

Dieses Dokument wird bereitgestellt von tuprints,

E-Publishing-Service der TU Darmstadt

<http://tuprints.ulb.tu-darmstadt.de>

tuprints@ulb.tu-darmstadt.de

Die Veröffentlichung steht unter folgender Creative Commons Lizenz:

Namensnennung – Nicht kommerziell – Keine Bearbeitungen 4.0 International

<https://creativecommons.org/licenses/by-nc-nd/4.0/>

Erklärungen laut Promotionsordnung

§8 Abs. 1 lit. c PromO

Ich versichere hiermit, dass die elektronische Version meiner Dissertation mit der schriftlichen Version übereinstimmt.

§8 Abs. 1 lit. d PromO

Ich versichere hiermit, dass zu einem vorherigen Zeitpunkt noch keine Promotion versucht wurde. In diesem Fall sind nähere Angaben über Zeitpunkt, Hochschule, Dissertationsthema und Ergebnis dieses Versuchs mitzuteilen.

§9 Abs. 1 PromO

Ich versichere hiermit, dass die vorliegende Dissertation selbstständig und nur unter Verwendung der angegebenen Quellen verfasst wurde.

§9 Abs. 2 PromO

Die Arbeit hat bisher noch nicht zu Prüfungszwecken gedient.

Darmstadt, 08. September 2022

M. Ziemba

Publications

Parts of this thesis have been published so far in peer reviewed journals and at national and international conferences.

Journal articles:

- [M. Ziemba](#), J. Weyel, C. Hess, Approaching C1 Reaction Mechanisms Using Combined *Operando* and Transient Analysis: A Case Study on Cu/CeO₂ Catalysts during the LT-Water–Gas Shift Reaction, ACS. Catal. 12 (2022) 9503-9514.
- [M. Ziemba](#), M. Radtke, L. Schumacher, C. Hess, Aufklärung der CO₂-Hydrierung über In₂O₃-Nanopartikeln mittels Operando UV/Vis- und Impedanzspektroskopie, Angew. Chem. 134 (2022) e202209388.
- [M. Ziemba](#), M. Radtke, L. Schumacher, C. Hess, Elucidating CO₂ Hydrogenation over In₂O₃ Nanoparticles using Operando UV/Vis and Impedance Spectroscopies, Angew. Chem. Int. Ed. 61 (2022) e202209388.
- J. Weyel, [M. Ziemba](#), C. Hess, Elucidating Active CO–Au Species on Au/CeO₂(111): A Combined Modulation Excitation DRIFTS and Density Functional Theory Study, Top. Catal. 65 (2022) 779–787.
- [M. Ziemba](#), J. Weyel, C. Hess, Elucidating the mechanism of the reverse water–gas shift reaction over Au/CeO₂ catalysts using *operando* and transient spectroscopies, Appl. Catal. B Environ. 301 (2022) 120825.
- [M. Ziemba](#), C. Schilling, M.V. Ganduglia-Pirovano, C. Hess, Toward an Atomic-Level Understanding of Ceria-Based Catalysts: When Experiment and Theory Go Hand in Hand, Acc. Chem. Res. 54 (2021) 2884–2893.
- [M. Ziemba](#), L. Schumacher, C. Hess, Reduction Behavior of Cubic In₂O₃ Nanoparticles by Combined Multiple *In Situ* Spectroscopy and DFT, J. Phys. Chem. Lett. 12 (2021) 3749–3754.
- [M. Ziemba](#), D. Stark, C. Hess, Combined DFT and *operando* Spectroscopic Study of the Water-Gas Shift Reaction over Ceria based Catalysts: The Role of the Noble Metal and Ceria Faceting, Chem. Proc. 2 (2020) 23.
- [M. Ziemba](#), M.V. Ganduglia-Pirovano, C. Hess, Elucidating the Oxygen Storage-Release Dynamics in Ceria Nanorods by Combined Multi-Wavelength Raman Spectroscopy and DFT, J. Phys. Chem. Lett. 11 (2020) 8554–8559.
- [M. Ziemba](#), C. Hess, Influence of gold on the reactivity behaviour of ceria nanorods in CO oxidation: combining *operando* spectroscopies and DFT calculations, Catal. Sci. Technol. 10 (2020) 3720–3730.
- [M. Ziemba](#), M.V. Ganduglia-Pirovano, C. Hess, Insight into the mechanism of the water–gas shift reaction over Au/CeO₂ catalysts using combined *operando* spectroscopies, Faraday Discuss. 229 (2021) 232–250.

-
- C. Schilling, M. Ziemba, C. Hess, M.V. Ganduglia-Pirovano, Identification of single-atom active sites in CO oxidation over oxide-supported Au catalysts, *J. Catal.* 383 (2020) 264–272.

Oral Presentations:

- Ziemba, M.; Weyel, J.; Hess, C.: CO₂ activation over Au/CeO₂ catalysts in the reverse water-gas shift reaction: an operando spectroscopic study. Short lecture at the online poster workshop at 54. Jahrestreffen Deutscher Katalytiker (2021).
- Ziemba, M.; Stark, D.; Hess, C.: Combined DFT and Operando Spectroscopic Study of the Water-Gas Shift Reaction over Ceria-Based Catalysts: The Role of the Noble Metal and Ceria. Virtual presentation at 1st International Electronic Conference on Catalysis Sciences (2020).
- Ziemba, M., Schilling, C., Ganduglia-Pirovano, M. V., Hess, C.: The influence of CeO₂ surface facets on oxygen activation: A combined *in situ* Raman spectroscopic and DFT study. Oral presentation at EuropaCat (2019), Aachen, Germany.

Posters Presentations:

- Ziemba, M.; Hess, C.: Elucidating the reducibility behavior and CO₂ activation of In₂O₃ nanoparticles using multiple *in situ* / *operando* spectroscopy. Poster at ZCAM-ASEVA Workshop on Metal-Oxide Ultrathin Films and Nanostructures (2022).
- Ziemba, M.; Hess, C.: Elucidating the CO₂ Conversion via Reverse Water-gas Shift over In₂O₃ using *In Situ* / *Operando* Spectroscopies. Poster at 55. Jahrestreffen Deutscher Katalytiker (2022).
- Ziemba, M.; Weyel, J.; Hess, C.: CO₂ activation over Au/CeO₂ catalysts in the reverse water-gas shift reaction: an *operando* spectroscopic study. Online poster at 54. Jahrestreffen Deutscher Katalytiker (2021).
- Ziemba, M., Hess, C.: Elucidating the role of ceria in Au/CeO₂ catalysts during CO oxidation using *operando* Raman and UV-Vis spectroscopy. Poster at GeCatS Infoday - Operando Spectroscopy in Catalysis (2020), Frankfurt, Germany.
- Ziemba, M., Schilling, C., Ganduglia-Pirovano, M. V., Hess, C.: The potential of combining *in situ* Raman spectroscopy and DFT calculations: Elucidating the influence of CeO₂ surface facets on oxygen activation. Poster at The South-West-German Catalysis Course (2019), Höchst-Hassenroth, Germany.

Danksagung

Hiermit möchte ich mich bei allen bedanken, die mir während der Anfertigung dieser Dissertation durch ihre fachliche und/oder persönliche Unterstützung zur Seite standen. Zusätzlich möchte ich mich ausdrücklich bedanken bei ...

... Prof. Dr. Christian Hess für die hervorragende Betreuung und die vielen hilfreichen Diskussionen während dieser Thesis sowie während meiner gesamten Arbeitszeit in seiner Arbeitsgruppe. Außerdem bedanke ich mich für die im Rahmen dieser Arbeit gewährten Freiheiten.

... Dr. M. Verónica Ganduglia Pirovano für die Betreuung der DFT-Studien sowie die kontinuierliche Unterstützung und enge Zusammenarbeit.

... Dr. Christian Schilling für die Einarbeitung an der Apparatur und die Begeisterung für die Materie.

... Dr. Stefan Lauterbach aus der Gruppe von Prof. Dr. Hans-Joachim Kleebe für transmissionselektronenmikroskopische Messungen und Unterstützung bei der Auswertung.

... Dr. Martin Brodrecht und Till Wissel aus der Gruppe von Prof. Dr. Gerd Buntkowsky für Stickstoff-Adsorptionsmessungen.

... Dr. Katrin Hofmann aus der Gruppe von Prof. Dr. Barbara Albert für XRD-Messungen.

... Dr. Jochen Rohrer aus der Gruppe von Prof. Dr. Karsten Albe für die Unterstützung im VASP Code.

... Danny Stark, Antonia Poser, Henrik Hoyer und Lukas Broll, die im Rahmen ihrer Bachelorarbeit Messungen durchführten und zur Diskussion beitrugen.

... Martin Schwarz, Jürgen Ühlken und Matthias Guse stellvertretend für alle Mitarbeiter der Mechanik- und Elektrowerkstatt des Fachbereichs Chemie.

... Leon Schumacher und Jakob Weyel für diverse Messungen, Diskussionen und schöne Abende auch nach Feierabend.

... Karl Kopp für XPS Messungen sowie technische Unterstützung.

... den (ehemaligen) Kollegen Xu Cheng, Matthias Enders, Dr. Anastasia Filtschew, Dr. Marcel Heber, Karl Kopp, Maximilian Pfeiffer, Dr. Mariusz Radtke, Dr. Simone Rogg, Dr. Philip Ruff, Leon Schumacher, Jun Shen, Jan Welzenbach und Jakob Weyel für die angenehme Arbeitsatmosphäre und die ständige Hilfsbereitschaft.

... Claudia Jochem für alle administrativen Aufgaben sowie das offene Ohr bei allen anderen Problemen.

... Nina Pfuderer für das gründliche Korrekturlesen.

... meiner Familie, Freunden und meiner Freundin für die Unterstützung in allen Situationen.

Für diese Forschungsarbeit wurden Rechnungen auf dem Lichtenberg-Hochleistungsrechner der Technischen Universität Darmstadt durchgeführt.

Zusammenfassung

In der vorliegenden Arbeit werden mechanistische Studien an CeO_2 basierten und In_2O_3 Katalysatoren während der CO-Oxidation, der WGS und/oder der rWGS Reaktion durchgeführt. Um an mechanistische Informationen zu gelangen, werden verschiedenste *in situ/operando* Methoden miteinander kombiniert. So ist es durch die Kombination von *operando* Raman und *operando* UV-Vis Spektroskopie möglich, die Sauerstoffdynamiken der Metalloxide während der Reaktionen zu untersuchen. Mittels (transienter) DRIFT Spektroskopie können Adsorbate auf der Oberfläche während der Reaktion identifiziert werden und die Photoelektronenspektroskopie (XPS, UPS) liefert oberflächensensitive Informationen über Oxidationszustände der Metalle und die Oberflächenszusammensetzung. Zusätzlich zur Spektroskopie werden theoretische Rechnungen mithilfe der Dichtefunktionaltheorie (DFT) herangezogen, um ein Verständnis auf atomarer Ebene zu erzielen und so beispielsweise unbekannte Banden im Raman oder IR Spektrum zuzuordnen. Das Ziel dieser Arbeit besteht also darin, die Reaktionsmechanismen im Detail aufzuklären und den Einfluss der Trägereigenschaften und der Metalle zu ermitteln.

In diesem Kontext wird für Au/CeO_2 die aktive Spezies als $\text{O}_{\text{lattice}}-\text{Au}^+-\text{CO}$ ermittelt und die Beteiligung des Trägers an der CO-Oxidation nachgewiesen, der Sauerstoff für die Oxidation von CO zur Verfügung stellt. Für die Katalysatoren auf CeO_2 -Basis, die mit Gold oder Kupfer beladen wurden, sind außerdem facettenabhängige Untersuchungen für die (r)WGS Reaktion durchgeführt worden. In diesem Zusammenhang hat sich gezeigt, dass die facettenabhängigen Eigenschaften durch die Verwendung von Ceroxid-Nanopartikeln wie Platten, Oktaedern, Stäben und Würfeln ausgenutzt werden können, da so Eigenschaften wie z. B. die Defektbildungsenergien oder die Adsorptionsenergien verändert werden können. Zumindest die Defektbildungsenergie scheint jedoch in beiden Reaktionen keine übergeordnete Rolle zu spielen, denn obwohl sich die 100 und 110 Oberflächen leichter reduzieren lassen, sind diese weniger aktiv. Des Weiteren konnte für die WGS Reaktion ein Redox Mechanismus als der Reaktionshauptweg identifiziert werden, und zwar sowohl bei Gold als auch bei Kupfer. Interessant ist an dieser Stelle, dass die Cu/CeO_2 Katalysatoren zwar etwas geringere Aktivitäten als die Au/CeO_2 Katalysatoren aufweisen, dafür aber stabiler sind und es zu keiner Agglomeration von Kupferatomen auf der Oberfläche kommt. Bei der Betrachtung der Rückreaktion (rWGS) könnte zunächst einen ähnlicher Mechanismus erwartet werden. Jedoch haben unsere Studien gezeigt, dass im Gegensatz zur WGS Reaktion der Mechanismus ein assoziativer ist. Dies bedeutet, dass der Mechanismus über Intermediate wie z. B. Hydroxide, Formate oder Carbonate abläuft, welche mittels transienter DRIFT Spektroskopie ermittelt werden konnten.

Zuletzt wird $\text{c-In}_2\text{O}_3$ in der rWGS Reaktion betrachtet, da es auch ohne zusätzliche Metallbeladung vergleichbare Aktivitäten zu den CeO_2 Systemen aufweist. Zunächst wird jedoch das Reduktionsverhalten von $\text{c-In}_2\text{O}_3$ genauer untersucht, wobei mittels *in situ* Raman Spektroskopie und DFT erstmals eine theoretische Identifizierung der Natur der defektbezogenen Banden in reduziertem In_2O_3 erfolgen konnte. Die anschließende Betrachtung der rWGS Reaktion mittels *operando* UV-Vis sowie einem neuartigem *operando* Impedanzspektroskopie Ansatz zeigt, dass die Oxidation durch CO_2 der geschwindigkeitsbestimmende Schritt ist. Außerdem stimmen die Ergebnisse mit Redox-Prozessen überein, bei denen wasserstoffhaltige Oberflächenspezies nachweislich eine fördernde Wirkung haben.

Die Kombination von *operando* Methoden, transienten Methoden und DFT ist also ein leistungsfähiges Instrument zur Untersuchung einer breiten Palette von Oxidkatalysatoren, was für das Verständnis ihrer

Funktionsweise und die rationelle Entwicklung verbesserter Katalysatoren unerlässlich ist. Außerdem ist es wichtig, mehrere Methoden zu kombinieren, um ein umfassendes Bild sowohl von der Oberfläche als auch vom Bulk zu erhalten, da beides in das Reaktionsgeschehen involviert sein kann.

Abstract

In the present work, mechanistic studies are performed on CeO₂ based and In₂O₃ catalysts during CO oxidation, WGS and/or rWGS reaction. A wide variety of *in situ/operando* methods are combined to obtain mechanistic information. Thus, by combining *operando* Raman and *operando* UV-Vis spectroscopy, it is possible to study the oxygen dynamics of the metal oxides during the reactions. Using (transient) DRIFT spectroscopy, adsorbates on the surface can be identified during the reaction and photoelectron spectroscopy (XPS, UPS) provides surface sensitive information about oxidation states of the metals and surface composition. In addition to spectroscopy, theoretical calculations using density functional theory (DFT) are used to achieve an atomic level understanding to assign, for example, unknown bands in the Raman or IR spectrum. Thus, the goal of this work is to elucidate the reaction mechanisms and to determine the influence of the support properties and the metals.

In this context, for Au/CeO₂, the active species is determined as O_{lattice}-Au⁺-CO and the role of the support in CO oxidation is demonstrated, providing oxygen for the oxidation of CO. Facet-dependent studies on the (r)WGS reaction have also been carried out for the CeO₂-based catalysts loaded with gold or copper. In this context, it has been shown that the facet-dependent properties can be exploited by using ceria nanoparticles such as sheets, octahedra, rods, and cubes, since properties such as the defect formation energies or adsorption energies can be changed. However, at least the defect formation energy does not seem to play a predominant role in both reactions, because although the 100 and 110 surfaces are easier to reduce, they are less active. Furthermore, for the WGS reaction, a redox mechanism could be identified as the main pathway, which is the case for both gold and copper. It is interesting to note at this point that although the Cu/CeO₂ catalysts have slightly lower activities than the Au/CeO₂ catalysts, they are more stable and that there is no agglomeration of copper atoms on the surface. When considering the reverse reaction (rWGS), a similar mechanism would initially be expected. However, our studies have shown that unlike the WGS reaction, the mechanism is an associative one. This means that the mechanism proceeds via intermediates such as hydroxides, formates or carbonates, which could be determined by transient DRIFT spectroscopy.

Lastly, c-In₂O₃ is considered in the rWGS reaction since it exhibits comparable activities to the CeO₂ systems even without additional metal loading. First, however, the reduction behavior of c-In₂O₃ is examined in more detail, with *in situ* Raman spectroscopy and DFT providing the first theoretical identification of the nature of the defect-related bands in reduced In₂O₃. Subsequent consideration of the rWGS reaction using *operando* UV-Vis as well as a novel *operando* impedance spectroscopy approach shows that oxidation by CO₂ is the rate-determining step. Moreover, the results are consistent with redox processes where hydrogen-containing surface species have been shown to have a promoting effect. Thus, the combination of *operando* methods, transient methods, and DFT is a powerful tool for studying a wide range of oxide catalysts, which is essential for understanding their mode of operation and rational design of improved catalysts. Moreover, it is important to combine several methods to obtain a comprehensive picture of both the surface and the bulk, since both may be involved in the reaction processes.

Inhaltsverzeichnis

1	Einleitung	1
2	Experimentelle und theoretische Methoden	5
2.1	<i>In situ/operando</i> spektroskopischer Ansatz	5
2.1.1	Raman und UV-Vis Messungen	6
2.1.2	Transiente DRIFTS Messungen	7
2.1.3	Elektrochemische Impedanzspektroskopie (EIS)	8
2.2	Quasi <i>in situ</i> Photoelektronenspektroskopie (UPS, XPS)	8
2.3	Theoretische Berechnungen (DFT) als Ergänzung zum Experiment	8
2.3.1	Details zur Berechnung der Raman-Spektren[35]	11
3	Experimentalteil	15
3.1	Probenpräparation	15
3.2	Charakterisierung der CeO ₂ und In ₂ O ₃ Proben	16
3.2.1	<i>Ex situ</i> Charakterisierungsmethoden	16
3.2.2	Multi <i>in situ</i> Apparatur	17
3.2.3	Weitere <i>in situ/operando</i> Charakterisierungsmethoden	20
4	Ergebnisse und Diskussion	21
5	Ausblick	133
	Literaturverzeichnis	137
	Abkürzungsverzeichnis	139

1 Einleitung

Katalysatoren sind für chemische Reaktionen unerlässlich und daher in der chemischen Industrie unverzichtbar. In diesem Kontext werden mehr als 85 % aller großtechnisch hergestellten Chemikalien mithilfe von festen Katalysatoren hergestellt.[1] Aber auch bei der Vermeidung von Emissionen leisten sie einen großen Beitrag, wobei das wohl bekannteste Beispiel der Autoabgaskatalysator ist, bei welchem nicht verbrannte Kohlenwasserstoffe oder CO zu CO₂ oxidiert werden. Für solche Oxidationsreaktionen werden oft Edelmetalle (Pd, Pt, Rh, Au) eingesetzt. Durch die Trägerung der Edelmetalle auf Metalloxiden werden deutlich geringere Mengen der Edelmetalle benötigt, was diese Klasse von Katalysatoren deutlich ressourcenschonender macht. In diesem Zusammenhang können die Trägermaterialien die katalytische Aktivität über Metall-Träger-Wechselwirkungen oder durch die Beteiligung an der Katalyse selbst stark beeinflussen. Sie lassen sich in inaktive (z. B. SiO₂, Al₂O₃) und aktive (z. B. TiO₂, CeO₂, In₂O₃) Materialien unterteilen. Aber nicht nur der Träger oder das Metall haben Einfluss auf die katalytischen Eigenschaften, sondern auch die Oberflächenterminierung der Nanopartikel, weshalb für Ceroxid auch facettenabhängige Nanopartikel betrachtet werden. In diesem Kontext hat sich gezeigt, dass die facettenabhängigen Eigenschaften durch die Verwendung von Ceroxid Nanopartikeln wie Oktaedern, Stäben und Würfeln ausgenutzt werden können.[2, 3] So unterscheiden sich die Oberflächenterminierungen dieser Partikel, wobei die Oktaeder die 111-, die Würfel die 100- und die Stäbchen die 100- sowie 110-Oberfläche ausbilden.[4, 5] Beispielsweise unterscheiden sich die Adsorptionsenergien für Reaktionsgase, die Metall-Träger-Wechselwirkungen oder das Reduktionsverhalten.[2] Somit bietet die Veränderung der Form jener Ceroxid-Nanopartikel ein zusätzliches leistungsfähiges Instrument zur Entwicklung von Materialien mit verbesserten katalytischen Eigenschaften. Für eine detaillierte Beschreibung sowie Darstellung dieser Oberflächenterminierungen soll auf die erste Publikation in Kapitel 4 hingewiesen werden.

Aktive Trägermaterialien wie Ceroxid oder Indiumoxid zeichnen sich durch ihre Reduzierbarkeit und ihre direkte Beteiligung am Redoxzyklus aus. So lässt sich beispielsweise CeO₂ aufgrund der guten Redoxeigenschaften und der hohen Sauerstoffmobilität als Sauerstoffspeicher verwenden. Daher ist das Verständnis der O₂-Adsorption, -Aktivierung und -Dynamik der Schlüssel zur Erreichung einer verbesserten katalytischen Effizienz in Oxidationsreaktionen. Aus diesem Grund soll in dieser Arbeit auch die Aktivierung von O₂ auf CeO₂ ein Thema sein, um ein grundlegendes Verständnis zu generieren, bevor zu den Reaktionen übergegangen wird. In diesem Kontext wurde in früheren Studien von YANG *et al.* die Abhängigkeit der Sauerstoffaktivierung mit der CeO₂ Oberflächenterminierung anhand von Einkristalloberflächen untersucht,[6] während sich die Arbeit von SCHILLING *et al.* mit katalytisch interessanten Cerdioxid-Pulverproben mit entweder CeO₂(111)- oder CeO₂(100)-Oberflächenterminierung befasst hat.[7] In dieser Arbeit wird mittels *in situ* Raman Spektroskopie und DFT die Dynamik der Sauerstoffspeicherung und -freisetzung für CeO₂-Nanostäbe (110 und 100) untersucht. Eine Zusammenfassung dieser Eigenschaften (Adsorptionsenergien, O-O Bindungslängen, Defektbildungsenergien) ist für alle low-index Oberflächen von CeO₂ in der ersten Publikation von Kapitel 4 zu finden. Für ein guten Überblick über die Sauerstoffdefektbildung auf den CeO₂ Oberflächen soll zusätzlich auf die Literatur verwiesen werden.[8]

In Hinblick auf die Katalysatoren sollen in dieser Arbeit die aktiven Metalloxide CeO₂ und In₂O₃ näher untersucht werden. CeO₂ wird dabei als Träger für Gold oder Kupfer verwendet, In₂O₃ fungiert selbst als Katalysator. Der Vergleich zwischen Gold und Kupfer ist von besonderem Interesse, da auf den ersten Blick

ähnliche Eigenschaften zu erwarten sind, Kupfer aber beispielsweise eine höhere Affinität zu Sauerstoff und eine bessere Stabilität bei Reaktionen aufweist. Des Weiteren ist Kupfer deutlich kostengünstiger und als Rohstoff besser verfügbar, was die Verwendung von Kupfer interessanter macht.

Im Rahmen der CeO₂ basierten Katalysatoren werden die CO-Oxidation, die Wassergas-Shift (WGS) Reakti-

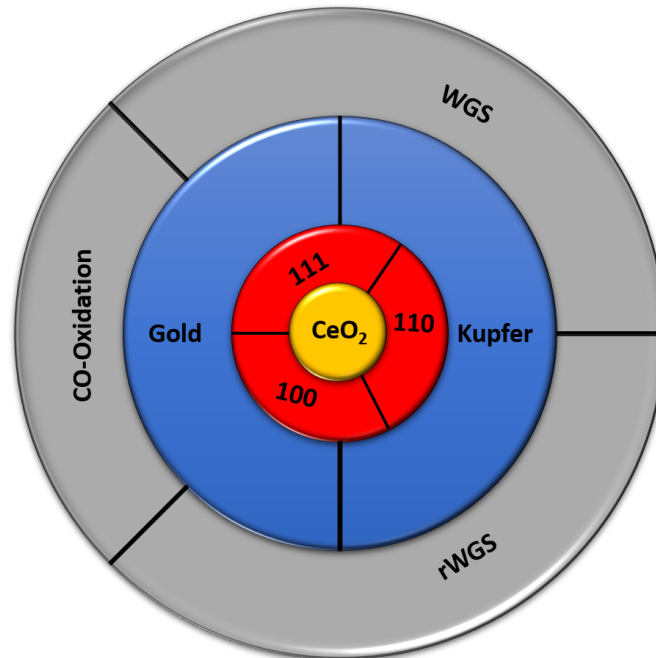
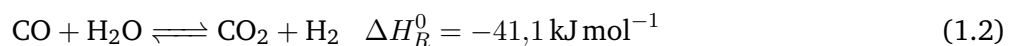


Abbildung 1.1: Überblick der verwendeten CeO₂ basierten Katalysatoren und deren Verwendung in den verschiedenen Reaktionen.

on und die reverse Wassergas-Shift (rWGS) Reaktion betrachtet. Die CO-Oxidation wird nur für die Au/CeO₂ Katalysatoren untersucht. Die Reaktionsgleichung für die CO-Oxidation ist in Gleichung (1.1) und für die (reverse) Wassergas-Shift Reaktion in Gleichung (1.2) dargestellt. Hierbei wird sofort deutlich, dass es sich bei der CO-Oxidation um eine hoch exotherme Reaktion und bei der (reversen) Wassergas-Shift Reaktion um eine Gleichgewichtsreaktion handelt, die bezüglich der Bildung von CO₂ und H₂O (WGS) exotherm und in umgekehrter Richtung (rWGS) endotherm ist. Einen Überblick der in dieser Arbeit betrachteten Reaktionen sowie der Kombination des CeO₂ Trägers und des Metalls soll Abb. 1.1 schaffen. Hierbei wird deutlich, dass CeO₂ zwar als Träger dient, die Oberflächenterminierung sowie das Metall aber variiert werden kann. Für In₂O₃ werden lediglich das Reduktionsverhalten unter H₂ und die reverse Wassergas-Shift Reaktion untersucht.



Im Folgenden soll kurz auf die Relevanz und den Stand der Forschung der drei Reaktionen eingegangen werden, wobei für einen ausführlicheren Stand der Forschung auf die einzelnen Publikationen aus Kapitel 4 verwiesen werden soll. Angefangen mit der CO-Oxidation, die bei niedrigen Temperaturen nicht nur von praktischer Bedeutung ist, sondern auch eine wichtige Prototypreaktion in der heterogenen Katalyse darstellt, spielt sie in Kombination mit der Wassergas-Shift Reaktion eine wichtige Rolle bei Prozessen, in denen

die Reinheit des H₂-Stroms entscheidend ist, wie z. B. bei Brennstoffzellenanwendungen. So ist es allein durch die Hoch- und Tieftemperatur Wassergas-Shift Reaktion nicht möglich, den CO-Gehalt auf <30 ppm zu reduzieren, weshalb die anschließende CO-Oxidation essentiell ist.[9, 10] Aus diesen Gründen wird sie auch in dieser Arbeit für die Au/CeO₂ Katalysatoren betrachtet, um ein erstes fundamentales Verständnis zu generieren, während die Komplexität in Hinblick auf die Reaktion möglichst klein gehalten wird. Trotz der geringen Komplexität der Reaktion selbst wird der Mechanismus der CO-Oxidation über Goldkatalysatoren auf Ceroxidträgern in der Literatur immer noch diskutiert. Des Weiteren hat sich gezeigt, dass sowohl die Beschaffenheit des Trägers (spezifische Oberfläche, Oberflächenterminierung, Partikelgröße) als auch die Natur der Goldpartikel von Bedeutung sind.[3, 11–13] Beide Aspekte sollen daher auch Thema dieser Arbeit sein.

Wie oben bereits erwähnt, spielt die WGS Reaktion eine wichtige Rolle bei der Einstellung der Wasserstoff- und Kohlenmonoxidgehalt für Brennstoffzellenanwendungen. Darüber hinaus besitzt Wasserstoff eine zentrale Rolle bei der Herstellung von Feinchemikalien und im Energiesektor. Da seine Hauptquelle die Reformierung von Kohlenwasserstoffen ist,[14] wird es in Zukunft unerlässlich sein, alternative Quellen wie die Wasserspaltung und die Umwandlung von Wasser im Rahmen der Wassergas-Shift Reaktion (WGS) zu nutzen. Es ist daher von großer Bedeutung, effiziente und kostengünstige WGS Katalysatoren zu finden, die auch bei niedrigen Temperaturen (<200 °C) effizient arbeiten. In der Industrie werden für die Tieftemperatur Wassergas-Shift Reaktion (<300 °C) Kupfer-Zinkoxid-Katalysatoren verwendet.[10] Metallbeladenes Ceroxid hat sich jedoch als eine gute Alternative zu den herkömmlich verwendeten Katalysatoren erwiesen[15, 16] und bietet den Vorteil, dass es an Luft nicht pyrophor ist sowie keine Vorbehandlungen vor der Verwendung benötigt.[10]

Die WGS Reaktion kann zwar zur Erzeugung von H₂ eingesetzt werden, jedoch ist die Rückreaktion zur Erzeugung von CO aus CO₂ ebenfalls von großem Interesse. Denn die ständig steigenden CO₂-Emissionen[17] und die sich daraus ergebenden Auswirkungen auf den Treibhauseffekt machen es notwendig, sich mit dem Thema CO₂ zu befassen. Bei einer zunehmenden Zahl von CO₂-Abscheidungstechnologien ist seine Aktivierung und Nutzung als C1-Quelle auch als eine attraktive Strategie anzusehen.[18] Die Nutzung von CO₂ als nicht-fossile Quelle für die Herstellung von Synthesegas ist aufgrund seiner Vielseitigkeit und Eignung für eine Vielzahl von Anwendungen von besonderem Interesse. In diesem Zusammenhang spielt die rWGS Reaktion eine wichtige Rolle im Energiesektor, bei der CO₂ zunächst in CO und dann durch CO-Hydrierung (Fischer-Tropsch-Verfahren) in flüssige Brennstoffe umgewandelt werden kann.

Edelmetallbeladene CeO₂-Katalysatoren haben sich zwar als aktiv für die WGS und rWGS Reaktion erwiesen,[15, 16, 18] ihre Funktionsweise (Redox- oder Assoziationsmechanismus) ist jedoch noch umstritten. Bezüglich der Mechanismen lässt sich allgemein sagen, dass ein regenerativer Redoxmechanismus ohne Intermediate verläuft, während der assoziative Mechanismus über Intermediate wie beispielsweise Carbonate, Formate oder Carboxylate abläuft. Ein gleichzeitiges Auftreten beider Mechanismen ist ebenfalls denkbar. Für In₂O₃ ist dies ebenfalls der Fall, welches sogar bereits ohne zusätzliches Metall merkliche Aktivitäten in der rWGS Reaktion aufweist.[19] Somit ist die Komplexität bei In₂O₃ in Hinblick auf das Katalysatorsystem etwas reduziert, da es die Eigenschaften des Metalloxids alleine sind, die die katalytischen Eigenschaften steuern. Des Weiteren ist In₂O₃ ein interessantes Material für die Methanolsynthese und gewinnt immer mehr an Aufmerksamkeit.[20, 21]

Zusammenfassend wird in dieser Arbeit also die CO-Oxidation, die WGS und die rWGS Reaktion behandelt. Ziel ist es, durch die Kombination verschiedener *operando* spektroskopischer Methoden ein tiefergehendes Verständnis bezüglich der Reaktionsmechanismen zu erhalten. Dieses Vorgehen wird außerdem durch die Dichtefunktionaltheorie (DFT) unterstützt, um ein Verständnis auf atomarer Ebene zu erzielen.

2 Experimentelle und theoretische Methoden

2.1 *In situ/operando* spektroskopischer Ansatz

Bei der Aufklärung von Mechanismen in der heterogenen Katalyse ist es essentiell, spektroskopische Methoden unter Arbeitsbedingungen zu implementieren. Dies ist der Tatsache geschuldet, dass die Oberflächenchemie von Katalysatoren, wie z.B. von reduzierbaren Oxiden (z.B. CeO_2 , In_2O_3 , TiO_2), stark von den Arbeitsbedingungen beeinflusst wird. Außerdem können die Umweltbedingungen auch Einfluss auf den Reaktionsmechanismus haben.[22] Aus diesem Grund hat sich in diesem Bereich die *in situ* und *operando* Spektroskopie etabliert und ist für ein fundamentales Verständnis nicht mehr wegzudenken. Während die *in situ* Spektroskopie eine Methodik bezeichnet, die auf den Katalysator unter spezifischen Bedingungen angewendet wird, werden bei der *operando* Spektroskopie gleichzeitig auch die katalytische Aktivität sowie die Selektivität bestimmt. Oft wird *operando* auch im Rahmen von realistischen Bedingungen der entsprechenden chemischen Prozesse verwendet. Dies bezieht sich dann auf den Reaktortyp und/oder die katalytischen Bedingungen (z.B. Druck, Temperatur, Gaszusammensetzung). In dieser Arbeit soll jedoch von *operando* die Rede sein, sobald sich das System unter Reaktionsbedingungen befindet und gleichzeitig die katalytische Aktivität aufgenommen wird. Zusammenfassend lassen sich mit der *in situ* Spektroskopie somit zwar wichtige strukturelle Informationen gewinnen, Struktur-Aktivitäts-Beziehungen lassen sich jedoch nur mittels *operando* Spektroskopie erhalten.

Zunächst soll ein kurzer Einblick in die Literatur hinsichtlich der *operando* Spektroskopie in der heterogenen Katalyse gegeben werden. Der Begriff *operando* tauchte im Zusammenhang mit der Katalyse dabei erstmals im Jahr 2002 in mehreren Veröffentlichungen der BAÑARES-Gruppe auf.[23–25] Dennoch gab es schon zuvor Studien, die sich mit *operando* Spektroskopie beschäftigten, allerdings ohne den Begriff namentlich zu erwähnen.[26, 27] Einen guten Überblick über die *operando* Spektroskopie an verschiedenen Katalysatorsystemen sowie Reaktionen bietet der Übersichtsartikel von WACHS *et al.* aus dem Jahr 2017.[28] Im Zusammenhang mit reduzierbaren Oxiden als Trägermaterialien (CeO_2 , TiO_2) für verschiedenste Metalle zeigt der Übersichtsartikel von WANG *et al.*, dass zum Verständnis des Zusammenspiels zwischen Metall und Träger sowie der Charakterisierung der aktiven Stellen an den Grenzflächen zwischen Metall und Träger unterschiedliche *operando* Methoden essentiell sind.[22] Spezifischer behandelt schließlich der Übersichtsartikel von ABDEL-MAGEED *et al.* die *in situ / operando* Spektroskopie (XAS, DRIFTS, Raman) und TAP-Reaktor-Studien über Au/CeO_2 Katalysatoren während der CO-Oxidation.[29] So kann der Oxidationszustand von Gold unter Reaktionsbedingungen als weitestgehend metallisch identifiziert werden und die Entstehung von Ce^{3+} unter Reaktionsbedingungen konnte beobachtet werden. Des Weiteren zeigt sich, dass die Goldpartikelgröße unter Reaktionsatmosphäre zunimmt, was zur Deaktivierung des Katalysators beiträgt.

Zusammenfassend wird aufgrund der Komplexität von Katalysatorsystemen deutlich, dass es in den meisten Fällen essentiell ist, verschiedene *operando* Methoden zu kombinieren, da eine einzige Methode meist nicht ausreichend ist, um genug Informationen zur Aufklärung des Reaktionsmechanismus zu erhalten. Folglich werden auch in dieser Arbeit verschiedene Methoden miteinander kombiniert, um so einen möglichst detaillierten Einblick in die Aufklärung des Reaktionsmechanismus zu erhalten. Die Grundlagen dieser Methoden werden in den folgenden Kapiteln näher beschrieben. So soll in dieser Arbeit vor allem ein bereits

bestehendes Setup verwendet werden, welches *operando* Raman und *operando* UV-Vis Spektroskopie kombiniert. Diese Kombination hat sich bereits in früheren Studien bewährt,[30, 31] und im nächsten Kapitel wird nochmals auf diese Kombination eingegangen. Des Weiteren werden transiente DRIFTS Messungen verwendet, um Informationen über mögliche Reaktionsintermediate zu erhalten (siehe Abschnitt 2.1.2). Zuletzt wurde außerdem ein neuartiger *operando* Impedanzspektroskopie Ansatz entwickelt (siehe Abschnitt 2.1.3). Auf diesen soll jedoch nur kurz eingegangen werden, da er nur einen kleinen Teil der Arbeit repräsentiert und nur zum Teil an dessen Entwicklung mitgewirkt wurde.

2.1.1 Raman und UV-Vis Messungen

Mit Hilfe der Raman Spektroskopie lassen sich wichtige Informationen über Schwingungszustände gewinnen. Grundlage hierfür ist der Raman-Effekt, der die inelastische Streuung von Licht an Molekülen beschreibt. Die Voraussetzung für die Raman-Aktivität ist eine Änderung der Polarisierbarkeit während der Schwingung. Das Spektrum ergibt sich dann aus der Differenz zwischen der Anregungswellenlänge und dem inelastisch gestreuten Licht. Dies ist einer der Gründe, warum eine monochromatische Lichtquelle benötigt wird, bei der es sich in der Regel um einen Laser handelt. Folglich werden im Spektrum Frequenzverschiebungen zu kleineren und zu größeren Energien beobachtet, welche als Stokes- bzw. Anti-Stokes-Linien bezeichnet werden. Aufgrund der höheren Population des Grundschwingungszustands ($v = 0$) ist die Stokes-Streuung in der Praxis jedoch relevanter als die Anti-Stokes-Streuung. Für weitergehende Informationen bezüglich der Raman Spektroskopie soll jedoch auf folgende Literatur hingewiesen werden.[32, 33]

Im Folgenden werden die für diese Arbeit relevanten Aspekte der Raman Spektroskopie kurz erläutert. So liefert sie Informationen über die Struktur von Festkörpern, aber auch im Hinblick auf Sauerstoffdefekte oder Adsorbate können Informationen gewonnen werden. Einen umfassenden Überblick für die Anwendung und das Potential der Raman Spektroskopie in der Katalyse bietet der Übersichtsartikel von C. HESS.[34] Für polykristallines CeO_2 hat die Arbeit von SCHILLING *et al.* die Grundlage für ein tiefergehendes Verständnis der Interpretation der Banden geschaffen.[35] Diese theoretische Studie zeigt beispielsweise, dass die Raman-aktive Mode erster Ordnung (F_{2g}) bei der Entstehung von Sauerstoffdefekten im Kristallgitter rot verschoben wird, was sich durch die Volumenausdehnung des Gitters erklären lässt. Diese wird durch die Ce^{3+} -Ionen hervorgerufen, da diese einen größeren Ionenradius als Ce^{4+} haben (Ce^{4+} : 1,143 Å; Ce^{3+} : 0,970 Å).[36] Des Weiteren können wertvolle Informationen über die Aktivierung von Sauerstoff gewonnen werden.[7] Dieser Aspekt wird jedoch in Kapitel 4 erneut aufgegriffen und soll deshalb an dieser Stelle nicht weiter diskutiert werden. Eine gute Zusammenfassung des Potentials der Raman Spektroskopie im Kontext von CeO_2 -basierten Materialien bietet der Übersichtsartikel von S. LORIDANT.[37]

Dadurch, dass die meisten elektronischen Übergänge von Festkörpern im sichtbaren oder UV-Bereich liegen, lassen sich durch die UV-Vis Spektroskopie auch Informationen elektronischer Natur gewinnen. So kann eine Änderung der elektronischen Struktur beispielsweise durch die Entstehung von intrinsischen Defekten im Kristallgitter, die Änderung des Oxidationszustands oder durch die Entstehung von Adsorbaten auf der Oberfläche hervorgerufen werden. Somit ist eine Kombination zwischen Raman und UV-Vis Spektroskopie ein guter sich ergänzender Ansatz für die Katalysatorforschung, welcher sich schon in früheren Studien von WECKHUYSEN *et al.* auf $\text{Cr}/\text{Al}_2\text{O}_3$, $\text{Mo}/\text{Al}_2\text{O}_3$ oder Mo/SiO_2 erprobt hat.[38–40] Für dynamische Systeme wie CeO_2 ist dies von besonderem Interesse, da sich durch die leichte Reduzierbarkeit sowie die Gittersauerstoff-Mobilität die Oxidationszustände der Cer-Atome an die Umgebung anpassen, wobei sich eine Reduktion von CeO_2 im sichtbaren Bereich bemerkbar machen würde. Bei der Entstehung einer Sauerstoffleerstelle wird ein $\text{Ce}4f$ -Zustand besetzt und es kommt zu einer Lokalisierung des Elektrons. Dieser Zustand liegt zwischen dem $\text{O}2p$ (besetzt)- und dem $\text{Ce}4f$ (unbesetzt)-Zustand. Diese Energiedifferenz zwischen $\text{O}2p$ (besetzt) und $\text{Ce}4f$ (unbesetzt) wird zwischen 1,5 eV und 2,5 eV (820–496 eV) erwartet, was zu einem Ladungstransfer von $\text{Ce}4f$ (besetzt) \rightarrow $\text{Ce}4f$ (unbesetzt) ($\text{Ce}^{3+} \rightarrow \text{Ce}^{4+}$) führen kann.[31, 41] Für Au/CeO_2 Katalysatoren

während der CO Oxidation zeigte sich mittels UV-Vis Spektroskopie schon eine Abhängigkeit der Absorption im sichtbaren Bereich und des Reduktionsgrades, was mittels Raman Spektroskopie validiert wurde.[30, 31]

Für In_2O_3 gibt es bezüglich der Raman Spektroskopie und dem Absorptionsverhalten im UV-Vis zwar einige fundamentale Studien,[42–45] jedoch sind vor allem in Hinblick auf Sauerstoffdefekte noch nicht alle Aspekte vollständig geklärt. Aus diesem Grund wird an dieser Stelle auf die zehnte Publikation in Kapitel 4 verwiesen.

2.1.2 Transiente DRIFTS Messungen

Zur Identifizierung von Adsorbaten auf der Katalysatoroberfläche wurde in dieser Studie die diffuse Reflexions-Fourier-Transformations-Infrarot-Spektroskopie (DRIFTS) eingesetzt. Im Gegensatz zur Raman Spektroskopie basiert die Infrarot-Spektroskopie nicht auf der Streuung von Licht, sondern auf der Absorption. So wird bei der Infrarot-Spektroskopie ein Photon mit der Frequenz $h\tilde{\nu}_{\text{vib}}$ absorbiert, um beispielsweise ein Molekül vom Grundzustand ($v = 0$) in einen höheren Zustand ($v = 1$) anzuregen.

Eine große Herausforderung bei der Infrarot-Spektroskopie an katalytisch interessanten Pulverproben ist die Vielzahl an Signalen, welche unter anderem auch überlagern können. Diese Signale setzen sich beispielsweise aus Adsorbaten wie Carbonaten, Formaten oder Hydroxiden zusammen. Zwar kann eine Vielzahl der Adsorbate durch geeignete Vorbehandlungen von der Oberfläche entfernt werden, stabile Adsorbate bleiben aber dennoch bestehen. Unter *operando* Bedingungen können außerdem stabile Adsorbate gebildet werden, welche nicht am Reaktionsfortschritt beteiligt sind, sogenannte Beobachter-Spezies. Zur Aufklärung von Reaktionsmechanismen sind jedoch lediglich Intermediate von Interesse, die zur Bildung der Produkte beitragen und meist nur kurzlebig sind. Des Weiteren reagieren diese auch auf die Veränderung der Gasumgebung, was in den transienten Messungen ausgenutzt werden kann. Um genau diese Intermediate zu identifizieren, wird das System zunächst in Sauerstoffatmosphäre bei der jeweiligen Reaktionstemperatur ausgeheizt, um die Oberfläche durch eine Oxidation der Adsorbate zu CO_2 oder H_2O so sauber wie möglich zu bekommen. Anschließend wird das System in einen stationären Zustand gebracht, indem es vor den eigentlichen Messungen schon der Reaktionsatmosphäre ausgesetzt wird. Im Anschluss wird der Hintergrund unter Anwesenheit einer oder beider Edukte an der Probe selbst aufgenommen. Die eigentliche Messung erfolgt schließlich unmittelbar nach Einschalten des anderen Edukts oder nach dem Ausschalten eines Eduktes. Unter diesen Bedingungen zeigt sich, welche Adsorbate bei Zu- oder Abschalten eines Eduktes von der Oberfläche verschwinden (negatives Signal) oder entstehen (positives Signal). Beim Vergleich der An- und Abschalt-Experimente, welche bei zwei Edukten jeweils vier Messungen ergeben, können so bei gleicher Signatur der Banden Intermediate eindeutig identifiziert werden.

Eine besondere Methode stellt hier die Modulations-Anregungs-Spektroskopie dar, welche von BAURECHT und FRINGELI 2001 vorgestellt wurde.[46] Hierbei werden Reaktionsparameter wie beispielsweise Konzentration, Temperatur, Druck oder andere Parameter periodisch geändert. Während dieser Modulation werden schließlich kontinuierlich Spektren aufgenommen, so dass auch die Reaktion des Systems auf die Stimulation sichtbar wird. Dabei reagieren die verschiedenen Spezies unterschiedlich auf die Stimulationen. In diesem Kontext verschwindet beispielsweise das Rauschen, da dieses nicht von der Stimulation beeinflusst wird und zufällig ist. Beobachter-Spezies folgen zwar zunächst der Stimulation, erreichen dann aber ein stabiles Signal. Aus diesem Grund verschwinden auch solche Signale aus den Spektren. Spezies, die durch die Stimulation gestört werden, folgen dieser mit der gleichen Frequenz, jedoch mit einer Zeitverzögerung. Aus diesem Grund können mittels ME-DRIFTS zusätzliche Informationen gewonnen werden. Ein weiterer Vorteil ist auch die Detektion von Spezies mit sehr kleinen Konzentrationen an der Oberfläche, die bei der konventionellen DRIFTS durch das Rauschen nicht sichtbar wären. Für weitere Informationen soll auf die Literatur verwiesen werden.[47, 48]

2.1.3 Elektrochemische Impedanzspektroskopie (EIS)

Bei der elektrochemischen Impedanzspektroskopie (EIS) wird der frequenzabhängige Wechselstromwiderstand einer Probe vermessen. Dabei gibt es verschiedene Messmodi, wobei in dieser Arbeit die potentiostatische EIS (PEIS) verwendet wird. Hierbei wird die Probe mit einer sinusförmigen Spannung angeregt, während der Strom gemessen wird. Eine andere Möglichkeit wäre die Anregung über einen sinusförmigen Strom, wobei die Spannung gemessen wird. Diese Methode bezeichnet man als galvanostatische EIS (GEIS). EIS eignet sich gut, um Informationen über Redoxprozesse in Metalloxiden während verschiedener Temperatur- und/oder Gasbehandlungen zu gewinnen. So wird sie bereits bei der Untersuchung von Solarzellen, Ionen-Batterien oder Elektro- und Photokatalysatoren eingesetzt.[49] Trotz der breiten Anwendung und des Potentials der Methode wird sie in der (thermischen) heterogenen Katalyse nur selten eingesetzt und geschieht in der Regel an Pellets.[42, 50–52] *Operando* Studien an katalytisch interessanten Pulverproben sind nach dem Wissen des Autors in der Literatur noch nicht vertreten. Des Weiteren erfolgt keine detaillierte Auswertung in Bezug auf Ersatzschaltbilder, trotz der Möglichkeit auf signifikante neue Einblicke in Hinblick auf den Reaktionsmechanismus.

2.2 Quasi *in situ* Photoelektronenspektroskopie (UPS, XPS)

Die Photoelektronenspektroskopie beruht auf dem äußeren Photoeffekt, wobei mit Röntgenstrahlung Rumpfelektronen und mit UV-Strahlung Elektronen aus dem Valenzband herausgelöst werden. Durch die Bestimmung der Bindungsenergie über ihre kinetische Energie bei einer definierten Wellenlänge können mittels XPS Aussagen über die Elementzusammensetzung oder sogar die jeweiligen Oxidationsstufen der enthaltenen Elemente im Oberflächenbereich gemacht werden. Mittels UPS können Aussagen über die Valenzbandstruktur gemacht werden, welche durch Adsorption von Gasmolekülen beeinflusst werden kann. Aufgrund der Detektion von Elektronen bei der Photoelektronenspektroskopie wird in der Regel ein Ultrahochvakuum benötigt.

In dieser Arbeit finden die Messungen ebenfalls unter Ultrahochvakuumbedingungen statt, jedoch kann die Probe zuvor mittels Temperatur- und Gasabfolgen vorbehandelt werden. Der Proben transfer in die Messkammer kann dann unter Luftausschluss stattfinden. Diese Messungen werden als quasi *in situ* bezeichnet. Durch den hohen Druckunterschied zwischen den realen Katalyse- und den XPS/UPS-Bedingungen können jedoch stabile Adsorbate auf der Oberfläche desorbieren, weshalb der Oberflächenzustand von den *in situ* Bedingungen abweichen kann. Des Weiteren können durch die Zeitverzögerungen Umstrukturierungen zwischen Oberfläche und Bulk stattfinden, was ebenfalls einen Einfluss auf die Oberflächenzusammensetzung haben kann. Dennoch können diese Messungen wertvolle Informationen liefern, da beispielsweise auch schon geringe Mengen an Gold oder Kupfer detektiert werden können.

In Hinblick auf *in situ* Messungen gibt es jedoch bereits XPS-Ansätze, die einen Druck von wenigen mbar an der Probe zulassen. Solche NAP-XPS-Ansätze kamen in dieser Arbeit jedoch nicht zum Einsatz, weshalb an dieser Stelle auf die Literatur verwiesen werden soll.[53]

2.3 Theoretische Berechnungen (DFT) als Ergänzung zum Experiment

Als unterstützende Methode zum Experiment wird in dieser Arbeit die Dichtefunktionaltheorie (DFT) verwendet. So ist es möglich, die Schwingungsstrukturen der Festkörper In_2O_3 und CeO_2 genauer zu analysieren sowie Informationen über Adsorptionsenergien oder Schwingungsfrequenzen möglicher Adsorbate auf deren Oberflächen zu erhalten. Dabei ist es erwähnenswert, dass die DFT in letzter Zeit aufgrund der Genauigkeit und des vergleichbar niedrigen Rechenaufwands große Bedeutung in der Beschreibung der

Funktionsweise von Katalysatoren erlangt hat und für ein detailliertes Verständnis auf molekularer Ebene nicht mehr wegzudenken ist.[6, 7, 35, 54]

Im Rahmen der DFT soll zuerst eine kurze allgemeine Einführung gegeben werden, bevor zu den arbeitsspezifischen Details übergegangen wird. Außerdem soll angemerkt werden, dass im Folgenden bei allen Beschreibungen atomare Einheiten verwendet werden, d.h. alle Konstanten besitzen den Wert 1 und werden somit nicht aufgeführt.

Die zentrale Größe der Dichtefunktionaltheorie ist die Elektronendichte $\rho(\vec{r})$, wobei diese über das folgende Mehrfachintegral definiert ist:

$$\rho(\vec{r}) = N \int \dots \int |\Psi(\vec{x}_1, \vec{x}_2, \dots, \vec{x}_N)|^2 ds_1 d\vec{x}_2 \dots d\vec{x}_N \quad (2.1)$$

Somit gibt ρ die Wahrscheinlichkeit an, eines der N Elektronen innerhalb des Volumenelements $d\vec{r}_1$ anzutreffen, mit beliebigem Spin, während die anderen $N - 1$ Elektronen beliebige Positionen und Spins in dem durch die Wellenfunktion ψ dargestellten Zustand haben.[55]

Die Dichtefunktionaltheorie beruht im Wesentlichen auf den zwei HOHENBERG-KOHN-Theoremen. Dabei besagt das erste, dass die exakte Grundzustandsenergie durch ein Funktional der Elektronendichte $F[\rho(\vec{r})]$ dargestellt werden kann. Dieses Funktional ist universell, d.h. es ist für jedes System identisch. Die Elektronendichte ρ ist dabei selbst eine Funktion von Ort \vec{r} und weist Maxima am Ort der Atomkerne auf. Ein Integral über die Dichte ergibt somit die Anzahl der Elektronen im System.

Das zweite HOHENBERG-KOHN-Theorem besagt, dass für die Elektronendichte das Variationsprinzip gilt. Dies bedeutet, dass das universelle Funktional nur dann die minimale Energie wiedergibt, wenn es sich um die exakte Elektronendichte handelt.[55–57] Dies lässt sich wie folgt beschreiben:

$$F[\rho(\vec{r})_{\text{Test}}] \geq E_{\text{exakt}, 0} \quad (2.2)$$

Das Funktional für die Energie setzt sich aus der Summe der kinetischen Energie der Elektronen $T_e[\rho]$, der Elektron-Kern-Anziehung $E_{eK}[\rho]$ und der Elektron-Elektron-Wechselwirkung $E_{ee}[\rho]$ zusammen. Dabei wird gemäß der BORN-OPPENHEIMER-Näherung die kinetische Energie der Kerne vernachlässigt und die Kern-Kern-Abstoßung als konstant angenommen. Die Elektronen-Elektronen-Wechselwirkung kann in die Coulomb- und Austauschfunktionale $J[\rho]$ und $E_X[\rho]$ aufgespalten werden. Das Coulombfunktional $J[\rho]$ lässt sich durch die klassische Gleichung (2.3) beschreiben. Dies gilt auch für die Elektron-Kern-Anziehung $E_{eK}[\rho]$ (siehe Gleichung (2.4)).[56, 57]

$$J[\rho] = \frac{1}{2} \iint \frac{\rho(\vec{r}_1)\rho(\vec{r}_2)}{|\vec{r}_1 - \vec{r}_2|} d^3\vec{r}_1 d^3\vec{r}_2 \quad (2.3)$$

$$E_{eK}[\rho] = \sum_{I=1}^{N_K} \int \frac{Z_I \rho(\vec{r})}{|\vec{R}_I - \vec{r}|} d^3\vec{r} \quad (2.4)$$

Die genauen Ausdrücke für das Austauschfunktional $E_X[\rho]$ und die kinetische Energie sind jedoch nicht bekannt. Zur Beschreibung dieses Problems gibt es zwei Ansätze für das Modell des homogenen Elektronengases. Dies ist zum einen der THOMAS-FERMI-Ansatz und der THOMAS-FERMI-DIRAC-Ansatz. Der Unterschied zwischen diesen beiden Ansätzen ist, dass beim THOMAS-FERMI-DIRAC-Ansatz ein Term für die Austauschenergie hinzukommt. Aus diesem Grund soll lediglich letzterer Ansatz gezeigt werden. So setzt sich die Energie nach THOMAS-FERMI-DIRAC $E_{\text{TFD}}[\rho]$ aus der Summe der kinetischen Energie für das

homogene Elektronengas $T_{TF}[\rho]$, der Energie für die Elektron-Kern-Anziehung $E_{eK}[\rho]$, der Coulombenergie ($J[\rho]$) und der Austauschenergie $E_X[\rho]$ zusammen (siehe Gleichung (2.5)). [55–57]

$$E_{TFD} = T_{TF}[\rho] + E_{eK}[\rho] + J[\rho] + E_X[\rho] \quad (2.5)$$

Dabei wird die kinetische Energie durch

$$T_{TF}[\rho] = \frac{3}{10} (3\pi^2)^{2/3} \int \rho^{5/3}(\vec{r}) d\vec{r} \quad (2.6)$$

und die Austauschenergie für ein homogenes Elektronengas durch

$$E_X[\rho] = -\frac{3}{4} (3/\pi)^{1/3} \int \rho^{4/3}(\vec{r}) d\vec{r} \quad (2.7)$$

beschrieben. Aufgrund der Annahme eines homogenen Elektronengases wird zur Berechnung der kinetischen Energie und der Austauschenergie überall die gleiche lokale Elektronendichte angenommen. Aus diesem Grund wird der Ansatz auch *Local Density Approximation* (LDA) genannt. Die Elektronenkorrelation E_C kann ebenfalls durch eine lokale Approximation für das homogene Elektronengas durch den Ansatz von WIGNER (1938) ergänzt werden (Gleichung (2.8)). [56]

$$E_C[\rho] = -0,056 \int \frac{\rho^{4/3}(\vec{r})}{0,079 + \rho(\vec{r})^{1/3}} d\vec{r} \quad (2.8)$$

Ein weiter Ansatz wurde von KOHN und SHAM im Jahr 1965 vorgestellt. Sie führten Orbitale in die DFT ein, wodurch die Energie von der Anzahl der Elektronen abhängig wird. Des Weiteren lässt sich die Elektronendichte aus den Orbitalen berechnen (Gleichung (2.10)). Durch das Verwenden von Orbitalen ist es außerdem möglich, einen Großteil der kinetischen Energie T_S zu berechnen. Sie spalten die kinetische Energie in den Teil, der exakt berechnet werden kann, und einen Korrekturterm auf. Der Ausdruck für die kinetische Energie T_S unter der Annahme nicht wechselwirkender Elektronen besitzt folgenden Ausdruck:

$$T_S = \sum_{i=1}^N \left\langle \varphi_i \left| -\frac{1}{2} \nabla^2 \right| \varphi_i \right\rangle, \quad (2.9)$$

wobei φ_i für die Orbitale und ∇ für den Nabla-Operator steht. [55–57]

$$\rho = \sum_i^N |\varphi_i|^2 \quad (2.10)$$

Nun gilt es die KS-Orbitale φ_i zu finden, für die $E[\rho]$ unter der Nebenbedingung orthonormaler KS-Orbitale minimal wird. So führt die Einführung der Lagrange-Multiplikatoren ε_i zu den Kohn-Sham-Gleichungen (KSG), die ein gekoppelter Satz von Eigenfunktionen sind:

$$\begin{aligned} & \left(-\frac{1}{2} \nabla^2 + \left[\int \frac{\rho(\vec{r}_2)}{r_{12}} d\vec{r}_2 + V_{XC}(\vec{r}_1) - \sum_A^M \frac{Z_A}{r_{1A}} \right] \right) \varphi_i \\ & = \left(-\frac{1}{2} \nabla^2 + V_{\text{eff}}(\vec{r}_1) \right) \varphi_i = \varepsilon_i \varphi_i \end{aligned} \quad (2.11)$$

Zur Berechnung der Kohn-Sham-Gleichungen wird eine Basissatz-Erweiterung verwendet, die das Problem von einem Satz gekoppelter Differentialgleichungen auf ein Matrix-Eigenwertproblem reduziert, welches

mit algebraischen Methoden gelöst werden kann.[55] Bei Festkörpern ist es oft ratsam, ebene Wellen als Basisfunktionen zu verwenden. Würde theoretisch eine unendliche Anzahl an ebenen Wellen berücksichtigt werden, so entspräche dies einer vollständigen Basis, praktisch wird diese Menge jedoch an einem bestimmten Punkt abgeschnitten, der durch eine *Cutoff*-Energie (E_{cutoff}) definiert ist.

Zur Reduzierung des numerischen Rechenaufwands werden die Kernelektronen zusammen mit den Kernen als Pseudopotentiale behandelt und nur die Valenzelektronen explizit berücksichtigt. Hier werden die PAW-Potentiale (*projector augmented wave*) verwendet,[58] die es erlauben, die Dichte aller Elektronen zu rekonstruieren, da die Kernelektronen eingefroren sind.

Zuletzt ist zu beachten, dass die KSG aufgrund der Periodizität des Systems an jedem k-Punkt in der Brillouin-Zone gelöst werden muss. Die Gesamtdichte wird schließlich durch Summierung der berechneten Dichte an den k-Punkten $n_k(\vec{r})$ erhalten. Als k-Punkt-Sampling-Methode wird das Monkhorst-Pack-Schema verwendet, das gleichmäßig verteilte k-Punkte in der irreduziblen Brillouin-Zone erzeugt.[59]

Der gesamte Ausdruck für die Energie E_{DFT} ist in Gleichung (2.12) dargestellt, wobei E_{XC} die *exchange-correlation*-Energie ist, welche sich aus dem fehlenden Teil der exakten kinetischen Energie, der Energie für die Elektronenkorrelation und der Austauschenergie zusammensetzt (Gleichung (2.13)).

$$E_{\text{DFT}}[\rho] = T_{\text{S}}[\rho] + E_{\text{ek}}[\rho] + J[\rho] + E_{\text{XC}}[\rho] \quad (2.12)$$

$$E_{\text{XC}}[\rho] = (T[\rho] - T_{\text{S}}[\rho]) + (E_{\text{ee}}[\rho] - J[\rho]) \quad (2.13)$$

Das Austauschkorrelationsfunktional $E_{\text{XC}}[\rho]$ kann jedoch nicht exakt berechnet werden, weshalb für das Funktional Näherungen gemacht werden müssen. Dazu gibt es verschiedene Methoden, von denen hier nur zwei Methoden näher beschrieben werden sollen. Dies ist zum einen das LDA-Funktional, welches zuvor schon erläutert wurde. Dieses Funktional kann Moleküle nur sehr schlecht beschreiben. Für Metalle hingegen liefert es oft zufriedenstellende Ergebnisse, weshalb es auch heute noch zum Einsatz kommt.

Zum anderem wurde die *Generalized Gradient Approximation* (GGA) entwickelt. Hierbei wird nicht wie bei LDA nur die Elektronendichte an einem Ort verwendet, sondern auch die Dichtegradienten $\nabla\rho$. Für die Austausch- und Korrelationsenergien gibt es verschiedene Ansätze, wobei die exakte Parametrisierung empirisch ist, statt einem physikalischen Hintergrund nachzugehen. [55–57] Einer dieser Ansätze ist das PBE (PERDEW, BURKE und ERNZERHOF) Funktional, welches nur auf physikalischen Konstanten (parameterfrei) basiert. Für weitergehende Details soll an diesem Punkt jedoch auf die Literatur [60] hingewiesen werden. Aufgrund der starken lokalen Coulomb-Wechselwirkungen lokalisierter Elektronen, die für lokalisierte d- oder f-Elektronen besonders stark sind, wird für CeO_2 der DFT+U Ansatz verwendet, da diese durch LDA oder GGA nicht richtig beschrieben werden können. $U_{\text{eff}} = U + J$, wobei U die Vor-Ort-Coulomb- und J die Vor-Ort-Austausch-Wechselwirkungen beschreibt, kann als Parameter für ein Elektron verstanden werden, der beschreibt, wie nahe es an ein anderes Elektron lokalisiert.[61] Für das Ce4f-Orbital wird in dieser Arbeit der Wert von $U_{\text{eff}} = 4,5$ eV zusammen mit dem PBE-Funktional verwendet. Der U_{eff} -Parameter von 4,5 eV hat sich bereits in der Vergangenheit im Zusammenhang mit Ceroxid bewährt.[35, 62, 63]

2.3.1 Details zur Berechnung der Raman-Spektren[35]

Alle DFT Rechnungen werden mithilfe des *Vienna Ab initio Simulation Package* (VASP, Version 5.3.5, <https://www.vasp.at/>) durchgeführt. Dabei wird für alle Berechnungen der GGA- (In_2O_3) oder der GGA+U-Ansatz (CeO_2) mit einer Parametrisierung von PERDEW, BURKE und ERNZERHOF (PBE) und einem U_{eff} -Parameter von 4,5 eV für das Ce4f Orbital verwendet (PBE+U/4,5 eV). Außerdem werden nur Valenzelektronen mit einem *plane wave cutoff* von 400 eV (CeO_2) und 500 eV (In_2O_3) betrachtet. Die verwendeten Pseudopotentiale stammen aus der VASP Version 5.4 und die KOHN-SHAM Gleichungen werden mithilfe der *projector augmented wave* (PAW) Methode gelöst. Als Gitterkonstante für die CeO_2 Strukturen wird

5,484 Å[35] und für In₂O₃ 10,298 Å verwendet. Für die Relaxation der Strukturen wird als Konvergenzkriterium die maximale Kraft, die auf ein Atom wirkt, auf 10⁻² eV Å⁻¹ gesetzt und die Gesamtenergie für einen *self consistent loop* bis auf 10⁻⁶ eV konvergiert. Für weitergehende Details soll auf die einzelnen Publikationen aus Kapitel 4 verwiesen werden.

Zur Berechnung der Schwingungsfrequenzen wird ein störungstheoretischer Ansatz (engl.: *density functional perturbation theory*, DFPT) verwendet, welcher auch im VASP Code implementiert ist.

Für die Raman Intensitäten wird ein bereits publizierter Ansatz verwendet,[35] der im Folgenden näher erläutert werden soll. Dabei wird zuerst der differenzielle Raman-Querschnitt erster Ordnung für die Stokes-Komponente benötigt, der nach POREZAG und PEDERSON [64] durch Gleichung (2.14) gegeben ist.

$$\frac{d\sigma_i}{d\Omega} = \frac{(2\pi\nu_S)^4}{c^4} \frac{h(n_i^b + 1)}{8\pi^2\nu_i} \frac{I^{\text{Raman}}}{45} \quad (2.14)$$

Dabei ist ν_s die Frequenz des gestreuten Lichts, n_i^b der statistische BOSE-EINSTEIN Faktor, I^{Raman} die Raman-Streuaktivität und ν_i die Frequenz der i-ten Mode. Die Raman-Streuaktivität I^{Raman} lässt sich wie folgt ausdrücken:

$$I^{\text{Raman}} = 45 \left(\frac{d\alpha}{dQ} \right)^2 + 7 \left(\frac{d\beta}{dQ} \right)^2 = 45\alpha'^2 + 7\beta'^2 \quad (2.15)$$

Dabei ist die Ableitung der mittleren Polarisierbarkeit α' durch

$$\alpha' = \frac{1}{3} (\tilde{\alpha}'_{xx} + \tilde{\alpha}'_{yy} + \tilde{\alpha}'_{zz}) \quad (2.16)$$

und die Ableitung der Anisotropie des Polarisierbarkeitstensors β'^2 durch Gleichung (2.17) gegeben. $\tilde{\alpha}$ ist dabei der Polarisierbarkeitstensor der einzelnen Komponenten und Q eine Normal-Moden-Koordinate.

$$\beta'^2 = \frac{1}{2} \left[(\tilde{\alpha}'_{xx} - \tilde{\alpha}'_{yy})^2 + (\tilde{\alpha}'_{xx} - \tilde{\alpha}'_{zz})^2 + (\tilde{\alpha}'_{yy} - \tilde{\alpha}'_{zz})^2 + 6(\tilde{\alpha}'_{xy}{}^2 + \tilde{\alpha}'_{xz}{}^2 + \tilde{\alpha}'_{yz}{}^2) \right] \quad (2.17)$$

Basierend auf der Definition der Polarisierbarkeit kann die Ableitung dieser Eigenschaft in Bezug auf die Atomkoordinaten R_k als direkte Antwort auf ein externes elektrisches Feld gesehen werden.[64]

$$\frac{\partial \tilde{\alpha}_{ij}}{\partial R_k} = -\frac{\partial^3 E^{\text{el}}}{\partial E_i \partial E_j \partial R_k} \quad i, j = x, y, z \quad (2.18)$$

Hierbei ist E^{el} als die elektronische Energie des Systems zu verstehen. Nach LAZZERI und MAURI [65] kann der dielektrische Tensor ϵ_{ij}^{∞} durch

$$\epsilon_{ij}^{\infty} = \delta_{ij} - \frac{4\pi}{\Omega_{\text{cell}}} \frac{\partial^2 E^{\text{el}}}{\partial E_i \partial E_j} \Leftrightarrow \frac{\partial^2 E^{\text{el}}}{\partial E_i \partial E_j} = -\frac{\Omega_{\text{cell}}}{4\pi} \epsilon_{ij}^{\infty} + \frac{\Omega_{\text{cell}}}{4\pi} \delta_{ij} \quad (2.19)$$

ausgedrückt werden, wobei Ω_{cell} das Volumen der Einheitszelle ist. Mithilfe der Gleichungen (2.18) und (2.19) kann schließlich die dritte Ableitung der Energie als endliche Differenz ausgedrückt werden:

$$\frac{\partial \tilde{\alpha}_{ij}}{\partial R_k} = - \left[\left(\frac{\partial^2 E^{\text{el}}}{\partial E_i \partial E_j} \right)_+ - \left(\frac{\partial^2 E^{\text{el}}}{\partial E_i \partial E_j} \right)_- \right] \frac{1}{\Delta R_k} = \frac{\Omega_{\text{cell}}}{4\pi} \left[(\epsilon_{ij}^{\infty})_+ - (\epsilon_{ij}^{\infty})_- \right] \frac{1}{\Delta R_k} \quad (2.20)$$

$(\epsilon_{ij}^{\infty})_-$ und $(\epsilon_{ij}^{\infty})_+$ stellen dabei die ij -Komponenten der dielektrischen Matrix dar, bei der die Atome um $-0,005 \text{ \AA}$ bzw. $+0,005 \text{ \AA}$ entlang des Normal-Moden-Vektors verschoben werden. Damit ergibt sich für

$$\Delta R_k = 0,01 \text{ \AA}. [35]$$

VASP berechnet in einer DFPT-Rechnung die volle dielektrische Matrix (6 lineare Antwortberechnungen), jedoch sind zwei solcher Rechnungen notwendig, um die Raman-Intensität I^{Raman} für eine Mode zu berechnen. Daher sind insgesamt $3N_{\text{atom}} * 2 * 6 = 36N_{\text{atom}}$ lineare Antwortberechnungen notwendig, um ein Raman-Spektrum zu erhalten, wobei N_{atom} die Anzahl der Atome in einer Einheitszelle ist. Dies ist jedoch zurzeit nicht im VASP Code implementiert, weshalb ein Python Code, der von FONARI und STAUFFER geschrieben wurde,[66] in Kombination mit VASP verwendet wird, um die Berechnung der Raman-Intensitäten zu ermöglichen. Um ein fertiges Spektrum zu erhalten, werden die Intensitäten mit einer Lorentz-Funktion mit einer Halbwertbreite von 10 cm^{-1} (FWHM) multipliziert. Dieser Ansatz der Berechnung ist identisch mit dem Ansatz von SCHILLING *et al.* (2017) [35].

3 Experimentaltteil

3.1 Probenpräparation

In dieser Arbeit werden CeO_2 und $\text{c-In}_2\text{O}_3$ basierte Katalysatoren verwendet, wobei für CeO_2 vier verschiedene Morphologien untersucht werden.

Angefangen mit CeO_2 , erfolgt die Synthese zweier dieser Morphologien durch Hydrothermalsynthesen. Insgesamt handelt es sich somit um zwei Ansätze, bei welchen CeO_2 -Würfel und CeO_2 -Stäbe hergestellt werden. Die Synthese der CeO_2 -Würfel erfolgt in Anlehnung an MAI *et al.* (2005) [4] und die der CeO_2 -Stäbe in Anlehnung an Wu *et al.* (2008) [67]. Für beide Proben werden zuerst 79 mL einer NaOH-Lösung (98 %, Grüssing GmbH) hergestellt. In einem anderem Becherglas werden 11 mL deionisiertes Wasser vorgelegt, in dem dann der Präkursor gelöst wird. Für die Würfel dient $\text{Ce}(\text{NO}_3)_3 \cdot 6 \text{H}_2\text{O}$ (Alfa Aesar, 99,5 %) als Präkursor und für die Stäbe $\text{CeCl}_3 \cdot 7 \text{H}_2\text{O}$ (Alfa Aesar, 99 %). Diese Lösung wird anschließend der NaOH-Lösung hinzugegeben und für 30 min gerührt. Im Anschluss wird die Lösung in einen Teflon-Autoklaven mit einem Volumen von ca. 140 mL gegeben und in einem Ofen thermisch behandelt. Dieser startet bei ca. 25 °C mit einer Heizrate von 1 °C min^{-1} bis zur gewünschten Temperatur (siehe Tabelle 3.1). Nach Abkühlen auf ca. 25 °C wird das entstandene CeO_2 abzentrifugiert und dreimal mit entionisiertem Wasser gewaschen, bevor es für mindestens 24 h bei 85 °C im Trockenschrank getrocknet wird. Zuletzt werden die Proben durch Mörsern homogenisiert. Die Ausbeuten liegen alle über 90 %. Die Ofentemperatur, die Dauer im Ofen bei der gewünschten Temperatur, die resultierende Konzentration von NaOH und die eingesetzte Menge des Präkursors sind Tabelle 3.1 zu entnehmen.

Die Synthese der dritten Morphologie, dem polykristallinen CeO_2 (CeO_2 -Sheets), erfolgt durch thermische Zersetzung von $\text{Ce}(\text{NO}_3)_3 \cdot 6 \text{H}_2\text{O}$ (Alfa Aesar, 99,5 %). Dazu wird $\text{Ce}(\text{NO}_3)_3 \cdot 6 \text{H}_2\text{O}$ 12 h bei 600 °C mit einer Heizrate von 6 °C min^{-1} kalziniert. Nach dem Abkühlen auf Raumtemperatur wird das Pulver gesiebt (200 μm) und erneut nach demselben Protokoll kalziniert.

Die vierte CeO_2 Morphologie (CeO_2 -Oktaeder) wurde kommerziell erworben (Sigma Aldrich, <25 nm (BET)).

Tabelle 3.1: Synthesebedingungen der polykristallinen Ceroxid Proben.

Probe	Würfel	Stäbe
Temperatur / °C	180	140
Dauer / h	18	48
c(NaOH) / M	6	9
m(Präkursor) / g	1,95	2,01

Die Beladung von Ceroxid mit Kupfer oder Gold erfolgt durch Abscheidung mit einer 10^{-3} M $\text{CuCl}_2 \cdot 2 \text{H}_2\text{O}$ -Lösung (Sigma Aldrich, $\geq 99,5$ %) bzw. einer 10^{-3} M $\text{HAuCl}_4 \cdot 3 \text{H}_2\text{O}$ (Carl Roth, 99,9 %)-Lösung. Dazu

werden die Ceroxidproben zunächst im Verhältnis 1:150 in deionisiertem Wasser redispergiert und der pH-Wert mit einer 0,1 M NaOH-Lösung (98 %, Grüssing GmbH) auf 9 eingestellt. Anschließend wird die Kupferchloridlösung auf den pH-Wert 8 bzw. die Goldchlorsäurelösung auf den pH-Wert 9 eingestellt und der Ceroxid-Suspension zugegeben, um die gewünschte Beladung zu erreichen. Nach der Zugabe wird der pH-Wert erneut überprüft und gegebenenfalls auf 9 eingestellt. Anschließend wird das Reaktionsgemisch 2 h bei 65 °C erhitzt und nach dem Abkühlen 30 min lang in ein Ultraschallbad gestellt. Schließlich wird der Rückstand zentrifugiert, viermal mit entionisiertem Wasser gewaschen und mindestens 24 h lang bei 85 °C getrocknet.

c-In₂O₃-Sheets werden durch Kalzinierung von In(OH)₃ bei 600 °C synthetisiert. Zu diesem Zweck wird In(NO₃)₃ · xH₂O (Alfa Aesar, ≥ 99,99 %) in deionisiertem Wasser gelöst und mit einer Ammoniaklösung (Carl Roth, ≥ 25 %) wird ein pH-Wert von 10 eingestellt. Das ausgefallene In(OH)₃ wird abfiltriert und fünfmal mit deionisiertem Wasser gewaschen. Der Rückstand wird im Luftstrom getrocknet und an Luft bei 600 °C 2 h mit einer Heizrate von 10 °C min⁻¹ kalzinieren. Anschließend werden die erhaltenen c-In₂O₃-Partikel gesiebt (200 µm).

3.2 Charakterisierung der CeO₂ und In₂O₃ Proben

3.2.1 *Ex situ* Charakterisierungsmethoden

In dieser Arbeit werden verschiedenste *ex situ* Methoden verwendet, um die hergestellten Katalysatoren genauer zu charakterisieren. Je nach Probe werden entweder alle hier aufgelisteten Methoden zur Charakterisierung verwendet oder nur eine Auswahl. Für genauere Details soll an dieser Stelle jedoch auf Kapitel 4 verwiesen werden.

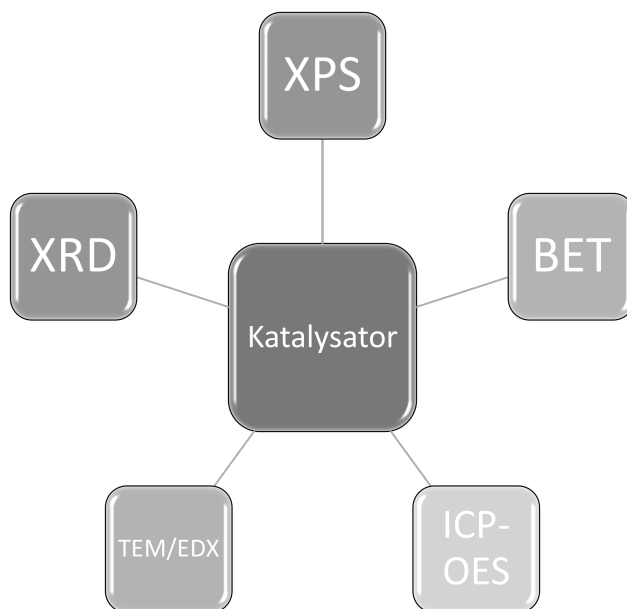


Abbildung 3.1: Übersicht der angewendeten *ex situ* Charakterisierungsmethoden.

Röntgenphotoelektronenspektroskopie (XPS). Ein Teil der *ex situ* XP-Spektren wurde mit einem SSX

100 ESCA-Spektrometer (Surface Science Laboratories Inc.) unter Verwendung einer monochromatischen Al K_{α} -Quelle mit einer Energie von 9 kV (10 mA) aufgenommen. Der Probenhalter und das Analysegerät waren in einem Winkel von 55° zur Horizontalen ausgerichtet. Der Röntgenstrahl stand in einem Winkel von 35° zur Horizontalen des Analysators, und die Probe wurde um 16° gegenüber dem Röntgenstrahl gedreht. Die Auflösung betrug 0,054 eV.

Stickstoffphysisorption (BET). Die N_2 -Adsorption bei 77 K wurde auf einem SURFER (Thermo Fisher Scientific) durchgeführt. Vor der Messung wurde die Probe bei 80 °C im Hochvakuum für mindestens 24 h entgast. Zur Bestimmung der spezifischen Oberfläche wurde die N_2 -Adsorptionskurve an das BET-Modell [68] im P/P^0 -Bereich zwischen 0,03 und 0,3 angepasst.

Optische Emissionsspektrometrie mit induktiv gekoppeltem Plasma (ICP-OES). Quantitative Analysen zur Bestimmung des Kupfer- bzw. Gold-Anteils wurden mittels ICP-OES vom Analytischen Zentrum Berlin-Adlershof (AZBA) GmbH durchgeführt.

Transmissionselektronenmikroskopie (TEM) und energiedispersive Röntgenspektroskopie (EDX). Die TEM-Messungen wurden mit einem JEOL JEM-2100F (Tokio, Japan) durchgeführt, das mit einem Schottky-Feldemitter ausgestattet ist und mit einer Nennbeschleunigungsspannung von 200 kV arbeitet. Zur Vorbereitung wurde die Probe in einem Ultraschallbad für 30 s in Ethanol dispergiert und dann auf einen Kohlelochfilm (Plano GmbH) aufgebracht, der auf einem Kupfer- oder Gold-Netzchen geträgert ist. Nach dem Trocknen wurde das Gitter mit Kohlenstoff (Bal-Tec MED010) beschichtet, um eine Aufladung durch den Elektronenstrahl zu verhindern. Die EDX-Spektren wurden mit einem Oxford X-MAX 80 Silizium-Driftdetektor (Oxford Instruments Nanoanalysis, High Wycombe, UK) aufgenommen, der an das JEOL JEM-2100F angebunden ist.

Röntgendiffraktometrie (XRD). Pulver-Röntgendiffraktogramme wurden mit einem Stoe Stadi P Diffraktometer mit einem Ge(111)-Monochromator, Cu K_{α} -Strahlung ($\lambda = 1,54060 \text{ \AA}$) und einem MYTHEN-1K Dectris-Detektor unter Verwendung eines flachen Probenhalters in Transmissionsgeometrie aufgenommen.

3.2.2 Multi *in situ* Apparatur

Die katalytische Aktivität sowie die *operando* UV-Vis, *operando* Raman und quasi *in situ* Photoelektronenspektroskopie-Messungen (UPS, XPS) wurden mithilfe eines Versuchsaufbaus durchgeführt, welcher bereits zuvor beschrieben wurde. [69, 70] Im Detail handelt es sich hierbei um ein modifiziertes LHS/SPECS-EA200-MCD-System, welches im Folgenden näher beschrieben werden soll. Zu diesem Zweck ist in Abb. 3.2 ein schematischer Aufbau der Apparatur dargestellt. Im Wesentlichen besteht der Aufbau aus einem beweglichen Probenstab, auf dem die Probe mithilfe eines Probenträgers aus Edelstahl (Durchmesser: 8 mm; Tiefe: 0,5 mm) geschraubt werden kann, und aus vier Messkammern: der *in situ* Zelle, der Präparationskammer, dem Doppelkreuz sowie der Messkammer. Mithilfe des Probenstabs können alle Kammern erreicht werden, wobei in allen ein unterschiedlicher Druck herrscht. In der *in situ* Zelle, in welcher Umgebungsdruck herrscht, können Temperatur und Gasbehandlungen erfolgen, wobei zeitgleich Raman und UV-Vis Spektren aufgenommen werden können. Die Temperatur kann dabei mithilfe eines Ni/Cr-Ni-Thermoelements (Typ K) bestimmt werden, welches sich unmittelbar an der Probe befindet. Für einen anschließenden Transfer in das Ultrahochvakuum kann der Druck dann auf <25 mbar reduziert werden. Eine schematische Veranschaulichung ist unten links in Abb. 3.2 dargestellt. Die Zelle ist dabei mit zwei Ultra-Torr-Verschraubungen (1/2" und 1/4") ausgestattet, in welche dann die Raman Sonde mit Saphir-Optik (1/2") (Kaiser Optical

Systems Inc.) und die UV-Vis Hochtemperatur-Reflexionssonde (Avantes) (1/4") eingeführt werden können.

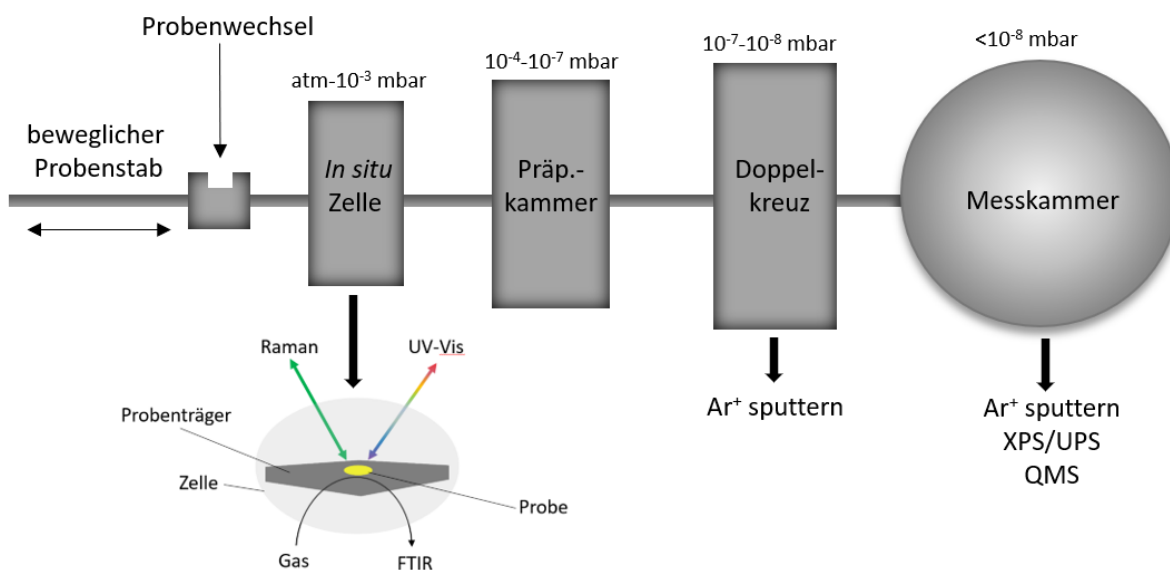


Abbildung 3.2: Schematischer Aufbau der multi *in situ* Apparatur.

Bei allen Messungen wurde jeweils 20 mg bis 30 mg der Probe auf den Probenhalter aus Edelstahl platziert und einem Gasfluss ausgesetzt, der die Probe überströmt. Die Gase CO (99,997 %, Westfalen), H₂ (99,999 %, Westfalen), CO₂ (99,999 %, Westfalen), O₂ (99,999 %, Westfalen) und Argon (99,996 %, Westfalen) wurden mit digitalen Massendurchflussreglern (MFCs, Bronkhorst) dosiert, während H¹⁶O (elektrische Leitfähigkeit < 3 μSm⁻¹), H¹⁸O (97 % + ¹⁸O, Eurisotop) und D¹⁶O (99,9 % D, Sigma Aldrich) mit einem Flüssigkeits-Dosiersystem mit geregelter Verdampfung (Bronkhorst) und einem Flüssigkeitsmassendurchflussmesser (Bronkhorst) dosiert wurden. Der Gesamtdurchfluss wurde in der Regel auf 100 mL min⁻¹ eingestellt. Alle Gaszusammensetzungen wurden mit Argon verdünnt, um den Umsatz niedrig zu halten und den Einfluss möglicher Transporteffekte zu eliminieren, so dass der Fokus auf der Aufklärung des Reaktionsmechanismus liegen kann. Des Weiteren soll erwähnt sein, dass aufgrund der Zellengeometrie und der Tatsache, dass die Probe von den Gasen überströmt wird, die eingesetzte Menge an Katalysator keinen signifikanten Einfluss auf die Gesamtaktivität hat, falls der Probenhalter vollständig bedeckt ist.

Im Falle eines Transfers zur Messkammer dienen die Präparationskammer und das Doppelkreuz lediglich als zusätzliche Druckstufen, um das Ultrahochvakuum in der Messkammer aufrechtzuerhalten. Dabei ist die Messkammer durch ein Plattenventil vom Doppelkreuz separiert. Bei geöffnetem Plattenventil lässt sich der Probenstab schließlich in die Messkammer transferieren, in der die Probe mit Ar⁺ besputtert werden kann oder UPS und/oder XPS Messungen gemacht werden können. Zusätzlich lässt sich mittels eines Quadrupol-Massenspektrometers (QMS) eine Restgasanalyse machen.

Details zu den oben genannten Messungen werden in den folgenden Abschnitten kurz beschrieben. Für genauere Details bezüglich der Messparameter soll jedoch auf die einzelnen Publikationen in Kapitel 4 verwiesen werden.

Raman Spektroskopie ($\lambda_{\text{ex}} = 532 \text{ nm}$). Raman-Spektren wurden mit einem HL5R-Transmissionsspektrometer (Kaiser Optical Systems Inc.) aufgenommen, das einen frequenzverdoppelten Nd:YAG-Laser (Cobolt Inc., Hübner Photonics GmbH) zur Anregung bei 532 nm verwendet. Für die Messungen wird eine 1/2"-Tauchsonde mit Saphiroptik (Kaiser Optical Systems Inc.) in die Reaktionskammer eingesetzt. Die spektrale

Auflösung ist mit 5 cm^{-1} angegeben, und die Stabilität der Bandenpositionen ist besser als $0,3 \text{ cm}^{-1}$. [30] Die Laserleistung an der Position der Probe wurde auf 1 mW für CeO_2 oder 6 mW für In_2O_3 eingestellt, mit einer Spotgröße von ca. $30 \mu\text{m}$ im Durchmesser. Für alle Messungen wurde außerdem ein Filter für kosmische Strahlung verwendet, wobei bei jeder Akkumulation ein zweites Spektrum aufgenommen wird, um durch kosmische Strahlung verursachte Spikes zu eliminieren, was die Gesamtmesszeit verdoppelt. Für die CeO_2 Proben wurde außerdem die Anwendung *Auto New Dark* verwendet. Dies bedeutet, dass vor jeder Messung zweimal der Untergrund bei geschlossenem Shutter aufgenommen wird, um die Hintergrundintensität zu bestimmen. Zusammen mit dem Filter für kosmische Strahlung vervierfacht sich somit die Messzeit. Für ein Teil der Messungen wird das entsprechende Dunkelspektrum zu Beginn der Messreihe aufgenommen. In diesem Zusammenhang ist zu erwähnen, dass ein separates Dunkelspektrum vor jeder Einzelmessung zu keinen signifikanten Unterschieden führt. Die Gesamtmesszeit wird jedoch halbiert.

UV-Vis Spektroskopie. UV-Vis Spektren wurden in diffuser Reflexion mit einem AvaSpec ULS2048-Spektrometer (Avantes) aufgenommen, das mit einer Deuteriumlampe und einer Halogenentladungslampe ausgestattet ist (AvaLight-D-S-DUV, Avantes). Die Messzeit wurde auf 60 s eingestellt, die sich aus einer Belichtungszeit von 300 ms und 200 Einzelmessungen zusammensetzt. Ein Teil der Messungen wurde mit einem AvaSpec ULS2048CL-EVO-Spektrometer (Avantes) aufgenommen, das mit einer ausbalanciertem Deuteriumlampe und einer Halogenentladungslampe (AvaLight-D-S-BAL, Avantes) ausgestattet ist. Hierbei setzt sich die Messzeit von 60 s aus 400 Einzelmessungen mit einer Messzeit von 150 ms zusammen. Als Weißstandard wurde Bariumsulfatpulver (BaSO_4 , Sigma Aldrich) oder Magnesiumoxidpulver (MgO , Sigma Aldrich) verwendet, welche zwischen 175 nm und 1100 nm keine Absorptionen aufweisen.

Messung der katalytischen Aktivität. Parallel zu den oben genannten Messungen kann außerdem die Gasphase mit einem Fourier-Transformations-Infrarot-Spektrometer (FTIR) (Tensor 20, Bruker) analysiert werden, wobei die Auflösung 4 cm^{-1} und die Messzeit 60 s beträgt, was die Aufnahme von 125 Spektren ermöglicht. Anhand von Kalibriergeraden kann die CO -, H_2O - und CO_2 -Konzentration berechnet werden, um den Umsatz zu bestimmen. Die katalytische Aktivität (CO_2 oder CO Umsetzung) ist definiert als das Verhältnis zwischen der vom FTIR-Spektrometer am Ausgang der Zelle gemessenen CO bzw. CO_2 -Menge und der Menge des zugegebenen CO_2 oder CO .

Röntgenphotoelektronenspektroskopie (XPS). XP-Spektren wurden mit einem modifizierten LHS/SPECS EA200 MCD-System unter Verwendung einer Mg K_α -Quelle (1253,6 eV, 168 W) aufgenommen. Die Kalibrierung der Bindungsenergieskala wurde mit $\text{Au } 4f_{7/2} = 84,0 \text{ eV}$ und $\text{Cu } 2p_{3/2} = 932,67 \text{ eV}$ Signalen von Folienproben durchgeführt. Vor der Messung kann die Probe mit den oben genannten Gasen und Temperaturprogrammen behandelt werden, der anschließende Transfer der Probe in die Analysechamber erfolgt dann ohne Luftexposition (quasi *in situ*). Um die partielle Aufladung zu minimieren, wurde ein Teil der Proben statt auf dem Edelstahlträger auf einen goldbeschichteten Probenhalter aus Edelstahl vermessen. Eine weitere Aufladung der Probe wurde berücksichtigt, indem der Peak des C 1s-Signals auf 284,8 eV verschoben wurde. Die Übersichtsspektren wurden mit einer Auflösung von 0,4 eV und die Bindungsspektren mit einer Auflösung von 0,1 eV oder 0,025 eV aufgenommen.

Ultraviolettphotoelektronenspektroskopie (UPS). UP-Spektren wurden mit unserem modifizierten LHS/SPECS EA200 MCD-System aufgenommen (siehe XPS). Als UV-Quelle dient dabei ein UVS 10/35 (SPECS) in Kombination mit Helium. Der Gaseinlass wird durch ein differenzielles Pumpsystem gesteuert, das aus einer Drehschieberpumpe und einer Turbomolekularpumpe besteht. Die erste Pumpstufe ist die Drehschieberpumpe (10^{-2} mbar), die zweite Pumpstufe eine Kombination aus Drehschieber- und Turbomolekularpumpe ($5 \cdot 10^{-7}$ mbar). Die Kalibrierung der Bindungsenergieskala erfolgt mit einer Goldfolie

(Alfa Aesar, 99,985 %) nach Ar⁺-Ionen-Sputtern. Die UP-Spektren wurden mit einer Auflösung von 0,025 eV aufgenommen.

Restgasanalyse mittels QMS. In der Messkammer besteht ebenfalls die Möglichkeit, eine Restgasanalyse mittels eines Quadrupol-Massenspektrometers (Quadrupac Q100, Leybold-Heraeus) durchzuführen. Mithilfe eines Spannungsdatenloggers (Picolog 1216, Pico Technology) können die Signale ausgelesen und aufgezeichnet werden. Durch Heizen der Probe ist es außerdem möglich, Adsorbate zu entfernen, die in der Gasphase qualitativ nachgewiesen werden können. Anschließende XPS/UPS Analysen können somit zusätzliche Informationen über den Oberflächenzustand generieren.

3.2.3 Weitere *in situ/operando* Charakterisierungsmethoden

Raman Spektroskopie ($\lambda_{\text{ex}} = 385 \text{ nm}$). *In situ* Raman-Spektren mit einer Anregungswellenlänge von 385 nm wurden mit einem zuvor beschriebenen Raman-Spektrometer [71, 72] unter Verwendung einer handelsüblichen CCR1000-Zelle (Linkam Scientific Instruments) mit einem CaF₂- oder Saphir-Fenster aufgenommen. Die Leistung des Lasers an der Probe wurde auf 8,5 mW für In₂O₃ bzw. auf 5,1 mW für CeO₂ eingestellt, wobei die Spotgröße 0,6 mm² betrug. Für die Gasbehandlungen und Messzeiten soll auf die Publikationen in Kapitel 4 verwiesen werden.

Impedanzspektroskopie. Potentiostatische elektrochemische Impedanzspektroskopie (PEIS) wurde in einem Zwei-Elektroden-System mit einem BioLogic VSP-Potentiostat/Galvanostaten im Bereich von 1 MHz bis 10 Hz mit 50 mV Amplitude und 10 Messpunkten pro Dekade in einem Potenzialbereich von 0,05-1 V gegen eine Referenz von +0.338 V (In³⁺ zu In⁰) [73] betrieben. Das positive Reduktionspotenzial wurde auf die Standard-Wasserstoffelektrode (SHE) bezogen und das Potenzialintervall auf dE = 0,095 V eingestellt. Impedanzspektren wurden in einer handelsüblichen CCR1000-Zelle (Linkam Scientific Instruments) aufgenommen, die mit einer PTFE-Platte und zwei Löchern für die Kupferelektroden ausgestattet war. In diesem Zusammenhang wurden auch Experimente mit Goldelektroden (Alfa Aesar, 99,999 %) durchgeführt, bei denen kein Einfluss des Elektrodenmaterials auf die elektrochemische Leistung beobachtet wurde, mit Ausnahme eines parasitären Potenzial iR-Abfalls, der auf die Besonderheiten der Zellenmontage zurückzuführen ist. Die Kompensation wurde vor der eigentlichen Messung manuell in der Erfassungssoftware EC-Lab v. 11.33 (BioLogic) vorgenommen. Für die Messungen wurden immer 70 mg Material verwendet, welches jeweils auf die gleiche Füllhöhe komprimiert wurde. Zeitgleich mit den Impedanzmessungen wurde die Gasphase mit einem FTIR-Spektrometer (Tensor 20, Bruker) gemessen, was analog zu Abschnitt 3.2.2 geschah.

Diffuse Reflexions-Fourier-Transformations-Infrarot-Spektroskopie (DRIFTS). Die IR-Fourier-Transformations-Spektroskopie in diffuser Reflexion wurde mit einem Vertex 70 oder Invenio (Bruker) FTIR-Spektrometer durchgeführt, das mit einem mit flüssigem Stickstoff gekühlten Quecksilber-Cadmium-Tellurid-Detektor (MCT) und einer handelsüblichen Reaktionszelle (Praying MantisTM High Temperature Reaction Chamber, Harrick Scientific Products) mit infrarot-transparenten KBr-Fenstern ausgestattet ist. Aufgrund der Empfindlichkeit für Wasser wurden für die Wassergas-Shift Reaktion ZnSe-Fenster verwendet. Des Weiteren wurden in dieser Arbeit drei verschiedene Messmodi verwendet. In diesem Kontext wurden stationäre, transiente oder Modulations-Anregungs-Messungen durchgeführt. Für Details soll jedoch auf die einzelnen Publikationen in Kapitel 4 verwiesen werden.

4 Ergebnisse und Diskussion

Mit den in Abschnitt 3.2 beschriebenen Methoden wurden die CeO₂ basierten Katalysatoren während der CO-Oxidation, der Wassergas-Shift Reaktion und der reversen Wassergas-Shift Reaktion untersucht, die CO-Oxidation wurde nur für die Au/CeO₂ Katalysatoren untersucht. Ein besonderes Augenmerk lag hierbei auf der Kombination von *operando* Raman und *operando* UV-Vis Spektroskopie, um die Sauerstoffdynamiken der Metalloxide während der Reaktionen zu untersuchen. DRIFT Spektroskopie wurde schließlich zur Charakterisierung von Adsorbaten auf der Oberfläche während der Reaktion verwendet. Für die CeO₂ Stäbe wurde außerdem die O₂ Aktivierung betrachtet, um die Redox-Eigenschaften und die Verwendung als Sauerstoffspeicher des reinen CeO₂ besser zu verstehen. Zuletzt wurde In₂O₃ genauer in Hinblick auf das Reduktionsverhalten mittels H₂ charakterisiert, welches im Anschluss als Katalysator für die rWGS Reaktion dient. Der Großteil dieser Arbeiten wurde durch die Dichtefunktionaltheorie ergänzt, um beispielsweise unbekannte Schwingungsmoden im Raman- oder IR-Spektrum zu identifizieren und so ein besseres Verständnis zu erzielen. Die Ergebnisse dieser Arbeit sind in den unten aufgeführten Fachartikeln veröffentlicht, deren Inhalte im Folgenden kurz zusammengefasst sind. Die entsprechenden Artikel folgen am Ende dieses Kapitels.

Die erste Publikation soll als einleitender Teil dienen. In dieser Arbeit wird zuerst auf die Struktur von CeO₂, dessen low-index Oberflächenterminierungen sowie deren Eigenschaften eingegangen. Im Anschluss wird die Sauerstoffaktivierung auf den verschiedenen CeO₂ Facetten diskutiert. Dies passiert hauptsächlich im Rahmen der Arbeit von SCHILLING *et al.* [7] und der zweiten Publikation in dieser Arbeit. Danach werden die Ergebnisse der CO-Oxidation und der WGS Reaktion für Au/CeO₂ aus dieser Arbeit nochmals aufgegriffen und diskutiert. Es zeigt sich, dass das enge Zusammenspiel von *in situ/operando* Raman Spektroskopie und Theorie (DFT) einen leistungsstarken Ansatz für ein Verständnis von Ceroxid und CeO₂ basierten Katalysatoren auf atomarer Ebene darstellt. Der Einfluss der kristallographischen Ausrichtung der Oberfläche auf das Reaktivitätsverhalten wird durch die hydrothermale Synthese von Ceroxid-Nanopartikeln zugänglich, die als Katalysatoren eingesetzt werden können und so die Materiallücke zwischen idealisierten (einkristallinen) und realen katalytischen Systemen schließen.

1. M. Ziemba, C. Schilling, M.V. Ganduglia-Pirovano, C. Hess, Toward an Atomic-Level Understanding of Ceria-Based Catalysts: When Experiment and Theory Go Hand in Hand, *Acc. Chem. Res.* 54 (2021) 2884–2893.

In der zweiten Publikation wird die Sauerstoffaktivierung über CeO₂ Nanostäben mit einer (110) und (100) Oberflächenterminierung mittels DFT und *in situ* Raman Spektroskopie untersucht. Da in einer früheren Publikation die (100)-Oberfläche auf den Würfeln bereits untersucht werden konnte, soll diese als Referenz dienen.[7] So ist es möglich, dass die (110)-Oberfläche im Fokus stehen kann, da die O₂-Aktivierung sowie die Dynamik auf CeO₂ Nanostäben aufgrund des Vorhandenseins von zwei Ceroxid-Facetten durchaus komplex ist. Dennoch zeigt sich, dass die Peroxidbildung auf den (100)-Facetten energetisch gegenüber den (110)-Facetten begünstigt ist, während bei der Defektbildung das gegenteilige Verhalten der Fall ist. Somit tragen beide Facetten entweder durch die Bildung aktiver Sauerstoffspezies (z.B. Peroxide) oder durch den Einbau von Gittersauerstoff zur Sauerstoffspeicherung bei. Genauer gesagt kann Sauerstoff bei niedrigen Temperaturen (< 100 °C) in Form von aktiviertem Sauerstoff oder als Gittersauerstoff gespeichert werden, der

bei höheren Temperaturen ($>100\text{ }^{\circ}\text{C}$) freigesetzt wird. So adsorbieren aktivierte Peroxidspezies auf beiden Facetten, die Dynamik dieser Spezies bei unterschiedlichen Temperaturen hängt allerdings von der Facette ab. Während auf den (100)-Facetten die stärker gebundenen Peroxidspezies zunächst eingelagert werden und die Oberfläche als gasförmiger Sauerstoff verlassen, ist auf der (110)-Facette die Bildung von oberflächennahen Leerstellen einfacher und die schwächer gebundenen Peroxidspezies zerfallen in Sauerstoffatome, die die Leerstellen füllen und dann ebenfalls als gasförmiger Sauerstoff freigesetzt werden. Somit ermöglichen CeO_2 Nanostäbe eine Kombination verschiedener Sauerstoffspeicher- und Aktivierungsfunktionen, deren Verständnis für die Entwicklung von Systemen mit verbesserter Speicherkapazität nützlich sein könnte.

2. M. Ziemba, M.V. Ganduglia-Pirovano, C. Hess, Elucidating the Oxygen Storage-Release Dynamics in Ceria Nanorods by Combined Multi-Wavelength Raman Spectroscopy and DFT, *J. Phys. Chem. Lett.* 11 (2020) 8554–8559.

Anschließend wird die CO-Oxidation über Au/CeO_2 thematisiert, die in den nächsten drei Publikationen behandelt wird. Hierfür wurde zuerst polykristallines Au/CeO_2 mithilfe einer Kombination von DRIFTS und DFT während der CO-Oxidation untersucht. Ziel dieser Studie ist die Identifizierung der aktiven Spezies während der Reaktion, wobei vor allem der Goldzustand von Interesse ist. Des Weiteren wurde der Einfluss der Vorbehandlung des Katalysators auf die katalytische Aktivität untersucht. Hierbei zeigt sich beispielsweise, dass bei Raumtemperatur die Bildung von (Hydrogen-)Carbonaten (oder adsorbiertem CO) auf dem bloßen Träger eine Rolle bei der Blockierung aktiver Stellen spielt, was besonders bei den ausgeheizten Proben aufgefallen ist. Die größte Errungenschaft ist jedoch, dass durch unseren Ansatz die aktive $\text{O}_{\text{lattice}}-\text{Au}^+-\text{CO}$ Spezies identifiziert werden konnte. Diese Spezies wurde auf einzelnen isolierten Goldatomen und/oder auf Goldatomen, die von größeren Clustern abstrahiert wurden, beobachtet. Größere Goldcluster oder Nanopartikel spielen in diesem Kontext eine untergeordnete Rolle. Somit bietet dieser kombinierte Ansatz von DRIFTS und DFT ein mächtiges Werkzeug zur Identifizierung von aktiven Stellen im Rahmen von metallbeladenen Oxid Katalysatoren.

3. C. Schilling, M. Ziemba, C. Hess, M.V. Ganduglia-Pirovano, Identification of single-atom active sites in CO oxidation over oxide-supported Au catalysts, *J. Catal.* 383 (2020) 264–272.

Als nächstes soll der Einfluss des Trägers für Au/CeO_2 Katalysatoren während der CO-Oxidation geklärt werden. Zu diesem Zweck werden CeO_2 Nanostäbe mit 100 und 110 Terminierung verwendet. Dies ermöglicht außerdem die Einbeziehung der Facettenabhängigkeit der Reaktion, was ein weiterer Parameter zur Steuerung der katalytischen Aktivität sein kann. Untersucht wurde dieses System mittels *operando* Raman und UV-Vis Spektroskopie sowie DFT. So zeigt sich die Bedeutung der Defektbildungsenergie für die CO-Oxidation über Au/CeO_2 Katalysatoren, welche stark von der CeO_2 Facette und der Goldbeladung beeinflusst wird. Bei der Wahl der $\text{CeO}_2(110)$ Facette, welche die niedrigste Defektbildungsenergie aufweist, sowie einer Beladung mit Gold wirkt sich dies positiv auf die Aktivität aus. Die gesteigerte katalytische Aktivität durch die Goldbeladung kann jedoch thermisch kompensiert werden, da die unbeladenen Proben ähnliche CO-Umsätze erzielen wie die goldbeladenen Proben bei niedrigeren Temperaturen. Somit verliert die Rolle des Goldes als aktive Stelle bei höheren Temperaturen an Bedeutung, und ein Mechanismus über Carbonat-ähnliche Intermediate wird ermöglicht. Bei niedrigeren Temperaturen können jedoch aktive Stellen durch Carbonate blockiert werden, da die Adsorption von Carbonaten auf $\text{CeO}_2(100)$ und $\text{CeO}_2(110)$ hoch exotherm ist.

4. M. Ziemba, C. Hess, Influence of gold on the reactivity behaviour of ceria nanorods in CO oxidation: combining *operando* spectroscopies and DFT calculations, *Catal. Sci. Technol.* 10 (2020) 3720–3730.

In dieser Publikation soll wie auch in der dritten Publikation die CO-Oxidation über Au/CeO₂(111) untersucht werden. Hier soll jedoch der CO-Au Adsorbat-Bereich im Fokus liegen, welcher mittels ME-DRIFTS und DFT genauer untersucht wird. Dies erfolgt anhand von polykristallinen CeO₂ (Platten) und CeO₂ Oktaedern, welche beide hauptsächlich mit der 111 Facette terminieren, die Platten weisen jedoch zusätzlich Stufen auf. In dieser Studie wird deutlich, dass CO, das an Clustern mit mehr als zwei Goldatomen adsorbiert ist, und CO, das an reinem Ceroxid adsorbiert ist, nicht an der Entstehung von CO₂ beteiligt ist. Des Weiteren zeigt sich, dass die Modifikation durch Stufen bereits eine Änderung in der CO Schwingungssignatur auf dem reinen Träger bewirkt. In diesem Kontext weisen die Platten deutlich mehr Sauerstoffdefekte auf. Somit zeigt dieser Ansatz, dass die Kombination von transienten spektroskopischen Techniken, wie ME-DRIFTS, mit DFT-Berechnungen unser Verständnis von Reaktionsmechanismen in der heterogenen Katalyse erheblich verbessern kann.

5. J. Weyel, M. Ziemba, C. Hess, Elucidating Active CO–Au Species on Au/CeO₂(111): A Combined Modulation Excitation DRIFTS and Density Functional Theory Study, *Top. Catal.* 65 (2022) 779–787.

Als nächstes soll die Wassergas-Shift Reaktion Thema sein, die auf mit Gold oder Kupfer beladenen sowie facettierten CeO₂ untersucht wurde. Zuerst soll Au/CeO₂ diskutiert werden, das in der folgenden Publikation mittels *operando* Raman und UV-Vis Spektroskopie sowie Isotopenaustausch-Experimenten mithilfe von H¹⁸O untersucht wurde. Daraus lassen sich Rückschlüsse auf das Reduktionsverhalten und den Austausch von Oberflächensauerstoff ziehen. Des Weiteren erleichtern zusätzliche DFT-Rechnungen die Zuordnung der Schwingungsbanden und verbessern die Interpretation der Ergebnisse auf molekularer Ebene. In diesem Kontext zeigt sich, dass unter Reaktionsbedingungen eine Reduktion der Ceroxidträger stattfindet, an der auch Sauerstoff aus dem Bulk beteiligt ist, jedoch gibt es keine Korrelation zwischen dem Ausmaß der Reduktion und der katalytischen Aktivität. Trotzdem stehen die beobachtete Rotverschiebung der F_{2g}-Bande und der Austausch von Sauerstoff aus H¹⁸O im Einklang mit einem Redox-Mechanismus. Unseren Ergebnissen zufolge zeigt Gold, das auf einer abgestuften CeO₂(111)-Oberfläche abgeschieden wurde, wie im Falle der Platten, die höchste WGS Aktivität. Die beiden weniger stabilen Oberflächen, d. h. CeO₂(110) und CeO₂(100), sind in der Lage, CO in Form von Carbonaten zu adsorbieren, die die aktiven Stellen blockieren und zu einer geringeren CO-Umwandlung führen können. Schließlich kommt es bei Au/CeO₂ Katalysatoren unter Reaktionsbedingungen zu einer Agglomeration der Goldpartikel, was mit einer Deaktivierung einhergeht. Zusammenfassend zeigen die Ergebnisse das Potenzial der Kombination von *operando* Spektroskopie mit Isotopenexperimenten zur Überwachung der facettenabhängigen Dynamik verschiedener Sauerstoffspezies an der Oberfläche und im Bulk in Au/CeO₂ Katalysatoren unter WGS Bedingungen.

6. M. Ziemba, M.V. Ganduglia-Pirovano, C. Hess, Insight into the mechanism of the water–gas shift reaction over Au/CeO₂ catalysts using combined *operando* spectroscopies, *Faraday Discuss.* 229 (2021) 232–250.

Diese Studie soll lediglich als Einstieg in die Anwendung von Cu/CeO₂ Katalysatoren dienen, da diese hier mit den Au/CeO₂ Katalysatoren aus der sechsten Publikation verglichen werden. Es zeigt sich, dass die Cu/CeO₂ Katalysatoren eine allgemein niedrigere Aktivität im Rahmen der Wassergas-Shift Reaktion aufweisen als die mit Gold beladenen Proben. In beiden Fällen zeigt sich jedoch eine starke Facettenabhängigkeit, wobei die Platten (gestufte 111 Oberfläche) in beiden Fällen am aktivsten sind. Mechanistisch stimmen die *operando* Raman-Spektren mit einem Redox-Mechanismus überein, an dem Gittersauerstoff beteiligt ist. Außerdem zeigt die Untersuchung verschiedener Ceroxid-Facetten, dass eine niedrige Defektbildungsenergie für hohe katalytische Aktivitäten nicht ausreicht und vielmehr andere Aspekte wie die Wasserdissoziation, die Desorption von CO₂ oder die Wechselwirkung mit dem Metallträger eine wichtige Rolle spielen.

-
7. M. Ziemba, D. Stark, C. Hess, Combined DFT and *operando* Spectroscopic Study of the Water-Gas Shift Reaction over Ceria based Catalysts: The Role of the Noble Metal and Ceria Faceting, Chem. Proc. 2 (2020) 23.

In dieser Publikation sollen schließlich die Cu/CeO₂ Katalysatoren im Detail betrachtet werden. Zu diesem Zweck wurde aufgrund der seit langem geführten Diskussion zwischen Redox- und Assoziationsmechanismen über Metall-Oxiden (wie z. B. CeO₂, In₂O₃, TiO₂) während C1-basierter Reaktionen ein *operando* spektroskopischer Ansatz entwickelt, welcher an facettierten Cu/CeO₂ Katalysatoren während der Wassergas-Shift Reaktion (WGS) validiert wird. In diesem Zusammenhang können Informationen über die Bulkstruktur von CeO₂ durch Raman- und UV-Vis-Spektroskopie gewonnen werden, während UV-Vis Spektren zusätzliche Informationen über die dispergierten Kupferspezies liefern. ME-DRIFTS-Messungen werden zur Identifizierung von Oberflächenintermediaten eingesetzt. Auf diese Weise ist es möglich, die Prozesse am Katalysator genauer zu bestimmen und die Art des Mechanismus zu ermitteln, wobei ein Redox-Mechanismus auf Cu/CeO₂ während der WGS Reaktion zu dominieren scheint. In Bezug auf Kupfer ergibt sich, dass seine Beteiligung an der Katalyse hauptsächlich auf elektronischen Effekten beruht. Im Gegensatz zu unseren Au/CeO₂ Katalysatoren zeigt sich außerdem, dass Cu/CeO₂ stabiler ist, da *operando* Raman- und UV-Vis Untersuchungen keinen Hinweis auf Kupferagglomeration ergeben. Zusammenfassend ist diese Kombination also ein leistungsfähiges Instrument zur Untersuchung einer breiten Palette von metallbeladenen Oxidkatalysatoren und zum detaillierten Verständnis ihrer Funktionsweise, z. B. bei C1-Prozessen wie der rWGS Reaktion.

8. M. Ziemba, J. Weyel, C. Hess, Approaching C1 Reaction Mechanisms Using Combined *Operando* and Transient Analysis: A Case Study on Cu/CeO₂ Catalysts during the LT-Water-Gas Shift Reaction, ACS. Catal. 12 (2022) 9503-9514.

In dieser Studie soll die rWGS Reaktion über Au/CeO₂(111) mittels *operando* Raman, *operando* UV-Vis, transienter DRIFTS sowie DFT Rechnungen genauer betrachtet werden. Der Vergleich verschiedener Ceroxid-Trägermaterialien (Platten und Oktaeder) zeigt, dass die Defektkonzentration nicht ausschlaggebend für die Aktivität ist, was sich auch durch die Analyse der Raman und UV-Vis Daten gezeigt hat. Mithilfe von transientem DRIFTS in Kombination mit DFT-Rechnungen können zum ersten Mal die einzelnen Schritte der H₂-Aktivierung über Au/CeO₂(111) aufgeklärt werden, somit sind Goldatome für einen assoziativen Mechanismus essentiell. Des Weiteren zeigt sich, dass die Vorbehandlung (H₂ oder CO₂) einen Einfluss auf den Reaktionsweg und die katalytische Aktivität hat. So begünstigt die CO₂-Reduktion über einer reduzierten Ceroxid-Oberfläche Carbonat-Zwischenprodukte, während über einer defektarmen Oberfläche eine Reduktion über Formiate bevorzugt ist. Eine bereits reduzierte Oberfläche vor der Reaktion (H₂-Vorbehandlung) führt außerdem zu höheren Aktivitäten. Unter Berücksichtigung aller spektroskopischen Befunde wird für die rWGS Reaktion über Au/CeO₂(111) Katalysatoren ein assoziativer Mechanismus über Carbonat- und Formiat-Zwischenstufen als Hauptweg vorgeschlagen, während ein Redox-Mechanismus nur eine untergeordnete Rolle spielt.

9. M. Ziemba, J. Weyel, C. Hess, Elucidating the mechanism of the reverse water-gas shift reaction over Au/CeO₂ catalysts using *operando* and transient spectroscopies, Appl. Catal. B Environ. 301 (2022) 120825.

Kubisches Indiumoxid (c-In₂O₃) hat sich als äußerst aktiver Katalysator für die rWGS Reaktion oder die Methanolsynthese durch die CO₂-Hydrierung herausgestellt. Dies macht In₂O₃ neben CeO₂ zu einem interessanten Material, da kein zusätzliches Metall für die katalytische Aktivität benötigt wird. Um einen Einblick in die Funktionsweise von In₂O₃ Katalysatoren zu gewinnen, ist ein detailliertes Verständnis

ihres Redox-Verhaltens erforderlich, einschließlich der damit verbundenen Sauerstoffdynamik und der In_2O_3 -Defektstruktur, welche jedoch noch nicht verstanden sind. Dies ist vermutlich damit verbunden, dass die Anwendung von *operando* Schwingungsspektroskopie aufgrund von Absorptionseffekten deutlich erschwert ist. Aus diesem Grund soll diese Arbeit die Grundlage für das Verständnis des Reduktionsverhaltens und der Sauerstoffdynamik von kubischen In_2O_3 -Nanopartikeln durch *in situ* Raman und UV-Vis Spektroskopie in Kombination mit der Dichtefunktionaltheorie schaffen. In diesem Kontext zeigt sich, dass Sauerstoffdefekte an der Oberfläche bei Temperaturen über 120 °C im Gleichgewicht mit dem Bulk sind und im Gleichgewichtszustand Bulkdefekte gegenüber Oberflächendefekten bevorzugt werden, was zu einer geringeren Defektkonzentration an der Oberfläche führt. Darüber hinaus stimmen die experimentellen Raman-Schwingungsspektren von In_2O_3 und $\text{In}_2\text{O}_{3-x}$ hervorragend mit den durch DFT berechneten Spektren überein, wodurch die Grundlage für das Verständnis der defektinduzierten Banden geschaffen wird.

10. M. Ziemba, L. Schumacher, C. Hess, Reduction Behavior of Cubic In_2O_3 Nanoparticles by Combined Multiple *In Situ* Spectroscopy and DFT, *J. Phys. Chem. Lett.* 12 (2021) 3749–3754.

In der vorherigen Arbeit konnten die Grundlagen zum Reduktionsverhalten über $\text{c-In}_2\text{O}_3$ geschaffen werden, weshalb in dieser Studie die rWGS Reaktion genauer betrachtet werden soll. Dazu verwenden wir (quasi) *in situ* und *operando* Spektroskopie (Raman, UV-Vis, XPS, UPS), um die Oberflächen- und Suboberflächendynamik von In_2O_3 während der rWGS Reaktion zu untersuchen. Die Eigenschaften des Bulks werden direkt durch *operando* Impedanzspektroskopie untersucht, unterstützt durch *ex situ* XRD. Der *operando* Impedanzspektroskopie Ansatz stellt dabei einen neuartigen Zugang für thermische Pulverkatalysatoren dar. Auf der Grundlage von temperaturabhängigen *operando* UV-Vis Studien kann die Oxidation durch CO_2 als geschwindigkeitsbestimmender Schritt für die rWGS Reaktion identifiziert werden. Die Ergebnisse stehen außerdem im Einklang mit Redox-Prozessen, wobei wasserstoffhaltige Oberflächenspezies nachweislich eine fördernde Wirkung haben. Unsere Ergebnisse zeigen, dass die Sauerstoff-/Wasserstoffdynamik zusätzlich zu Oberflächenprozessen wichtig für die Aktivität ist, was nicht nur für In_2O_3 , sondern auch für andere reduzierbare Oxidkatalysatoren von Bedeutung sein dürfte.

11. M. Ziemba, M. Radtke, L. Schumacher, C. Hess, Elucidating CO_2 Hydrogenation over In_2O_3 Nanoparticles using Operando UV-vis and Impedance Spectroscopies, *Angew. Chem. Int. Ed.* 61 (2022) e202209388.

Toward an Atomic-Level Understanding of Ceria-Based Catalysts: When Experiment and Theory Go Hand in Hand

Marc Ziemba, Christian Schilling, M. Verónica Ganduglia-Pirovano,* and Christian Hess*



Cite This: *Acc. Chem. Res.* 2021, 54, 2884–2893



Read Online

ACCESS |

Metrics & More

Article Recommendations

CONSPECTUS: Because ceria (CeO_2) is a key ingredient in the formulation of many catalysts, its catalytic roles have received a great amount of attention from experiment and theory. Its primary function is to enhance the oxidation activity of catalysts, which is largely governed by the low activation barrier for creating lattice O vacancies. Such an important characteristic of ceria has been exploited in CO oxidation, methane partial oxidation, volatile organic compound oxidation, and the water–gas shift (WGS) reaction and in the context of automotive applications. A great challenge of such heterogeneously catalyzed processes remains the unambiguous identification of active sites.

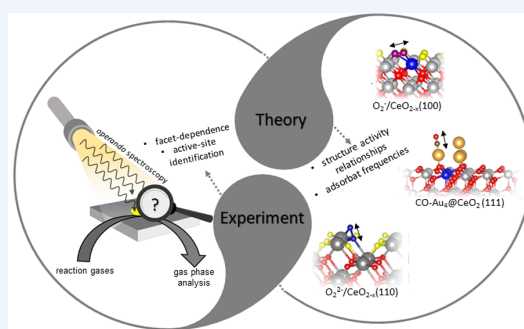
In oxidation reactions, closing the catalytic cycle requires ceria reoxidation by gas-phase oxygen, which includes oxygen adsorption and activation. While the general mechanistic framework of such processes is accepted, only very recently has an atomic-level understanding of oxygen activation on ceria powders been achieved by combined experimental and theoretical studies using *in situ* multiwavelength Raman spectroscopy and DFT.

Recent studies have revealed that the adsorption and activation of gas-phase oxygen on ceria is strongly facet-dependent and involves different superoxide/peroxide species, which can now be unambiguously assigned to ceria surface sites using the combined Raman and DFT approach. Our results demonstrate that, as a result of oxygen dissociation, vacant ceria lattice sites are healed, highlighting the close relationship of surface processes with lattice oxygen dynamics, which is also of technical relevance in the context of oxygen storage-release applications.

A recent DFT interpretation of Raman spectra of polycrystalline ceria enables us to take account of all (sub)surface and bulk vibrational features observed in the experimental spectra and has revealed new findings of great relevance for a mechanistic understanding of ceria-based catalysts. These include the identification of surface oxygen (Ce–O) modes and the quantification of subsurface oxygen defects. Combining these theoretical insights with *operando* Raman experiments now allows the (sub)surface oxygen dynamics of ceria and noble metal/ceria catalysts to be monitored under the reaction conditions.

Applying these findings to Au/ceria catalysts provides univocal evidence for ceria support participation in heterogeneous catalysis. For room-temperature CO oxidation, *operando* Raman monitoring the (sub)surface defect dynamics clearly demonstrates the dependence of catalytic activity on the ceria reduction state. Extending the combined experimental/DFT approach to *operando* IR spectroscopy allows the elucidation of the nature of the active gold as (pseudo)single Au^+ sites and enables us to develop a detailed mechanistic picture of the catalytic cycle. Temperature-dependent studies highlight the importance of facet-dependent defect formation energies and adsorbate stabilities (e.g., carbonates). While the latter aspects are also evidenced to play a role in the WGS reaction, the facet-dependent catalytic performance shows a correlation with the extent of gold agglomeration. Our findings are fully consistent with a redox mechanism, thus adding a new perspective to the ongoing discussion of the WGS reaction.

As outlined above for ceria-based catalysts, closely combining state-of-the-art *in situ/operando* spectroscopy and theory constitutes a powerful approach to rational catalyst design by providing essential mechanistic information based on an atomic-level understanding of reactions.



KEY REFERENCES

- Schilling, C.; Ganduglia-Pirovano, M. V.; Hess, C. Experimental and Theoretical Study on the Nature of Adsorbed Oxygen Species on Shaped Ceria Nanoparticles. *J. Phys. Chem. Lett.* **2018**, 9(22), 6593–6598.¹ *The shape-dependent adsorption and activation of oxygen on*

Received: April 9, 2021

Published: June 17, 2021



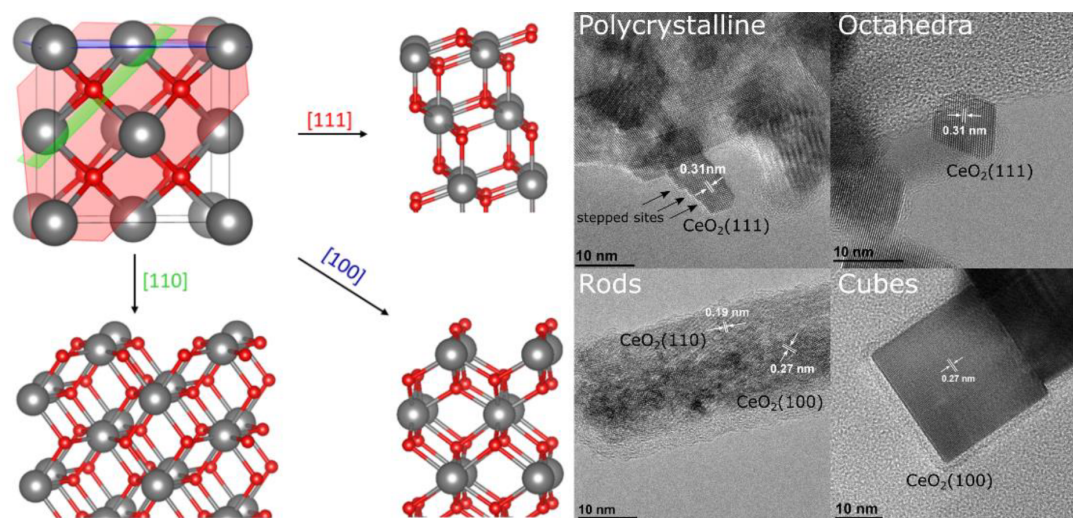


Figure 1. (Left) Overview of the different ceria facets. On the top left, the conventional unit cell of CeO_2 is shown (Ce^{4+} , gray; O^{2-} , red). Furthermore, the $[111]$ plane (red), the $[100]$ plane (blue), and the $[110]$ plane (green) can be seen. A cut through the ceria lattice along the direction perpendicular to those planes yields differently oriented ceria facets: $\text{CeO}_2(110)$ (bottom left), $\text{CeO}_2(111)$ (top right), and $\text{CeO}_2(100)$ (bottom right). (Right) Detailed TEM images of polycrystalline ceria (sheets), octahedra, rods, and cubes. The white arrows indicate the distance between the lattice planes in the direction of the particle surface.

ceria nanoparticles with (111) and (100) facets is elucidated by in situ Raman spectroscopy and related to unique adsorption sites using DFT calculations.

- Ziemba, M.; Ganduglia-Pirovano, M. V.; Hess, C. Elucidating the Oxygen Storage-Release Dynamics in Ceria Nanorods by Combined Multi-Wavelength Raman Spectroscopy and DFT. *J. Phys. Chem. Lett.* **2020**, *11*, 8554–8559.² Ceria nanorods are shown to exhibit facet-dependent properties regarding oxygen activation, decomposition, and lattice oxygen dynamics, which are of great interest for oxygen storage–release functions.
- Ziemba, M.; Hess, C. Influence of Gold on the Reactivity Behaviour of Ceria Nanorods in CO Oxidation: Combining Operando Spectroscopies and DFT Calculations. *Catal. Sci. Technol.* **2020**, *10*(11), 3720–3730.³ Structure–activity relations are established for CO oxidation over ceria and Au/ceria nanocubes/nanorods, elucidating the roles of (110) and (100) facet termination, employing operando spectroscopy combined with DFT calculations.
- Ziemba, M.; Ganduglia-Pirovano, V.; Hess, C. Insight into the Mechanism of the Water-Gas Shift Reaction over Au/ CeO_2 Catalysts Using Combined Operando Spectroscopies. *Faraday Discuss.* **2021**, *229*, 232–250.⁴ The role of ceria termination in the mechanism of the WGS reaction over ceria-supported gold catalysts is elucidated by operando spectroscopy combined with isotope labeling and DFT calculations.

1. INTRODUCTION

Heterogeneous catalysis is a key enabling technology for achieving an efficient and more sustainable utilization of resources. The rational design of better catalysts requires an atomic-level understanding of their mode of operation, including the identification and characterization of active sites. For model catalysts, methods for characterizing the structure of the catalytic surface have been developed (e.g., STM, AFM) and

applied to oxide-based systems.^{5,6} However, the establishment of structure–activity relationships in catalysis using model catalysts remains challenging, and these methods cannot be applied in a straightforward manner to powder systems, the technologically relevant form of catalysts. Thus, new approaches are urgently needed to achieve a better and ultimately an atomic-level understanding of real-world catalysts.

Unravelling the working principle of catalysts requires the development and application of methods that enable the identification and characterization of active sites. To be of relevance, the structural analysis should be performed under real working conditions and in real time and should be combined with the simultaneous detection of activity (*operando* approach). However, the synergy between theory and experiment using model and powder catalysts is crucial to unravelling the structure of the working catalysts while bridging the materials and complexity gaps in catalysis. While efforts have already been made to enable an atomic-level characterization of active sites under *operando* conditions,⁷ further development is necessary.

Ceria (CeO_2) is among the catalytically most active metal oxides, with particular redox properties and relatively high abundance. Ceria and ceria-containing materials are of great interest for environmental and energy conversion applications and thus have received a great deal of attention from experiment and theory. For instance, the low-temperature water–gas shift reaction, which increases the H_2/CO ratio after steam reforming, is commonly run over $\text{Cu}/\text{ZnO}/\text{Al}_2\text{O}_3$ catalysts, which are pyrophoric and thermally unstable. Alternatively, reducible oxides such as ceria supporting low loadings of noble metals (Pt, Au) have been discussed.^{8–10} Moreover, ceria-based catalysts are used in automotive emission control¹¹ and oxidation catalysis^{3,4,8,12,13} and are discussed in the context of fuel cell applications^{14–16} and biology.^{17–19} Furthermore, ceria is a reducible oxide, the intrinsic physical and chemical properties of which are current research topics on their own.

The booming interest in ceria, particularly in catalysis, is reflected in the number of review articles in the liter-

ature^{5,15,16,20–31} addressing the surface chemistry of ceria, its defect structure, and the relation of both to catalytic properties. While in those earlier works either an experimental^{5,15,16,21,22,25–29} or a theoretical^{20,23,24,30,31} perspective has been taken, there has been no account of the close combination and interplay of *in situ/operando* spectroscopy and theory and its potential to gain an atomic-level understanding of ceria and ceria-based powder catalysts. To this end, we hope that our account triggers new research activities and discussions in the context of ceria catalysis but also regarding other catalytically relevant and/or reducible oxide materials such as TiO₂ and V₂O₅.

2. STRUCTURE OF CERIA

The low-index (111), (110), and (100) surfaces of fluorite-type ceria (*Fm* $\bar{3}$ *m*) are shown in Figure 1. In the (111) facet, each atomic plane is charged but the repeat unit corresponds to an O–Ce–O trilayer, whereas in the (110) facet, each atomic layer contains a stoichiometric proportion of cerium and oxygen atoms. A cut through the ceria lattice along the $\langle 100 \rangle$ direction results in a surface with an excess of anions or cations (i.e., a polar surface). Such polar surfaces are not stable, and the polarity can be compensated for by the formation of oxygen or cerium vacancies, leading to a reconstructed surfaces, or by the adsorption of background gases, mostly leading to hydroxylated surfaces.³⁰ The nature of the stable (100) surface reconstruction is a matter of debate.^{32–35} One of such reconstructions presents half oxygen monolayer termination, matching a checkerboard-like pattern (Figure 1), hereinafter referred to as a CeO₂(100) facet.

The relative stability of the low-index ceria surfaces decreases in the following order: (111) > (110) > (100).^{30–32,36} Importantly, the surface properties of ceria depend on the exposed facet which has a different surface oxygen defect formation energy, $E_{\text{vac},\text{O}}$. For instance, if we compare the calculated values (PBE+U/4.5 eV) for vacancy structures for which the closest distance between surface oxygen defects is comparable, $E_{\text{vac},\text{O}}$ follows the (111) > (100) > (110) trend ($E_{\text{vac},\text{O}} = 2.27$ eV (2×2), 1.82 eV ($p(2 \times 2)$), and 1.32 eV (2×2), respectively).^{1,2}

The facet-dependent properties are of importance in catalysis and can be exploited by using nanoshaped ceria such as octahedra, rods, and cubes. Engineering the shape of ceria particles offers a powerful tool for developing materials with enhanced catalytic properties.^{37,38} For example, polycrystalline ceria can be prepared by the thermal decomposition of cerium nitrate,³⁹ which mainly terminates with the (111) surface due to its thermal stability. Octahedra, rods, and cubes can be synthesized by hydrothermal synthesis,^{40,41} and since the growth is kinetically controlled, less stable surfaces such as the (100) and (110) surfaces can also be obtained. The octahedra expose the (111) surface, the cubes the (100), and the rods the (110) as well as the (100). TEM images of such particles are shown in Figure 1, where in each case the distance of the lattice planes is indicated by white arrows. While the polycrystalline sheets and polyhedra terminate with the (111) surface, the sheets expose additional stepped sites.

3. ADSORPTION AND ACTIVATION OF OXYGEN

The ability of ceria to reduce and oxidize (oxygen storage capacity) and its oxygen mobility play crucial roles in its catalytic applications, and thus an in-depth understanding of the O₂

adsorption, activation, and dynamics is key to achieving improved catalytic efficiency. In this context, the exposed ceria surface facet has been shown to have a strong effect on the oxygen storage capacity of nanoshaped ceria.^{37,42,43} The reason is that oxygen activation at vacant surface oxygen sites, in the form of weakly adsorbed oxygen (O₂^{δ-}), superoxide (O₂⁻), and peroxide (O₂²⁻) species, is highly dependent on the ease with which surface oxygen defects can be created, which depends on the ceria facet exposed.¹ Furthermore, after the initial oxygen activation, a complete dissociation of the adsorbed species with O atoms filling oxygen vacant sites can occur (i.e., oxygen is incorporated into the ceria lattice). For a detailed structural investigation of oxygen adsorbates on ceria surfaces, a combination of Raman spectroscopy and density functional theory (DFT) calculations has proven to be a powerful tool.^{1–3,7,44} As shown in Figure 2, peroxides (830 cm⁻¹) are

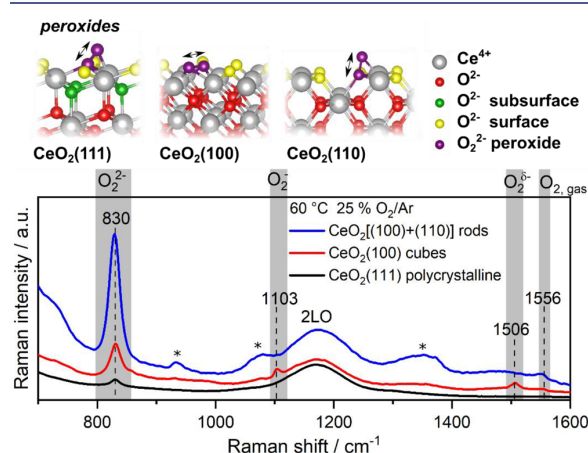


Figure 2. Atomic structure of the most stable peroxide species on (111), (100), and (110) ceria surfaces as calculated by DFT. The lower panel depicts the region of adsorbed oxygen species of *in situ* 532 nm Raman spectra of polycrystalline CeO₂(111), CeO₂(100) cubes, and CeO₂[(100) + (110)] rods recorded in 25% O₂/Ar at 60 °C with a total flow rate of 100 mL/min. Residues from the synthesis are marked (*).

present on all facets, while weakly adsorbed oxygen (1506 cm⁻¹) and superoxides (1103 cm⁻¹) can be detected only on the (100) facet of the nanocubes. The absence of these two bands for the rods, exposing (100) and (110) facets, suggests that the coexistence of the two facets modifies the (100) facets, resulting in different properties as compared to those of ceria cubes.²

A closer inspection of the peroxide Raman bands in Figure 2 reveals a facet-dependent intensity as well as an asymmetry toward higher wavenumbers. The band is most intense for the rods and weakest for polycrystalline ceria. The observed behavior can be explained on the basis of different effects: the magnitude of the defect formation energy, the magnitude of the adsorption energy of O₂²⁻ species, $E_{\text{ads},\text{O}_2^{2-}}$, which follows the trend (100) > (111) > (110) ($E_{\text{ads},\text{O}_2^{2-}} = -2.141$ p(2×2), -1.919 (2×2), and -1.170 eV (2×2), respectively),^{1,2} the vibrational frequencies on the corresponding structures [(110) (898 cm⁻¹) > (100) (868 cm⁻¹) > (111) (855 cm⁻¹)],^{1,2} and the surface area of the nanoshapes.

The low intensity on the sheets originates from the high defect formation energy on the (111) surface (as discussed above). Despite the high reducibility of the (110) facets, DFT shows that

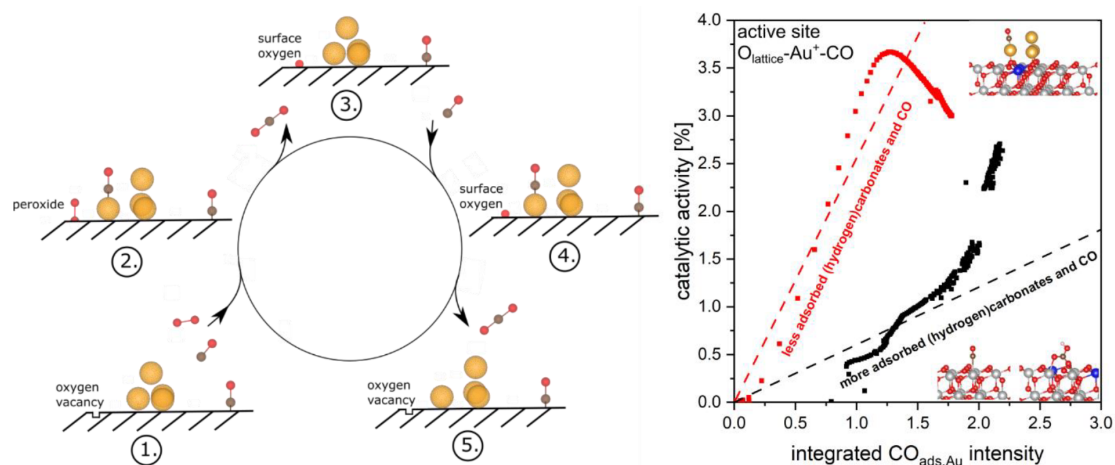


Figure 3. (Left) Proposed mechanism for the CO oxidation over Au/CeO₂ catalysts based on combined *operando* spectroscopy and theory. (Right) The intensity of CO adsorbed on polycrystalline Au/CeO₂(111) (2125–2130 cm⁻¹) is initially correlated with the conversion of the Au/CeO₂ catalyst for two pretreatments (equilibration in 25% O₂ for 1 h at 21 °C, red; 1 h at 200 °C in 25% O₂, black). The dashed lines are a rough interpolation indicating an initial relation between the adsorbed species and the conversion. The black line refers to a high and the red line refers to a lower concentration of adsorbed CO and (hydrogen)carbonate species. Data are from ref 13.

peroxides on (110) are less stable, likely decompose into the lattice,² and possess the highest vibrational frequency, which we do *not* observe in the experiment. Consequently, the presence of peroxides on the rods can be attributed to the (100) facets. The higher peroxide intensity on the rods as compared to that on the cubes can then be explained by the large surface area of the rods, which is 3.5 times greater than that of the cubes³ while the fraction of (110) facets of the rods represents slightly more than half of their surface,⁴⁵ and the larger number of intrinsic defects (caused by synthesis) in the rods; peroxide species will strongly adsorb to those surface defects. Thus, despite various contributions to the intensity behavior, a detailed understanding of adsorbed species becomes accessible by combined efforts from experiment and theory.

Furthermore, an examination of the stable peroxide species on the individual facets reveals that on the (111) and (110) facets, O₂²⁻ species are oriented perpendicular to the surface, whereas on the (100) facet, O₂²⁻ species lie flat (Figure 2). Moreover, the O–O bond length is facet-dependent (1.445 Å (2 × 2)-(110) ≈ 1.446 Å (2 × 2)-(111) < 1.468 Å p(2 × 2)-(100)).^{1,2} The above-mentioned asymmetry of the peroxide bands originates from higher coverages of peroxides on the surface since as the peroxide coverage increases, the O–O bond length decreases, resulting in a blue shift of the vibration, which is observed for all low-index surfaces.^{1,2}

Finally, it is of interest to consider the facet dependence of the oxygen storage mechanism. In this regard, the rods have been shown to possess superior properties^{40,42,43} compared to the cubes and polycrystalline ceria based on the better ability of the rods to incorporate oxygen into the crystal lattice upon dissociation of adsorbed peroxide species, which originates from the smaller distance between surface oxygen vacant sites on the (110) facet and the higher exothermicity of the reaction leading to the reoxidation of such a facet.²

4. AU/CERIA CATALYSTS: SUPPORT PARTICIPATION AND STRUCTURAL DYNAMICS

Catalyst support materials are essential to stabilizing metal nanoparticles in many industrial processes. Common attributes

of support materials are a high surface area, chemical stability, and the ability to disperse metal particles over the surface. Moreover, support materials may strongly influence the catalytic performance via metal–support interactions or even participation in the catalysis and may be divided into inactive (e.g., SiO₂, Al₂O₃) and active (e.g., TiO₂, CeO₂) ones. Active support materials such as ceria are characterized by their reducibility and their direct participation in the redox cycle.

Ceria and ceria-based catalysts are known for their dynamic behavior upon variations in the gas environment, and thus the use of suitable *in situ/operando* approaches is required to capture the structural changes. Despite progress in the field, a detailed understanding of the structural properties of bulk and surfaces of ceria powders during reaction has been achieved only recently by combining Raman and IR spectroscopy with DFT, including vibrational frequency and intensity calculations. In the following text, the potential of such a combined approach for providing essential mechanistic information will be illustrated by the CO oxidation and WGS reactions over Au/ceria catalysts.

4.1. CO Oxidation

The low-temperature CO oxidation is of practical relevance but also an important prototype reaction in heterogeneous catalysis. The mechanistic details of the CO oxidation over ceria and in particular Au/ceria catalysts have been vigorously debated in the literature, including the role of the support and the nature of the active site.^{38,46–51}

Starting with bare ceria, our recent study on differently shaped ceria nanoparticles has demonstrated their activity in CO oxidation at higher temperatures as well as the influence of the surface termination.³ In particular, the comparison of ceria rods, exhibiting CeO₂(110) and CeO₂(100) terminations, with ceria cubes with only the CeO₂(100) termination reveals the superiority of the (110) facets over the (100) facets for CO oxidation, which is easily explained by the more facile formation of surface oxygen defects on the CeO₂(110) facet (see above). Using the bare samples at a higher temperature (121 °C), CO conversions similar to those with gold-loaded samples (0.2 wt % Au) at a lower temperature (45 °C) could be obtained,

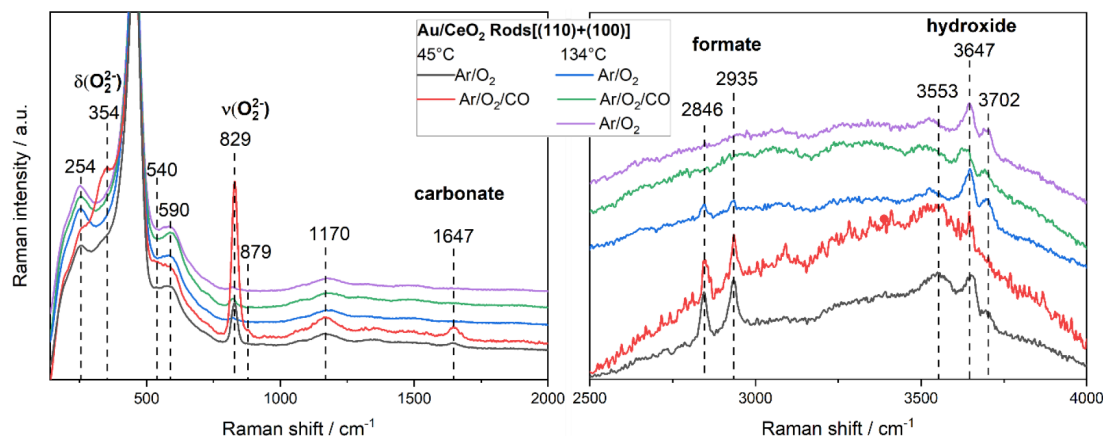


Figure 4. *In situ* and *operando* 532 nm Raman spectra of the low-wavenumber (left) and high-wavenumber (right) regions of gold-loaded ceria rods. Spectra were recorded at 45 °C/134 °C (flow rate: 100 mL/min) and feed compositions of 2% CO/25% O₂/Ar and 25% O₂/Ar for reactive and oxidative conditions, respectively. Spectra were offset for clarity. Data were taken from ref 3.

highlighting that the reactivity of surface oxygen is a key aspect of the CO oxidation mechanism and that the presence of gold facilitates the availability of reactive surface oxygen by lowering the barrier for defect formation. In addition, CO adsorption is preferred on Au/ceria over the bare support, allowing gold to play a coordinating role in the course of the reaction. As will be discussed in the following text, a combination of recent *operando* spectroscopic and theoretical results has enabled us to develop a detailed mechanistic picture of room-temperature CO oxidation over Au/CeO₂ catalysts.

Regarding the mechanism of CO oxidation over Au/ceria catalysts (polycrystalline ceria), previous studies have shown that the Au–oxide interfacial perimeter plays a major role and that the activation of molecular oxygen occurs at the surface of the support via initial peroxide formation at ceria defect sites (see above).^{52,53} The latter was directly evidenced in our previous studies on a 0.5 wt % Au/CeO₂ catalyst during room-temperature CO oxidation by using time-dependent *operando* Raman spectroscopy.⁵⁴ As illustrated in Figure 3, molecular oxygen adsorbs onto a ceria surface oxygen vacancy in the vicinity of gold, leading to peroxide formation. The outer oxygen atom reacts with CO adsorbed onto gold, while the second oxygen atom fills the vacancy. Next, this lattice oxygen is consumed by reaction with adsorbed CO.^{13,48,49} Finally, oxygen vacancies are replenished by molecular oxygen, completing the catalytic cycle.

Very recent combined *operando* IR and theoretical results have elucidated further details about the catalyst dynamics and the state of the active gold, highlighting the role of cationic sites.^{13,49,51} For a detailed assignment of the experimentally observed IR frequencies, the CO adsorption on model Au/ceria catalysts, consisting of single Au₁ and Au₄ gold clusters adsorbed on a CeO₂(111) surface, was studied by employing DFT calculations. Interestingly, the CO stretch frequencies (2125–2130 cm⁻¹) under *operando* conditions are consistent with CO adsorbed onto both single isolated Au⁺ sites and/or pseudosingle sites in direct contact with the CeO₂(111) surface. The latter refer to the gold ions that were slightly abstracted from a gold cluster, forming O_{lattice}–Au⁺–CO species under the reaction conditions. After CO₂ formation, it is energetically favorable for the abstracted gold ion to reintegrate into the gold

cluster until further CO adsorption occurs. It is noteworthy that, independent of the pretreatment history (as-prepared or dehydrated, cf. Figure 3), the Au/ceria catalyst approaches the same state but after different times, underlining the structural dynamics of the catalyst in the presence of the reaction mixture. This observation can be attributed to the fact that at room temperature the formation of (hydrogen)carbonates (or adsorbed CO) on the bare support plays a role in blocking active sites, which is particularly noticeable in the dehydrated samples (black symbols in Figure 3). However, as the reaction continues, these spectator species can be displaced and a state of equilibrium is reached.¹³

The above combined *operando* and theoretical studies could resolve apparent differences in the literature regarding the nature of the active gold sites on low-loaded ceria, as metallic gold, interfacial gold atoms, isolated cationic gold ions, and mixtures of different sites had previously been considered.⁵⁵ An interesting aspect concerns the role of water, which has been shown to facilitate CO oxidation by catalyzing the reaction of CO with OH groups, leading first to carboxyl formation followed by decarboxylation, as proposed both experimentally and theoretically.^{56–59} However, in such a scenario, the exact role of hydroxyl is still an open question, as *operando* IR spectra do not show a direct relation of the OH intensity changes to the activity.

4.1.1. Facet Dependence. Because ceria directly participates in the catalytic reaction, it is of great interest to further explore the influence of the support on the mode of operation. In addition to above-mentioned facet-dependent differences in the ease with which oxygen vacancies can be created, the exposed facet may affect the interactions between ceria and the supported gold^{23,60,61} as well as between gas-phase molecules (CO, H₂O) and the catalyst surface.^{1,2,30,62} Recently, we have examined structure–activity relations for CO oxidation over Au/rods (CeO₂(110), CeO₂(100)) and Au/cubes (CeO₂(100)) using combined *operando* Raman/UV–vis spectra and DFT calculations,³ with the former showing higher low-temperature CO oxidation activity. In the following text, we will first illustrate important aspects of the facet-dependent behavior and then include our previous work on polycrystalline ceria supported gold in the discussion.^{13,54,63}

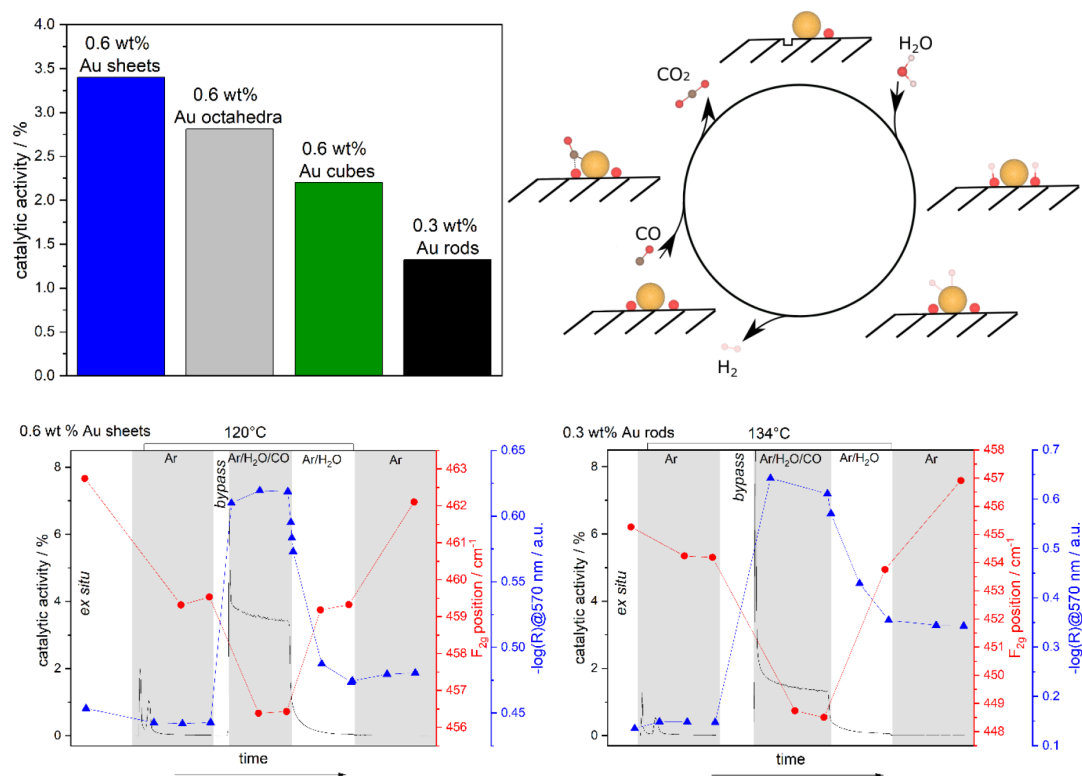


Figure 5. (Top left) CO conversion (in %) during the LT-WGS reaction of Au/ceria catalysts with different morphologies. The catalytic activity was measured after at least 1 h on stream at about 130 °C in 2% CO/8% H₂O/Ar (flow rate: 100 mL/min). (Top right) Proposed mechanism for the WGS reaction over Au/CeO₂ catalysts. (Bottom) *Operando* 532 nm Raman (red) and UV-vis (blue) results shown together with the catalytic activity (black) of 0.6 wt % Au/CeO₂ sheets (left) and 0.3 wt % Au/CeO₂ rods (right) during the WGS reaction (2% CO/8% H₂O/Ar) at a flow rate of 100 mL/min. Prior to reaction, the catalyst was exposed to Ar, and after reaction, the catalyst was exposed to 8% H₂O/Ar, followed by cooling to 48 °C in Ar. Data are from ref 4.

Figure 4 shows *in situ/operando* Raman spectra of Au/rods at low and elevated temperatures, containing characteristic solid-state phonons (254, 540, 590, and 1170 cm⁻¹) and adsorbate-related features (354, 829, 1647, 2846, 2935, 3553, 3647, and 3702 cm⁻¹). While details of the assignments based on DFT calculations of differently oriented ceria facets have been discussed elsewhere,^{2,3,44} we note that in the case of the Au/rods, switching from oxidative to reactive conditions at 45 °C results in a strong increase in the signals at 354 and 829 cm⁻¹, i.e., those arising from peroxide species at surface oxygen defect sites (for high peroxide coverages).^{2,3} Furthermore, a subsurface/bulk reduction of the ceria support is observed by *operando* UV-vis spectra via an increased absorption at 570 nm (due to Ce⁴⁺–Ce³⁺ charge transfer).³ The larger changes in the intensity of the peroxide Raman bands as well as in the UV-vis absorption at around 570 nm for the Au/rods result from the easier reducibility of the CeO₂(110) facets in the rods and can readily explain the higher catalytic activity of the rods in low-temperature CO oxidation.

At elevated temperatures, *operando* Raman spectra of Au/rods show a strongly decreased peroxide signal (Figure 4, left), indicating more facile peroxide dissociation and reaction with CO (see above). Regarding other adsorbate-related features, the carbonate band at 1647 cm⁻¹ exhibits interesting behavior, increasing in intensity under the reaction conditions at low temperature but disappearing at higher temperatures (Figure 4,

left).^{3,54} At low temperatures, we propose CO to react with lattice oxygen to form stable carbonate species, fully consistent with the theoretical results for CeO₂(110) and CeO₂(100) surfaces, showing carbonate formation to be highly exothermic.⁴ As a result, carbonate formation strongly inhibits CO oxidation at low temperatures because active sites are blocked. On the other hand, at elevated temperatures, the absence of the carbonate band indicates thermally induced carbonate decomposition (Figure 4, left).

Similarly, *operando* Raman spectra of the high-frequency region show formate-related bands at 2846 and 2935 cm⁻¹, which decrease in intensity at elevated temperature and are no longer observed under the reaction conditions (Figure 4, right). By comparison with the corresponding spectra of the bare rods,³ we can conclude that gold promotes formate decomposition via proton transfer from formate species to surface oxygen, leading to hydroxide formation as evidenced in the *operando* spectra (Figure 4, right) as well as CO₂ formation, as has been discussed previously for Pt/CeO₂ systems.⁵⁹

In contrast to the (100) and (110) facets in cubes and rods, the CeO₂(111) surface does not support stable carbonate formation for geometric reasons which may favor CO oxidation reaction. On the other hand, the defect formation energy is largest for the (111) facet (see above). Interestingly, our polycrystalline ceria-supported gold catalysts have shown superior CO oxidation activity as compared to rods. Thus,

besides facet-dependent effects, also the presence of stepped sites (Figure 1) needs to be taken into account to fully explain the reactivity behavior.⁶⁴

4.2. WGS Reaction

4.2.1. Facet Dependence. As an alternative to the industrial low-temperature WGS reaction catalyst Cu/ZnO/Al₂O₃, low-loaded noble metal-based catalysts (Pt, Au) on reducible oxides such as ceria have been suggested and shown to be highly active. However, important aspects such as the metal–support interaction and the state of the noble metal as well as the role of the ceria surface termination have not been unraveled. There is agreement on the participation of both the metal particles and the support material, but the detailed functioning of the catalyst has been subject to debate, as two types of mechanisms have been proposed in the literature (i.e., a redox mechanism and an associative mechanism). Recently, we have explored the influence of the surface termination on the performance and mode of operation of ceria-supported Au catalysts in more detail using combined *operando* spectroscopies and DFT calculations.^{4,12}

Figure 5 compares the catalytic activity of a series of Au/ceria catalysts with low gold loading using ceria sheets (polycrystalline, mainly CeO₂(111)), octahedra (CeO₂(111)), cubes (CeO₂(100)), and rods (CeO₂(110), CeO₂(100)) as support materials. Please note that a higher Au loading further decreases the performance of the rods. A clear dependence on the ceria surface termination is observed, with polycrystalline ceria showing the best performance. To gain insight into the facet-dependent behavior, various aspects need to be considered, such as the stability of the ceria surfaces, their interaction with the reactants and products, and the Au–ceria interaction. Considering the latter, electron microscopy analysis has revealed the presence of highly dispersed gold, whereas a combination of UV–vis and XP spectroscopy indicated the presence of both metallic and cationic gold, with the fraction of metallic gold ranging from 70% for Au/sheets to 40% for Au/cubes.

Combined *operando* Raman and UV–vis spectroscopy allowed the exploration of the catalyst dynamics under the reaction conditions (Figure 5, bottom). In fact, *operando* UV–vis spectra show facet-dependent changes in the absorption at around 570 nm, which are related to Au plasmons and Ce⁴⁺–Ce³⁺ transitions.^{65,66} As shown exemplarily for polycrystalline ceria and ceria rods at the bottom of Figure 5, upon switching from reaction conditions (CO/H₂O/Ar) to water (H₂O/Ar) and finally an inert environment (Ar), the absorption significantly drops but does not return to the level observed prior to the reaction conditions. This behavior can be attributed to an agglomeration of gold particles during the WGS reaction, leading to an enrichment of neutral gold and thus an increase in plasmon absorption. These findings are consistent with observations made for gold particles supported on ceria–zirconia.⁶⁷ Interestingly, the amount of absorbance increase for the two argon phases (i.e., before and after the reaction conditions) is smallest for sheets and largest for rods, thus showing an inverse trend compared to activity, strongly suggesting an influence of agglomeration on catalytic performance. Therefore, it is of great interest to maintain the metal dispersion on the support during the reaction. In this context, stable single-atom catalysts have recently been prepared by noble metal deposition onto CeO₂–TiO₂ or activated γ -alumina.^{68,69}

To explore the support-related dynamics, we employed *operando* Raman spectroscopy. The bottom of Figure 5 shows the gas-phase-dependent position of the F_{2g} mode at around 450 cm⁻¹, which at constant temperature is a quantitative measure of the changes in ceria stoichiometry. All Au/ceria catalysts show mode softening upon exposure to the reaction conditions, originating from a unit cell expansion due to the larger ionic radius of Ce³⁺ (Ce³⁺, 1.143 Å; Ce⁴⁺, 0.970 Å) formed upon ceria reduction (as supported by DFT).⁴⁴ These observations are fully consistent with the *operando* UV–vis results (Figure 5), revealing a maximum 570 nm absorption under the reaction conditions, which besides gold surface plasmons (see above) is related to a reduction of the support due to charge-transfer Ce⁴⁺–Ce³⁺ transitions. On the other hand, neither the absolute F_{2g} shift nor the absolute absorption changes of the facet-dependent catalysts are directly related to the catalytic activity and to their facet-dependent defect formation energies, pointing to the fact that other aspects need to be considered besides reducibility, such as catalyst interactions with reactants (CO, H₂O) and products (CO₂, H₂). Regarding the facet-dependent role of adsorbates, combined *operando* Raman and DFT studies provided new insights into ceria adsorbates, in particular, the role of carbonates. In fact, the less-stable surfaces (i.e., CeO₂(110) and CeO₂(100)) were shown to form stable carbonate species, which may block active sites and may therefore reduce the catalytic activity.

The proposed mechanism for LT-WGS over Au/ceria catalysts is summarized in Figure 5. As discussed above, CO oxidation takes place at the Au/ceria interface by the reaction between lattice oxygen and CO adsorbed on gold. As a result of the consumption of ceria lattice oxygen, an oxygen vacancy is created, which is proposed to strongly facilitate the dissociation of water. This latter step has been considered to be crucial for the feasibility of a redox mechanism.¹² To this end, additional H₂¹⁸O isotope exchange experiments provided evidence for the facile dissociation of water on Au/ceria catalysts.^{4,12} As the final step, H atoms from hydroxyl groups, located close to gold particles, recombine to molecular hydrogen over gold. In summary, the observed facet-dependent catalytic activity is attributed to a combination of active site blocking and Au agglomeration effects. This knowledge will facilitate the design of more active LT-WGS catalysts by focusing on the role of the support and engineering its properties toward enhanced gold stabilization.

5. CONCLUDING REMARKS

As illustrated above, the close interaction of *in situ/operando* Raman spectroscopy and theory represents a powerful approach to an atomic-level understanding of ceria and ceria-based catalysts. The influence of the surface crystallographic orientation on reactivity behavior has become accessible by the hydrothermal synthesis of ceria nanoparticles, which can be employed as working catalysts, thus bridging the material gap between idealized (single-crystal) and real catalytic systems. When this approach is applied, the ceria facet-dependent behavior is found to be specific to the reaction and can also be related to the facet-dependent reducibility, adsorbate stabilities, and gold–support interactions.

Generally, there have been an increasing number of combined Raman/IR and theory studies related to heterogeneous catalysts in recent years. As illustrated for the CO oxidation and the WGS reactions, combining *operando* vibrational spectroscopy with DFT calculations allows us to gain detailed insight into the mode of operation of ceria-based gold catalysts, including the

participation of the support (sub)surface, oxygen dynamics, and specification of active sites.

Due to the overall complexity of heterogeneous catalysts, the application of other techniques (UV-vis, XAS, XRD, XPS, etc.) and their coupling with vibrational spectroscopy will be of great importance. Recent advances in vibrational spectroscopic techniques include shell-isolated nanoparticle-enhanced Raman spectroscopy (SHINERS) and tip-enhanced Raman spectroscopy (TERS), exploiting surface-enhanced Raman effects as well as transient techniques.⁷ On the other hand, the theoretical description of reduced ceria³¹ and the accurate determination of vibrational frequencies through the use of computational chemistry remain challenging for contemporary DFT methods,⁷⁰ with the hybrid DFT methodology generally performing better.⁷¹ Combining highly sensitive vibrational spectroscopic techniques with highly accurate calculations will bring us closer to the ultimate goal of an atomic-level understanding of working catalysts, both spatially and temporally resolved.

AUTHOR INFORMATION

Corresponding Authors

M. Verónica Ganduglia-Pirovano – Instituto de Catálisis y Petroleoquímica - Consejo Superior de Investigaciones Científicas, 28049 Madrid, Spain; orcid.org/0000-0003-2408-8898; Email: vgp@icp.csic.es

Christian Hess – Eduard-Zintl-Institute of Inorganic and Physical Chemistry, Technical University of Darmstadt, 64287 Darmstadt, Germany; orcid.org/0000-0002-4738-7674; Email: christian.hess@tu-darmstadt.de

Authors

Marc Ziemba – Eduard-Zintl-Institute of Inorganic and Physical Chemistry, Technical University of Darmstadt, 64287 Darmstadt, Germany

Christian Schilling – Eduard-Zintl-Institute of Inorganic and Physical Chemistry, Technical University of Darmstadt, 64287 Darmstadt, Germany

Complete contact information is available at:

<https://pubs.acs.org/10.1021/acs.accounts.1c00226>

Notes

The authors declare no competing financial interest.

Biographies

Marc Ziemba studied chemistry at the Technical University of Darmstadt and is currently a Ph.D. student in the group of Prof. Christian Hess. His research focuses on the combination of *operando* spectroscopy and DFT in C1 catalysis over ceria-based materials.

Christian Schilling studied chemistry at the Technical University of Darmstadt and obtained his Ph.D. in 2018. His thesis focused on the development of combined *operando* spectroscopy and DFT methods at ceria-based catalysts. Since then, he has been a manager for product development at Umicore AG & Co. KG, Hanau-Wolfgang, Germany.

M. Verónica Ganduglia-Pirovano studied physics at the Balseiro Institute of the National Atomic Energy Commission, National University of Cuyo, S.C. de Bariloche, Argentina. She obtained her Ph.D. in physics from the University of Stuttgart and the Max Planck Institute for Solid State Research in Stuttgart. After several research associate positions at the Exxon Corporation, Annandale, NJ, USA, the Fritz Haber Institute in Berlin, the Center for Atomic-Scale Materials

Physics-DTU, Denmark, she was a research and teaching assistant at the Humboldt University in Berlin. Since 2009, she has been the leader of the Modeling for Theoretical Catalysis Group at the Institute of Catalysis and Petrochemistry of the Spanish National Research Council (CSIC) in Madrid, where she conducts research on surface chemistry and fundamentals of catalytic reactions at metal oxide surfaces and supported oxide and metal catalysts.

Christian Hess studied chemistry at the Universities of Würzburg, Cambridge, and Göttingen. He obtained his Ph.D. at the Fritz Haber Institute in Berlin. After postdoctoral research at Texas A&M University and the University of California, Berkeley/LBNL as a Feodor-Lynen and Otto-Hahn Fellow, he returned to the Fritz Haber Institute to lead an Emmy Noether Group. Since 2008, he has been a professor at the Technical University of Darmstadt. In his research, he focuses on understanding the mode of operation of functional materials used in catalysis, gas sensing, and energy science.

ACKNOWLEDGMENTS

The DFT calculations were conducted on the Lichtenberg high-performance computer of the TU Darmstadt. We thank Stefan Lauterbach and Hans-Joachim Kleebe for TEM measurements, Kathrin Hofmann for XRD analysis, Martin Brodrecht for nitrogen adsorption/desorption experiments, and Karl Kopp for XPS analysis and technical support. M.V.G.-P. thanks the MICINN-Spain (RTI2018-101604-B-I00) and C.H. thanks the Deutsche Forschungsgemeinschaft (DFG) for support.

REFERENCES

- Schilling, C.; Ganduglia-Pirovano, M. V.; Hess, C. Experimental and Theoretical Study on the Nature of Adsorbed Oxygen Species on Shaped Ceria Nanoparticles. *J. Phys. Chem. Lett.* **2018**, *9* (22), 6593–6598.
- Ziemba, M.; Ganduglia-Pirovano, M. V.; Hess, C. Elucidating the Oxygen Storage-Release Dynamics in Ceria Nanorods by Combined Multi-Wavelength Raman Spectroscopy and DFT. *J. Phys. Chem. Lett.* **2020**, *11*, 8554–8559.
- Ziemba, M.; Hess, C. Influence of Gold on the Reactivity Behaviour of Ceria Nanorods in CO Oxidation: Combining Operando Spectroscopies and DFT Calculations. *Catal. Sci. Technol.* **2020**, *10* (11), 3720–3730.
- Ziemba, M.; Ganduglia-Pirovano, V.; Hess, C. Insight into the Mechanism of the Water-Gas Shift Reaction over Au/CeO₂ Catalysts Using Combined Operando Spectroscopies. *Faraday Discuss.* **2021**, *229*, 232–250.
- Mullins, D. R. The Surface Chemistry of Cerium Oxide. *Surf. Sci. Rep.* **2015**, *70* (1), 42–85.
- Setvín, M.; Wagner, M.; Schmid, M.; Parkinson, G. S.; Diebold, U. Surface Point Defects on Bulk Oxides: Atomically-Resolved Scanning Probe Microscopy. *Chem. Soc. Rev.* **2017**, *46* (7), 1772–1784.
- Hess, C. New Advances in Using Raman Spectroscopy for the Characterization of Catalysts and Catalytic Reactions. *Chem. Soc. Rev.* **2021**, *50*, 3519.
- Fu, Q.; Saltsburg, H.; Flytzani-Stephanopoulos, M. Active Nonmetallic Au and Pt Species on Ceria-Based Water-Gas Shift Catalysts. *Science* **2003**, *301* (5635), 935–938.
- Li, Y.; Kottwitz, M.; Vincent, J. L.; Enright, M. J.; Liu, Z.; Zhang, L.; Huang, J.; Senanayake, S. D.; Yang, W.-C. D.; Crozier, P. A.; Nuzzo, R. G.; Frenkel, A. I. Dynamic Structure of Active Sites in Ceria-Supported Pt Catalysts for the Water Gas Shift Reaction. *Nat. Commun.* **2021**, *12* (1), 914.
- Abdel-Mageed, A. M.; Kučerová, G.; Bansmann, J.; Behm, R. J. Active Au Species During the Low-Temperature Water Gas Shift Reaction on Au/CeO₂: A Time-Resolved Operando XAS and DRIFTS Study. *ACS Catal.* **2017**, *7* (10), 6471–6484.

- (11) Yao, H. C.; Yao, Y. F. Y. Ceria in Automotive Exhaust Catalysts. I. Oxygen Storage. *J. Catal.* **1984**, *86* (2), 254–265.
- (12) Schilling, C.; Hess, C. Elucidating the Role of Support Oxygen in the Water–Gas Shift Reaction over Ceria-Supported Gold Catalysts Using Operando Spectroscopy. *ACS Catal.* **2019**, *9* (2), 1159–1171.
- (13) Schilling, C.; Ziemba, M.; Hess, C.; Ganduglia-Pirovano, M. V. Identification of Single-Atom Active Sites in CO Oxidation over Oxide-Supported Au Catalysts. *J. Catal.* **2020**, *383*, 264–272.
- (14) Park, S.; Vohs, J. M.; Gorte, R. J. Direct Oxidation of Hydrocarbons in a Solid-Oxide Fuel Cell. *Nature* **2000**, *404* (6775), 265–267.
- (15) Wang, Q.; Yeung, K. L.; Bañares, M. A. Ceria and Its Related Materials for VOC Catalytic Combustion: A Review. *Catal. Today* **2020**, *356* (April), 141–154.
- (16) Montini, T.; Melchionna, M.; Monai, M.; Fornasiero, P. Fundamentals and Catalytic Applications of CeO₂-Based Materials. *Chem. Rev.* **2016**, *116* (10), 5987–6041.
- (17) Xu, C.; Qu, X. Cerium Oxide Nanoparticle: A Remarkably Versatile Rare Earth Nanomaterial for Biological Applications. *NPG Asia Mater.* **2014**, *6* (3), e90–e90.
- (18) Pulido-Reyes, G.; Rodea-Palomares, I.; Das, S.; Sakthivel, T. S.; Leganes, F.; Rosal, R.; Seal, S.; Fernández-Piñas, F. Untangling the Biological Effects of Cerium Oxide Nanoparticles: The Role of Surface Valence States. *Sci. Rep.* **2015**, *5* (1), 15613.
- (19) Choi, S. W.; Kim, J. Recent Progress in Autocatalytic Ceria Nanoparticles-Based Translational Research on Brain Diseases. *ACS Appl. Nano Mater.* **2020**, *3* (2), 1043–1062.
- (20) Ganduglia-Pirovano, M. V. The Non-Innocent Role of Cerium Oxide in Heterogeneous Catalysis: A Theoretical Perspective. *Catal. Today* **2015**, *253*, 20–32.
- (21) Zhu, L.; Jin, X.; Zhang, Y.-Y.; Du, S.; Liu, L.; Rajh, T.; Xu, Z.; Wang, W.; Bai, X.; Wen, J.; Wang, L. Visualizing Anisotropic Oxygen Diffusion in Ceria under Activated Conditions. *Phys. Rev. Lett.* **2020**, *124* (5), 056002.
- (22) Rodríguez, J. A.; Grinter, D. C.; Liu, Z.; Palomino, R. M.; Senanayake, S. D. Ceria-Based Model Catalysts: Fundamental Studies on the Importance of the Metal-Ceria Interface in CO Oxidation, the Water-Gas Shift, CO₂ Hydrogenation, and Methane and Alcohol Reforming. *Chem. Soc. Rev.* **2017**, *46* (7), 1824–1841.
- (23) Zhang, C.; Michaelides, A.; Jenkins, S. J. Theory of Gold on Ceria. *Phys. Chem. Chem. Phys.* **2011**, *13* (1), 22–33.
- (24) Zhao, X.; Susman, M. D.; Rimer, J. D.; Bollini, P. Synthesis, Structure and Catalytic Properties of Faceted Oxide Crystals. *ChemCatChem* **2021**, *13* (1), 6–27.
- (25) Loridant, S. Raman Spectroscopy as a Powerful Tool to Characterize Ceria-Based Catalysts. *Catal. Today* **2021**, *373*, 98–111.
- (26) Schmitt, R.; Nanning, A.; Kraynis, O.; Korobko, R.; Frenkel, A. I.; Lubomirsky, I.; Haile, S. M.; Rupp, J. L. M. A Review of Defect Structure and Chemistry in Ceria and Its Solid Solutions. *Chem. Soc. Rev.* **2020**, *49* (2), 554–592.
- (27) Coduri, M.; Checchia, S.; Longhi, M.; Ceresoli, D.; Scavini, M. Rare Earth Doped Ceria: The Complex Connection Between Structure and Properties. *Front. Chem.* **2018**, *6* (OCT), 1–23.
- (28) García, X.; Soler, L.; Divins, N. J.; Vendrell, X.; Serrano, I.; Lucentini, I.; Prat, J.; Solano, E.; Tallarida, M.; Escudero, C.; Llorca, J. Ceria-Based Catalysts Studied by Near Ambient Pressure X-Ray Photoelectron Spectroscopy: A Review. *Catalysts* **2020**, *10* (3), 286.
- (29) Boaro, M.; Colussi, S.; Trovarelli, A. Ceria-Based Materials in Hydrogenation and Reforming Reactions for CO₂ Valorization. *Front. Chem.* **2019**, *7*(28), DOI: 10.3389/fchem.2019.00028.
- (30) Nolan, M. Surface Effects in the Reactivity of Ceria. *Catalysis by Materials with Well-Defined Structures*; Elsevier, 2015; pp 159–192. DOI: 10.1016/B978-0-12-801217-8.00006-2.
- (31) Paier, J.; Penschke, C.; Sauer, J. Oxygen Defects and Surface Chemistry of Ceria: Quantum Chemical Studies Compared to Experiment. *Chem. Rev.* **2013**, *113* (6), 3949–3985.
- (32) Pan, Y.; Nilius, N.; Stiehler, C.; Freund, H.-J.; Goniakowski, J.; Noguera, C. Ceria Nanocrystals Exposing Wide (100) Facets: Structure and Polarity Compensation. *Adv. Mater. Interfaces* **2014**, *1* (9), 1400404.
- (33) Capdevila-Cortada, M.; López, N. Entropic Contributions Enhance Polarity Compensation for CeO₂(100) Surfaces. *Nat. Mater.* **2017**, *16* (3), 328–334.
- (34) Matz, O.; Calatayud, M. Breaking H₂ with CeO₂: Effect of Surface Termination. *ACS Omega* **2018**, *3* (11), 16063–16073.
- (35) Zhou, C.-Y.; Wang, D.; Gong, X.-Q. A DFT+ U Revisit of Reconstructed CeO₂(100) Surfaces: Structures, Thermostabilities and Reactivities. *Phys. Chem. Chem. Phys.* **2019**, *21* (36), 19987–19994.
- (36) Ganduglia-Pirovano, M. V.; Hofmann, A.; Sauer, J. Oxygen Vacancies in Transition Metal and Rare Earth Oxides: Current State of Understanding and Remaining Challenges. *Surf. Sci. Rep.* **2007**, *62* (6), 219–270.
- (37) Trovarelli, A.; Llorca, J. Ceria Catalysts at Nanoscale: How Do Crystal Shapes Shape Catalysis? *ACS Catal.* **2017**, *7* (7), 4716–4735.
- (38) Ha, H.; Yoon, S.; An, K.; Kim, H. Y. Catalytic CO Oxidation over Au Nanoparticles Supported on CeO₂ Nanocrystals: Effect of the Au–CeO₂ Interface. *ACS Catal.* **2018**, *8* (12), 11491–11501.
- (39) Filtschew, A.; Hofmann, K.; Hess, C. Ceria and Its Defect Structure: New Insights from a Combined Spectroscopic Approach. *J. Phys. Chem. C* **2016**, *120* (12), 6694–6703.
- (40) Mai, H.-X.; Sun, L.-D.; Zhang, Y.-W.; Si, R.; Feng, W.; Zhang, H.-P.; Liu, H.-C.; Yan, C.-H. Shape-Selective Synthesis and Oxygen Storage Behavior of Ceria Nanopolyhedra, Nanorods, and Nanocubes. *J. Phys. Chem. B* **2005**, *109* (51), 24380–24385.
- (41) Wu, Q.; Zhang, F.; Xiao, P.; Tao, H.; Wang, X.; Hu, Z.; Lü, Y. Great Influence of Anions for Controllable Synthesis of CeO₂ Nanostructures: From Nanorods to Nanocubes. *J. Phys. Chem. C* **2008**, *112* (44), 17076–17080.
- (42) Li, J.; Zhang, Z.; Tian, Z.; Zhou, X.; Zheng, Z.; Ma, Y.; Qu, Y. Low Pressure Induced Porous Nanorods of Ceria with High Reducibility and Large Oxygen Storage Capacity: Synthesis and Catalytic Applications. *J. Mater. Chem. A* **2014**, *2* (39), 16459–16466.
- (43) Ishikawa, Y.; Takeda, M.; Tsukimoto, S.; Nakayama, K. S.; Asao, N. Cerium Oxide Nanorods with Unprecedented Low-Temperature Oxygen Storage Capacity. *Adv. Mater.* **2016**, *28* (7), 1467–1471.
- (44) Schilling, C.; Hofmann, A.; Hess, C.; Ganduglia-Pirovano, M. V. Raman Spectra of Polycrystalline CeO₂: A Density Functional Theory Study. *J. Phys. Chem. C* **2017**, *121* (38), 20834–20849.
- (45) Liu, Z.; Li, X.; Mayyas, M.; Koshy, P.; Hart, J. N.; Sorrell, C. C. Growth Mechanism of Ceria Nanorods by Precipitation at Room Temperature and Morphology-Dependent Photocatalytic Performance. *CrystEngComm* **2017**, *19* (32), 4766–4776.
- (46) Camellone, M. F.; Fabris, S. Reaction Mechanisms for the CO Oxidation on Au/CeO₂ Catalysts: Activity of Substitutional Au³⁺/Au⁺ Cations and Deactivation of Supported Au⁺ Adatoms. *J. Am. Chem. Soc.* **2009**, *131* (30), 10473–10483.
- (47) Ghosh, P.; Farnesi Camellone, M.; Fabris, S. Fluxionality of Au Clusters at Ceria Surfaces during CO Oxidation: Relationships among Reactivity, Size, Cohesion, and Surface Defects from DFT Simulations. *J. Phys. Chem. Lett.* **2013**, *4* (14), 2256–2263.
- (48) Kim, H. Y.; Lee, H. M.; Henkelman, G. CO Oxidation Mechanism on CeO₂-Supported Au Nanoparticles. *J. Am. Chem. Soc.* **2012**, *134* (3), 1560–1570.
- (49) Wang, Y.-G.; Mei, D.; Glezakou, V.-A.; Li, J.; Rousseau, R. Dynamic Formation of Single-Atom Catalytic Active Sites on Ceria-Supported Gold Nanoparticles. *Nat. Commun.* **2015**, *6* (1), 6511.
- (50) Zhou, Z.; Kooi, S.; Flytzani-Stephanopoulos, M.; Saltsburg, H. The Role of the Interface in CO Oxidation on Au/CeO₂ Multilayer Nanotowers. *Adv. Funct. Mater.* **2008**, *18* (18), 2801–2807.
- (51) Chang, M.-W.; Zhang, L.; Davids, M.; Pilot, I. A. W.; Hensen, E. J. M. Dynamics of Gold Clusters on Ceria during CO Oxidation. *J. Catal.* **2020**, *392*, 39–47.
- (52) Lohrenscheidt, M.; Hess, C. Direct Evidence for the Participation of Oxygen Vacancies in the Oxidation of Carbon Monoxide over Ceria-Supported Gold Catalysts by Using Operando Raman Spectroscopy. *ChemCatChem* **2016**, *8* (3), 523–526.

(53) Guzman, J.; Carretin, S.; Corma, A. Spectroscopic Evidence for the Supply of Reactive Oxygen during CO Oxidation Catalyzed by Gold Supported on Nanocrystalline CeO₂. *J. Am. Chem. Soc.* **2005**, *127* (10), 3286–3287.

(54) Schilling, C.; Hess, C. Real-Time Observation of the Defect Dynamics in Working Au/CeO₂ Catalysts by Combined Operando Raman/UV–Vis Spectroscopy. *J. Phys. Chem. C* **2018**, *122* (5), 2909–2917.

(55) Flytzani-Stephanopoulos, M.; Gates, B. C. Atomically Dispersed Supported Metal Catalysts. *Annu. Rev. Chem. Biomol. Eng.* **2012**, *3* (1), 545–574.

(56) Zhao, S.; Chen, F.; Duan, S.; Shao, B.; Li, T.; Tang, H.; Lin, Q.; Zhang, J.; Li, L.; Huang, J.; Bion, N.; Liu, W.; Sun, H.; Wang, A.-Q.; Haruta, M.; Qiao, B.; Li, J.; Liu, J.; Zhang, T. Remarkable Active-Site Dependent H₂O Promoting Effect in CO Oxidation. *Nat. Commun.* **2019**, *10* (1), 3824.

(57) Zhang, S.; Li, X.-S.; Chen, B.; Zhu, X.; Shi, C.; Zhu, A.-M. CO Oxidation Activity at Room Temperature over Au/CeO₂ Catalysts: Disclosure of Induction Period and Humidity Effect. *ACS Catal.* **2014**, *4* (10), 3481–3489.

(58) Li, Z.; Li, W.; Abroshan, H.; Ge, Q.; Li, G.; Jin, R. Dual Effects of Water Vapor on Ceria-Supported Gold Clusters. *Nanoscale* **2018**, *10* (14), 6558–6565.

(59) Wang, C.; Gu, X.-K.; Yan, H.; Lin, Y.; Li, J.; Liu, D.; Li, W.-X.; Lu, J. Water-Mediated Mars–Van Krevelen Mechanism for CO Oxidation on Ceria-Supported Single-Atom Pt₁ Catalyst. *ACS Catal.* **2017**, *7* (1), 887–891.

(60) Chutia, A.; Willock, D. J.; Catlow, C. R. A. The Electronic Properties of Au Clusters on CeO₂ (110) Surface with and without O-Defects. *Faraday Discuss.* **2018**, *208*, 123–145.

(61) Zhu, K.-J.; Yang, Y.-J.; Lang, J.-J.; Teng, B.-T.; Wu, F.-M.; Du, S.-Y.; Wen, X.-D. Substrate-Dependent Au Cluster: A New Insight into Au/CeO₂. *Appl. Surf. Sci.* **2016**, *387*, 557–568.

(62) Wu, Z.; Li, M.; Overbury, S. H. On the Structure Dependence of CO Oxidation over CeO₂ Nanocrystals with Well-Defined Surface Planes. *J. Catal.* **2012**, *285* (1), 61–73.

(63) Schilling, C.; Hess, C. CO Oxidation on Ceria Supported Gold Catalysts Studied by Combined Operando Raman/UV–Vis and IR Spectroscopy. *Top. Catal.* **2017**, *60* (1–2), 131–140.

(64) Kim, H. Y.; Henkelman, G. CO Oxidation at the Interface of Au Nanoclusters and the Stepped-CeO₂(111) Surface by the Mars–van Krevelen Mechanism. *J. Phys. Chem. Lett.* **2013**, *4* (1), 216–221.

(65) Hernández, J. A.; Gómez, S. A.; Zepeda, T. A.; Fierro-González, J. C.; Fuentes, G. A. Insight into the Deactivation of Au/CeO₂ Catalysts Studied by In Situ Spectroscopy during the CO-PROX Reaction. *ACS Catal.* **2015**, *5* (7), 4003–4012.

(66) Castleton, C. W. M.; Kullgren, J.; Hermansson, K. Tuning LDA +U for Electron Localization and Structure at Oxygen Vacancies in Ceria. *J. Chem. Phys.* **2007**, *127* (24), 244704.

(67) Carter, J. H.; Liu, X.; He, Q.; Althabban, S.; Nowicka, E.; Freakley, S. J.; Niu, L.; Morgan, D. J.; Li, Y.; Niemantsverdriet, J. W. H.; Golunski, S.; Kiely, C. J.; Hutchings, G. J. Activation and Deactivation of Gold/Ceria-Zirconia in the Low-Temperature Water-Gas Shift Reaction. *Angew. Chem., Int. Ed.* **2017**, *56* (50), 16037–16041.

(68) Jeong, H.; Kwon, O.; Kim, B.-S.; Bae, J.; Shin, S.; Kim, H.-E.; Kim, J.; Lee, H. Highly Durable Metal Ensemble Catalysts with Full Dispersion for Automotive Applications beyond Single-Atom Catalysts. *Nat. Catal.* **2020**, *3* (4), 368–375.

(69) Yoo, M.; Yu, Y.-S.; Ha, H.; Lee, S.; Choi, J.-S.; Oh, S.; Kang, E.; Choi, H.; An, H.; Lee, K.-S.; Park, J. Y.; Celestre, R.; Marcus, M. A.; Nowrouzi, K.; Taube, D.; Shapiro, D. A.; Jung, W.; Kim, C.; Kim, H. Y. A Tailored Oxide Interface Creates Dense Pt Single-Atom Catalysts with High Catalytic Activity. *Energy Environ. Sci.* **2020**, *13* (4), 1231–1239.

(70) Merrick, J. P.; Moran, D.; Radom, L. An Evaluation of Harmonic Vibrational Frequency Scale Factors. *J. Phys. Chem. A* **2007**, *111* (45), 11683–11700.

(71) Lustemberg, P. G.; Plessow, P. N.; Wang, Y.; Yang, C.; Nefedov, A.; Studt, F.; Wöll, C.; Ganduglia-Pirovano, M. V. Vibrational

Frequencies of Cerium-Oxide-Bound CO: A Challenge for Conventional DFT Methods. *Phys. Rev. Lett.* **2020**, *125* (25), 256101.

Elucidating the Oxygen Storage-Release Dynamics in Ceria Nanorods by Combined Multi-Wavelength Raman Spectroscopy and DFT

Marc Ziemba, M. Verónica Ganduglia-Pirovano, and Christian Hess*

Cite This: *J. Phys. Chem. Lett.* 2020, 11, 8554–8559

Read Online

ACCESS |



Metrics & More

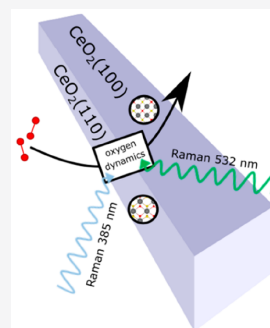


Article Recommendations



Supporting Information

ABSTRACT: The oxygen storage-release dynamics in ceria nanorods is elucidated by using a combination of in situ multi-wavelength Raman spectroscopy and density functional theory calculations. Ceria nanorods exposing $\text{CeO}_2(100)$ and $\text{CeO}_2(110)$ facets are shown to be characterized by highly facet-dependent properties regarding molecular oxygen activation and decomposition as well as lattice oxygen dynamics. Temperature-dependent Raman results show that oxygen is stored in the form of peroxide species on the (100) facets, which are then released as gaseous oxygen, whereas lattice oxygen is involved with the (110) facets. On the latter, peroxide species first decompose into oxygen atoms that heal vacant lattice oxygen sites before being released as gaseous oxygen. The exposure of different facets makes ceria nanorods an interesting material for catalytic applications, because they allow the use of a mixture of oxygen storage-release functions, as well as their synergistic interactions, in a single system.



Ceria is an important support material for precious metals in oxidation reactions such as the CO oxidation or the water–gas shift reaction.^{1–4} It is therefore of great interest to understand the reduction and reoxidation of the support during reaction. In addition, ceria is used as an oxygen storage component in the formulation of automotive catalysts. Whereas the choice of the surface facet has been shown to have a strong effect on the oxygen storage capacity,^{5,6} a detailed understanding of the oxygen storage properties of nanostructured ceria is still missing. In the context of ceria materials, Raman spectroscopy has proved to be a powerful method to detect adsorbed oxygen species or oxygen defects.^{7–12} In previous studies, the dependence of oxygen activation on the exposed ceria facet has been investigated employing single-crystal surfaces,¹³ while we have addressed catalytically interesting ceria powder samples with either $\text{CeO}_2(111)$ or $\text{CeO}_2(100)$ surface termination.⁸ Our previous study has revealed a facet-dependent behavior regarding oxygen adsorption and activation, resulting in the formation of peroxide (O_2^{2-}), superoxides (O_2^-), and weakly bound oxygen ($\text{O}_2^{\delta-}$) species.⁸ The relevance of investigating the adsorption of O_2 species on ceria surfaces lies in the fact that O_2 species not only serve as probe a molecule, as, for example, CO,¹⁴ but may also be involved in the dynamic exchange of lattice oxygen and the catalytic activity of ceria-based systems.^{1,4,15–18}

In this work, we study the facet-dependent oxygen adsorption, activation, and dynamics at ceria rods, exposing (110) and (100) facets, employing a combined multi-wavelength Raman/density functional theory (DFT) approach,

where our previous study on ceria nanocubes serves as a reference for the (100) facet.⁸ We show that the oxygen storage-release mechanism depends largely on the exposed facet and is related to differences in the molecular oxygen activation and decomposition properties as well as in the ease of formation of lattice oxygen vacancies.

On the basis of the growth mechanism of ceria rods and findings from the literature, we know that the proportion of both (110) and (100) facets is significant, whereby that of the former is slightly higher.¹⁹ The (110) facet has been shown to be the facet with the lowest surface oxygen defect formation energy.^{13,20–22} Thus, this facet is particularly interesting for reactions in which lattice oxygen is involved. After the hydrothermal synthesis of the ceria rods (for details see the Supporting Information), they were characterized using transmission electron microscopy (TEM), X-ray diffraction (XRD), and N_2 adsorption at 77 K. The TEM images in Figure 1A and Figure S2 demonstrate the successful synthesis of ceria rods containing (100) and (110) surface terminations, based on the observed distances between the lattice planes of 0.27 and 0.19 nm, respectively.^{23,24} Using the fast Fourier transform (FFT) of the individual domains and masking the diffraction

Received: August 26, 2020

Accepted: September 15, 2020

Published: September 24, 2020



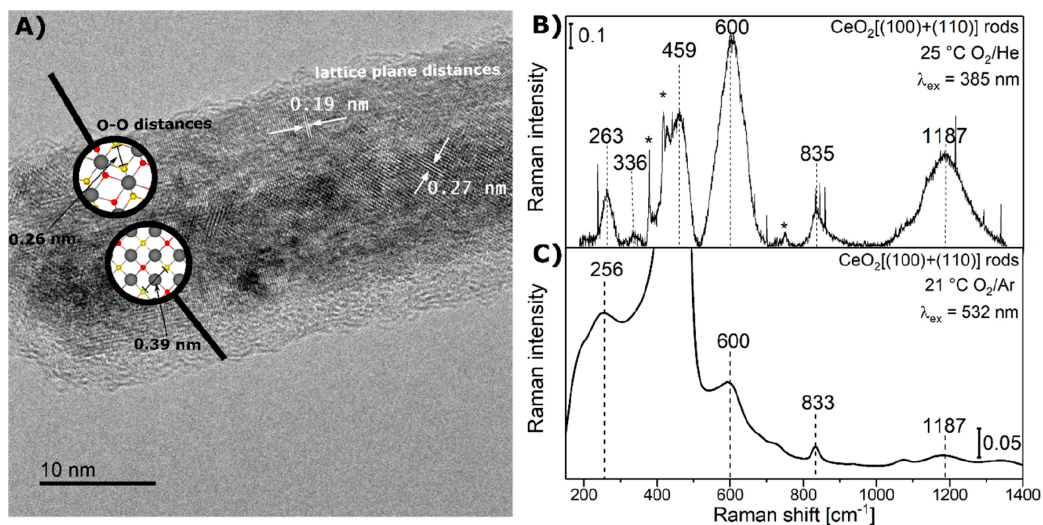


Figure 1. (A) TEM image of ceria nanorods. White arrows on the right side indicate the distance of the lattice planes in the direction of the particle surface. The two magnifying glasses on the left side show the theoretical top view images of the $\text{CeO}_2(110)$ (at the top) and $\text{CeO}_2(100)$ (at the bottom) surfaces together with the calculated smallest distance between two surface oxygen atoms (PBE+U/4.5 eV). (B) In situ 385 nm Raman spectrum of ceria nanorods recorded at 25 °C in 25% O_2/He (pretreatment: 2 h, 120 °C, 25% O_2/He , 50 mL/min), at a total flow rate of 50 mL/min. The asterisk (*) marks bands originating from the sapphire window, while other sharp features result from cosmic rays. (C) In situ 532 nm Raman spectrum of ceria nanorods recorded at 21 °C in 25% O_2/Ar , at a total flow rate of 100 mL/min. The high-intensity F_{2g} peak at 455.1 cm^{-1} was cut off to allow an enlarged view of the other features.

patterns with subsequent inverse FFT, the surface terminations were analyzed in more detail (see Figures S3 and S4). To exclude the presence of the (111) surface termination, Raman spectroscopy with an excitation wavelength of 385 nm was used as a more integral method than TEM. Comparing the spectra of the rods with those of particles exhibiting a (111) termination reveals that the rods do not show the characteristic transversal surface mode of the (111) surface at $\sim 402 \text{ cm}^{-1}$, in contrast to the sheets and polyhedra (see Figure S5).⁷ The XRD results show that only cubic CeO_2 is present (see Figure S6). Using N_2 adsorption and the Brunauer-Emmett-Teller (BET) model, a specific surface area of 88 m^2/g and a pore volume of 0.22 cm^3/g were determined (for isotherms see Figure S7), and by means of the BJH model an average pore diameter of 28 nm could be determined (see Figure S8). Our previous detailed TEM analysis has confirmed that the morphology and size of the particles does not change during exposure to water–gas shift conditions, which are much harsher than the conditions applied in this study.¹⁷ Thus, we can safely assume that the surface termination and the shape of the particles are preserved during the here-performed experiments.

Multi-wavelength Raman spectroscopy with excitation wavelengths of 385 and 532 nm was employed to monitor the oxygen dynamics of the ceria rods, where the penetration depth at 385 nm is less than that at 532 nm, and since ceria shows absorption at 385 nm, a selective (resonance) enhancement of the ceria-related vibrational modes is possible. The use of an additional visible excitation wavelength (633 nm; see Figure S9) does not provide any fundamentally new insight compared to 532 nm excitation, in contrast to the 385 nm spectrum, as described in the following. The in situ Raman spectra of ceria nanorods in 25% O_2 at room temperature are shown in Figure 1B,C. In the 385 nm Raman spectrum (see Figure 1B), due to the resonance enhancement, the defect

band at 600 cm^{-1} is more intense than the F_{2g} band at 459 cm^{-1} , indicating the presence of near-surface oxygen defects.⁷ The bands at 263 and 1187 cm^{-1} are assigned to the 2TA (transverse acoustic) and the 2LO (longitudinal optical) overtones, respectively.⁷ Furthermore, a peroxide-related band at 835 cm^{-1} appears, which originates from the adsorption of molecular oxygen at the surface oxygen vacant sites with the excess electrons located at nearby cerium atoms.^{8,13,25} The asymmetry of the 835 cm^{-1} band can be explained by the occurrence of agglomerated peroxides, which are characterized by a blue-shift, as shown previously for the (100) surface, and will be here discussed in more detail for the (110) surface in the context of Figure 2A.⁸ In the 385 nm spectrum, a small band at 336 cm^{-1} is observed, which is assigned to the deformation vibration of peroxides on the surface of the ceria rods based on the results of the DFT calculations (see below, Figure 2B). Note that typically this band cannot be observed by visible Raman spectroscopy (532 nm) due to overlays in this region (see Figure 1C), thus making the use of different excitation wavelengths essential.⁴ Moreover, it is also noticeable that, despite the presence of the $\text{CeO}_2(100)$ facet, no or only very weak superoxide bands (1103 and/or 1137 cm^{-1})⁸ are observed, in contrast to our previous studies on ceria cubes exposing (100) facets only. The absence of superoxide bands strongly suggests that the presence of the (110) facet next to the $\text{CeO}_2(100)$ facet modifies the latter, resulting in different properties as compared to those of ceria cubes.

The adsorption energy of peroxide species, O_2^{2-} , on ceria surfaces is the result of two energy contributions with opposite effects $E_{\text{ads},\text{O}_2^{2-}} = -E_{\text{vac},\text{O}} + E_{\text{ads},\text{O}}$, namely, the energy gain upon healing the surface vacancies on the reduced facet $-E_{\text{vac},\text{O}} = -[E_{\text{CeO}_{2-x}} + \frac{1}{2}E_{\text{O}_2} - E_{\text{CeO}_2}]$, and the repulsive interactions between the charged chemisorbed species, $E_{\text{ads},\text{O}} = E_{\text{O}_2^{2-}/\text{CeO}_{2-x}}$

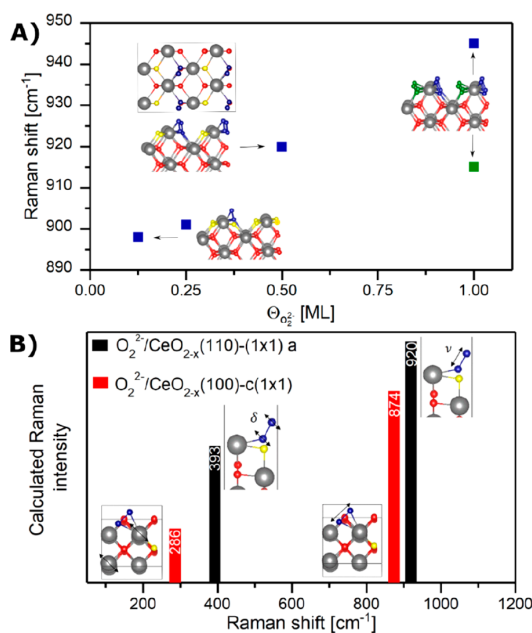


Figure 2. (A) Relationship between the coverage and the Raman shift of peroxides species on the $\text{CeO}_2(110)$ facet, based on the most stable structures for coverages of $\Theta_{\text{O}_2^{2-}} = 0.125, 0.25, 0.5,$ and 1 ML (see Figures S11G,F,A,E, respectively). Surface oxygen is shown in yellow, cerium atoms in gray, and lattice oxygen in red. For the 1 ML structure, the two different peroxide species are shown in green and blue. (B) Calculated Raman intensities for the most stable peroxide structure at 0.5 ML coverage on $\text{CeO}_2(110)$ with (1×1) periodicity (black) (see Figure S11A) and on $\text{CeO}_2(100)$ with $c(1 \times 1)$ periodicity (red), according to our previous study.³ The symmetry (δ, ν) of the vibrations is indicated.

$-\frac{1}{2}E_{\text{O}_2} - E_{\text{CeO}_2} - E_{\text{ads,O}}$ is the adsorption energy of the resulting O atom on the corresponding clean facet resulting from the vacancy healing by the peroxide species. In the following, we consider the process of oxygen vacancy formation and healing using the examples of the (100) and (110) surfaces with $c(2 \times 2)$ (see Figure S11) and (2×2) periodicity, respectively ($\Theta_{\text{vac}} = \Theta_{\text{O}_2^{2-}} = 0.125$). The healing of a surface oxygen vacancy ($-E_{\text{vac,O}}$) is an exothermic process on both surfaces, but on the (100) facet the energy released is by ~ 0.07 eV higher than on the (110) facet (cf. -1.39 eV, Figure S7A and Table S4 in ref 8, and -1.32 eV, Figure S10F and Table S1, respectively), which is in line with the corresponding values for the surface oxygen defect formation energy ($+E_{\text{vac,O}}$) in the literature.¹³ However, the oxygen adsorption energy after the vacancy has been healed by the adsorption of peroxide species, $E_{\text{ads,O}}$ is exothermic on the (100) facet (-0.34 eV, see Figure S8A and Table S4 in ref 8) and endothermic on the (110) ($+0.15$ eV, see Figure S11G and Table S2). As a consequence of the facet-dependent $E_{\text{vac,O}}$ and $E_{\text{ads,O}}$ energy values, the calculated peroxide adsorption energy on the (100) facet is by 0.56 eV higher than on the (110) one (cf. -1.73 eV, Table S4 in ref 8, and -1.17 eV, Table S2, respectively). Summarizing, on ceria rods, O_2^{2-} species are strongly bound on the (100) facets, and the removal of lattice oxygen is more facile at the (110) facets.

Comparing the $\text{O}_2^{2-}/\text{CeO}_{2-x}(100)$ and $\text{O}_2^{2-}/\text{CeO}_{2-x}(110)$ structures at a peroxide coverage of 0.125 ML, we found that

the O–O bond length of the chemisorbed O_2^{2-} species on the (110) facet is smaller by 2.3 pm than on the (100) facet (cf. 1.445 Å, (2×2) -(110), Table S2, and 1.468 Å, $c(2 \times 2)$ -(100), Table S4 in ref 8), which is in line with previous studies.¹³ This difference in bond length results in a higher stretching vibrational frequency by 30 cm^{-1} for the O_2^{2-} species on the (110) facet compared to those on the (100) one. Thus, the presence of peroxides on the surface of CeO_2 rods exposing both facets may lead to band broadening due to the facet-dependent O–O bond lengths of the chemisorbed O_2^{2-} species. Moreover, as previously discussed for the (111) and (100) facets,⁸ on the (110) one, the O–O bond length also decreases with increasing O_2^{2-} coverage from 0.125 to 1 ML (see Table S2), which is reflected in an increase of the stretching vibrational frequency (see Figure 2A), with the consequent broadening of the peroxide band due to the simultaneous presence of different local coverages. As a special feature of the (110) facet, we found that, in the complete peroxide monolayer ($\Theta_{\text{O}_2^{2-}} = 1\text{ML}$), two peroxide configurations with different O–O bond lengths exist (see Figure S11E and Table S2), which is reflected in two different vibrational frequencies (indicated as green and blue dots in Figure 2A), that may also contribute to the broadening of the peroxide band in the experimental spectra. Summarizing these results, the observed band broadening in the experimental spectra for the rods is due to both the presence of different local coverages and the existence of two facets. Note that, on the $\text{CeO}_2(110)$ surface, the creation of a surface oxygen defect next to an existing peroxide is energetically favorable. For example, a surface oxygen atom from the $\text{O}_2^{2-}/\text{CeO}_{2-x}(110)$ -(1×1) structure with $\Theta_{\text{vac}} = \Theta_{\text{O}_2^{2-}} = 0.5$ (see Figure S11D) is removed for a cost of 1.63 eV, that is, 0.48 eV less compared to the case without a nearby peroxide (2.11 eV, see Figure S10A and Table S1). For a comparison of our results with previous theoretical studies,^{26,27} see the Supporting Information.

Moreover, Figure 2B shows that, for peroxides on ceria surfaces, besides the O–O stretching vibration, another vibration occurs at lower wavenumbers, which is also Raman-active but less intense than the stretching vibration. Note that this vibration is observed for all peroxide coverages (not shown). The symmetry of this vibration can be best described as a deformation vibration (δ). Both the stretching and deformation vibrations of the O_2^{2-} species on the (100) facet are at significantly lower wavenumbers compared to those on the (110). On the basis of the above-mentioned higher stability of the O_2^{2-} species on the $\text{CeO}_2(100)$ facet, we assigned the experimentally observed band at 336 cm^{-1} on CeO_2 rods (see Figure 1B) to peroxide deformation vibrations of species predominantly adsorbed on the (100) facets. While a band and a shoulder have previously been reported for $\text{CeO}_2(111)$, at 357 and 340 cm^{-1} , respectively, no clear assignment was provided.¹¹

On the $\text{CeO}_2(110)$ facets, for which peroxide species are weaker bound as compared to the (100) facets, a more facile dissociation of the peroxide species after O_2 adsorption at an oxygen vacant site is expected, where the resulting oxygen atoms heal adjacent oxygen vacancies, consistent with the behavior observed previously for single crystals.¹³ As discussed above, it is likely that surface oxygen vacancies would form in the immediate neighborhood of adsorbed peroxide species on the (110) facets. This would also occur on the (100) facets.⁸ For instance, the removal of a surface oxygen atom from the

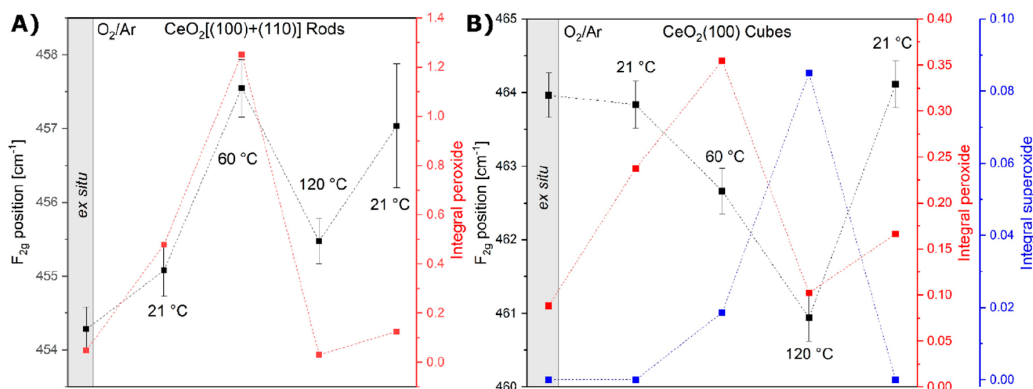


Figure 3. (A) Temperature-dependent Raman F_{2g} position and peroxide integral for ceria rods at 532 nm excitation. (B) Raman F_{2g} position, peroxide, and superoxide integrals for ceria cubes at 532 nm excitation based on previous data.⁸ The data points for in situ conditions correspond to the mean value of two measurements for rods and three measurements for cubes. Inaccuracies of the F_{2g} position are given as standard deviations. The scaling range for the F_{2g} positions is the same for rods and cubes.

$O_2^{2-}/CeO_{2-x}(100)-c(1 \times 1)$ structure with $\Theta_{O_{vac}} = \Theta_{O_2^{2-}} = 0.5$ is by 0.45 eV energetically less costly compared to the case without a nearby peroxide (cf. 2.13 and 1.68 eV, respectively⁸). However, two factors would favor the breakage of the O_2^{2-} species into two O atoms on the (110) facets compared to the (100) ones, namely, the closer distance by 1.3 Å between anionic surface sites on the former (see Figure 1A), as well as the higher exothermicity of the reaction leading to the reoxidation of the surface (e.g., the reaction energy of O_2^{2-}/CeO_{2-x} ($\Theta_{O_{vac}} = 1$, $\Theta_{O_2^{2-}} = 0.5$) $\rightarrow CeO_2$ equals to -1.895 and -1.360 eV for the (110) and (100) facets, respectively). Consequently, we conclude that the observed peroxides on the rods mostly originate from peroxides adsorbed on the (100) facets. In this context, it is worth mentioning that previous theoretical studies have shown that oxygen vacancy migration in bulk ceria^{28–30} and at the (111) surface³¹ can occur with barriers below 0.5 eV. Oxygen vacancy migration is not just conceivable on the (110) and (100) facets but is likely to play an important role after peroxide dissociation occurs.

Figure 3 shows the temperature-dependent oxygen activation and dynamics for rods (A) and cubes (B), as probed by the formation of peroxides/superoxides species and the F_{2g} shift, as a measure of near-surface oxygen defects. For the ex situ measurement at 21 °C, the F_{2g} band position for the ceria rods is at 454.3 cm^{-1} (see Figure 3A) corresponding to a red-shift of $\sim 10\text{ cm}^{-1}$ as compared to ceria cubes exposing (100) facets (464.0 cm^{-1} , see Figure 3B). This red-shift is indicative of a high defect concentration in the rods,³² in line with the observed small intensity of the F_{2g} band (451.1 cm^{-1}) and the strong defect band at 600 cm^{-1} when using a 385 nm excitation (see Figure 1B), as well as with the greatest ease with which oxygen defects can be created on the (110) facet. Note that the position of the F_{2g} band varies if different excitation wavelengths are used, which can be related to the associated different penetration depths. In fact, if 532 nm excitation is employed for in situ Raman measurements on rods, the F_{2g} band is red-shifted by 3.9 cm^{-1} (455.1 cm^{-1} , see Figures 1C and 3A) compared to the position observed at 385 nm excitation (459 cm^{-1} , see Figure 1B). For an excitation wavelength of 532 nm, due to weaker absorption,⁴ the laser penetrates deeper into the sample increasing the contribution of subsurface layers.³³ Thus, the observed red-shift of the F_{2g}

band at 532 nm excitation indicates that the subsurface of the rods is also defect-rich.

Furthermore, Figure 3 shows that the F_{2g} position varies with temperature. According to previous studies,³⁴ an increase in temperature leads to a red-shift of the F_{2g} band. However, within the temperature range considered here, those changes are small ($<1\text{ cm}^{-1}$) and thus within the experimental error. Hence, a temperature effect alone cannot explain the observed changes of the F_{2g} band position (see Figure 3). When the temperature is switched from 21 to 60 °C, a blue-shift of 2.3 cm^{-1} is observed for the rods, and a red-shift of 1.2 cm^{-1} is seen for the cubes, indicating ceria oxidation and reduction, respectively.⁷ At the same time, for both rods and cubes, the peroxide band shows its maximum intensity. The increase in the amount of adsorbed peroxide species, as the temperature increases from 21 to 60 °C, is related to the above-discussed ease with which oxygen vacancies can be created close to an existing peroxide on both surfaces. Peroxide species bind at those vacant sites on both surfaces, which is consistent with the observed maximum intensity of the peroxide bands (see Figure 3). However, as stated above, the stability of peroxide species on the different facets is *not* the same.

Referring back to the DFT data and our previous argument, peroxides on (100) facets are more strongly bound than on (110) ones, and peroxide dissociation—followed by the healing of lattice oxygen vacancies—is more exothermic on the (110) facets. Thus, we here propose that, on ceria rods exposing (110) and (100) facets, two different oxygen storage mechanisms operate simultaneously, as follows. The weaker bound peroxide species on the (110) facets decompose, and oxygen atoms are stored in the lattice, which is in line with the observed blue-shift of the F_{2g} band (see Figure 3A). At the same time, oxygen is also stored in the form of chemisorbed O_2^{2-} species on the (100) facets of the rods. Conversely, for the cubes, exposing solely (100) facets, as the temperature increases from 21 to 60 °C, oxygen vacancies are created near the surface, and O_2^{2-} species strongly adsorb (i.e., are stored) on those vacant sites on the surface, but the deeper layers remain reduced, because the O_2^{2-} species do not decompose, which is consistent with the observed red-shift of the F_{2g} band (see Figure 3B). We turn now to the question of oxygen release from rods and cubes.

When the temperature of the rods is further increased to 120 °C, a red-shift of 2.0 cm^{-1} is observed (see Figure 3A), indicating the onset of ceria reduction, and simultaneously, the peroxide band fully loses intensity. Moreover, the F_{2g} position is slightly blue-shifted by 0.3 cm^{-1} as compared to the initial position at 21 °C, indicating that, comparatively, the system is oxidized. What is happening is that all of the stored oxygen in the form of O_2^{2-} on the (100) facets is released as gaseous oxygen, consistent with the loss in intensity of the peroxide band, although part of the oxygen stored in the lattice is also released. Such operating release mechanisms leave near-surface oxygen vacant sites, and that is why a red-shift of the F_{2g} band is observed as the temperature increases from 60 to 120 °C. The fact that the F_{2g} position at 120 °C is slightly blue-shifted compared to that at 21 °C indicates that some of the stored oxygen in the lattice at 60 °C, for which the existence of the (110) facets is essential, has not been removed at 120 °C. We note that, as a result of the oxidative treatment, the initial reduced state is not recovered after the sample is cooled to 21 °C.

As the temperature is raised from 60 to 120 °C, the cubes, exposing exclusively (100) facets, behave once more differently than the rods (cf. Figure 3A,B). The peroxide band loses intensity, and a red-shift of the F_{2g} band is observed (1.7 cm^{-1}), but differently from the rods, superoxides, O_2^- , are formed on the cubes. Hence, the stored oxygen in the form of O_2^{2-} on the (100) surfaces of the cubes is converted into O_2^- species, and it is the release of lattice oxygen that is consistent with the red-shift of the F_{2g} band. On the basis of this observation, we propose that at higher temperatures on the cubes a thermal equilibrium between the O_2^{2-} and O_2^- species exists and that these species do not decompose, which is related to the high stability of peroxides/superoxides on the (100) surface. However, if we now compare the stability of the O_2^{2-} species on the (100) surfaces of the cubes with that of the O_2^{2-} species on the (100) facets of the rods (cf. Figure 3A,B), we realize that on the cubes there is a $\text{O}_2^{2-} \leftrightarrow \text{O}_2^-$ conversion, whereas on the rods, O_2^{2-} species are released as gaseous oxygen. This reveals that there are synergistic interactions between the existing (100) and (110) facets in the rods, which make the former behave differently than in the absence of (110) facets, as in case of the cubes.

Summarizing, a combined in situ multiwavelength Raman and DFT approach has been employed to elucidate the oxygen storage-release mechanism on ceria nanorods. It is shown that the molecular oxygen activation, decomposition, and oxygen dynamics in ceria nanorods is quite complex due to the presence of two ceria facets. Peroxide formation on the (100) facets is energetically favored over the (110) facets, whereas the opposite behavior is observed for defect formation. Both facets are proposed to contribute to oxygen storage either by the formation of active oxygen species, such as peroxides, or by the incorporation of lattice oxygen. Moreover, using a combination of DFT calculations and Raman spectroscopy, the band at 336 cm^{-1} (see Figures 1 and 2) could be univocally assigned to the deformation vibration of peroxides on (100).

Generally speaking, the understanding of the oxygen-release storage mechanisms in ceria-based systems is of great importance for catalytic applications. Moreover, it is known that the ceria surface structure may alter the catalytic activity of ceria-based catalysts, and thus, ceria nanocrystals with controlled morphologies, such as nanocubes and nanorods, are fabricated. The coexistence of the (100) and (110) facets is

assumed to be responsible for the excellent oxygen storage capacity of ceria rods, as demonstrated previously by experiment,^{5,6,23} but not understood in detail. The microscopic understanding gained in this study reveals that, in ceria rods, two different oxygen-release storage mechanisms operate simultaneously. Oxygen can be stored in the form of activated oxygen or as lattice oxygen at low temperatures (<100 °C), which will be released at higher temperatures (>100 °C). Activated peroxide species adsorb on both facets, but the dynamics of such species with varying temperature depends on the facet. Whereas, on the (100) facets the strongest bound peroxide species are initially stored and leave the surface as gaseous oxygen, on the (110), the creation of near-surface vacancies is easier, and the weakest bound peroxide species decompose into oxygen atoms that fill the vacancies, which then are also released as gaseous oxygen. Thus, ceria rods enable a combination of different oxygen storage and activation functions. Our results should be useful in the design of systems with improved storage capacity.

■ ASSOCIATED CONTENT

Supporting Information

The Supporting Information is available free of charge at <https://pubs.acs.org/doi/10.1021/acs.jpcllett.0c02607>.

Detailed information on experimental and theoretical methods as well as additional theoretical data for peroxide species on the reduced $\text{CeO}_2(110)$ surface and a comparison of the $\text{O}_2^{2-}/\text{CeO}_{2-x}(110)$ and $\text{O}_2^{2-}/\text{CeO}_{2-x}(100)$ structures with work in the literature (PDF)

■ AUTHOR INFORMATION

Corresponding Author

Christian Hess – *Eduard Zintl Institute of Inorganic and Physical Chemistry, Technical University of Darmstadt, 64287 Darmstadt, Germany*; orcid.org/0000-0002-4738-7674; Email: christian.hess@tu-darmstadt.de

Authors

Marc Ziemba – *Eduard Zintl Institute of Inorganic and Physical Chemistry, Technical University of Darmstadt, 64287 Darmstadt, Germany*

M. Verónica Ganduglia-Pirovano – *Instituto de Catálisis y Petroleoquímica, Consejo Superior de Investigaciones Científicas, 28049 Madrid, Spain*; orcid.org/0000-0003-2408-8898

Complete contact information is available at: <https://pubs.acs.org/10.1021/acs.jpcllett.0c02607>

Notes

The authors declare no competing financial interest.

■ ACKNOWLEDGMENTS

The DFT calculations were conducted using the Lichtenberg high-performance computer of the TU Darmstadt. J. Rohrer and K. Albe are acknowledged for support with the VASP code. We thank S. Lauterbach and H.-J. Kleebe for TEM measurements, M. Brodrecht for BET measurements, K. Hofmann for XRD measurements, S. Rogg for in situ Raman measurements at 385 nm excitation, and P. Pérez-Bailac and P. G. Lustemberg for helpful discussions on the $\text{CeO}_2(110)$ vacancy structure. M.V.G.P. acknowledges support by the MICINN-Spain (Project No. RTI2018-101604-B-I00).

REFERENCES

- (1) Trovarelli, A.; Llorca, J. Ceria Catalysts at Nanoscale: How Do Crystal Shapes Shape Catalysis? *ACS Catal.* **2017**, *7* (7), 4716–4735.
- (2) Fu, Q.; Saltsburg, H.; Flytzani-Stephanopoulos, M. Active Nonmetallic Au and Pt Species on Ceria-Based Water-Gas Shift Catalysts. *Science* **2003**, *301* (5635), 935–938.
- (3) Schilling, C.; Ziemba, M.; Hess, C.; Ganduglia-Pirovano, M. V. Identification of Single-Atom Active Sites in CO Oxidation over Oxide-Supported Au Catalysts. *J. Catal.* **2020**, *383*, 264–272.
- (4) Ziemba, M.; Hess, C. Influence of Gold on the Reactivity Behaviour of Ceria Nanorods in CO Oxidation: Combining Operando Spectroscopies and DFT Calculations. *Catal. Sci. Technol.* **2020**, *10* (11), 3720–3730.
- (5) Li, J.; Zhang, Z.; Tian, Z.; Zhou, X.; Zheng, Z.; Ma, Y.; Qu, Y. Low Pressure Induced Porous Nanorods of Ceria with High Reducibility and Large Oxygen Storage Capacity: Synthesis and Catalytic Applications. *J. Mater. Chem. A* **2014**, *2* (39), 16459–16466.
- (6) Ishikawa, Y.; Takeda, M.; Tsukimoto, S.; Nakayama, K. S.; Asao, N. Cerium Oxide Nanorods with Unprecedented Low-Temperature Oxygen Storage Capacity. *Adv. Mater.* **2016**, *28* (7), 1467–1471.
- (7) Schilling, C.; Hofmann, A.; Hess, C.; Ganduglia-Pirovano, M. V. Raman Spectra of Polycrystalline CeO₂: A Density Functional Theory Study. *J. Phys. Chem. C* **2017**, *121* (38), 20834–20849.
- (8) Schilling, C.; Ganduglia-Pirovano, M. V.; Hess, C. Experimental and Theoretical Study on the Nature of Adsorbed Oxygen Species on Shaped Ceria Nanoparticles. *J. Phys. Chem. Lett.* **2018**, *9* (22), 6593–6598.
- (9) Taniguchi, T.; Watanabe, T.; Sugiyama, N.; Subramani, A. K.; Wagata, H.; Matsushita, N.; Yoshimura, M. Identifying Defects in Ceria-Based Nanocrystals by UV Resonance Raman Spectroscopy. *J. Phys. Chem. C* **2009**, *113* (46), 19789–19793.
- (10) Agarwal, S.; Zhu, X.; Hensen, E. J. M.; Mojet, B. L.; Lefferts, L. Surface-Dependence of Defect Chemistry of Nanostructured Ceria. *J. Phys. Chem. C* **2015**, *119* (22), 12423–12433.
- (11) Pushkarev, V. V.; Kovalchuk, V. I.; D'Itri, J. L. Probing Defect Sites on the CeO₂ Surface with Dioxygen. *J. Phys. Chem. B* **2004**, *108* (17), 5341–5348.
- (12) Choi, Y. M.; Abernathy, H.; Chen, H.-T.; Lin, M. C.; Liu, M. Characterization of O₂-CeO₂ Interactions Using In Situ Raman Spectroscopy and First-Principle Calculations. *ChemPhysChem* **2006**, *7* (9), 1957–1963.
- (13) Yang, C.; Yu, X.; Heißler, S.; Weidler, P. G.; Nefedov, A.; Wang, Y.; Wöll, C.; Kropp, T.; Paier, J.; Sauer, J. O₂ Activation on Ceria Catalysts-The Importance of Substrate Crystallographic Orientation. *Angew. Chem., Int. Ed.* **2017**, *56* (51), 16399–16404.
- (14) Yang, C.; Yu, X.; Heißler, S.; Nefedov, A.; Colussi, S.; Llorca, J.; Trovarelli, A.; Wang, Y.; Wöll, C. Surface Faceting and Reconstruction of Ceria Nanoparticles. *Angew. Chem., Int. Ed.* **2017**, *56* (1), 375–379.
- (15) Lohrenscheid, M.; Hess, C. Direct Evidence for the Participation of Oxygen Vacancies in the Oxidation of Carbon Monoxide over Ceria-Supported Gold Catalysts by Using Operando Raman Spectroscopy. *ChemCatChem* **2016**, *8* (3), 523–526.
- (16) Guzman, J.; Carretin, S.; Corma, A. Spectroscopic Evidence for the Supply of Reactive Oxygen during CO Oxidation Catalyzed by Gold Supported on Nanocrystalline CeO₂. *J. Am. Chem. Soc.* **2005**, *127* (10), 3286–3287.
- (17) Ziemba, M.; Ganduglia-Pirovano, V.; Hess, C. Insight into the Mechanism of the Water-Gas Shift Reaction over Au/CeO₂ Catalysts Using Combined Operando Spectroscopies. *Faraday Discuss.* **2020**. DOI: 10.1039/C9FD00133F.
- (18) Kim, H. Y.; Henkelman, G. CO Oxidation at the Interface between Doped CeO₂ and Supported Au Nanoclusters. *J. Phys. Chem. Lett.* **2012**, *3* (16), 2194–2199.
- (19) Liu, Z.; Li, X.; Mayyas, M.; Koshy, P.; Hart, J. N.; Sorrell, C. C. Growth Mechanism of Ceria Nanorods by Precipitation at Room Temperature and Morphology-Dependent Photocatalytic Performance. *CrystEngComm* **2017**, *19* (32), 4766–4776.
- (20) Kullgren, J.; Hermansson, K.; Castleton, C. Many Competing Ceria (110) Oxygen Vacancy Structures: From Small to Large Supercells. *J. Chem. Phys.* **2012**, *137* (4), 044705.
- (21) Wu, Z.; Overbury, S. H. *Catalysis by Materials with Well-Defined Structures*; Elsevier, 2015.
- (22) Nolan, M.; Parker, S. C.; Watson, G. W. The Electronic Structure of Oxygen Vacancy Defects at the Low Index Surfaces of Ceria. *Surf. Sci.* **2005**, *595* (1–3), 223–232.
- (23) Mai, H.-X.; Sun, L.-D.; Zhang, Y.-W.; Si, R.; Feng, W.; Zhang, H.-P.; Liu, H.-C.; Yan, C.-H. Shape-Selective Synthesis and Oxygen Storage Behavior of Ceria Nanopolyhedra, Nanorods, and Nanocubes. *J. Phys. Chem. B* **2005**, *109* (51), 24380–24385.
- (24) Wu, Q.; Zhang, F.; Xiao, P.; Tao, H.; Wang, X.; Hu, Z.; Lü, Y. Great Influence of Anions for Controllable Synthesis of CeO₂ Nanostructures: From Nanorods to Nanocubes. *J. Phys. Chem. C* **2008**, *112* (44), 17076–17080.
- (25) Esch, F.; Fabris, S.; Zhou, L.; Montini, T.; Africh, C.; Fornasiero, P.; Comelli, G.; Rosei, R. Electron Localization Determines Defect Formation on Ceria Substrates. *Science (Washington, DC, U. S.)* **2005**, *309* (5735), 752–755.
- (26) Nolan, M. Healing of Oxygen Vacancies on Reduced Surfaces of Gold-Doped Ceria. *J. Chem. Phys.* **2009**, *130* (14), 144702.
- (27) Kullgren, J.; Hermansson, K.; Broqvist, P. Reactive Oxygen Species in Stoichiometric Ceria: Bulk and Low-Index Surfaces. *Phys. Status Solidi RRL* **2014**, *8* (6), 600–604.
- (28) Nolan, M.; Fearon, J.; Watson, G. Oxygen Vacancy Formation and Migration in Ceria. *Solid State Ionics* **2006**, *177* (35–36), 3069–3074.
- (29) Sun, L.; Huang, X.; Wang, L.; Janotti, A. Disentangling the Role of Small Polarons and Oxygen Vacancies in CeO₂. *Phys. Rev. B: Condens. Matter Mater. Phys.* **2017**, *95* (24), 245101.
- (30) Chen, H.-T.; Chang, J.-G. Oxygen Vacancy Formation and Migration in Ce_{1-x}Zr_xO₂ Catalyst: A DFT+U Calculation. *J. Chem. Phys.* **2010**, *132* (21), 214702.
- (31) Zhang, D.; Han, Z.-K.; Murgida, G. E.; Ganduglia-Pirovano, M. V.; Gao, Y. Oxygen-Vacancy Dynamics and Entanglement with Polaron Hopping at the Reduced CeO₂(111) Surface. *Phys. Rev. Lett.* **2019**, *122* (9), 096101.
- (32) Lee, Y.; He, G.; Akey, A. J.; Si, R.; Flytzani-Stephanopoulos, M.; Herman, I. P. Raman Analysis of Mode Softening in Nanoparticle CeO_{2-δ} and Au-CeO_{2-δ} during CO Oxidation. *J. Am. Chem. Soc.* **2011**, *133* (33), 12952–12955.
- (33) Guo, M.; Lu, J.; Wu, Y.; Wang, Y.; Luo, M. UV and Visible Raman Studies of Oxygen Vacancies in Rare-Earth-Doped Ceria. *Langmuir* **2011**, *27* (7), 3872–3877.
- (34) Popović, Z. V.; Dohčević-Mitrović, Z.; Konstantinović, M. J.; Šćepanović, M. Raman Scattering Characterization of Nanopowders and Nanowires (Rods). *J. Raman Spectrosc.* **2007**, *38* (6), 750–755.



Identification of single-atom active sites in CO oxidation over oxide-supported Au catalysts

Christian Schilling^{a,1}, Marc Ziemba^{a,1}, Christian Hess^{a,*}, M. Verónica Ganduglia-Pirovano^{b,*}

^a Eduard-Zintl-Institut für Anorganische und Physikalische Chemie, Technische Universität Darmstadt, Alarich-Weiss-Str. 8, 64287 Darmstadt, Germany

^b Instituto de Catálisis y Petroleoquímica-Consejo Superior de Investigaciones Científicas, Marie Curie 2, 28049 Madrid, Spain



ARTICLE INFO

Article history:

Received 16 December 2019

Revised 18 January 2020

Accepted 20 January 2020

Keywords:

Single site catalysis

Gold

CO oxidation

Operando infrared spectroscopy

Density functional theory

ABSTRACT

Here we present a combined *operando* infrared spectroscopic and theoretical analysis of ceria-supported gold catalysts during room temperature CO oxidation that identifies an active site for the reaction as a single gold site on the ceria support forming an $O_{\text{lattice}}\text{-Au}^+\text{-CO}$ species. As monitored by *operando* infrared spectroscopy, the isolated Au^+ gold site is either present as a result of the catalyst synthesis or formed under reaction conditions after CO adsorption at the perimeter of the Au–ceria interface. Our results provide new insights into the chemical nature of the active gold site and the reaction mechanism by detecting the formation of active and inhibiting species simultaneously.

© 2020 Elsevier Inc. All rights reserved.

1. Introduction

Strongly interacting gold with an oxide support has aroused a great deal of attention as a catalyst since its discovery [1,2], owing to its high reactivity for a number of important reactions [3], such as CO oxidation [4], water–gas shift [5], acetylene hydrochlorination [6], and preferential oxidation of CO [7]. The use of reducible oxides, such as ceria (CeO_2), as a support for Au catalysts, has been found to lead to highly active catalytic systems for numerous reactions, e.g., CO oxidation [4] and water–gas shift [5]. However, despite extensive research on ceria-supported gold catalysts (Au/ CeO_2) in the past [8–15], even for a seemingly simple reaction such as CO oxidation, the nature of the active catalytic site as well as other important details of the reaction mechanism, such as the role of water/hydroxide, are still under debate [16–24].

Previous work on CO oxidation over ceria-supported Au nanoparticles has shown that the Au–oxide interfacial perimeter plays a major role [25] and that the oxygen activation proceeds at the ceria support [12] via peroxide formation at ceria defect sites [13–15]. On the other hand, there is controversy in the literature regarding whether the active gold sites are gold clusters or interfacial gold atoms, or isolated cationic gold ions, or a mixture of

different sites [16]. More recently, based on *in situ* X-ray absorption fine structure analysis, the metallic gold component in the ceria-supported Au clusters has been proposed to play a crucial role in the catalysis [18], in contrast to recent theoretical work reporting the formation of cationic gold ions [17] or dimeric gold species [26] as catalytically active sites, however, without providing experimental evidence for the existence of such species in either report. Previous calculations on Au_1 [27], Au_3 [28], Au_{13} [29], and Au_{20} [25] have predicted that oxidized gold species – in direct contact with the ceria support – are the preferred sites for CO adsorption. CO bound to oxidized gold species has also been reported for other oxides such as ZnO and TiO_2 [30,31]. Not long ago, the structural changes of Au(1 1 1) and Au ceria-supported small (~2 nm) gold clusters have been demonstrated by employing *in situ* STM [32] and environmental transmission electron microscopy [33] in the presence of CO at reduced pressures ($\sim 10^{-4}$ mbar).

In this contribution, we report on the identification and characterization of an active site in ceria-supported gold catalysts in CO oxidation. We show that infrared spectroscopy enables the monitoring of the active sites and inhibiting species as well as their formation behavior. Assignment of vibrational frequencies based on DFT calculations allows detailed insight into the active site of supported gold catalysts. In particular, our results provide clear evidence that isolated cationic Au^+ in close interaction with the support are creating active $O_{\text{lattice}}\text{-Au}^+\text{-CO}$ species during CO oxidation over ceria supported gold catalysts.

* Corresponding authors.

E-mail addresses: christian.hess@tu-darmstadt.de (C. Hess), vgp@icp.csic.es (M.V. Ganduglia-Pirovano).

¹ Both authors contributed equally.

2. Methods

2.1. Catalyst preparation

Ceria nanoparticles were prepared by decomposition of Ce (NO₃)₃·6 H₂O (99.5%, Alfa Aesar) at 600 °C for two periods of 12 h and were thoroughly characterized as described elsewhere [15,34]. Please note that the ceria nanoparticles possess a termination in the (1 1 1) direction as well as stepped sites, as is evident from transmission electron microscopy data and *in situ* Raman spectra. Therefore, the experimental results are directly comparable to the DFT calculations employing (1 1 1)-oriented ceria slabs. Au/CeO₂ samples with 0.5 wt% Au loading were synthesized via deposition precipitation from HAuCl₄·3 H₂O (>99.99%, Sigma Aldrich). An *ex situ* characterization of the gold content and the oxidation state has already been carried out in earlier work by XP spectroscopy and is described there in more detail [15,34]. TEM studies have revealed the presence of a small number of larger gold particles (~10 nm) [15]. However, as discussed previously, the catalytic activity of the Au/ceria catalyst is attributed to highly dispersed gold rather than the particles we observe in TEM [15].

2.2. Operando IR spectroscopy

We used diffuse reflectance infrared Fourier transform spectroscopy (DRIFTS) in a Vertex 70 (Bruker) to examine a 0.5 wt% Au/CeO₂ catalyst exposed to reaction conditions. Gas phase infrared analysis was employed to quantitatively monitor the conversion over the catalyst and can be directly correlated with the spectroscopic information gained from infrared spectroscopy at the catalyst (*operando* approach). For further details, refer to the Supporting Information and Ref. [42].

2.3. Density functional theory (DFT)

Density functional theory calculations were performed employing the VASP package (version 5.3.5 <https://www.vasp.at>) with the PBE functional adding an effective onsite Coulomb interaction parameter $U_{\text{eff}} = 4.5$ eV for the Ce 4f states (PBE + U/4.5 eV) and a hybrid DFT functional (HSE06). Vibrational analyses were performed by calculating the Hessian either analytically or with a finite differences approach. For further details, refer to the Supporting Information and Ref. [35].

3. Results and discussion

3.1. Catalytic activity

The Au/CeO₂ catalyst contains a gold loading of 0.5 wt% prepared by deposition precipitation onto polycrystalline CeO₂ exhibiting a (1 1 1) termination (see Supporting Information for details of the synthesis and characterization). Fig. 1 depicts the temporal evolution of the conversion over the 0.5 wt% Au/CeO₂ catalyst during CO oxidation at 21 °C for two different catalyst pretreatments (A and B in Fig. 1A and B, respectively) prior to exposure to reaction conditions. Pretreatment A consists of equilibration in 25% O₂/Ar flow for 1 h, whereas pretreatment B involves an outgassing step at 200 °C (25% O₂/Ar flow, 1 h), leading to the removal of adsorbed water. After equilibration, the as-prepared catalyst starts to show activity after 5 min in reaction conditions, reaching maximum conversion after 20 min, and then slowly declines to the steady-state conversion (~3%). In contrast, after outgassing at 200 °C, the catalyst activates only slowly (2 h) without reaching steady-state conversion. This activation process continues after a regeneration phase in 25% O₂/Ar for 1 h (Fig. 1). The

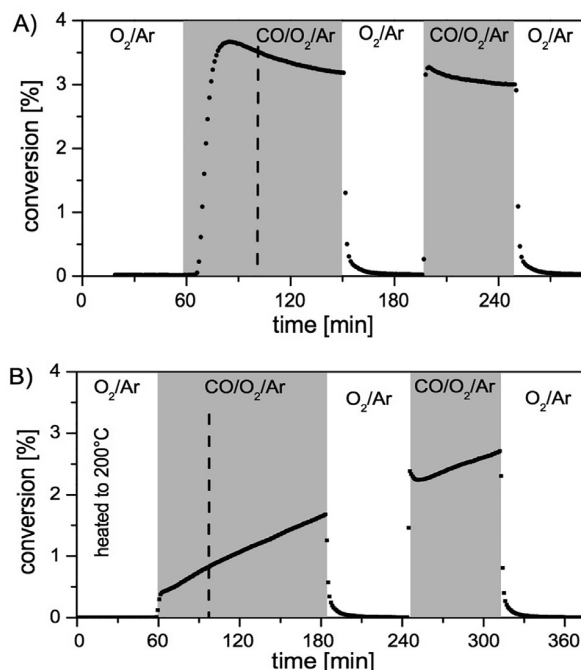


Fig. 1. Conversion (CO oxidation) over a 0.5 wt% Au/CeO₂ catalyst during two exposures to reaction conditions (2% CO, 10% O₂, Ar) at 21 °C after (A) 25% O₂/Ar flow for 1 h and (B) 25% O₂/Ar flow at 200 °C for 1 h. The dashed line indicates the time of the infrared spectroscopy measurement during reaction depicted in Figs. 2 and 4 as well as in Figs. S1 and S2.

steady-state conversion of ~3% after equilibration is not reached even after exposure to reaction conditions for 3 h. Such a prolonged activation period has been observed previously for room temperature CO oxidation in dry reaction gas streams and has been assigned to the positive influence of water on the activation behavior of Au/CeO₂ catalysts [36].

3.2. Catalyst behavior under reaction conditions

To explore the behavior of the catalyst under reaction conditions, we performed *operando* infrared spectroscopy during the course of the reactivity experiment in Fig. 1 by recording spectra every minute. Exemplary *operando* infrared spectra during reaction (dashed lines in Fig. 1) are depicted in Fig. 2 (red spectra) showing an excerpt of the CO stretching mode region. The rotational–vibrational fine structure of CO can be resolved in the infrared spectra (1 cm⁻¹ resolution), and thus gas-phase CO molecules, possessing a rotational–vibrational fine structure, are distinguished from vibrations of adsorbed CO, which do not possess a fine structure. On the bare ceria support (blue spectra) no adsorbed CO species are observed under reaction conditions, which were detected in the region 2154–2177 cm⁻¹ in prior CO adsorption experiments by stabilization at lower temperatures and reduced pressures [37–40]. After subtraction of the gas-phase spectrum from the spectrum of the Au/CeO₂ catalyst, the residual signal can be de-convoluted into three distinct spectral regions at (i) 2125–2130 cm⁻¹ (present for all active samples), (ii) 2160–2170 cm⁻¹ (present for all samples, but with a very different intensity), and at (iii) 2090 cm⁻¹ (low intensity, only present for the outgassed sample).

3.3. Identification of active sites

For a detailed assignment of the experimentally observed CO stretch frequencies, the CO chemisorption and vibrational proper-

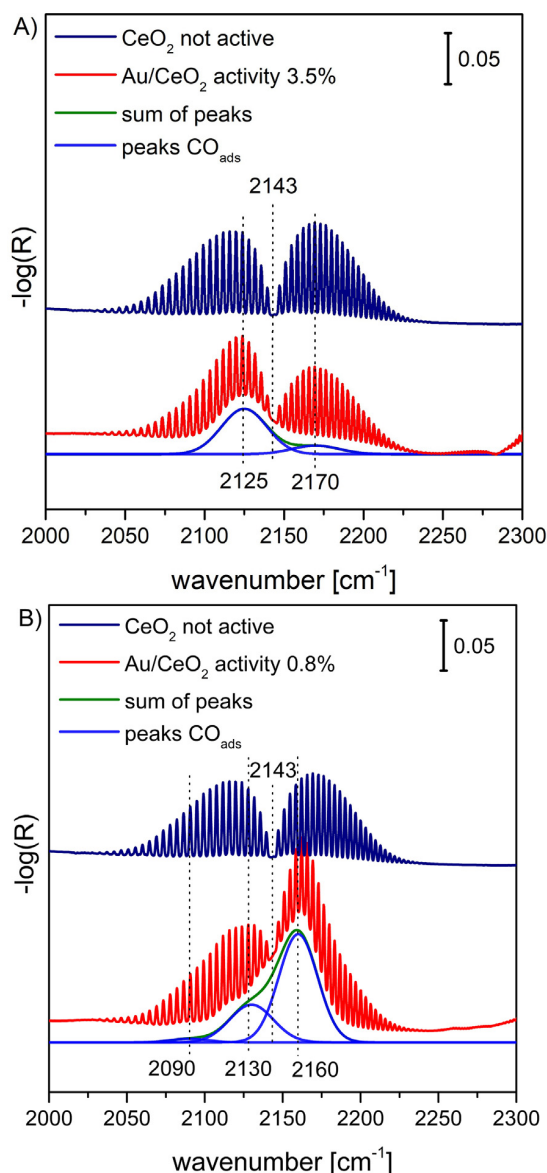


Fig. 2. CO stretch frequency region of the *operando* infrared spectra under reaction conditions (red) after (A) equilibration in 25% O₂/Ar flow and (B) outgassing in 25% O₂/Ar at 200 °C for 1 h. Subtraction of the infrared spectrum of gas-phase CO over a bare CeO₂ sample (no adsorbed CO, dark blue) yields the residual spectrum (green), which can be deconvoluted into three components at 2160–2170 cm⁻¹, 2125–2130 cm⁻¹, and 2090 cm⁻¹.

ties on model Au–CeO₂ catalysts consisting of single Au₁ and Au₄ gold clusters adsorbed on CeO₂(1 1 1) surface were calculated employing DFT (Fig. 3) with either PBE + U/4.5 eV or hybrid HSE06 exchange–correlation functionals. The PBE + U/4.5 eV functional revealed comparable results independently of whether van der Waals (vdW) contributions were considered, and thus vdW contributions were not included in combination with HSE06 (see Supporting Information). All computational frameworks predict that the most stable Au₁ site is an O–O bridge (Au@O–O bridge), in which the Au 6s electron is transferred to the ceria support (Au⁺), accompanied by the formation of a Ce³⁺ ion in a next nearest neighbor (NNN) cationic position to the Au atom (Fig. 3D), in agreement with previous results [41–45,27,28].

With respect to ceria-supported Au₄ clusters, a pyramidal-shaped cluster has been predicted to be the most stable configura-

tion for adsorption on either the stoichiometric CeO₂(1 1 1) [28,46] or the reduced CeO_{2-x}(1 1 1) surfaces [47]. In the case of the CeO₂(1 1 1) surface, two Ce³⁺ ions – resulting from the Au–ceria interaction – are located in nearest neighbor (NN) cationic positions to the Au₄ cluster (Fig. 3M); hence, we have adopted such a Ce³⁺ configuration for the Au₄/CeO₂(1 1 1) [48,28] system with a pyramidal-shaped Au₄ cluster in which the bottom three Au atoms – in direct contact with the ceria support – are charged positively (Au^{+0.67}), whereas the gold atom at the top is practically not charged (Au⁰), see Table S3 [28]. Thus, there is a rapid weakening of the Au–ceria interactions as clusters become three-dimensional, in line with previous findings for other metals such as Ni [48,49]. In this context, other Au₄/CeO₂(1 1 1) structures were also considered in which, for example, there are two Ce³⁺ ions in next-nearest cationic positions (NNN) to the Au₄ cluster; however, all of these structures were found to be higher in energy and were not considered further.

For Au₁/CeO₂(1 1 1), upon CO adsorption on the gold atom, the formation of O_{lattice}–Au⁺–CO species is observed (Table 1 and Table S3), regardless of the starting structure, the charge state of gold, or the employed computational framework (see Supporting Information). The CO molecule is adsorbed on top of the Au⁺ ion at O–O bridge sites in an almost upright position forming a linear O_{lattice}–Au⁺–CO species (only slightly tilted for the Ce³⁺ localization in a NN position), with an adsorption energy of $E_{\text{ads,CO}} = -2.43$ and -2.30 eV (HSE06) for the Au@O–O bridge structure with the Ce³⁺ in NNN and NN positions, respectively (Fig. 3I and J, and Table S3).

For CO adsorption on the Au₄/CeO₂(1 1 1) cluster, three different adsorption sites are possible:

- (i) On top of the gold atom at the apex of the pyramid (Au_{top}) with an adsorption energy of $E_{\text{ads,CO}} = -0.77$ eV (HSE06) and a linear upright adsorption geometry (Table 1 and Fig. 3N).
- (ii) On the gold atom in the base that has two Ce³⁺ in NN positions (Au_{bottom,1}) with an adsorption energy of $E_{\text{ads,CO}} = -1.26$ eV (HSE06). Interestingly, the Au_{bottom,1} atom, onto which CO is adsorbed, is abstracted from the Au₄ cluster, forming a *pseudo single Au site*, i.e., an O_{lattice}–Au⁺–CO species slightly separated from the remaining Au₃ particle, that stays perpendicular to the surface (Table 1 and Fig. 3O). The gold atom abstracted from the Au₄ cluster to form a O_{lattice}–Au⁺–CO species (Fig. 3I) has practically the same positive charge than *true* isolated species (Table S3). The abstraction of Au atoms from ceria-supported Au clusters upon CO adsorption at the Au–ceria interface has previously been reported [17,28].
- (iii) On one of the gold atoms located between nearest neighboring Ce³⁺ and Ce⁴⁺ cations (Au_{bottom,2}) with an adsorption energy of $E_{\text{ads,CO}} = -1.29$ eV (HSE06). Au_{bottom,2} sites are also abstracted from the cluster upon CO adsorption (Table 1 and Fig. 3P) and *pseudo single Au sites* are formed (Table S3). The corresponding $E_{\text{ads,CO}}$ values calculated with the PBE functional for the three distinct sites in the Au₄ cluster (Table S1) compare well with those in the literature for either a Au₄ [28], a Au₁₃ [29] (the Au–CO species is not abstracted from the gold particle) or a Au₂₀ [17] cluster supported on the CeO₂(1 1 1) surface.

In addition, the adsorption of CO on the clean CeO₂(1 1 1) surface was also modeled (Fig. 3A): CO adsorbs linearly on the clean CeO₂(1 1 1) surface on top of a Ce⁴⁺ ion with an adsorption energy of $E_{\text{ads,CO}} = -0.15$ eV (HSE06), in agreement with previous studies [39,40].

For a thorough analysis of the calculated C–O stretch vibrational frequency of CO adsorbed on the Au/CeO₂ model systems, the

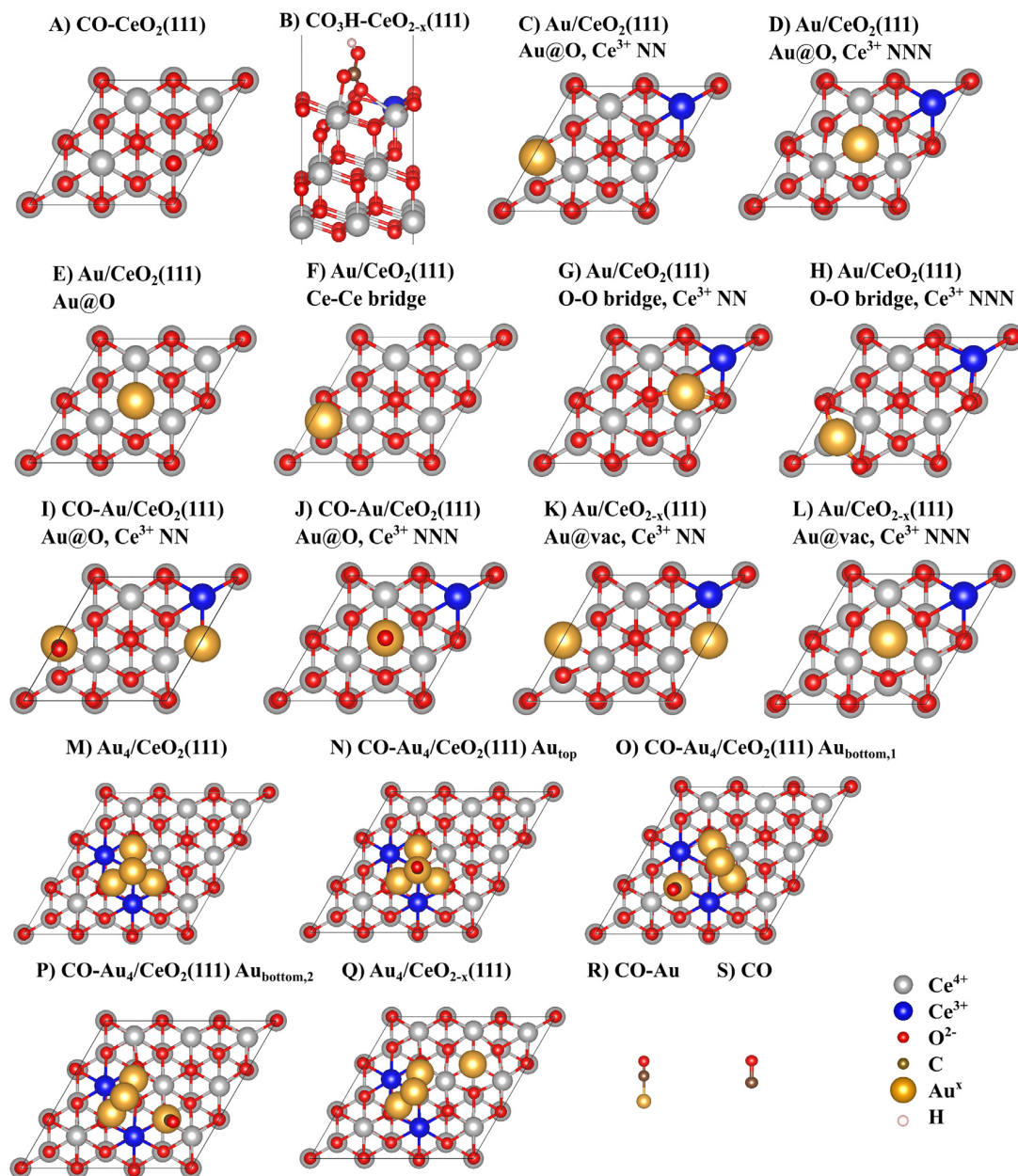


Fig. 3. Structural model of (A) CO adsorbed to CeO₂(1 1 1), (B) adsorbed hydrogen carbonate on CeO_{2-x}(1 1 1) with Ce³⁺ in NNN position, Au adsorbed on-top of O (Au⁺@O) with Ce³⁺ in (C) NN and (D) NNN position, (E) Au⁰@O, (F) Au⁺ adsorbed in Ce-Ce bridge position, Au⁺ in O-O bridge with Ce³⁺ in (G) NN, and (H) NNN position. CO adsorbed on Au₁/CeO₂(1 1 1) structures, i.e., CO-Au@O with Ce³⁺ in (I) NN and (J) NNN position. Au⁻ adsorbed on the CeO_{2-x}(1 1 1) surface with Ce³⁺ in (K) NN and (L) NNN position. (M) Stable Au₄/CeO₂(1 1 1) structure, CO adsorbed on (N) Au_{top}, (O) Au_{bottom,1}, and (P) Au_{bottom,2} positions in Au₄/CeO₂(1 1 1). (Q) Au₄²⁺/Au⁻ adsorbed on CeO_{2-x}(1 1 1). (R) Au-CO, (S) CO in the gas phase.

stretch frequency of the isolated CO molecule ($\nu_{\text{CO,gas}}$) has also been calculated in order to determine the corresponding CO frequency shifts ($\Delta\nu_{\text{CO,gas}}$) upon adsorption (Table 1 and Supporting Information); the calculated gas-phase CO stretch frequency is 2236 cm⁻¹ (HSE06) and the experimentally determined value is 2143 cm⁻¹ (Fig. 2). Hence, the stretch frequency of CO adsorbed on the CeO₂(1 1 1) surface (2251 cm⁻¹, HSE06) corresponds to a blueshift of $\Delta\nu_{\text{CO,gas}} = +15$ cm⁻¹ with respect to isolated gas-phase CO. This value is in good agreement with the corresponding shift ($\Delta\nu_{\text{CO,gas}} = +17$ – $+27$ cm⁻¹) of the experimental band observed at 2160–2170 cm⁻¹ (Fig. 2) and thus this band is attributed to CO

adsorbed on the ceria support [CO/CeO₂(1 1 1)], in agreement with previous experimental results [37–40]. In Table 1 the structures are sorted with respect to the value of the calculated CO stretch frequency, starting with the highest frequency value that was obtained for the CO/CeO₂(1 1 1) system. All structures in which CO is adsorbed on gold exhibit a redshifted frequency with respect to the frequency of gas-phase CO ($\Delta\nu_{\text{CO,gas}} < 0$). For the Au₁/CeO₂(1 1 1) structure, which has an isolated Au₁ atom adsorbed on the CeO₂(1 1 1) surface [CO-Au₁/CeO₂(1 1 1)], stretch frequencies of 2219 cm⁻¹ and 2217 cm⁻¹ (HSE06) are predicted for the structures with Ce³⁺ in NN and NNN sites to Au, respectively. These

Table 1

Summary of the calculated and experimental CO stretch frequency (ν_{CO}) and the difference of the CO stretch frequency with respect to the gas phase ($\Delta \nu_{\text{CO,gas}}$) employing the PBE + U/4.5 eV and HSE06 functionals. CO adsorption on $\text{CeO}_2(111)$, $\text{Au}_1/\text{CeO}_2(111)$, and $\text{Au}_4/\text{CeO}_2(111)$ is considered. For $\text{Au}_1/\text{CeO}_2(111)$ two Ce^{3+} configurations, and for $\text{Au}_4/\text{CeO}_2(111)$ three non-equivalent CO adsorption sites (top, bottom₁, and bottom₂), are considered.

Structure x Ce^{3+} config. CO ads. site	$\text{CO}/\text{CeO}_2(111)$ x Ce_{top}	$\text{CO}(\text{gas})$	$\text{CO-Au}_1/\text{CeO}_2(111)$ $1 \times \text{Ce}^{3+} \text{ NN}^a$ Au_{top}	$\text{CO-Au}_1/\text{CeO}_2(111)$ $1 \times \text{Ce}^{3+} \text{ NNN}^a$ Au_{top}	$\text{CO-Au}_4/\text{CeO}_2(111)$ $2 \times \text{Ce}^{3+} \text{ NN}^a$ $\text{Au}_{\text{bottom},1}$	$\text{CO-Au}_4/\text{CeO}_2(111)$ $1 \times \text{Ce}^{3+} \text{ NN}^a$ $\text{Au}_{\text{bottom},2}$	$\text{CO-Au}_4/\text{CeO}_2(111)$ Au_{top}
Structure							
PBE + U/4.5 eV							
$E_{\text{ads,CO}}$ [eV]	-0.19		-2.41	-2.51	-1.37	-1.40	-0.92
ν_{CO} [cm^{-1}]	2126	2122	2095	2092	2086	2086	2070
$\Delta \nu_{\text{CO,gas}}$ [cm^{-1}]	+4.3	0	-27.3	-30.4	-35.6	-35.4	-52.4
HSE06							
$E_{\text{ads,CO}}$ [eV]	-0.15		-2.30	-2.43	-1.26	-1.29	-0.77
ν_{CO} [cm^{-1}]	2251	2236	2219	2217	2215	2214	2199
$\Delta \nu_{\text{CO,gas}}$ [cm^{-1}]	+15.0	0	-16.3	-18.5	-21.0	-21.8	-36.3
Experimental							
ν_{CO} [cm^{-1}]	2160–2170	2143	2130	2130	2125	2125	2090
$\Delta \nu_{\text{CO,gas}}$ [cm^{-1}]	+17 – +27	0	-13	-13	-18	-18	-53

^a Number of neighboring Ce^{3+} ions to the $\text{O}_{\text{lattice}}-\text{Au}^+-\text{CO}$ species.

values correspond to a redshift of $\Delta \nu_{\text{CO,gas}} = -17 \text{ cm}^{-1}$ and -19 cm^{-1} , respectively.

As mentioned above, upon CO adsorption onto either the $\text{Au}_{\text{bottom},1}$ (two NN Ce^{3+}) or $\text{Au}_{\text{bottom},2}$ (one NN Ce^{3+}) atoms at the base of the pyramidal Au_4 nanoparticle, pseudo-single $\text{O}_{\text{lattice}}-\text{Au}^+-\text{CO}$ species are formed. The corresponding calculated CO stretch frequencies are 2215 cm^{-1} and 2214 cm^{-1} (HSE06) for the $\text{Au}_{\text{bottom},1}$ and $\text{Au}_{\text{bottom},2}$ sites, respectively, which are slightly redshifted ($2\text{--}5 \text{ cm}^{-1}$) compared to that of a (true) isolated Au site [$\text{CO-Au}_1/\text{CeO}_2(111)$]. In contrast, adsorption on top of the Au atom at the apex of the Au_4 cluster (Au_{top}) revealed a stretch frequency of 2199 cm^{-1} (HSE06), i.e., $\Delta \nu_{\text{CO,gas}} = -37 \text{ cm}^{-1}$. Summarizing, based on the DFT calculations, the observed CO stretch frequency at $2125\text{--}2130 \text{ cm}^{-1}$ (Fig. 2) is attributed to CO adsorbed onto gold species in direct contact with the CeO_2 support, i.e., a $\text{O}_{\text{lattice}}-\text{Au}^+-\text{CO}$ species. Note that, based on ^{13}CO experiments, the presence of a Ce^{3+} related electronic transition can be ruled out (see Supporting Information, Fig. S1) [50]. The CO-related feature at $2160\text{--}2170 \text{ cm}^{-1}$ is attributed to CO adsorbed on the ceria support, and that at 2090 cm^{-1} to CO adsorbed on-top of a gold atom of 3D Au clusters which are not in direct contact with the support.

3.4. Insight into the reaction mechanism

In general, the *operando* infrared spectra of the Au/CeO_2 catalyst for CO oxidation can be divided into the carbonate region ($800\text{--}1800 \text{ cm}^{-1}$), the carbonyl region ($2000\text{--}2300 \text{ cm}^{-1}$) discussed in detail above, and the O–H stretching region ($>3000 \text{ cm}^{-1}$). In the carbonate region, CO_3 carbonates (mainly bidentate: 988, 1298, and 1575 cm^{-1}), COOH hydrogen carbonates (1023, 1218, 1393, 1620, and 3619 cm^{-1}), and HCOO formates [37,38,51–53] are identified on the catalyst sample, with a strong increase of hydrogen carbonate under reaction conditions after outgassing at $200 \text{ }^\circ\text{C}$ (Fig. 4 and Supporting Information). Bidentate carbonates, largely removed by the outgassing treatment, accumulate on the surface with increasing activity of the catalyst, in agreement with the literature [53]. The assignment of these bands is based on a comparison of theory and experiment from previous studies [52] and on isotope exchange experiments using ^{13}CO (Fig. S2) and the corresponding DFT calculations (see Table S1), as described in detail in the Supporting Information.

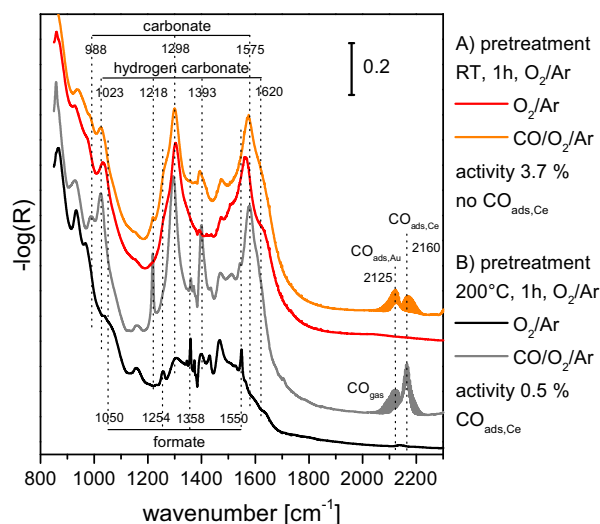


Fig. 4. *Operando* diffuse reflectance infrared spectra (carbonate, CO region) of a 0.5 wt% Au/CeO_2 catalyst in 25% O_2 at $21 \text{ }^\circ\text{C}$ recorded directly after equilibration in 25% O_2 (pretreatment A, red), after ~ 30 min in reaction conditions (2% CO , 10% O_2 , activity 3.7%, no $\text{CO}_{\text{ads,Ce}}$) (orange), directly after 1 h at $200 \text{ }^\circ\text{C}$ in 25% O_2 (pretreatment B, black), and after ~ 30 min in reaction conditions (activity 0.5%, $\text{CO}_{\text{ads,Ce}}$) (grey). Please note that spectra are offset for clarity.

Moreover, the infrared spectra of the as-prepared (broad band between 3000 and 3500 cm^{-1} as well as a band at 3694 cm^{-1}) and outgassed catalysts show the presence of adsorbed water; the amount of water is significantly decreased in the case of the outgassed sample (Figs. S2 and S3). This behavior indicates that catalyst pretreatment leading to water removal influences the catalyst behavior, as well be discussed below.

To determine potential active gold sites, the temporal behavior of the spectroscopically observed species with respect to the catalyst conversion was studied based on conversion–intensity plots (Fig. 5). Fig. 5A shows a positive correlation of the band intensity at $2125\text{--}2130 \text{ cm}^{-1}$ with the conversion values for both treatments at the initial stage of the reaction, providing direct experimental evidence for CO adsorption at the active site; as the concentration of the active CO species increases, so does the conversion. Actually,

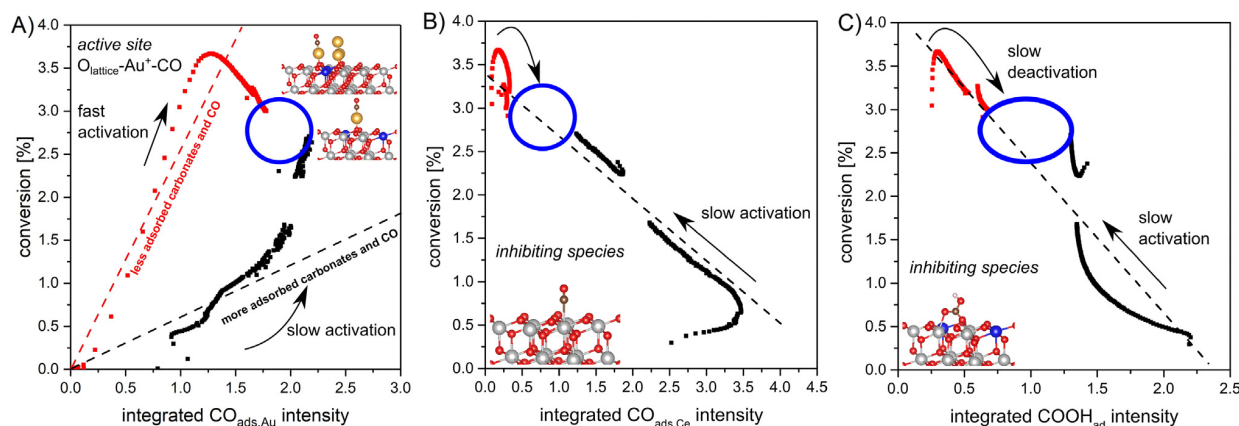


Fig. 5. (A) The intensity of CO adsorbed on Au/CeO₂(1 1 1) (2125–2130 cm⁻¹) is initially correlated with the conversion of the Au/CeO₂ catalyst for pretreatment A (equilibration in 25% O₂, red) and pretreatment B (1 h at 200 °C in 25% O₂, black). The dashed lines are a rough interpolation indicating an initial relation between the adsorbed species and the conversion (active site). The black line refers to a high and the red line to a lower concentration of adsorbed CO and carbonate species. The intensity of the band assigned to (B) adsorbed CO on the CeO₂(1 1 1) surface (2160–2170 cm⁻¹) and to (C) hydrogen carbonate adsorbed on CeO₂(1 1 1) (1218 cm⁻¹) is correlated to the conversion of the Au/CeO₂ catalyst. The dashed lines in (B) and (C) show the indirect relation between the adsorbed species and the conversion (inhibiting species). The blue circle is the steady state (operation window) that is approached from two sides for the two pretreatment procedures.

as stated above, based on our DFT results, the observed CO stretching frequency at 2125–2130 cm⁻¹ is assigned to CO adsorbed at an isolated gold ion in direct contact with the CeO₂(1 1 1) surface, thus forming O_{lattice}-Au⁺-CO species. The calculated frequencies for CO at pseudo-single sites, i.e., gold ions slightly abstracted from a gold cluster [17,28] are predicted to be separated by < 6 cm⁻¹ from the frequency of a true single site and thus are experimentally not distinguishable: both true and pseudo Au₁ sites are possible active sites. Thus, by combining *operando* infrared spectroscopy with DFT calculations, the gold active sites for CO oxidation over ceria-supported gold catalysts can be directly observed and identified as isolated Au⁺ for the first time. As shown in Fig. 5A, at a later stage, the conversion and band intensity at 2125–2130 cm⁻¹ are not correlated anymore. Thus, when approaching the steady state other aspects of the reaction start to gain importance, which will be the focus of future studies.

We note that the rate-determining step in the CO oxidation reaction over non-hydroxylated ceria-supported gold nanoparticles has been predicted to be the formation of COO_{latt} species, i.e., the abstraction of a lattice oxygen by CO [17,27,28] the activation energy for such a Mars-van-Krevelen mechanism is generally expected to be quite large. However, DFT + U calculations predict values such as 0.86 eV for reaction over Au₁ single atoms [27], 0.77 eV over an abstracted atom from a Au₂₀ cluster [17], and 0.68 eV over a very flexible Au₃ cluster [28]. These values of the activation energy, which are lower than expected, are in agreement with the fact that the CO oxidation reaction is facilitated over ceria-supported gold nanoparticles, as observed previously by experiment [18], although our results now reveal that the cationic gold active site is formed under reaction conditions at (or separated from) the Au-ceria interface. Thus by directly probing O_{lattice}-Au⁺-CO species prior to the rate-determining step, we can resolve apparent differences in the literature regarding the nature of the active gold site.

As shown in Fig. 5A, for both pretreatment procedures, initially a direct relationship is observed, but with different proportionality factors (indicated by the black and red dashed lines). For pretreatment A (red, as-prepared) there is initially a fast activation and later a slow deactivation. In contrast, outgassing pretreatment B (black) results in an activation, that is slow, but finally approaches the same level of conversion (~3%) as for pretreatment A. Interestingly, for both pretreatments deviations from the linearity are

observed at a similar CO intensity (~1.25) indicating changes in the reaction mechanism at higher CO coverages. Please note that the infrared intensities finally approach each other, indicating the same 'final' concentrations for both experiments (see blue circle for the operation window). Thus, our results strongly suggest, that owing to catalyst structural changes in the presence of the reaction mixture, the catalyst properties approach a common (steady-state) behavior, independent of the initial state.

To elucidate further details of the reaction mechanism, the intensity of the band assigned to CO adsorbed on CeO₂(1 1 1) at 2160–2170 cm⁻¹ [37–40] (Fig. 5B) and also of the hydrogen carbonate species at 1218 cm⁻¹ (Fig. 5C) [50,37,38] were correlated with the catalysts' conversion. Interestingly, for both species, an inverse conversion vs. intensity relationship was found. This behavior strongly suggests that these species act as inhibitors for CO oxidation over Au/CeO₂ catalysts and thus, in their presence, a lowered turnover frequency per active species is expected. This interpretation is consistent with the observation, that under the reaction conditions described above bare ceria did not give any noticeable CO oxidation activity.

As a consequence of the reaction of CO with lattice oxygen, an oxygen vacancy is created. As has been previously proposed [16], the supply of oxygen occurs by adsorption of molecular oxygen on the oxygen vacancy resulting in the formation of a peroxide species. In the further course of the catalytic cycle the outer oxygen of the peroxide species undergoes reaction with CO, while the second oxygen fills the oxygen vacancy, closing the catalytic cycle [17], fully consistent with previous *operando* experiments showing the consumption of peroxide [14]. In this context, the inhibiting effect of the adsorption of CO on the bare support may be explained by the adsorption either on the clean CeO₂(1 1 1) surface, where further reaction, e.g. with residual OH, has been associated with a high barrier (1.05 eV, DFT + U) [54], or on oxygen vacancies on the ceria support, thereby blocking sites accessible to adsorption of molecular oxygen. However, compared to the low adsorption energy of CO at surface oxygen vacancies (-0.4 eV, 2157 cm⁻¹, DFT + U) [40], the adsorption of oxygen as peroxide species is more favorable (-1.9 to -2.0 eV, DFT + U) [55–57,34], and therefore oxygen can successfully displace CO (Fig. 5B). Note also that the calculated CO stretch frequencies for the clean and reduced surfaces [39] are both consistent with the range of observed frequencies (2160–2170 cm⁻¹) differing only

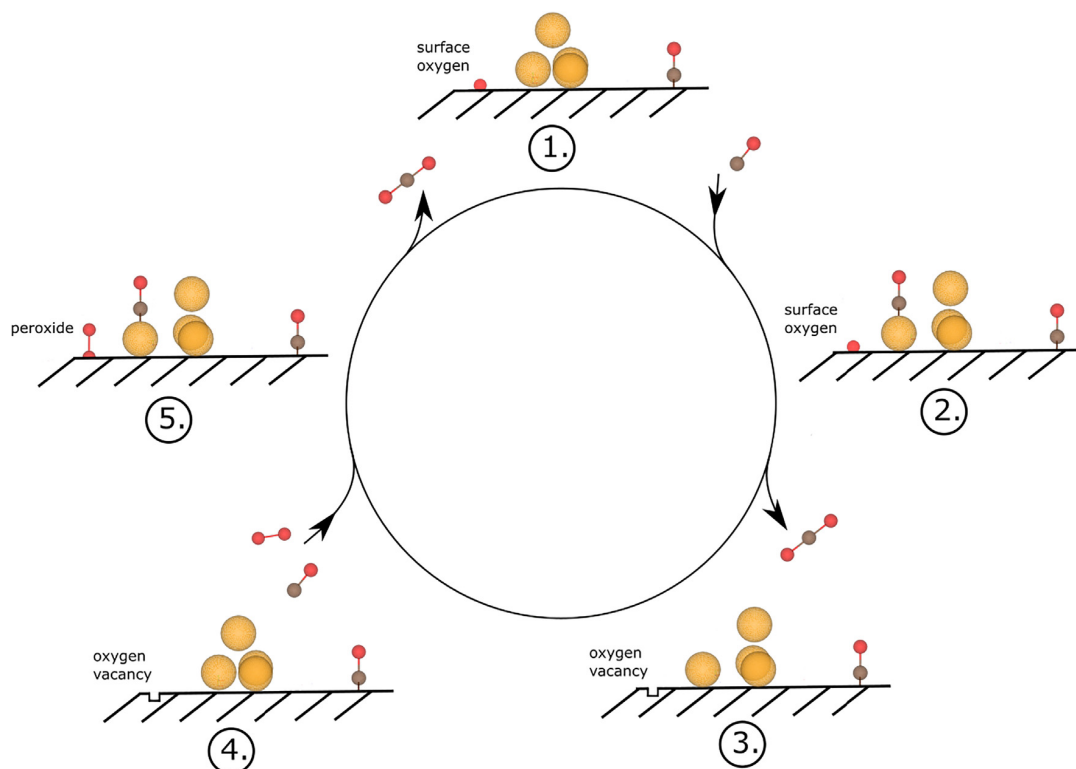


Fig. 6. Proposed mechanism for the room temperature CO oxidation over Au/CeO₂ catalysts. For clarity, only the reaction pathway mediated by pseudo-single sites is shown. For details see text.

by $\sim 12\text{ cm}^{-1}$, hence they are not expected to be distinguishable in our experiment. Previously, CO adsorbed on single-crystalline and defective CeO₂(1 1 1) has been detected at 2054 and 2063 cm^{-1} , respectively [40,58].

As shown in Fig. 5C, the situation is different for hydrogen carbonate species, which also show an inhibiting effect, but are bound much more strongly to the surface (-1.6 eV , see Table S1) and can therefore not be displaced by oxygen that easily. Note that the inhibition of the reaction by the adsorption of CO on the ceria support has not been reported in the literature [47,34,59]. Also, for both inhibiting species their respective concentrations approach a common operation window (indicated by the blue circles in Fig. 5), independent of the initial pretreatment. This behavior resembles the behavior observed for the active sites (Fig. 5A) and highlights the structural changes of the catalyst in the presence of the gas mixture. Fig. 6 summarizes the key features of the proposed mechanism for room temperature CO oxidation over Au/CeO₂ catalysts without participation of water and/or surface hydroxyl groups. For clarity, only the reaction pathway mediated by pseudo-single sites is shown. A crucial step in the catalytic cycle is the formation of CO₂ via O_{lattice}-Au⁺-CO species. As a result of the reaction, Au⁻ is formed as confirmed by Wang et al. for Au₂₀ [17]. As indicated in Fig. 6, the oxygen vacancy created by the oxidation of CO is refilled by gas phase oxygen, while the second oxygen undergoes reaction with CO (see discussion above).

Based on the activity results shown in Fig. 1, we conclude that the presence of water facilitates the oxidation of CO, e.g. by catalyzing the reaction between CO and hydroxyl groups via formation of a carboxyl intermediate followed by subsequent CO₂ and water formation, as proposed both experimentally and theoretically [38,59,60]. Changes in the hydroxyl region (Fig. S4) do not

show a direct relation to the activity of the catalyst and may result from changes in the coordination of surface water, in agreement with previous studies on CO oxidation over Au/TiO₂ catalysts [24]. In light of these studies, adsorbed water molecules, rather than support hydroxyl groups, may supply OH for carboxyl formation, followed by its deprotonation to yield CO₂.

4. Conclusion

In conclusion, cationic gold is evidenced to be an active site of the Au/CeO₂ catalyst for CO oxidation reactions by using vibrational spectroscopy in conjunction with DFT calculations, which provide a robust foundation for the spectroscopic assignment. The power of this approach is that we could “see” the active O_{lattice}-Au⁺-CO species. While the experimental frequencies are consistent with the calculated values for CO adsorbed on both single isolated Au⁺ sites and pseudo-single sites, i.e., a gold ion slightly abstracted from a gold cluster, exhibits a lower activation energy in the rate determining step, according to earlier theoretical work [25]. Depending on pretreatment, different reaction / activation regimes were observed providing new insight into the mode of operation of Au/CeO₂ catalysts during CO oxidation. Higher CO conversion is observed for the as-prepared catalyst, where the inhibiting species, namely, CO adsorbed on the ceria support and hydrogen carbonates, are rare, whereas high concentrations of these species result in a lower CO conversion, as in the case of the outgassed catalyst. Nevertheless, independent of the pretreatment history, the catalysts approach the same catalytic behavior, but after different times, as is apparent from the conversion-intensity plots, highlighting the structural changes of the catalyst in the presence of the reaction mixture.

Declaration of Competing Interest

The authors declare that they have no known competing financial interests or personal relationships that could have appeared to influence the work reported in this paper.

Acknowledgements

DFT calculations for this research were conducted using the Lichtenberg high performance computer of the TU Darmstadt. Computer time at the BSC in Barcelona is also acknowledged. We thank Jochen Rohrer and Karsten Albe for support with the VASP code. C.S. gratefully acknowledges the Merck'sche Gesellschaft für Kunst und Wissenschaft e.V. for providing a scholarship. C.H. acknowledges support by the Deutsche Forschungsgemeinschaft (DFG) and M.V.G.-P. acknowledges support by the MINECO-Spain (CTQ2015-71823-R) and the MICINN-Spain (RTI2018-101604-B-I00).

Appendix A. Supplementary material

Supplementary data to this article can be found online at <https://doi.org/10.1016/j.jcat.2020.01.022>.

References

- [1] M. Haruta, T. Kobayashi, H. Sano, N. Yamada, Novel gold catalysts for the oxidation of carbon monoxide at a temperature far below 0 °C, *Chem. Lett.* 16 (1987) 405–408.
- [2] G.J. Hutchings, Vapor phase hydrochlorination of acetylene: correlation of catalytic activity of supported metal chloride catalysts, *J. Catal.* 96 (1985) 292–295.
- [3] A.S.K. Hashmi, G.J. Hutchings, Gold catalysis, *Angew. Chem. Int. Ed.* 45 (2006) 7896–7936.
- [4] S. Carrettin, P. Concepción, A. Corma, J.M. López Nieto, V.F. Puntes, Nanocrystalline CeO₂ increases the activity of Au for CO oxidation by two orders of magnitude, *Angew. Chem. Int. Ed.* 43 (2004) 2538–2540.
- [5] Q. Fu, H. Saltsburg, M. Flytzani-Stephanopoulos, Active nonmetallic Au and Pt species on ceria-based water-gas shift catalysts, *Science* 301 (2003) 935–938.
- [6] G. Malta et al., Identification of single-site gold catalysis in acetylene hydrochlorination, *Science* 355 (2017) 1399–1403.
- [7] B. Qiao et al., Highly efficient catalysis of preferential oxidation of CO in H₂-rich stream by gold single-atom catalysts, *ACS Catal.* 5 (2015) 6249–6254.
- [8] M. Manzoli, F. Boccuzzi, A. Chiorino, F. Vindigni, W. Deng, M. Flytzani-Stephanopoulos, Spectroscopic features and reactivity of CO adsorbed on different Au/CeO₂ catalysts, *J. Catal.* 245 (2007) 308–315.
- [9] A. Chiorino et al., New insight on the nature of catalytically active gold sites: quantitative CO chemisorption data and analysis of FTIR spectra of adsorbed CO and of isotopic mixtures, *J. Catal.* 262 (2009) 169–176.
- [10] Y. Guan, D.A.J.M. Ligthart, O. Pirgon-Galin, J.A.Z. Pieterse, R.A. van Santen, E.J.M. Hensen, Gold stabilized by nanostructured ceria supports: nature of the active sites and catalytic performance, *Top. Catal.* 54 (2011) 424–438.
- [11] F. Vindigni, M. Manzoli, A. Chiorino, F. Boccuzzi, Catalytically active gold sites: nanoparticles, borderline sites, clusters, cations, anions? FTIR spectra analysis of ¹²CO and of ¹²CO-¹³CO isotopic mixtures, *Gold Bull.* 42 (2009) 106–112.
- [12] D. Widmann, R. Leppelt, R.J. Behm, Activation of a Au/CeO₂ catalyst for the CO oxidation reaction by surface oxygen removal/oxygen vacancy formation, *J. Catal.* 251 (2007) 437–442.
- [13] J. Guzman, S. Carrettin, A. Corma, Spectroscopic evidence for the supply of reactive oxygen during CO oxidation catalyzed by gold supported on nanocrystalline CeO₂, *J. Am. Chem. Soc.* 127 (2005) 3286–3287.
- [14] M. Lohrenscheid, C. Hess, Direct evidence for the participation of oxygen vacancies in the oxidation of carbon monoxide over ceria-supported gold catalysts by using operando Raman spectroscopy, *ChemCatChem* 8 (2016) 523–526.
- [15] C. Schilling, C. Hess, Real-time observation of the defect dynamics in working Au/CeO₂ catalysts by combined operando Raman/UV-Vis spectroscopy, *J. Phys. Chem. C* 122 (2018) 2909–2917.
- [16] M. Flytzani-Stephanopoulos, B.C. Gates, Atomically dispersed supported metal catalysts, *Annu. Rev. Chem. Biomol. Eng.* 3 (2012) 545–574.
- [17] Y.-G. Wang, D. Mei, V.-A. Glezakou, J. Li, R. Rousseau, Dynamic formation of single-atom catalytic active sites on ceria-supported gold nanoparticles, *Nat. Commun.* 6 (2015) 6511.
- [18] L.-W. Guo et al., Contributions of distinct gold species to catalytic reactivity for carbon monoxide oxidation, *Nat. Commun.* 7 (2016) 13481.
- [19] Y. He et al., Size-dependent dynamic structures of supported gold nanoparticles in CO oxidation reaction condition, *PNAS* 115 (2018) 7700–7705.
- [20] X.-L. Wang, X.-P. Fu, W.-W. Wang, C. Ma, R. Si, C.-J. Jia, Effect of structural evolution of gold species supported on ceria in catalyzing CO oxidation, *J. Phys. Chem. C* 123 (2019) 9001–9012.
- [21] J.-C. Liu, Y.-G. Wang, J. Li, Toward rational design of oxide-supported single-atom catalysts: atomic dispersion of gold on ceria, *J. Am. Chem. Soc.* 139 (2017) 6190–6199.
- [22] X. Zhou et al., Unraveling charge state of supported Au single-atoms during CO oxidation, *J. Am. Chem. Soc.* 140 (2018) 554–557.
- [23] F. Kettemann, S. Witte, A. Birnbaum, B. Paul, G. Clavel, P. Pinna, K. Rademann, R. Kraehnert, J. Polte, Unifying concepts in room-temperature CO oxidation with gold catalysts, *ACS Catal.* 7 (2017) 8247–8254.
- [24] J. Saavedra, H.A. Doan, C.J. Pursell, L.C. Grabow, B.D. Chandler, The critical role of water at the gold-titania interface in catalytic CO oxidation, *Science* 345 (2014) 1599–1602.
- [25] Z. Zhou, S. Kooi, M. Flytzani-Stephanopoulos, H. Saltsburg, The role of the interface in CO oxidation on Au/CeO₂ multilayer nanotowers, *Adv. Funct. Mater.* 18 (2008) 2801–2807.
- [26] Z.-K. Han, Y.-G. Wang, Y. Gao, Catalytic role of vacancy diffusion in ceria supported atomic gold catalyst, *Chem. Commun.* 53 (2017) 9125–9128.
- [27] M.F. Camellone, S. Fabris, Reaction mechanisms for the CO oxidation on Au/CeO₂ catalysts: activity of substitutional Au³⁺/Au⁺ cations and deactivation of supported Au⁺ adatoms, *J. Am. Chem. Soc.* 131 (2009) 10473–10483.
- [28] P. Ghosh, M.F. Camellone, S. Fabris, Fluxionality of Au clusters at ceria surfaces during CO oxidation: relationships among reactivity, size, cohesion, and surface defects from DFT simulations, *J. Phys. Chem. Lett.* 4 (2013) 2256–2263.
- [29] H.Y. Kim, H.M. Lee, G. Henkelman, CO oxidation mechanism on CeO₂-supported Au nanoparticles, *J. Am. Chem. Soc.* 134 (2012) 1560–1570.
- [30] H. Noei et al., Probing the mechanism of low-temperature CO oxidation on Au/ZnO catalysts by vibrational spectroscopy, *J. Phys. Chem. C* 116 (2012) 11181–11188.
- [31] M. Camellone et al., Molecular understanding of reactivity and selectivity for methanol oxidation at the Au/TiO₂ interface, *Angew. Chem. Int. Ed.* 52 (2013) 5780–5784.
- [32] J. Wang et al., Formation, migration, and reactivity of Au–CO complexes on gold surfaces, *J. Am. Chem. Soc.* 138 (2016) 1518–1526.
- [33] T. Uchiyama et al., Systematic morphology changes of gold nanoparticles supported on CeO₂ during CO oxidation, *Angew. Chem. Int. Ed.* 50 (2011) 10157–10160.
- [34] C. Schilling, C. Hess, CO oxidation on ceria supported gold catalysts studied by combined operando Raman/UV-Vis and IR spectroscopy, *Top. Catal.* 60 (2017) 131–140.
- [35] C. Schilling, A. Hofmann, C. Hess, M.V. Ganduglia-Pirovano, Raman spectra of polycrystalline CeO₂: a density functional theory study, *J. Phys. Chem. C* 121 (2017) 20834–20849.
- [36] S. Zhang, X.-S. Li, B. Chen, X. Zhu, C. Shi, A.-M. Zhu, CO oxidation activity at room temperature over Au/CeO₂ catalysts: disclosure of induction period and humidity effect, *ACS Catal.* 4 (2014) 3481–3489.
- [37] C. Binet, M. Daturi, J.-C. Lavalley, IR study of polycrystalline ceria properties in oxidised and reduced states, *Catal. Today* 50 (1999) 207–225.
- [38] C. Li, Y. Sakata, T. Arai, K. Domen, K.-I. Maruya, O.T. Carbon, Monoxide and carbon dioxide adsorption on cerium oxide studied by fourier-transform infrared spectroscopy. Part 1. – Formation of carbonate species on dehydroxylated CeO₂ at room temperature, *J. Chem. Soc., Faraday Trans. 1* (85) (1989) 929–943.
- [39] R. Farra et al., Understanding CeO₂ as a deacon catalyst by probe molecule adsorption and in situ infrared characterisations, *PCCP* 15 (2013) 3454–3465.
- [40] C. Yang et al., Chemical activity of oxygen vacancies on ceria: a combined experimental and theoretical study on CeO₂(111), *PCCP* 16 (2014) 24165–24168.
- [41] P.G. Lustemberg et al., Diffusion barriers block defect occupation on reduced CeO₂(111), *Phys. Rev. Lett.* 116 (2016) 236101.
- [42] C. Penschke, J. Paier, Reduction and oxidation of Au adatoms on the CeO₂(111) surface – DFT plus U versus hybrid functionals, *PCCP* 19 (2017) 12546–12558.
- [43] C. Zhang, A. Michaelides, D.A. King, S.J. Jenkins, Structure of gold atoms on stoichiometric and defective ceria surfaces, *J. Chem. Phys.* 129 (2008) 194708.
- [44] C. Zhang, A. Michaelides, S.J. Jenkins, Theory of gold on ceria, *PCCP* 13 (2011) 22–33.
- [45] N.C. Hernández, R. Grau-Crespo, N.H. de Leeuw, J.F. Sanz, Electronic charge transfer between ceria surfaces and gold adatoms: a GGA + U investigation, *PCCP* 11 (2009) 5246–5252.
- [46] B.-T. Teng, F.-M. Wu, W.-X. Huang, X.-D. Wen, L.-H. Zhao, M.-F. Luo, A DFT study of the structures of Au_x clusters on a CeO₂(111) surface, *ChemPhysChem* 13 (2012) 1261–1271.
- [47] C. Zhang, A. Michaelides, D.A. King, S.J. Jenkins, Positive charge states and possible polymorphism of gold nanoclusters on reduced ceria, *J. Am. Chem. Soc.* 132 (2010) 2175–2182.
- [48] J. Carrasco, L. Barrio, P. Liu, J.A. Rodriguez, M.V. Ganduglia-Pirovano, Theoretical studies of the adsorption of CO and C on Ni(111) and Ni/CeO₂(111): evidence of a strong metal-support interaction, *J. Phys. Chem. C* 117 (2013) 8241–8250.
- [49] P.G. Lustemberg et al., Room-temperature activation of methane and dry reforming with CO₂ on Ni-CeO₂(111) surfaces: effect of Ce³⁺ sites and metal-support interactions on C-H bond cleavage, *ACS Catal.* 6 (2016) 8184–8191.
- [50] H. Daly, J. Ni, D. Thompsett, F.C. Meunier, On the usefulness of carbon isotopic exchange for the operando analysis of metal-carbonyl bands by IR over ceria-containing catalysts, *J. Catal.* 254 (2008) 238–243.

- [51] G.N. Vayssilov, M. Mihaylov, P.S. Petkov, K.I. Hadjiivanov, K.M. Neyman, Reassignment of the vibrational spectra of carbonates, formates, and related surface species on ceria: a combined density functional and infrared spectroscopy investigation, *J. Phys. Chem. C* 115 (2011) 23435–23454.
- [52] C. Schilling, C. Hess, Elucidating the role of support oxygen in the water-gas shift reaction over ceria-supported gold catalysts using *Operando* spectroscopy, *ACS Catal.* 9 (2019) 1159–1171.
- [53] A. Abd El-Moemen, A.M. Abdel-Mageed, J. Bansmann, M. Parlinska-Wojtan, R.J. Behm, G. Kučerová, Deactivation of Au/CeO₂ catalysts during CO oxidation: influence of pretreatment and reaction conditions, *J. Catal.* 341 (2016) 160–179.
- [54] Y.-G. Wang, D. Mei, J. Li, R. Rousseau, DFT+U study on the localized electronic states and their potential role during H₂O dissociation and CO oxidation processes on CeO₂(111) surface, *J. Phys. Chem. C* 117 (2013) 23082–23089.
- [55] C. Yang et al., O₂ Activation on ceria catalysts – the importance of substrate crystallographic orientation, *Angew. Chem. Int. Ed.* 56 (2017) 16399–16404.
- [56] C. Schilling, M.V. Ganduglia-Pirovano, C. Hess, Experimental and theoretical study on the nature of adsorbed oxygen species on shaped ceria nanoparticles, *J. Phys. Chem. Lett.* 9 (2018) 6593–6598.
- [57] S. Chen, L. Luo, Z. Jiang, W. Huang, Size-dependent reaction pathways of low-temperature CO oxidation on Au/CeO₂ catalysts, *ACS Catal.* 5 (2015) 1653–1662.
- [58] C. Wöll, Structure and chemical properties of oxide nanoparticles determined by surface-ligand IR spectroscopy, *ACS Catal.* 10 (2020) 168–176.
- [59] C. Wang, X. Gu, H. Yan, Y. Lin, J. Li, D. Liu, W.-X. Li, J. Lu, Water-mediated Mars-Van Krevelen mechanism for CO oxidation on ceria-supported single-atom Pt₁ catalyst, *ACS Catal.* 7 (2017) 887–891.
- [60] P.G. Lustemberg, L. Feria, M.V. Ganduglia-Pirovano, Single Ni sites supported on CeO₂(111) reveal cooperative effects in the water-gas shift reaction, *J. Phys. Chem. C* 123 (2019) 7749–7757.

Cite this: *Catal. Sci. Technol.*, 2020,
10, 3720

Influence of gold on the reactivity behaviour of ceria nanorods in CO oxidation: combining *operando* spectroscopies and DFT calculations†

Marc Ziemba and Christian Hess *

Au/CeO₂ catalysts are commonly used for low-temperature CO oxidation. While many studies focus on the properties of gold and their relevance for activity, the influence of the support properties has received less attention. In this temperature-dependent study, we examine the relation between structure and activity for oxidation of CO over ceria nanorods (with/without gold), exhibiting CeO₂(110) and CeO₂(100) termination. Using ceria nanocubes with CeO₂(100) termination as a reference enables us to extract facet-specific characteristics. To characterize the adsorbate and structural dynamics we employ *operando* Raman and UV-vis spectroscopy combined with density functional theory (DFT) calculations. Our results reveal the superiority of CeO₂(110) over CeO₂(100) facets for CO oxidation as a result of their lower defect formation energy. Our findings are supported by the observed dynamics of the surface peroxide, the subsurface oxygen, and the bulk reduction under *operando* conditions. The lower activity of the unloaded samples can be compensated by higher temperatures (>120 °C) allowing new insight into the role of gold for CO oxidation activity. Our study highlights the importance of the surface termination for a detailed mechanistic understanding of ceria-based catalysts.

Received 28th February 2020,
Accepted 6th May 2020

DOI: 10.1039/d0cy00392a

rsc.li/catalysis

Introduction

In previous studies Haruta *et al.* have demonstrated the suitability of a gold catalyst for low-temperature CO oxidation.¹ Later it was shown that the combination of gold with support materials, such as ceria, can further improve the catalytic activity.² The beneficial influence of ceria has been explained by the easy reducibility from Ce⁴⁺ to Ce³⁺, the oxygen storage capacity, and its interaction with gas-phase molecules or the gold particles themselves.^{3,4}

The oxidation of CO, in combination with the water–gas shift reaction, plays an important role in processes in which the purity of the H₂ stream is crucial, such as fuel cell applications.⁵ Despite its relevance for low-temperature applications such as the latter process, as well as its importance as a prototype reaction in heterogeneous catalysis, the mechanism of the CO oxidation over ceria-supported gold catalysts is still hotly debated in the literature.

Previously, it has been shown that both the nature of the support (specific surface area, surface termination, particle size) and the nature of the gold particles is important.^{6–9} While there have been a large number of studies dealing with the state of gold,^{10–16} the changes in support properties that result from the presence of gold have attracted less attention. From density functional theory (DFT) studies it is known that gold particles can lower the defect formation energy and the energy for oxygen activation.^{13,17–19} On the other hand, previous experimental and theoretical work has demonstrated that the ceria surface termination affects properties such as the defect formation energy or the interaction with molecules from the gas phase.^{9,20–23} For example, according to DFT studies, CO interacts more strongly with the CeO₂(110) and CeO₂(100) surfaces than with the CeO₂(111) surface.^{24–26} In order to gain insights into the exact role of gold in CO oxidation and to assess its relevance in comparison to the surface termination, we have studied ceria samples with defined surface termination, with and without gold, at different reaction temperatures. On the basis of a Mars–van Krevelen type of mechanism, easy reducibility of the support is essential.^{16,19,27} Therefore, in this publication we will focus on the two least-stable low-index CeO₂ surface terminations, *i.e.*, CeO₂(100) and CeO₂(110), as they have been shown to possess lower defect formation energies than CeO₂(111).²¹ We have used a combination of

Eduard Zintl Institute of Inorganic and Physical Chemistry, Technical University of Darmstadt, Alarich-Weiss-Str. 8, 64287 Darmstadt, Germany.
E-mail: christian.hess@tu-darmstadt.de

† Electronic supplementary information (ESI) available: UV-vis, Raman, and XP spectra; reactivity data; results from theoretical calculations. See DOI: 10.1039/d0cy00392a

operando UV-vis and Raman spectroscopy and DFT calculations to elucidate the influence of the surface termination in the presence and absence of gold particles during CO oxidation.

Experimental section

Catalyst preparation

Ceria nanocrystals were prepared by hydrothermal synthesis, based on previous reports.^{28,29} For ceria cubes and rods, first 79 ml of a NaOH solution (98%, Grüssing GmbH) was prepared (cubes: 6 M NaOH, rods: 9 M NaOH). In another beaker, the ceria precursor was dissolved in 11 ml of deionized water (electrical conductivity <3 $\mu\text{S m}^{-1}$). For the cubes, $\text{Ce}(\text{NO}_3)_3 \cdot 6\text{H}_2\text{O}$ (Alfa Aesar, 99.5%) served as the precursor, and for the rods, $\text{CeCl}_3 \cdot 7\text{H}_2\text{O}$ (Alfa Aesar, 99%). This solution was then added to the NaOH solution and stirred for 30 min. After that, the solution was poured into a PTFE autoclave (volume: 140 ml) and heated in an oven (heating rate: 1 $^\circ\text{C min}^{-1}$) to the desired temperature (cubes: 180 $^\circ\text{C}$, 18 h; rods: 140 $^\circ\text{C}$, 48 h). After cooling to near room temperature, the resulting CeO_2 was centrifuged off and washed three times with deionized water before it was dried for at least 24 h at 85 $^\circ\text{C}$ in an oven.

Loading of the ceria nanoparticles with gold was carried out by means of electrolyte deposition. To this end, ceria samples were dispersed in a ratio of 1 : 150 in deionized water and the pH value was adjusted to 9 with a 0.1 M NaOH solution (98%, Grüssing GmbH). Subsequently, a 10^{-3} M $\text{HAuCl}_4 \cdot 3\text{H}_2\text{O}$ solution (Carl Roth, 99.9%) was prepared, also at pH 9. The $\text{HAuCl}_4 \cdot 3\text{H}_2\text{O}$ solution was then added to the ceria dispersion to obtain the desired loading of 0.5 wt% Au. After the addition, the pH value was checked again and adjusted to pH 9 if necessary. Then the mixture was heated for 2 h at 65 $^\circ\text{C}$. After cooling it was placed in an ultrasonic bath for 30 min. Finally, the residue was centrifuged and washed four times with deionized water before the product was dried at 85 $^\circ\text{C}$ for at least 24 h in an oven.

Catalyst characterization

BET. N_2 adsorption at 77 K was conducted on a Surfer (Thermo Fisher Scientific). Before measurement, the sample was outgassed at 80 $^\circ\text{C}$ in high vacuum (10^{-6} bar) for 48 h. To determine the specific surface area, the N_2 adsorption curve was fitted to the BET (Brunauer-Emmett-Teller) model.³⁰ For the rods a specific surface area of 88 $\text{m}^2 \text{g}^{-1}$ and a pore volume of 0.22 $\text{cm}^3 \text{g}^{-1}$ were obtained. For the cubes, we found 32 $\text{m}^2 \text{g}^{-1}$ for the specific surface and 0.08 $\text{cm}^3 \text{g}^{-1}$ for the pore volume.

Transmission electron microscopy (TEM). The transmission electron microscope (JEOL JEM-2100F, Tokyo, Japan) used is equipped with a Schottky field emitter and operates at a nominal acceleration voltage of 200 kV. For preparation, the sample was dispersed in an ultrasonic bath for 30 s in ethanol and then placed on a carbon grid (Plano). When the sample was dry, the grid was coated with carbon (Bal-Tec MED010), to prevent charging by the electron beam.³¹

X-ray photoelectron spectroscopy (XPS). XP spectra were recorded on an SSX 100 ESCA spectrometer (Surface Science Laboratories Inc.) employing a monochromatic Al $K\alpha$ source with an energy of 9 kV (10 mA). The sample holder and the analyser were aligned at an angle of 55 $^\circ$ to the horizontal. The X-ray beam was at an angle of 35 $^\circ$ to the analyser horizontal and the sample was rotated 16 $^\circ$ with respect to the X-ray beam. The resolution was 0.054 eV.

To ensure the comparability of the spectra, the u'' signal of the Ce 3d photoemission was shifted to the literature value of 916.7 eV for all spectra.³² The spectra were deconvoluted by Gaussian-Lorentz functions (30/70 ratio), whereby the background was subtracted according to Shirley.³³ For further details, please refer to previous studies.³⁴

Based on the XPS data, the amount of gold for the loaded rods was determined to be 0.3 wt% Au, and for the gold-loaded cubes, 0.6 wt% Au. In this context, the amount of gold is given in weight percentage directly at the surface, which is due to the penetration depth of the method. Contaminations caused by the synthesis, e.g. chlorine or nitrogen, can be excluded within the sensitivity of the XPS measurements.

ICP-OES. The weight percentage of gold was determined by ICP-OES, yielding a gold content of 0.2 wt% for the rods and of 0.18 wt% for the cubes.

Operando spectroscopy. The catalytic activity, *operando* Raman, and UV-vis spectra were measured using an experimental setup that has been described previously.³⁴⁻³⁶ Briefly, for the *operando* measurements about 20–25 mg of the sample was placed in a stainless-steel sample holder (8 mm in diameter, 0.5 mm deep). Raman spectra were recorded on an HL5R transmission spectrometer (Kaiser Optical) using a frequency-doubled Nd:YAG laser (Cobolt) for excitation at 532 nm (1 mW at sample). The spectral resolution was specified as 5 cm^{-1} and the stability of the band positions was better than 0.3 cm^{-1} . For the cubes an exposure time of 80 s with 5 accumulations was used, and for the rods, an exposure time of 250 s with 2 accumulations. For all measurements a cosmic ray filter and an auto new dark correction were used. This results in a total measuring time of about 1600 s for cubes and 2000 s for rods. All Raman spectra reported in this work were normalized to the highest intensity band, i.e., the F_{2g} band. Given F_{2g} positions were determined by curve fitting using Lorentz functions.

The UV-vis spectra were taken in diffuse reflection using an AvaSpec ULS2048 spectrometer (Avantes) equipped with a deuterium lamp and a halogen discharge lamp. The measuring time was 60 s, which is composed of an exposure time of 300 ms and 200 runs. As the white standard, magnesium oxide powder (MgO , Sigma Aldrich) was used, which shows no absorption between 170 nm and 1100 nm.

The sample temperature was determined by means of a Ni/Cr-Ni thermocouple (type K), which was located at the sample holder close to the sample. Sample temperatures deviated by a maximum of 2 $^\circ\text{C}$ from the set temperatures. The temperature difference for the unloaded and gold-loaded samples (121 $^\circ\text{C}$ and 134 $^\circ\text{C}$) corresponds to differences in

the heat of reaction, as the CO oxidation is a highly exothermic reaction.

The gases CO (99.997%, Air Liquide), O₂ (99.999%, Westfalen), and argon (99.996%, Westfalen) were dosed by digital mass flow controllers (MFCs, Bronkhorst). The total flow was always 100 ml min⁻¹. To analyse the gas phase and its composition, a Fourier transform infrared (FTIR) spectrometer (Tensor 20, Bruker) was installed at the outlet of the cell. The resolution was 4 cm⁻¹, and the measurement time was 1 min, in which 125 spectra were accumulated. Using calibration curves, the concentrations of CO and CO₂ can be calculated to determine the CO conversion. This catalytic activity is obtained as the ratio of the amount of CO₂, as measured by FTIR at the outlet of the cell, and the amount of CO dosed (2 ml min⁻¹), which corresponds to the conversion of CO to CO₂.

DFT calculations. The employed approach and procedures have been described previously.^{9,37} Briefly, spin-polarized DFT calculations were performed using the Vienna *ab initio* simulation package (VASP, Version 5.3.5, <https://www.vasp.at/>). For all calculations the DFT+U approach³⁸ with the generalized gradient-corrected approximation of Perdew, Burke and Ernzerhof (PBE) was employed,³⁹ and for the U_{eff} of the Ce 4f orbital parameter 4.5 eV (PBE + U/4.5 eV) was used. Only valence electrons with a plane-wave cutoff of 400 eV were considered. The pseudopotentials used originated from VASP version 5.4 and the Kohn–Sham equations were solved using the projector augmented wave (PAW) method. As the lattice constant for ceria we used 5.484 Å.³⁷ For all relaxations of the structures, the convergence criterion was set to 0.01 eV Å⁻¹, which describes the maximum force acting on an atom. The total energy for a self-consistent loop was converged up to 10⁻⁶ eV.

The supercell used for CeO₂(110) consists of seven atomic layers, the lowest of which is fixed. At the top and bottom of the cell, a vacuum layer of at least 10 Å was added. The choice of the number of atomic layers was based on the convergence of the surface energy. The relaxation energy plot for the CeO₂(110) facet is shown in Fig. S1.† For the calculations, unit cells with (1 × 1), (2 × 1), and (2 × 2) periodicities were used. The sampling of the Brillouin zone was realized according to the periodicity with a (6 × 4 × 1), (3 × 4 × 1), or (3 × 2 × 1) Monkhorst–Pack grid,⁴⁰ which correspond to the same *k*-point density in terms of the periodicity. To model the gold/ceria structures gold atoms were deposited on CeO₂(110) or CeO_{2-x}(110) structures, using previous theoretical studies as an orientation for modelling the structures.^{41–43} Furthermore, a Bader charge analysis was performed for the gold atoms (see Table S2†), which shows that when gold interacts with the oxidized ceria surface, a charge transfer to cerium takes place resulting in positively charged gold atoms. By interaction of gold with a reduced ceria surface this is reversed leading to negatively charged gold atoms, consistent with previous DFT studies.^{42,44}

The vibrational frequencies were calculated using density functional perturbation theory (DFPT), which is implemented in the VASP code. The calculation of Raman intensities has been described previously.³⁷

Results

Catalyst characterization

The prepared nanoparticles were characterized by BET, TEM (see Fig. 1), XPS (see Fig. S2 and S3†) and ICP-OES. The TEM images for ceria rods and ceria cubes, shown as Fig. 1A and B, respectively, indicate the characteristic surface terminations of the particles, based on the spacing of the lattice planes indicated by the white arrows. The rods exhibit two different lattice plane distances, *i.e.*, 0.27 nm and 0.19 nm, whereas the cubes are characterized by a single lattice plane distance of 0.27 nm. A distance of 0.27 nm can be assigned to a CeO₂(100) termination and a distance of 0.19 nm to a CeO₂(110) termination, in agreement with the literature.^{28,29} Using the cubes as a reference for CeO₂(100) throughout our study allows us to assign effects observed for the rods to a specific facet, *i.e.*, either CeO₂(110) or CeO₂(100). While we focus on the rods here, the corresponding results for the cubes are shown in the Supporting Information.

Analysis by XPS reveals a Ce³⁺ content of 15% for the bare ceria rods and 38% for the gold-loaded rods (see Fig. S2 and S3†). The increase of the Ce³⁺ content with the gold loading can be explained by a charge transfer from gold to the oxidized ceria resulting in Au^{δ+} and Ce³⁺ (see Fig. S10 and Table S2†), consistent with previous DFT+U calculations.^{13,42,45} In the Au 4f photoemission of the gold-loaded rods (see Fig. S4†), there are two components, located at 84.2 and 87.5 eV, originating from metallic and cationic gold, respectively. Although in previous studies Au³⁺ on CeO₂(111) has been observed by the adsorption of Au into cerium defects,⁴⁶ earlier studies for CeO₂(110) and CeO₂(100) have shown the absence of Au³⁺.¹⁸ Calculations from this study show that the presence of Au³⁺ cannot be excluded (see ESI†), because for the doped structures (structures H and I, Table S2†) the Bader charge is much higher than for the adsorbed gold species (*e.g.* structures F and G, Table S2†). However, theoretical studies have demonstrated that the adsorption of gold into cerium vacancies is only favored under extremely O-rich conditions compared to adsorption into oxygen defects,⁴⁷ because the formation of a cerium vacancy is a highly endothermic process, which is also in line with our calculations for the CeO₂(110) facet (see ESI†, Table S1). Based on these previously reported results we propose that the 87.5 eV component originates from Au^{δ+}, despite the high binding energy. In this context it should be mentioned that signals at such high binding energies have previously been assigned to Au³⁺, but this was based on gold salts and other gold reference compounds,⁴⁸ rather than supported gold particles.

Catalytic activity

Fig. 2 depicts the catalytic activity during CO oxidation (2% CO/25% O₂ / Ar; 100 ml min⁻¹) over bare CeO₂ nanorods and 0.3 wt% Au/CeO₂ nanorods at two temperatures. Bare rods were measured at 45 °C and 121 °C, and gold-loaded rods at 45 °C and 134 °C. Prior to and after reaction, samples were exposed to oxidative conditions (25% O₂ / Ar; 100 ml min⁻¹).

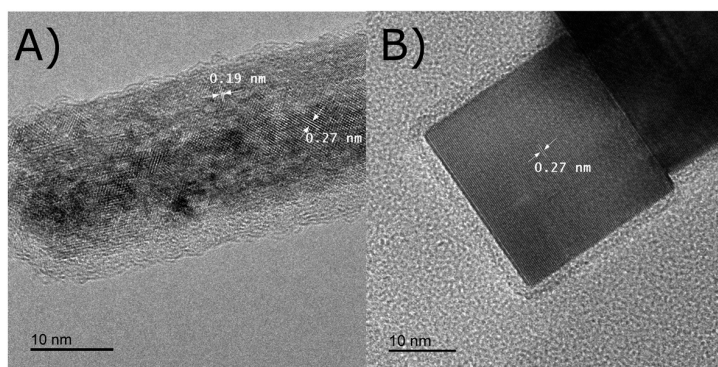


Fig. 1 TEM images of the synthesized ceria nanostructures: A) ceria rod, and B) ceria cube. The white arrows indicate the distance between lattice planes in the direction of the particle surface.

These measurements are also the basis of the *operando* measurements discussed below.

As can be seen in Fig. 2, at 45 °C, the sample without gold loading shows no CO conversion, whereas the gold-loaded sample shows a conversion of 0.4%. At the higher temperature, the unloaded sample shows a small conversion of about 0.2% too. In comparison, the gold-loaded sample shows a conversion of 19.6% at 134 °C. Thus, depending on

the conditions, both samples may show CO oxidation activity. Obviously, the presence of gold lowers the reaction barrier and/or assumes a stabilizing role of reaction intermediates. Regarding the reaction barrier, previous theoretical studies for CeO₂(100) have shown that Au₃ or larger gold clusters on CeO₂(100) can reduce the defect formation energy in contrast to unloaded CeO₂(100).¹⁴ Our results for Au₁ on CeO₂(110) (see Table S2†) also show that such small clusters do not reduce the defect formation energy as compared to unloaded ceria with CeO₂(110) facets. For this reason, we suggest that in case of the CeO₂(110) facet the presence of larger gold clusters is responsible for lowering the defect formation energy. However, the absence of gold can be compensated by higher temperatures, as will be discussed below in more detail in the context of the *operando* data.

A similar activity behaviour is also observed for the cubes (see Fig. S5†). However, it is noticeable that the CO conversion at 45 °C is lower than that of the rods, despite the higher gold loading at the surface (0.6 wt%). Based on this comparison, we attribute the higher activity of the rods to the CeO₂(110) facet. Interestingly, at higher temperatures, this difference is compensated again and similar conversions are observed for both the unloaded and gold-loaded samples at 45 °C. The catalytic activities for CO oxidation over unloaded and gold-loaded rods and cubes are summarized in Table 1.

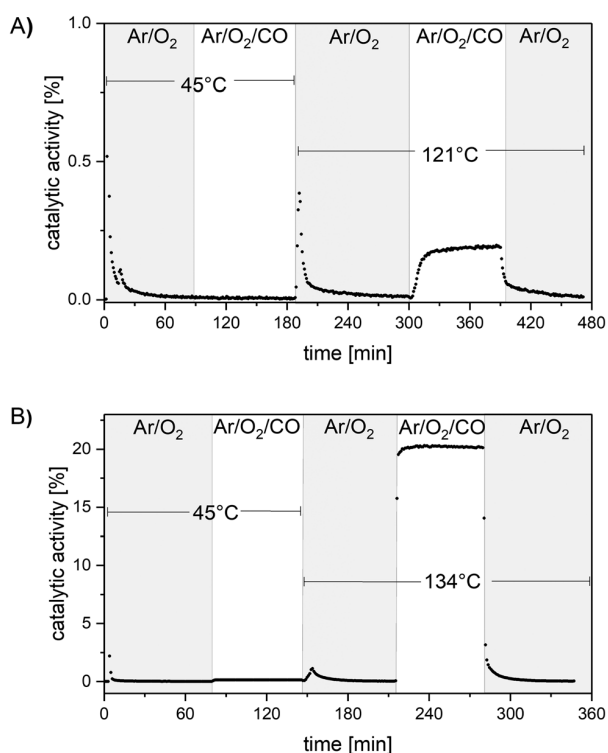


Fig. 2 Catalytic activity during CO oxidation over A) CeO₂ nanorods at 45 °C and 121 °C, and B) 0.3 wt% Au/CeO₂ nanorods at 45 °C and 134 °C. The samples were exposed to a CO/O₂/Ar stream (2% CO/25% O₂/Ar; 100 ml min⁻¹) under reaction conditions and to an O₂/Ar stream (25% O₂/Ar; 100 ml min⁻¹) prior to and after reaction conditions, respectively.

Table 1 Catalytic activities for the conversion of CO to CO₂ during CO oxidation of the unloaded and gold-loaded rods and cubes. The catalytic activity was measured after at least 1 h under reaction conditions (CO/O₂/Ar). Activities were determined at 45 °C and at an elevated temperature, i.e., at 121 °C for the unloaded samples and 134 °C for the gold-loaded samples.

Sample	Activity at 45 °C	Activity at >120 °C
CeO ₂ rods	0.0	0.2
Au/CeO ₂ rods	0.4	19.6
CeO ₂ cubes	0.0	0.2
Au/CeO ₂ cubes	0.1	20.1

Operando UV-vis spectroscopy

Changes of the electronic structure under reaction conditions can be detected using *operando* UV-vis spectroscopy. To this end, Fig. 3 depicts *operando* UV-vis spectra of bare ceria rods and gold-loaded rods. The spectra shown at the bottom (dashed lines) represent the measurements of the unloaded sample and the spectra at the top (solid lines) those of the loaded sample. Both samples exhibit strong absorption in the UV range, attributable to O 2p (occupied) \rightarrow Ce 4f (unoccupied) interband and $f \rightarrow d$ transitions.^{49,50} Comparison of the spectra of the two samples at 45 °C in CO/O₂/Ar shows that the presence of gold leads to increased absorption in the visible range (450–900 nm). This behaviour is attributed mainly to a charge transfer from Ce³⁺ to Ce⁴⁺,^{50,51} while absorption due to gold surface plasmons cannot be ruled out.⁵² Plasmon-induced absorption appears to be more important for the Au/CeO₂ cubes (see Fig. S6[†]), which show a stronger absorption in the visible wavelength region despite the lower Ce³⁺ content of 28% (XPS) (compare $-\log(R)$ at 570 nm (45 °C in O₂/Ar); rods: 0.17, cubes: 0.32). Interestingly, under reaction conditions at 45 °C, the gold-loaded rods exhibit an absorption band between 450 nm and 550 nm, which is barely noticeable for the other samples. To the best of our knowledge, this band has previously been associated with adsorbed oxygen species,⁵³ but has not been discussed in more detail in the literature. Based on its correlation with the appearance of the peroxide Raman band at 829 cm⁻¹ discussed below (see Fig. 4B), it is tentatively assigned to peroxides adsorbed on the ceria surface.

When the feed is switched from reactive conditions at 45 °C to O₂/Ar flow at higher temperature, an increase in

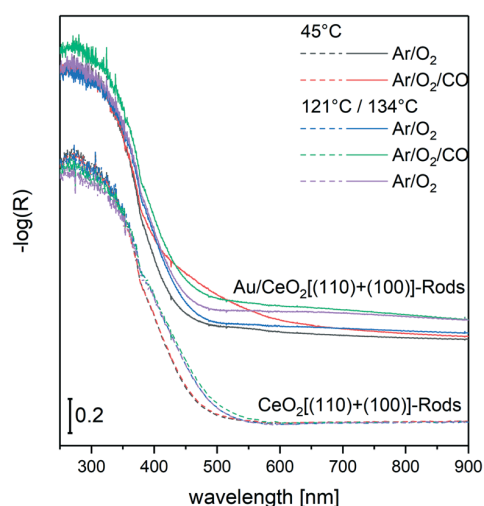


Fig. 3 *Operando* UV-vis spectra of bare ceria rods (at the bottom, dashed lines) and gold-loaded rods (at the top, solid lines). The spectra were recorded at the temperatures indicated, at a total flow rate of 100 ml min⁻¹ and feed compositions of 2% CO/25% O₂/Ar and 25% O₂/Ar for reactive and oxidative conditions, respectively. Spectra of the gold-loaded samples are offset for clarity.

absorption is observed between 400 nm and 500 nm, which is assigned to a temperature-induced decrease of the band gap, in agreement with the literature.⁵⁴ Exposure to reaction conditions leads to a further increase in visible absorption (green lines), which, however, shows a profile different to that at 45 °C (red lines). The absorption increase may originate from an agglomeration of gold particles, as previously described in the literature,^{10,52} and/or from a reduction of the support, as will be discussed below in the context of the *operando* Raman data. In contrast to the CeO₂(111) facet, an irreversible adsorption of gold into oxygen vacancies can be excluded on the CeO₂(110) facet, since this process is reversible on the CeO₂(110) facet due to the more open surface.⁵⁵ However, on the CeO₂(100) facet, such a process would be conceivable. Finally, switching the

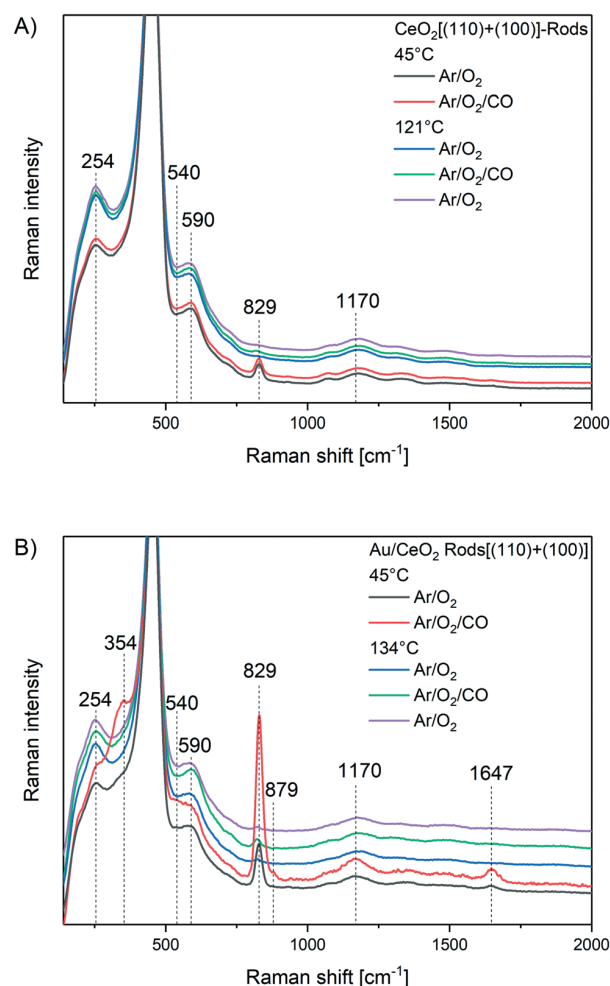


Fig. 4 *Operando* 532 nm Raman spectra of A) bare ceria rods, and B) gold-loaded rods. The spectra were recorded at the temperatures indicated, at a total flow rate of 100 ml min⁻¹ and feed compositions of 2% CO/25% O₂/Ar and 25% O₂/Ar for reactive and oxidative conditions, respectively. The high intensity F_{2g} peak at around 450 cm⁻¹ is cut off to allow an enlarged view of the other features. Spectra are offset for clarity.

feed to O₂/Ar leads to a small decrease in absorption but no regeneration of the initial state.

Operando Raman spectroscopy

Fig. 4 depicts the low-wavenumber region of the *operando* Raman spectra of bare ceria rods (Fig. 4A) and gold-loaded rods (Fig. 4B). As discussed in the following, this region contains features characteristic of solid-state phonons and adsorbate-related vibrations. Note that the high intensity F_{2g} peak at around 450 cm⁻¹ is cut off to allow an enlarged view of the other features. In all spectra, the 2TA and the 2LO overtones are observed at 254 and 1170 cm⁻¹, and defect-related bands at 540 and 590 cm⁻¹.³⁷ The Raman band located at 829 cm⁻¹ originates from peroxides adsorbed on the surface.²² For the gold-loaded rods at 45 °C, the 829 cm⁻¹ band contains a shoulder at 879 cm⁻¹, which is characteristic of the presence of peroxides at higher coverage, in agreement with our previous DFT calculations.²²

Interestingly, the gold-loaded sample shows greater dynamics among the defect-related bands and a higher intensity in the peroxide region, both of which can be attributed to a reduction of the defect formation energy with gold loading, consistent with the literature.^{13,14,17,18} Besides, the spectra of the loaded rods recorded at 45 °C in CO/O₂/Ar (red line in Fig. 4B) show an additional Raman feature at 354 cm⁻¹, which can be assigned to a deformation mode of peroxides on the ceria surface, as confirmed by DFT calculations (Fig. S7†), and in agreement with previous experimental observations on CeO₂(111), which, however, did not clarify the symmetry of this vibration.⁵⁶ Note that, owing to its overlap with other bands, the peroxide feature at 354 cm⁻¹ is only observed at higher peroxide coverages. For the cubes, this band is much less pronounced owing to the lower peroxide coverage, as inferred from the lower intensity of the 829 cm⁻¹ peroxide band (see Fig. S8†).

Regarding adsorbate-related features, for the gold-loaded sample at 45 °C, a band at 1647 cm⁻¹ is observed (see Fig. 4B), the intensity of which increases under reaction conditions. Based on previous DFT calculations, this band can be assigned to a C=O vibration of carbonates on the surface.³⁵ At higher temperatures, this band is not detected.

Fig. 5 covers the corresponding high-wavenumber region of the *operando* Raman spectra of bare ceria rods (shown at the bottom) and gold-loaded rods (shown at the top). In the spectra of both samples, bands appear at 2846 cm⁻¹ and 2935 cm⁻¹, which can be attributed to C-H stretching vibrations of formates.⁵⁷ Note that, in the case of the gold-loaded sample, these bands lose intensity at higher temperature (see blue solid line) and are no longer observed under and after reaction conditions (see green and purple solid lines). Together with the temperature-dependent activity behaviour (see Fig. 2), this observation may indicate a change in the reaction mechanism at higher conversions. As discussed previously for Pt/CeO₂ systems, at higher temperatures (98 °C) new reaction pathways *via* formates

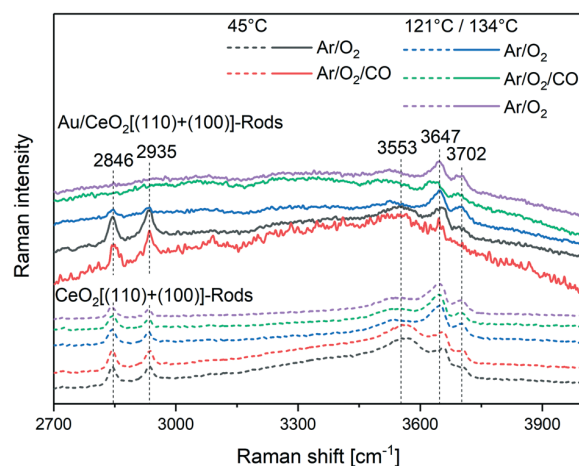


Fig. 5 *Operando* 532 nm Raman spectra of the high-wavenumber region of bare ceria rods (at the bottom, dashed lines) and gold-loaded rods (at the top, solid lines). The spectra were recorded at the temperatures indicated, at a total flow rate of 100 ml/min and feed compositions of 2% CO/25% O₂/Ar and 25% O₂/Ar for reactive and oxidative conditions, respectively. Spectra are offset for clarity.

and/or a direct route may open up.⁵⁸ For a reaction *via* formates, the presence of hydroxides or water is essential. In fact, as shown in Fig. 5, the presence of hydroxides in the range 3000–3800 cm⁻¹ can be confirmed by the *operando* spectra. However, this aspect will be discussed in more detail below.

Dynamical behaviour under working conditions

Fig. 6 depicts a summary of distinct *operando* Raman and UV-vis results of bare ceria rods (see Fig. 6A) and rods loaded with 0.3 wt% Au (see Fig. 6B). In particular, we will address the dynamical behaviour of the peroxide intensity, the Raman F_{2g} band position, and the absorption at 570 nm, in comparison to the simultaneously recorded catalytic activity. In the following, first the surface dynamics based on the peroxides, then the subsurface region as monitored by the F_{2g} band, and finally the visible absorption behaviour will be discussed.

As shown previously, peroxides can be regarded as an indicator for the presence of surface defects, as peroxide formation occurs *via* adsorption of gas-phase oxygen into a two-electron surface defect.^{22,59} In fact, switching from oxidative (O₂/Ar) to reactive (CO/O₂/Ar) conditions at 45 °C leads to a strong increase of the peroxide intensity at 829 cm⁻¹ of the gold loaded samples, as a result of the reduction by CO (see also Fig. S11†), whereas the bare ceria samples show no noticeable changes. However, as apparent from Fig. 6 and S11† there are significant differences in the absolute intensity of the peroxide band. The gold-loaded samples exhibit higher peroxide intensity than the bare samples, and the rods show a significantly higher intensity than the cubes. At higher temperature the peroxide bands decrease, as their formation is no longer preferred

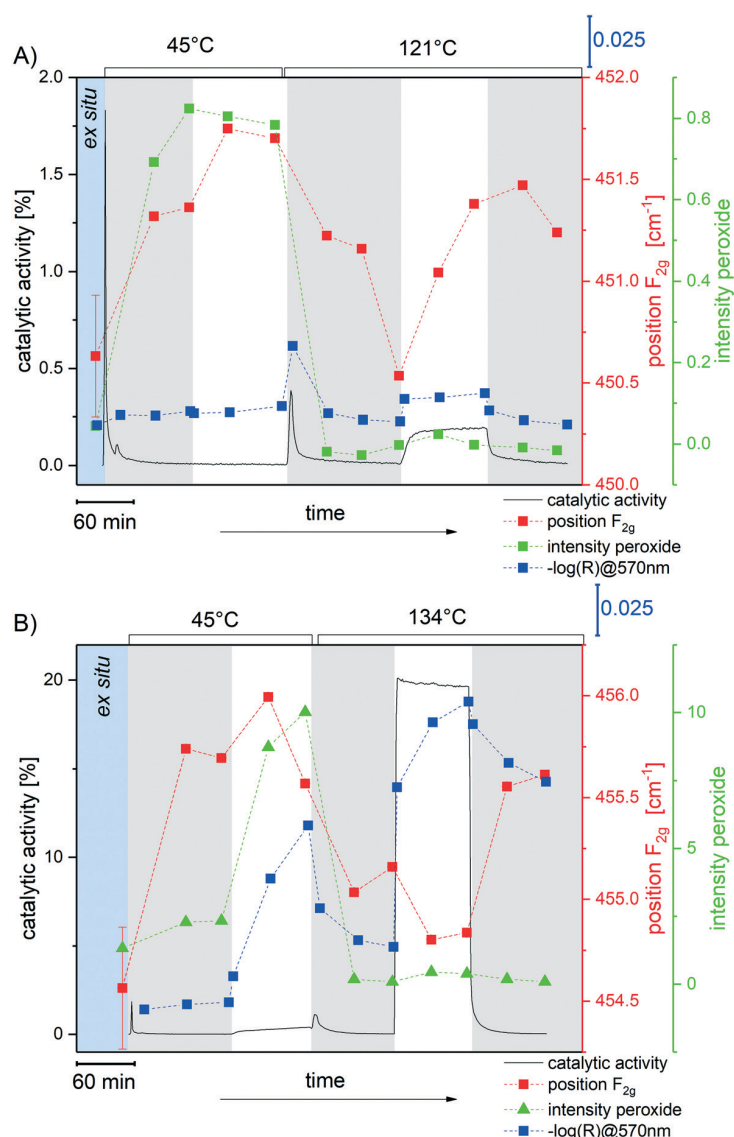


Fig. 6 Summary of *operando* Raman and UV-vis results for A) bare ceria rods and B) 0.3 wt% Au/CeO₂ rods during CO oxidation (2% CO/25% O₂/Ar) at a total flow rate of 100 ml/min at the temperatures indicated. As in Fig. 2, reaction conditions correspond to white areas, and oxidative conditions (25% O₂/Ar) to grey areas. The measurement error for the F_{2g} position is indicated as an example for the *ex situ* measurement but applies to all F_{2g} data points.

thermodynamically, as shown in our previous Raman and DFT studies.²²

Regarding the Raman F_{2g} band, which represents the degree of reduction in the subsurface region,³⁶ loading ceria rods with gold induces a blue-shift of 4 cm⁻¹ (see Fig. 6), strongly suggesting that gold adsorbs into oxygen defects. The observed F_{2g} blue-shift can be rationalized by an electron transfer from Ce³⁺ to gold, which results in Ce⁴⁺ formation. As a consequence, the lattice is contracted because of the smaller ionic radius of Ce⁴⁺, which is known to be accompanied by F_{2g} mode stiffening.³⁷ When exposed to O₂/Ar and reactive conditions at 45 °C, both rods and Au-loaded rods show an overall F_{2g} blue-shift, indicating sample

oxidation. In the case of the cubes (see Fig. S11), a contrary behaviour, *i.e.*, a red-shift, is observed, which is attributed to temperature-induced mode softening.^{60,61} This difference in behaviour between rods and cubes can be rationalized by the higher defect content of the rods (see XPS results in ESI†) and by the lower defect formation energy at the CeO₂(110) facet facilitating further oxidation in comparison to the cubes.

When exposed to higher temperature and oxidizing atmosphere, both rod-based samples undergo a further red-shift, which originates from the temperature effect (discussed above) and the (partial) removal of adsorbates, *i.e.*, peroxides and CO, from the surface. The observed F_{2g} red-shift is

significantly stronger for the gold-loaded cubes (2.8 cm^{-1}) than for the gold-loaded rods (0.5 cm^{-1}), as shown by Fig. 6 and S11†. This behaviour underlines the higher defect concentration of the rods indicated by the XPS measurements. If the feed is switched to reaction conditions at higher temperatures, the two rod samples show opposite behaviour regarding the F_{2g} position, *i.e.*, the bare rods exhibit a blue-shift whereas the gold-loaded rods show a red-shift. This behaviour originates from the significantly higher CO conversion of the gold-loaded sample leading to reduction of ceria in the subsurface, since under these conditions the regeneration of the support is slower than the reduction by CO oxidation. Upon subsequent switching to oxidizing conditions, the gold-loaded sample is re-oxidized, while the bare-rod sample undergoes only little change, as this sample has already been re-oxidized under reaction conditions. This is different for the loaded and unloaded cubes (see Fig. S11†), which do not show noticeable F_{2g} shifts on switching between oxidative and reactive conditions, thus underlining the importance of the surface facet. In this context we note that the presence of two facets present in rods, *i.e.*, (110) and (100), may mutually influence each other leading to a variation of properties from the isolated facets.

In the following, the change in absorption at 570 nm will be discussed. As can be seen in Fig. 6, the gold-loaded sample shows an increase in absorption under reaction conditions at both temperatures, which may originate from a reduction of the material and/or sintering of gold particles, as suggested on the basis of long-term studies.⁵² The observed increase in absorption is not completely reversible, which would be consistent with agglomeration of gold atoms, ceria reduction and/or irreversible gold adsorption into oxygen defects on $\text{CeO}_2(100)$ at high conversion. For the gold-loaded cubes (see Fig. S11†) a similar behaviour is observed, but there is no decrease in absorption after switching to oxidative conditions, indicating a larger contribution of gold agglomeration and irreversible gold adsorption into oxygen defects on $\text{CeO}_2(100)$. Regarding the latter explanation it should be noted that cubes possess a smaller defect concentration than rods (see above) and they contain only $\text{CeO}_2(100)$ facets in contrast to the rods. In contrast, the unloaded rod samples show only slight reversible changes in 570 nm absorption under reaction conditions at elevated temperature from reaction induced reduction, whereas for bare cubes no changes are observed (see Fig. S11†), which can be related to the absence of the $\text{CeO}_2(110)$ facet. Note that for the bare rods, the blue-shift of the Raman F_{2g} band points to an opposite oxidation behaviour in the subsurface region (see Fig. 6A). This apparent contradiction can be resolved by taking into account the different penetration depths of the two methods, which monitor either the subsurface (Raman F_{2g}) or the bulk (UV-vis), thus implying oxygen diffusion from the bulk to the subsurface region in the case of the bare rods.

In this final section, we would like to discuss the apparently different findings regarding the Ce^{3+}

contributions of the gold-loaded rods obtained by XPS (see Fig. S3†) and Raman (see Fig. 6B). This can be explained by the penetration depths of the two methods, *i.e.*, Raman probes the subsurface region³⁶ whereas XPS samples the surface region. Thus, gold adsorbed into the pores of ceria rods, causing the observed F_{2g} blue-shift, is not accessible by XPS. In contrast, such a F_{2g} blue-shift is absent for the cubes. This behaviour can be explained by taking into account the BET results, which show that the rods possess a significantly higher pore volume than the cubes.

Summarizing, our results show that the choice of the surface termination results in different structural dynamics of the surface, subsurface, and bulk. Based on these observations it is possible to obtain a more detailed understanding of the role of the support in Au/ CeO_2 catalysts. In the following, we will discuss the implications of our findings regarding the mechanism of CO oxidation.

Insight into the reaction mechanism

As demonstrated above, rods exposing $\text{CeO}_2(110)$ and $\text{CeO}_2(100)$ facets and cubes exposing $\text{CeO}_2(100)$ facets can be active in CO oxidation with or without gold loading, but the presence of gold allows milder reaction conditions. The main findings are summarized in Fig. 7 for the lower temperature, showing that bare ceria is not active and only CO adsorption and carbonate formation occurs. If gold is present, the sample becomes active for CO oxidation, as the presence of gold lowers the defect formation energy, making more surface oxygen available for reaction.^{14,19} Furthermore, a coordinating role of gold on reaction intermediates may be conceivable, since the adsorption of CO (no carbonate formation) on deposited gold on oxidized ceria is preferred over the bare support (see Table S3†). In fact, the identification of $\text{CO-Au}^+-\text{O}_{\text{lattice}}$ as an active site has already been demonstrated in our previous studies on Au/ $\text{CeO}_2(111)$ catalysts using a combination of DRIFTS and DFT calculations.⁶² At higher temperatures, a different situation arises, as now both the bare support and the gold-loaded sample are active, owing to the fact that surface oxygen that is not located in the neighbourhood of gold is also available for CO_2 formation (see Fig. 7). This behaviour can be explained by the thermally induced compensation of differences in the energy barrier for the formation of oxygen vacancies.

The importance of the defect formation energy for the catalytic activity is demonstrated by considering two different surface terminations. Generally, the rods show a higher activity at low temperatures than the cubes, consistent with the trends in the defect formation energies²¹ ($\text{CeO}_2(100)$: 1.392 eV;²² $\text{CeO}_2(110)$: 1.329 eV (see Table S1†)), which are lower for $\text{CeO}_2(110)$ present only at the rods. At higher temperatures, however, the activities are almost the same, owing to the loss of importance of the differences in defect formation energy.

Another aspect that may play a role regarding the activity at lower temperatures is the adsorption of peroxides. DFT

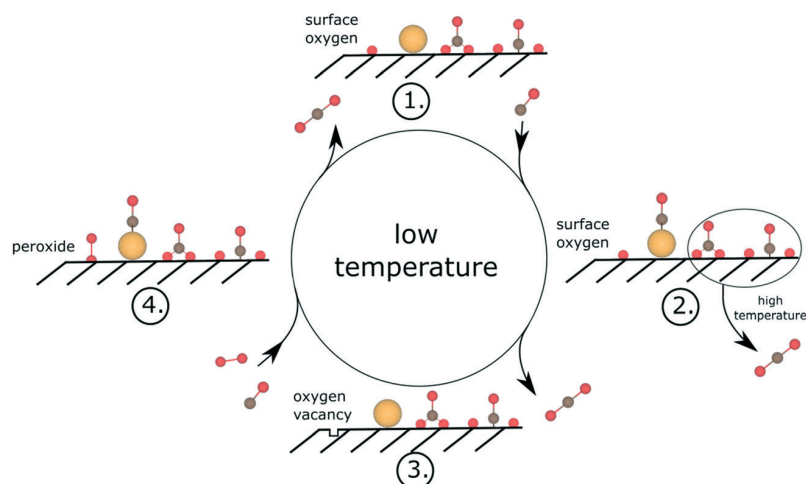


Fig. 7 Reaction pathways for CO oxidation over bare CeO₂ and Au/CeO₂ catalysts at low temperature. For details see text.

calculations show that on all ceria facets the adsorption of O₂ is preferred over CO if CO adsorbs as an isolated molecule (*i.e.*, without carbonate formation). Importantly, as shown by the activity profiles and peroxide intensity (see Fig. 6), increasing peroxide formation at high coverages may impede CO oxidation, as indicated by the strong peroxide signal during reaction conditions at 45 °C. While peroxides have been shown to participate in CO oxidation,^{63,64} stable peroxide formation is indicative of an oxygen-deficient surface, which inhibits the formation of carboxylates/carbonates. Thus, the formation of CO₂ is expected to be more favourable under conditions where peroxide formation by O₂ adsorption is thermodynamically no longer preferred, *e.g.* at higher temperatures (>120 °C), at which peroxide dissociation is facilitated, thereby healing a second oxygen defect. Therefore, under these conditions, between steps 4 and 1 in Fig. 7, dissociation of peroxide may take place, leading to adsorption of the outer oxygen atom into an adjacent oxygen vacancy (not shown) or a direct removal of the very reactive outer oxygen atom by CO, as shown in previous theoretical studies.⁶⁵

In the following, we will discuss the role of carbonates, which were observed for the gold-loaded rods during reaction conditions (45 °C) (see Fig. 4), and that of formates, which are present in all samples and disappear from the gold-loaded rods during reaction conditions at 134 °C (see Fig. 5). For the cubes, no carbonates are observed, but their absence may result from the stronger absorption and therefore lower Raman sensitivity of the gold-loaded cube sample (see Fig. S8†). It has previously been shown in the literature for cobalt-doped ceria systems that a carbonate-mediated mechanism may be feasible.⁶⁶ We may thus propose that at 45 °C CO adsorbs as carbonate without any CO conversion, consistent with theoretical results for CeO₂(110) and CeO₂(100) surfaces, demonstrating that carbonate formation is a strongly exothermic process.^{23–25,67} In contrast, for the CeO₂(111) surface, no stable carbonate formation has been reported in

the literature, which can be rationalized by the larger space between the surface oxygen atoms at the CeO₂(111) surface preventing carbonate formation without large surface reconstruction. As a consequence, the adsorption of carbonates at low temperatures negatively affects the activity, because active sites are blocked and carbonate adsorption is several times stronger than that of an isolated CO molecule.²⁵ Similarly, for CeO₂(111), the formation of hydrogencarbonates has been shown to inhibit CO oxidation by site blocking.^{62,68} The situation is different at higher temperatures, at which the absence of the band at 1647 cm⁻¹ may be explained by the formation of CO₂ *via* carbonates (indicated in Fig. 7), leaving an oxygen vacancy. In addition, the resulting higher oxygen defect concentration at higher temperatures may inhibit the renewed formation of carbonates, since less surface oxygen is available for carbonate formation. Formates are characterized in this study by their C–H stretching bands at 2846 and 2935 cm⁻¹ (see Fig. 5).⁶⁹ In contrast to the bare rods, for the gold-loaded rods the C–H bands disappear at the higher temperature. Our results imply that the energy barrier for formate desorption is reduced for gold-loaded samples, leading to the disappearance of the bands without any indication of intermediates. In the course of this desorption process gold may play a major role, as gold can promote the proton transfer from formate species to surface oxygen at higher temperatures, resulting in the formation of hydroxide. The transfer of a second proton may then lead to water desorption accompanied by oxygen vacancy creation. Thus, we propose that formates are only spectator species for CO₂ formation, the desorption of which is facilitated in the presence of gold. As explained above, for the cubes no precise statements regarding formates can be made.

Conclusions

In this study, we demonstrate the importance of the defect formation energy for CO oxidation over Au/CeO₂ catalysts.

The defect formation energy is strongly influenced by the surface termination of the ceria particles and by the gold loading. Thus, choosing a sample with a CeO₂(110) surface termination and loading it with gold positively influences the activity. At the same time, we show that unloaded samples can be as active as gold-loaded ones, *i.e.*, at higher temperatures it is possible to achieve similar CO conversion rates with the unloaded samples as with the gold loaded samples at lower temperatures. In this context, the barrier to making surface oxygen available for CO₂ formation is thermally compensated. Thus, the main role of gold on the low-index surfaces is to allow milder reaction conditions. However, the role of gold as an active site loses importance at higher temperatures, as the bare support becomes more active, by thermal activation of lattice oxygen. In addition, we observe strong peroxide formation at the gold-loaded samples under reaction conditions (45 °C). To this end, we propose that peroxide formation may suppress CO adsorption and thus reaction, because of the higher adsorption energy of O₂ compared to CO (not subject to carbonate formation) and due to steric effects. Furthermore, the formation of carbonate species at lower temperatures may block active sites because of high adsorption energies of carbonates on CeO₂(100) and CeO₂(110). To conclude, our results show the potential of combining *operando* spectroscopies and DFT calculations to gain new insight into the facet-dependent reactivity behaviour of ceria-based gold catalysts for CO oxidation. In particular, the rods show stronger oxygen dynamics than the cubes regarding peroxide and oxygen defect formation. Furthermore, in contrast to the cubes, the rods can be re-oxidized after reaction conditions.

Conflicts of interest

There are no conflicts to declare.

Acknowledgements

The DFT calculations were conducted on the Lichtenberg high performance computer of the TU Darmstadt. Jochen Rohrer and Karsten Albe are acknowledged for support with the VASP code. We thank Stefan Lauterbach and Hans-Joachim Kleebe for TEM measurements, Martin Brodrecht for BET measurements, and Karl Kopp for technical support as well as for XPS measurements.

References and notes

- M. Haruta, T. Kobayashi, H. Sano and N. Yamada, *Chem. Lett.*, 1987, **16**, 405–408.
- S. Carrettin, P. Concepción, A. Corma, J. M. López Nieto and V. F. Puntes, *Angew. Chem., Int. Ed.*, 2004, **43**, 2538–2540.
- A. Trovarelli and P. Fornasiero, *Catalysis by Ceria and Related Materials*, Imperial College Press, 2013, vol. 12.
- Y. Ren, K. Tang, J. Wei, H. Yang, H. Wei and Y. Yang, *Energy Technol.*, 2018, **6**, 379–390.
- T. Montini, M. Melchionna, M. Monai and P. Fornasiero, *Chem. Rev.*, 2016, **116**, 5987–6041.
- T. Tabakova, F. Boccuzzi, M. Manzoli, J. W. Sobczak, V. Idakiev and D. Andreeva, *Appl. Catal., B*, 2004, **49**, 73–81.
- H. Ha, S. Yoon, K. An and H. Y. Kim, *ACS Catal.*, 2018, **8**, 11491–11501.
- Z. A. Qiao, Z. Wu and S. Dai, *ChemSusChem*, 2013, **6**, 1821–1833.
- M. Ziemba, V. Ganduglia-Pirovano and C. Hess, *Faraday Discuss.*, DOI: 10.1039/C9FD00133F.
- X.-L. Wang, X.-P. Fu, W.-W. Wang, C. Ma, R. Si and C.-J. Jia, *J. Phys. Chem. C*, 2019, **123**, 9001–9012.
- M. Haruta, *Faraday Discuss.*, 2011, **152**, 11.
- M. Flytzani-Stephanopoulos and B. C. Gates, *Annu. Rev. Chem. Biomol. Eng.*, 2012, **3**, 545–574.
- Y.-G. Wang, D. Mei, V.-A. Glezakou, J. Li and R. Rousseau, *Nat. Commun.*, 2015, **6**, 6511.
- J. Wang, H. Tan, S. Yu and K. Zhou, *ACS Catal.*, 2015, **5**, 2873–2881.
- O. Bondarchuk, S. Shaikhutdinov and H.-J. Freund, *J. Phys. Chem. C*, 2019, **123**, 12376–12381.
- J.-C. Liu, Y.-G. Wang and J. Li, *J. Am. Chem. Soc.*, 2017, **139**, 6190–6199.
- M. Nolan, *J. Chem. Phys.*, 2009, **130**, 144702.
- M. Nolan, V. S. Verdugo and H. Metiu, *Surf. Sci.*, 2008, **602**, 2734–2742.
- H. Y. Kim and G. Henkelman, *J. Phys. Chem. Lett.*, 2012, **3**, 2194–2199.
- A. Trovarelli and J. Llorca, *ACS Catal.*, 2017, **7**, 4716–4735.
- M. Nolan, in *Catalysis by Materials with Well-Defined Structures*, Elsevier, 2015, pp. 159–192.
- C. Schilling, M. V. Ganduglia-Pirovano and C. Hess, *J. Phys. Chem. Lett.*, 2018, **9**, 6593–6598.
- Z. Wu, M. Li and S. H. Overbury, *J. Catal.*, 2012, **285**, 61–73.
- M. Nolan, S. C. Parker and G. W. Watson, *Surf. Sci.*, 2006, **600**, 175–178.
- M. Nolan and G. W. Watson, *J. Phys. Chem. B*, 2006, **110**, 16600–16606.
- N. M. Galea, D. O. Scanlon, B. J. Morgan and G. W. Watson, *Mol. Simul.*, 2009, **35**, 577–583.
- H. Y. Kim and G. Henkelman, *J. Phys. Chem. Lett.*, 2013, **4**, 216–221.
- Q. Wu, F. Zhang, P. Xiao, H. Tao, X. Wang, Z. Hu and Y. Lü, *J. Phys. Chem. C*, 2008, **112**, 17076–17080.
- H.-X. Mai, L.-D. Sun, Y.-W. Zhang, R. Si, W. Feng, H.-P. Zhang, H.-C. Liu and C.-H. Yan, *J. Phys. Chem. B*, 2005, **109**, 24380–24385.
- S. Brunauer, P. H. Emmett and E. Teller, *J. Am. Chem. Soc.*, 1938, **60**, 309–319.
- TEM analysis confirms that the morphology and size of the particles does not change during the gold loading and exposure to water-gas shift conditions, which are more drastically than CO oxidation conditions.
- A. Laachir, V. Perrichon, A. Badri, J. Lamotte, E. Catherine, J. C. Lavalley, J. El Fallah, L. Hilaire, F. Le Normand, E. Quéméré, G. N. Sauvion and O. Touret, *J. Chem. Soc., Faraday Trans.*, 1991, **87**, 1601–1609.

- 33 D. A. Shirley, *Phys. Rev. B: Solid State*, 1972, **5**, 4709–4714.
- 34 C. T. Nottbohm and C. Hess, *Catal. Commun.*, 2012, **22**, 39–42.
- 35 C. Schilling and C. Hess, *J. Phys. Chem. C*, 2018, **122**, 2909–2917.
- 36 C. Schilling and C. Hess, *ACS Catal.*, 2019, **9**, 1159–1171.
- 37 C. Schilling, A. Hofmann, C. Hess and M. V. Ganduglia-Pirovano, *J. Phys. Chem. C*, 2017, **121**, 20834–20849.
- 38 S. L. Dudarev, G. A. Botton, S. Y. Savrasov, C. J. Humphreys and A. P. Sutton, *Phys. Rev. B: Condens. Matter Mater. Phys.*, 1998, **57**, 1505–1509.
- 39 J. P. Perdew, K. Burke and M. Ernzerhof, *Phys. Rev. Lett.*, 1996, **77**, 3865–3868.
- 40 H. J. Monkhorst and J. D. Pack, *Phys. Rev. B: Solid State*, 1976, **13**, 5188–5192.
- 41 M. Nolan, *J. Chem. Phys.*, 2012, **136**, 134703.
- 42 A. Chutia, D. J. Willock and C. R. A. Catlow, *Faraday Discuss.*, 2018, **208**, 123–145.
- 43 K.-J. Zhu, Y.-J. Yang, J.-J. Lang, B.-T. Teng, F.-M. Wu, S.-Y. Du and X.-D. Wen, *Appl. Surf. Sci.*, 2016, **387**, 557–568.
- 44 S. Fabris, G. Vicario, G. Balducci, S. De Gironcoli and S. Baroni, *J. Phys. Chem. B*, 2005, **109**, 22860–22867.
- 45 C. Zhang, A. Michaelides and S. J. Jenkins, *Phys. Chem. Chem. Phys.*, 2011, **13**, 22–33.
- 46 M. F. Camellone and S. Fabris, *J. Am. Chem. Soc.*, 2009, **131**, 10473–10483.
- 47 C. Zhang, A. Michaelides, D. A. King and S. J. Jenkins, *J. Phys. Chem. C*, 2009, **113**, 6411–6417.
- 48 J. Moulder, W. Stickle, P. Sobol and K. Bomben, *Handbook of X-ray Photoelectron Spectroscopy*, Physical Electronics, Inc., 1995.
- 49 C. W. M. Castleton, J. Kullgren and K. Hermansson, *J. Chem. Phys.*, 2007, **127**, 244704.
- 50 G. Ranga Rao and H. R. Sahu, *J. Chem. Sci.*, 2001, **113**, 651–658.
- 51 G. C. Allen, M. B. Wood and J. M. Dyke, *J. Inorg. Nucl. Chem.*, 1973, **35**, 2311–2318.
- 52 J. A. Hernández, S. A. Gómez, T. A. Zepeda, J. C. Fierro-González and G. A. Fuentes, *ACS Catal.*, 2015, **5**, 4003–4012.
- 53 A. Bensalem, J. C. Muller and F. Bozon-Verduraz, *J. Chem. Soc., Faraday Trans.*, 1992, **88**, 153–154.
- 54 E. Ruiz-Trejo, *J. Phys. Chem. Solids*, 2013, **74**, 605–610.
- 55 W. Song and E. J. M. Hensen, *J. Phys. Chem. C*, 2013, **117**, 7721–7726.
- 56 V. V. Pushkarev, V. I. Kovalchuk and J. L. D'Itri, *J. Phys. Chem. B*, 2004, **108**, 5341–5348.
- 57 S. Agarwal, L. Lefferts and B. L. Mojet, *ChemCatChem*, 2013, **5**, 479–489.
- 58 C. Wang, X.-K. Gu, H. Yan, Y. Lin, J. Li, D. Liu, W.-X. Li and J. Lu, *ACS Catal.*, 2017, **7**, 887–891.
- 59 C. Yang, X. Yu, S. Heifler, P. G. Weidler, A. Nefedov, Y. Wang, C. Wöll, T. Kropp, J. Paier and J. Sauer, *Angew. Chem., Int. Ed.*, 2017, **56**, 16399–16404.
- 60 Z. V. Popović, Z. Dohčević-Mitrović, M. J. Konstantinović and M. Šćepanović, *J. Raman Spectrosc.*, 2007, **38**, 750–755.
- 61 Z. Dohčević-Mitrović, Z. V. Popović and M. Šćepanović, *Acta Phys. Pol., A*, 2009, **116**, 36–41.
- 62 C. Schilling, M. Ziemba, C. Hess and M. V. Ganduglia-Pirovano, *J. Catal.*, 2020, **383**, 264–272.
- 63 M. Lohrenscheid and C. Hess, *ChemCatChem*, 2016, **8**, 523–526.
- 64 H. Y. Kim, H. M. Lee and G. Henkelman, *J. Am. Chem. Soc.*, 2012, **134**, 1560–1570.
- 65 W. Song and E. J. M. Hensen, *Catal. Sci. Technol.*, 2013, **3**, 3020.
- 66 B. Liu, W. Li, W. Song and J. Liu, *Phys. Chem. Chem. Phys.*, 2018, **20**, 16045–16059.
- 67 M. Huang and S. Fabris, *J. Phys. Chem. C*, 2008, **112**, 8643–8648.
- 68 C. Schilling and C. Hess, *Top. Catal.*, 2017, **60**, 131–140.
- 69 S. Agarwal, L. Lefferts, B. L. Mojet, D. A. J. M. Ligthart, E. J. M. Hensen, D. R. G. Mitchell, W. J. Erasmus, B. G. Anderson, E. J. Olivier, J. H. Neethling and A. K. Datye, *ChemSusChem*, 2013, **6**, 1898–1906.



Elucidating Active CO–Au Species on Au/CeO₂(111): A Combined Modulation Excitation DRIFTS and Density Functional Theory Study

Jakob Weyel¹ · Marc Ziemba¹ · Christian Hess¹

Accepted: 15 February 2022 / Published online: 1 March 2022
© The Author(s) 2022

Abstract

In this work we elucidate the main steps of the CO oxidation mechanism over Au/CeO₂(111), clarifying the course of CO adsorption at a broad variety of surface sites as well as of transmutations of one CO species into another. By combining transient spectroscopy with DFT calculations we provide new evidence that the active centers for CO conversion are single gold atoms. To gain insight into the reaction mechanism, we employ Modulation Excitation (ME) DRIFT spectroscopy in combination with the mathematical tool of Phase Sensitive Detection to identify the active species and perform DFT calculations to facilitate the assignments of the observed bands. The transient nature of the ME-DRIFTS method allows us to sort the observed species temporally, providing further mechanistic insight. Our study highlights the potential of combined transient spectroscopy and theoretical calculations (DFT) to clarify the role of adsorbates observed and to elucidate the reaction mechanism of CO oxidation over supported gold and other noble-metal catalysts.

Keywords Gold-ceria · In situ spectroscopy · Transient spectroscopy · CO oxidation · Modulation excitation spectroscopy (MES) · Phase sensitive detection (PSD) · DRIFTS · DFT

1 Introduction

Ceria, especially in combination with noble metal nanoparticles, is a widely used catalyst for oxidation reactions such as (preferential) CO oxidation or the (reverse) water–gas shift reaction [1–6]. Gold in particular has proven to be a valuable choice for stable and high performing catalyst systems [7–10]. Ceria, chosen as the supporting material in this study, is known to exhibit extensive dynamics in creating and annihilating (oxygen) defects that are of great importance for the proposed Mars-van-Krevelen mechanism of CO oxidation over Au/CeO₂ [5, 6, 11]. Its detailed mechanistic understanding is motivated by the CO oxidation as a prototypical reaction for heterogeneous catalysis [12] but also because of its technical relevance for the three-way catalytic converter [13] as well as its potential usage for CO₂

activation in the context of future carbon capture and usage (CCU) processes [14, 15]. Due to its importance for CO oxidation, this study focuses on the signals and the temporal behavior of CO adsorbates that are readily accessible via DRIFT spectroscopy. The CO spectral region exhibits valuable information concerning the state of adsorbed CO, including its bonding partner, its geometry as well as the surface termination and topology of the adsorption site. These parameters of CO adsorbates, that have also been a topic of one of our previous studies [6] are still under debate in literature [6, 16–23].

Although CO oxidation over supported noble metal catalysts has been investigated for a long time and in numerous studies, a profound understanding of the dynamics of the different CO adsorbate structures has not been achieved to date. To this end, new mechanistic insight may be expected from a combination of transient time-resolved DRIFT spectra with theoretical calculations of possible adsorbate structures such as vibrational frequencies and adsorption energies.

The special DRIFTS approach chosen in this study is depicted in Fig. 1. We use Modulation Excitation Spectroscopy (MES) in combination with data processing via Phase Sensitive Detection (PSD), a technique first introduced by Baurecht and Fringeli in 2001 [24]. Following their publication,

Jakob Weyel and Marc Ziemba have contributed equally.

✉ Christian Hess
christian.hess@tu-darmstadt.de

¹ Eduard-Zintl-Institute of Inorganic and Physical Chemistry, Technical University of Darmstadt, Alarich-Weiss-Str. 8, 64287 Darmstadt, Germany

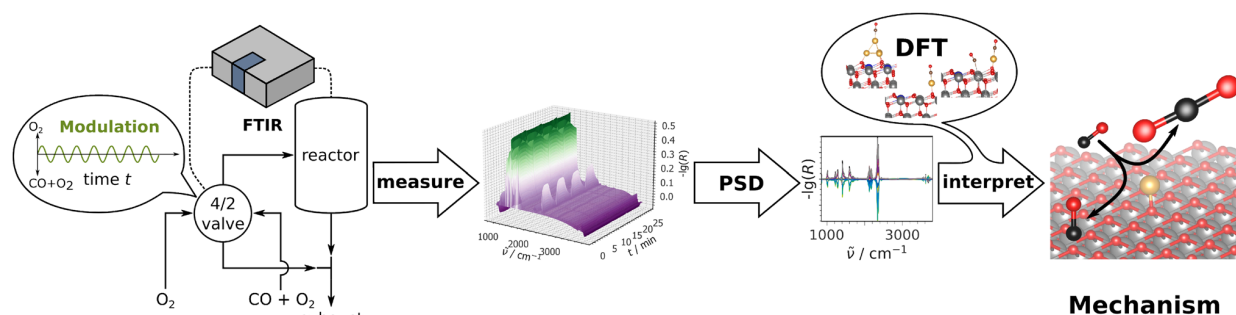


Fig. 1 Scheme of the experimental ME-DRIFTS setup, the data processing of the measured ME into PSD spectra, and the combination of these experimental spectra with DFT results allowing for new mechanistic insights. For details see text

interesting findings were made via the MES-PSD approach, especially in the field of heterogeneous catalysis, shining new light on the mechanistic course of reactions under consideration [25]. In previous studies, ME-DRIFTS was applied to (preferential) CO oxidation over supported catalysts including ceria as well [1, 16, 22, 26, 27].

MES and PSD are used to extract the dynamics from time-resolved spectra during periodic modulation of one process variable (in our case the concentration of one reactant) and to separate it from all time-constant signals (spectator species) as well as from the statistical background noise, thus providing valuable information on active species often hidden in conventional spectra. This is achieved via Fourier transformation of the time-resolved into phase-resolved spectra according to Eq. (1):

$$I(\tilde{\nu}, \varphi) = 2/T \int_{t_0}^{t_c} I(\tilde{\nu}, t) \cdot \sin(\omega t + \varphi) dt \quad (1)$$

with the signal intensity *I*, wavenumber $\tilde{\nu}$, duration of one period *T*, phase shift φ , time *t*, and the modulation frequency ω . After comparing different modulation functions and weighing the advantages and disadvantages, a sinusoidal modulation function was used in this work for reasons of simpler calculability. The DFT approach allows the calculation of IR active vibrational frequencies as well as their respective adsorption energies [6, 28]. As will be illustrated below for Au/CeO₂, the combination of transient ME-DRIFTS with theoretical DFT studies allows to obtain a more profound understanding of the first reaction steps of CO oxidation and especially the crucial CO adsorption processes.

2 Experimental Section

2.1 Catalyst Preparation and Characterization

Preparation and characterisation of the polycrystalline ceria catalyst used in this study was described in our previous work [5, 29, 30]. Summarizing, cerium nitrate hexahydrate (Alfa Aesar, 99.5%) is calcined for 12 h at 600 °C (ramp of 6 °C/min). After being cooled to room temperature, the powder is sieved (200 μm) and calcined a second time according to the protocol mentioned above. Ceria polyhedra were obtained commercially (Sigma Aldrich, < 25 nm (BET)). In both cases, the gold loading was achieved by utilizing electrolyte deposition of a 10⁻³ M HAuCl₄ · 3 H₂O aqueous solution.

As reported previously, the commercial ceria sample exhibits polyhedral particles with a specific surface area of 36 m²g⁻¹, and the sample prepared by decomposition of cerium nitrate consists of ceria sheets with a specific surface area of 57 m²g⁻¹ [4, 31]. Both samples show a CeO₂(111) surface termination, but the sheets additionally possess stepped CeO₂(111) sites [4, 31]. The gold loading was confirmed by ICP-OES, revealing a gold content of 0.31 wt% for the sheets and 0.27 wt% for the polyhedra [31]. Furthermore, our previous study on Au/CeO₂(111) sheets has revealed a large dispersion of gold due to presence of single atoms and/or smaller clusters as probed by the CO-Au vibrations using DRIFTS [6].

2.2 Modulation Excitation (ME) DRIFTS

ME-DRIFTS was performed on a Vertex 70 spectrometer (Bruker) equipped with a liquid nitrogen cooled mercury cadmium telluride (MCT) detector and a commercial reaction cell (Praying Mantis™ High Temperature Reaction Chamber, Harrick Scientific Products) with infrared transparent KBr windows. Please note, that a more detailed description of our basic DRIFTS setup was already given in our previous studies [6, 32], while the additionally needed MES setup (gas pipelines, communication channels, data processing) is schematically depicted in Fig. 1.

For our measurements, 25–35 mg was placed in a stainless steel sample holder (\varnothing : 8 mm; depth: 0.5 mm). Due to the cell geometry and the overflow of the sample, the exact weight of the sample has hardly any influence on the catalytic activity. As background, the catalyst itself was used after 15 min pretreatment in O₂ atmosphere (100 mL min⁻¹ of 10 mol% O₂ in Argon) at the reaction temperature of 37 °C and a subsequent gas phase modulation procedure (identical to the desired experiment), which ensures a reproducible state of the sample. The gas atmosphere during the background measurement consisted of 10 mol% O₂ in Ar (flow rate: 100 mL min⁻¹). For our measurements we used the rapid scan mode extension of the spectrometer software OPUS 7.2. Spectra were measured from 850 to 3800 cm⁻¹ with a resolution of 0.5 cm⁻¹, an aperture of 8 mm and a mirror speed of 40 kHz. A Valco Instruments 4/2 valve (Model E2CA, version ED), communicating with the Vertex 70, is used to rapidly switch the gas flows, which are set via digital mass flow controllers (MFCs, Bronkhorst).

During ME-DRIFTS, the sample is exposed to a feed with constant O₂ content of 10 mol% of the total flow, while a CO flux is pulsed over the sample changing from 0 to 2 mol% (total flow rate: 100 mL/min; residual: Ar), resulting in a conversion of 3.4% for the sheets and of 1.2% for the polyhedra. Switching the valve position initially resulted in a square wave modulation behavior of the CO concentration but due to the residence time behavior of the setup it is better fitted by a sine wave as shown in Fig. 1. These diluted concentrations were chosen to keep the turnover low and to eliminate the influence of possible transport effects.

The following gases are used: CO (99.997%, Westfalen), O₂ (99.999%, Westfalen), and argon (99.996%, Westfalen). One measurement series consisted of 20 periods, with a duration of 374.2 s each. For each spectrum, five consecutive interferograms were averaged, so that one spectrum is acquired approximately every 1.5 s. To estimate potential uncertainties of the via PSD derived time values, the MES experiment on Au/CeO₂ sheets was exemplary executed three times. This resulted in a maximum deviation of time values of 3 s, as determined based on the signal at 2092 cm⁻¹. The other signals discussed show a maximum

deviation of 1 or 2 s (see Table S1). For some signals the determining factor is the time resolution between two successive measurements of 1.5 s, for some it is the maximum deviation (see Table S1).

Intensities and peak positions were checked multiple times and found to be constant for all of the measured datasets.

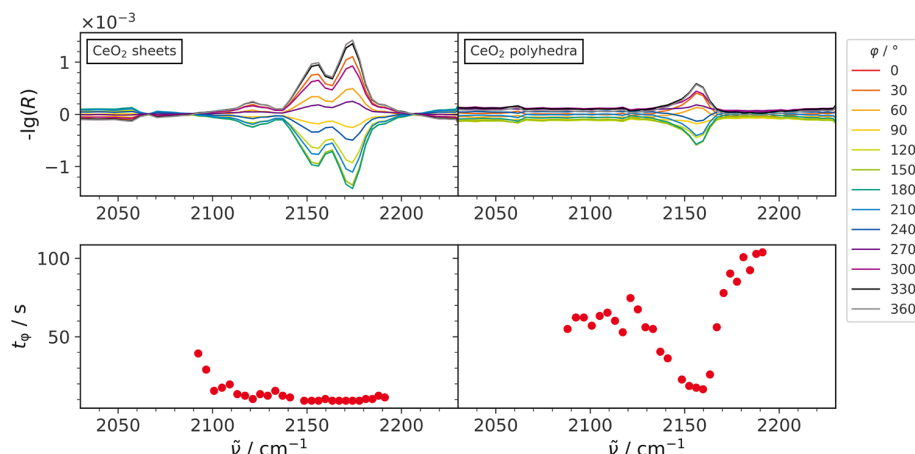
2.3 Density Functional Theory (DFT)

The approach and methods used in this study were described earlier [6, 30]. Briefly, calculations were performed using the spin-polarized DFT + U approach as implemented in the Vienna Ab initio Simulation Package (VASP, Version 5.3.5, <https://www.vasp.at/>), with the generalized gradient approximation of Perdew, Burke and Ernzerhof (PBE) [33] and an U_{eff} parameter of 4.5 eV for the Ce 4f states (PBE + U/4.5 eV). The Ce (4f, 5 s, 5p, 5d, 6 s), O (2 s, 2p), Au (5d, 6 s) and C (2 s, 2p) electrons were explicitly treated as valence states within the projector augmented wave (PAW) method [34] with a plane-wave cutoff of 400 eV, whereas the remaining electrons were treated as part of the atomic cores. The CeO₂(111) surface was modelled by supercells with (3 × 3) periodicities with the calculated ceria bulk equilibrium lattice constant (5.484 Å) [30]. A slab of three trilayers, separated by at least a 10 Å-thick vacuum layer, was used. The slab thickness has been chosen based on the convergence of the calculated surface energy. The sampling of the Brillouin zone is realized by a (2 × 2 × 1) Monkhorst–Pack grid [35]. All atoms in the bottom trilayer were fixed at their optimized bulk-truncated positions during geometry optimization, whereas the rest of the atoms were allowed to fully relax. Total energies and forces were calculated with a precision of 10⁻⁶ eV and 10⁻² eVÅ⁻¹ for electronic and force convergence, respectively. After relaxation a vibrational analysis was performed by calculating the mass-weighted Hessian matrix using density functional perturbation theory (DFPT).

3 Results and Discussion

Although many features of the CO oxidation mechanism over Au catalysts were clarified previously, some important details are still missing, such as processes related to the initial CO adsorption and the subsequent adsorbate rearrangement. To address these processes in detail, we will focus on the CO adsorbate region ranging from 2000 to 2250 cm⁻¹, while other spectral regions (carbonates, hydroxyl groups) will not be considered in this work. For completeness, full PSD spectra as well as time-resolved spectra of the CO region of all samples studied are shown in the Supporting Information (see Figures S1–S4, S6–S9).

Fig. 2 Top: PSD spectra of the CO region of CeO₂ sheets (left) and polyhedra (right) after removal of gas-phase contributions. Bottom: Corresponding time shifts of individual spectral positions



Comparing the spectra of the two bare ceria samples (see top of Fig. 2), it is apparent that the sheets exhibit three signals (2122 cm^{-1} , 2156 cm^{-1} and 2171 cm^{-1}), but the polyhedra only one signal at 2156 cm^{-1} . The latter is assigned to CO adsorbed onto the ideal CeO₂(111) surface [19, 20, 36]. The band located at higher wavenumbers, i.e. at 2171 cm^{-1} , indicates a stronger interaction of CO with the surface, and can therefore be attributed to CO adsorbed on reduced CeO₂(111), in agreement with the literature [18, 36]. The location of the band at 2122 cm^{-1} is fully consistent with Ce³⁺ related electronic transitions [17, 37].

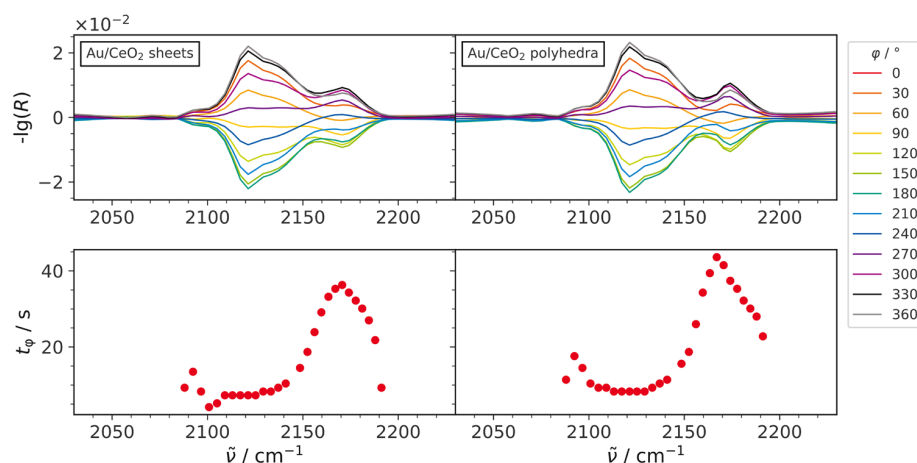
Although both ceria samples show a (111) termination, the sheets exhibit additional steps (see above), which have been shown to have a positive influence on the reduction behavior [31]. Thus the sheets possess more oxygen defects than the polyhedra, which is clearly reflected in the vibrational signature of the CO region.

In addition to the spectral position of each signal, MES-PSD is furthermore able to provide information on each signal's transient behavior via time values, which indicate the appearance of each signal relative to the others within the external modulation period. The time values shown at the bottom of Fig. 2 indicate differences between the bare ceria samples. In fact, in case of the sheets, signals appear within 11–15 s after turning on the reaction gas atmosphere, whereas for lower wavenumbers on the border of the sampled region, where no bands can be seen, a steep increase of the time values is visible. For the polyhedral-related band a time shift of about 13–20 s is detected. Again, outside the region of this feature, time values steeply increase up to roughly 70 s for wavenumbers lower than 2156 cm^{-1} and 100 s for wavenumbers higher than that. This increase can be related to a transition from the CO adsorbate signal to the background surrounding it, as can be seen in Figure S5 but will not be further addressed here as the background holds no useful information. The time values of the signal at 2156 cm^{-1} appear at 11 s for the sheets and at 15 s for the

polyhedra, respectively. Please note that these values contain an experimental uncertainty of 1.5 s due to the rate of spectra measurement (for details see Experimental) as well as a maximum deviation between different measurements of 1 s (see Table S1). Thus the observed difference of the time values of the 2156 cm^{-1} signal for ceria sheets and polyhedra appears significant; it may originate from the fact that the surrounding of a signal has an influence on these time values. The observed deviation for the same species on sheets and polyhedra might also be due to the fact that the surrounding of a signal has an influence on these time values. In case of ceria sheets, the signal is surrounded by other peaks exhibiting about the same time shift. In case of polyhedra, the signal stands alone and is weaker compared to the sheets. This weakness is expected to be partly due to the lower surface area and thus a lower number of possible adsorption sites. However, since the gold-loaded samples (see Fig. 3) show almost the same intensity at the same surface areas as the bare ceria samples, it becomes apparent that there is also a contribution from other effects, e.g. particle shape and degree of reduction. Via an overlap, the neighboring signals or even the background might influence the regarded signal according to the relative intensity of it and the overlapping contribution, thus a mixing of time values occurs, as has been already described elsewhere [38]. Therefore it might as well be the case that these overlap effects lead to different time values of the same species on ceria sheets and polyhedra. Nevertheless, these discrepancies neither affect the interpretations made here nor the mechanistic discussion of the results at the end.

The top of Fig. 3 depicts the PSD spectra of gold-loaded ceria sheets (left) and polyhedra (right). For both samples, the spectra show a similar vibrational profile and are dominated by signals at about 2122 cm^{-1} and 2171 cm^{-1} . The first signal corresponds to CO adsorbed onto a gold cluster, the second to CO adsorbed onto bare ceria, as discussed previously [6]. The signal at around 2171 cm^{-1}

Fig. 3 Top PSD spectra of the CO region of Au/CeO₂ sheets (left) and Au/CeO₂ polyhedra (right) after removal of gas-phase contributions. Bottom Corresponding time shifts of individual spectral positions



shows a slight asymmetry towards lower wavenumbers, which is less pronounced for the polyhedra than for the sheets. Vice versa the polyhedra samples exhibit a small asymmetry towards higher wavenumbers leading to a shift of the signal's maximum to 2174 cm^{-1} . A comparison to the spectra of the bare ceria samples in Fig. 2 shows, that the dominant CO-related band at about 2156 cm^{-1} appears to be blueshifted to 2171 cm^{-1} for the gold-loaded samples. In agreement with previous studies, this behavior is attributed to the increased number of defects formed in the presence of gold, and consistent with the observation of the 2171 cm^{-1} band on the bare ceria sheets (see above) [39]. In this context, our previous studies at the same gas concentrations also revealed the presence of defects on the Au/sheets by means of *operando* Raman and UV-Vis spectroscopy [5]. Furthermore, both spectra show a broad contribution at about 2133 cm^{-1} and a small foothill at about 2092 cm^{-1} . Please note that a significant contribution of electronic transitions of reduced ceria, which may be expected in the region at around 2125 cm^{-1} [17], can be excluded for the gold-loaded samples based on previous isotope experiments [6].

Interestingly, the time values of the gold-loaded catalysts, exhibit significant differences to the bare ceria samples. In fact, as can be seen at the bottom of Fig. 3 the CO@CeO₂ signals at around 2171 cm^{-1} exhibit a time shift of 30–40 s, compared to 10–20 s for bare ceria. The CO-Au@CeO₂ signals on the other hand show time shifts of about 5–10 s that are nearly the same for both gold-loaded sheets and polyhedra. The increased time value of the CO@CeO₂ signals in the presence of gold may be rationalized by a different type of adsorption (see below). This is supported by the observed increase in intensity by a factor of about 10 when gold is added, suggesting that there is another mechanism at work that overshadows simple adsorption from the gas phase. A possible scenario may be based on a spillover of unreacted CO from gold particles to the ceria surface, comparable to

the CO₂ formation mechanism proposed in the literature [2, 40].

According to previous studies, charge and coordination of gold have a major influence on the CO adsorption energy on Au/CeO₂ systems [41–43]. It is therefore conceivable that larger gold clusters lead to a spillover of CO to the surface, because in this case adsorption on the support may be preferred [36, 43]. On the other hand, studies show that Au single sites are also formed dynamically from larger gold clusters under reaction conditions, therefore being referred to as pseudo-single sites [11, 41]. To this end, based on DFT calculations the adsorption of CO onto such a gold single or pseudo-single site ($E_{\text{ads,CO}}(\text{Au}_1) = -2.58$ eV) instead of ceria ($E_{\text{ads,CO}}(\text{CeO}_2) = -0.19$ eV) [6] is energetically much more attractive [6, 40], thus a spillover seems energetically unfavorable at first, where the adsorption energies are consistent with previous studies [20, 44]. However, it is conceivable that CO adsorbed on gold may orient itself towards the ceria surface and be displaced by a second CO from the gas phase. This assumption is supported by our DFT calculations shown in the second structure in Fig. 4 (replaced single site) confirming (i) the displacement of CO previously adsorbed at a gold single site by another CO molecule from the gas phase and (ii) its relocation and migration onto the ceria surface ($E_{\text{ads, repl.CO}}(\text{CeO}_2) = -0.106$ eV).

This ensemble of two CO adsorbates, one adsorbed onto a single gold atom, the other to the adjacent ceria surface, is characterized by two vibrational frequencies at 2083 and 2096 cm^{-1} (see Fig. 4). These two frequencies cannot be easily separated because vibrational analysis yields primarily two stretching modes involving both CO molecules. One where both CO bonds oscillate in phase and one where they oscillate in opposing phases. This is indicative for dipolar interactions, as described in the literature [45–49].

A further distribution of CO molecules located at the gold-ceria interface is expected, since CO has a more favorable binding energy of -0.19 eV on the bare ceria support.

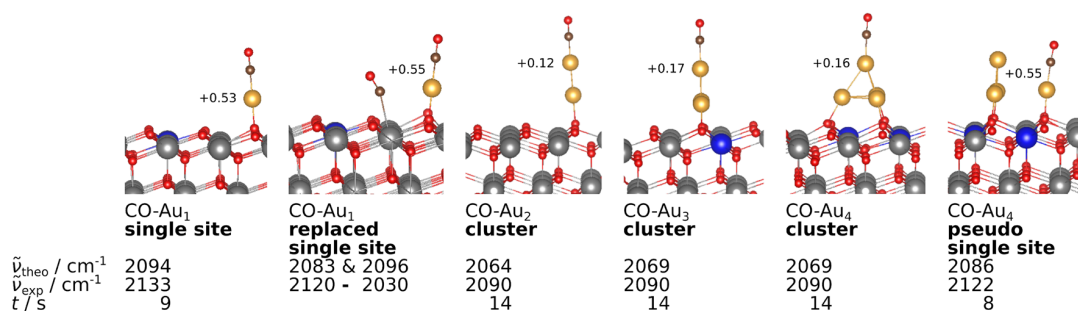


Fig. 4 Top: Most stable structures for CO adsorbed on Au₁₋₄/CeO₂(111) structures from DFT together with the Bader charges (ΔQ , in $|e|$) of the gold atom in direct contact with CO. Bottom: Cal-

culated and experimental vibrational frequencies of adsorbed CO, as well as the corresponding time values for ceria sheets derived from PSD calculations

This additional step offers an explanation for the considerably later appearance of the CO@CeO₂ signals when gold is involved. Hence, based on the observed time-shifts of the CO@CeO₂ signals, the following mechanism for CO adsorption on Au/CeO₂ may be proposed: (i) CO adsorption onto gold, (ii) subsequent spillover and/or displacement by gaseous CO, and (iii) CO movement away from the gold-ceria interface, leading to its dispersion on the carrier. Because of the easier adsorption of CO to gold than to CeO₂, such a spillover/displacement mechanism may largely facilitate the surface loading with CO molecules, thus accelerating the CO adsorption process. Such a scenario is supported by the signal intensity for the bands at 2156 and 2171 cm⁻¹, which is roughly ten times higher for the gold loaded than for the bare ceria samples (see Figs. 2 and 3).

The signal of gaseous CO₂ (not shown here) appears after ~20 s (maximum intensity) for the sheets and ~21 s for the polyhedra. As CO₂ formation occurs significantly before the appearance of the intense CO@CeO₂ signals, it stands to reason that product formation is independent of the postulated spillover/displacement processes. Nonetheless, a simultaneous accumulation of CO on ceria sites might still be possible, but due to the expected low intensities for such a species (compare the intensities in Figs. 2 and 3) their signals might either be very weak or completely absent. Based on this fact and the spillover/displacement processes, we may now exclude CO adsorbed on ceria to be active even if it shows an increased intensity in the PSD spectra when gold is present (see Fig. 3). This is in accordance with the literature, where the inactivity of bare ceria at the chosen reaction temperature has been clearly evidenced [5]. Thus CO adsorption on gold appears to be strictly necessary for catalytic activity.

Looking more closely at the spectral region attributed to CO adsorbed on gold, the vibrational profile surrounding the signal at around 2122 cm⁻¹ in Fig. 3 clearly indicates several contributions. These may be rationalized by different CO-Au species existing on the surface, ranging from

CO adsorbed on a single gold atom (single site), which is considered to be the most active species [6], up to larger gold clusters consisting of multiple atoms. To illustrate the effect of cluster size, the vibrational frequencies and the respective adsorption energies of several model structures of CO on gold (Au₁ to Au₄) were calculated using DFT (see Fig. 4). The structures for Au₂ and Au₃ were taken from Ghosh et al. [40], whereas Au₁ and Au₄ were part of our previous studies [6].

According to literature, the signals at 2122 cm⁻¹ and 2133 cm⁻¹ can be assigned to CO adsorbed to gold single sites: the signal at 2133 cm⁻¹ was often associated to CO on a single gold atom on the surface [6], while the one at 2122 cm⁻¹ is assigned to CO on a so called pseudo-single site, where one gold atom is slightly removed from a larger cluster, thus forming the CO adsorption site [6]. The single sites might as well be formed by such a dynamic process as there has been evidence, that completely isolated gold atoms tend to block the adsorption of CO, due to a negatively charged Au atom [11, 40]. Thus in the following we will refer to these sites as pseudo-single sites. The dynamic formation of pseudo-single sites has been demonstrated by earlier theoretical studies [6, 11]. CO on larger gold particles gives rise to a small shoulder at 2092 cm⁻¹ (see Fig. 3). According to our DFT calculations, it seems to be irrelevant whether the cluster comprises two, three or four atoms. This is illustrated in Fig. 4, showing quite similar vibrational frequencies of 2064 and 2069 cm⁻¹ for different cluster sizes. This underlines the impact of the charge of the gold atom on which the CO is located on the vibrational frequency, since this is lower for the latter structures. Continuing this thought, further contributions to this signal cannot be ruled out completely, as there may be contributions due to charge transfer from vacancies (formed during reaction) to gold clusters, changing the bond strength of adsorbed CO there. Computational evidence for such a bond weakening has been given by Ghosh et al. [40]. Experiments by Manzoli et al. provide

Fig. 5 Proposed mechanisms for **a** CO₂ formation on an exemplary gold (pseudo-) single site not showing the rest of the larger gold cluster and **b** CO spillover, leading to the formation of CO@CeO₂ species. For details see text

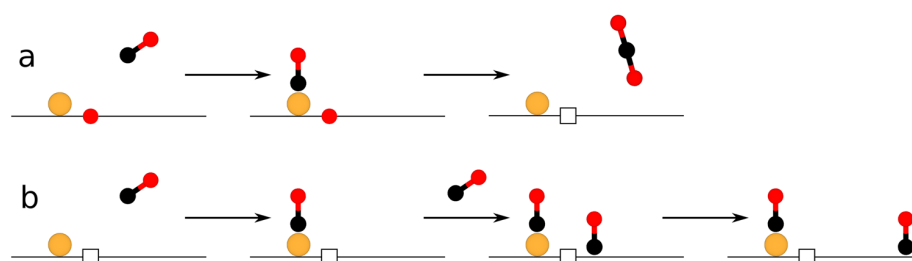


Table 1 Observed signals and their time values for gold-loaded and bare ceria sheets and polyhedra (in brackets)

$\tilde{\nu}/\text{cm}^{-1}$	$t(\text{Au}/\text{CeO}_2)/\text{s}$	$t(\text{CeO}_2)/\text{s}$	Assignment
2092	14 (18)	– (–)	CO-Au _n cluster
2122	8 (9)	– (–)	CO-Au pseudo-single site
2122	– (–)	12 (–)	Ce ³⁺ electr. transition
2133	9 (10)	– (–)	CO-Au pseudo-single site
2156	24 (26)	11 (15)	CO@CeO _{2, ideal}
2171	34 (39)	10 (–)	CO@CeO _{2, reduced}
2359	20 (21)	– (–)	CO ₂

experimental indications of red-shifted CO adsorbate signals on reduced gold-ceria catalysts during CO oxidation in the regarded spectral region [21].

Combining the above results on peak positions and signal intensities as well as the respective times extracted via PSD, a mechanistic picture of the first steps of CO oxidation on Au/CeO₂ can be drawn (see Fig. 5). Table 1 summarizes the relevant species and their assignment for sheets and polyhedra samples.

From Table 1 it is apparent, that the adsorption mechanism follows the same path for sheets and polyhedra. Thus, both samples will be discussed together in the following. A visual representation of our findings is shown in Fig. 5. First the adsorption of CO on pseudo-single gold sites occurs (7–10 s), giving rise to signals at 2133 and 2122 cm⁻¹, respectively. Conversion of these CO molecules seems to be the main reaction route towards CO₂. Next, the signal at 2092 cm⁻¹ is detected, which is associated with CO on larger gold clusters and/or their CO adsorption dynamics due to the reduction state of the surface (~ 14 s for sheets, ~ 15 s for polyhedra). Due to its low intensity in PSD spectra it is unlikely that these CO molecules play a major role in the reaction. The fact that this feature shows at least some intensity may be attributed to (limited) dynamics of adsorption and desorption when changing the gas atmosphere.

The next signal observed corresponds to gas phase CO₂, the product of the reaction, which is formed at 20 s for sheets and 21 s for polyhedra. The proposed mechanism for CO₂ formation is shown in Fig. 5a. Briefly summarized, it consists of (i) CO adsorption onto an active gold site,

and (ii) formation and dissociation of CO₂ via a proposed O_{lattice}-Au⁺-CO species [6, 11, 40, 50].

After this, the signals of CO on bare ceria are detected. Among these, first the signal of CO on the ideal surface appears at 24 (sheets) or 26 s (polyhedra), and then the signal of CO on the reduced surface at 34 (sheets) or 39 s (polyhedra). As discussed above, the late appearance of these signals indicates that they are not involved in the reaction mechanism but emerge due to a spillover/displacement mechanism, distributing unreacted CO adsorbed on gold particles to the surrounding ceria, as depicted in Fig. 5b. This spillover/displacement process may occur instead of a reaction because of a possible depletion of the CeO₂ surface of oxygen needed for CO oxidation. This depletion is indicated by the dominant CO@CeO₂ signal at 2171 cm⁻¹ which is assigned to a reduced surface. While being unreactive on the ceria surface, after spillover/displacement, the CO molecules may resemble those on bare ceria sheets (see Fig. 2) and exhibit adsorption–desorption dynamics upon exposure to changing gas atmospheres, thus explaining their intensity in PSD spectra.

4 Conclusion

Summarizing this work, we were able to further elucidate the reaction pathway of the CO oxidation, a prototype reaction in heterogeneous catalysis, using gold-loaded ceria catalysts as a showcase. We chose Modulation Excitation (ME) DRIFT Spectroscopy, which enables detailed analysis of the adsorbates as well as the adsorption and reaction process, focusing on CO and CO₂ signals. In combination with Phase Sensitive Detection (PSD), our transient experiments provide new information on the active species and their temporal order. Combining this experimental data with findings from DFT (structures, vibrational frequencies), allowed us to clarify the reaction sequence of CO adsorption and reaction on Au/CeO₂ catalysts.

Our results confirm the activity of dynamically formed pseudo-single sites. Furthermore, we show that CO adsorbed onto larger clusters of more than two gold atoms as well as CO adsorbed onto ceria is not involved in the reaction mechanism. CO on larger clusters is excluded as active species

due to its low intensity in PSD spectra. CO adsorbed to the ceria support, showed high intensity signals in PSD spectra. However, its participation in the reaction was excluded due to its late appearance in the mechanism, i.e., after that of the product CO₂. Based on a comparison with bare ceria, its signal intensity is rationalized by a spillover/displacement mechanism of unreacted CO from gold to the reduced and oxygen-depleted ceria surface.

Finally, our approach clearly demonstrates that the combination of transient spectroscopic techniques, such as ME-DRIFTS, with DFT calculations can greatly enhance our understanding of reaction mechanisms in heterogeneous catalysis.

Supplementary Information The online version contains supplementary material available at <https://doi.org/10.1007/s11244-022-01599-1>.

Acknowledgements We thank M. Verónica Ganduglia-Pirovano for fruitful discussions, and Karl Kopp for technical support. Calculations for this research were conducted on the Lichtenberg high performance computer of the TU Darmstadt. Jakob Weyel gratefully acknowledges a scholarship from the Fonds der Chemischen Industrie im Verband der Chemischen Industrie e.V.

Authors contributions All authors contributed to the conception and design of the study. Experiments were performed by Jakob Weyel, DFT calculations by Marc Ziemba. The first draft of the manuscript was written by Jakob Weyel. All authors commented and edited the first and following versions of the manuscript. All authors read and approved the final manuscript. Christian Hess was responsible for supervision and funding acquisition.

Funding Open Access funding enabled and organized by Projekt DEAL. Jakob Weyel gratefully acknowledges a scholarship from the Fonds der Chemischen Industrie im Verband der Chemischen Industrie e.V.

Code availability The software used for calculation of PSD spectra is available at https://github.com/Ja-We/Phase_Sensitive_Detection_for_Spectroscopy.

Declarations

Conflict of interest The authors do not have conflict of interest to declare.

Open Access This article is licensed under a Creative Commons Attribution 4.0 International License, which permits use, sharing, adaptation, distribution and reproduction in any medium or format, as long as you give appropriate credit to the original author(s) and the source, provide a link to the Creative Commons licence, and indicate if changes were made. The images or other third party material in this article are included in the article's Creative Commons licence, unless indicated otherwise in a credit line to the material. If material is not included in the article's Creative Commons licence and your intended use is not permitted by statutory regulation or exceeds the permitted use, you will need to obtain permission directly from the copyright holder. To view a copy of this licence, visit <http://creativecommons.org/licenses/by/4.0/>.

References

- Kydd R, Ferri D, Hug P et al (2011) Temperature-induced evolution of reaction sites and mechanisms during preferential oxidation of CO. *J Catal* 277:64–71. <https://doi.org/10.1016/j.jcat.2010.10.009>
- Wang LC, Widmann D, Behm RJ (2015) Reactive removal of surface oxygen by H₂, CO and CO/H₂ on a Au/CeO₂ catalyst and its relevance to the preferential CO oxidation (PROX) and reverse water gas shift (RWGS) reaction. *Catal Sci Technol* 5:925–941. <https://doi.org/10.1039/C4CY01030B>
- Meunier FC, Tibiletti D, Goguet A et al (2005) On the reactivity of carbonate species on a Pt/CeO₂ catalyst under various reaction atmospheres: application of the isotopic exchange technique. *Appl Catal A Gen* 289:104–112
- Schilling C, Hess C (2019) Elucidating the role of support oxygen in the water-gas shift reaction over ceria-supported gold catalysts using operando spectroscopy. *ACS Catal* 9:1159–1171. <https://doi.org/10.1021/acscatal.8b04536>
- Schilling C, Hess C (2018) Real-time observation of the defect dynamics in working Au/CeO₂ catalysts by combined operando Raman/UV–vis spectroscopy. *J Phys Chem C* 122:2909–2917. <https://doi.org/10.1021/acs.jpcc.8b00027>
- Schilling C, Ziemba M, Hess C, Ganduglia-Pirovano MV (2020) Identification of single-atom active sites in CO oxidation over oxide-supported Au catalysts. *J Catal* 383:264–272. <https://doi.org/10.1016/j.jcat.2020.01.022>
- Haruta M (2003) When gold is not noble: catalysis by nanoparticles. *Chem Rec* 3:75–87. <https://doi.org/10.1002/tcr.10053>
- Haruta M (2002) Catalysis of gold nanoparticles deposited on metal oxides. *CATTECH* 6:102–115. <https://doi.org/10.1023/A:1020181423055>
- Bond GC (2002) Gold: a relatively new catalyst. *Catal Today* 72:5–9. [https://doi.org/10.1016/S0920-5861\(01\)00522-3](https://doi.org/10.1016/S0920-5861(01)00522-3)
- Hutchings GJ (2018) Heterogeneous gold catalysis. *ACS Cent Sci* 4:1095–1101. <https://doi.org/10.1021/acscentsci.8b00306>
- Wang Y-G, Mei D, Glezakou V-A et al (2015) Dynamic formation of single-atom catalytic active sites on ceria-supported gold nanoparticles. *Nat Commun* 6:6511. <https://doi.org/10.1038/ncomms7511>
- Freund H-J, Meijer G, Scheffler M et al (2011) CO oxidation as a prototypical reaction for heterogeneous processes. *Angew Chemie Int Ed* 50:10064–10094. <https://doi.org/10.1002/anie.201101378>
- Diwell AF, Rajaram RR, Shaw HA, Truex TJ (1991) The role of ceria in three-way catalysts. *Stud Surf Sci Catal* 71:139–152. [https://doi.org/10.1016/S0167-2991\(08\)62975-4](https://doi.org/10.1016/S0167-2991(08)62975-4)
- Rezvani A, Abdel-Mageed AM, Ishida T et al (2020) CO₂ Reduction to methanol on Au/CeO₂ catalysts: mechanistic insights from activation/deactivation and SSITKA measurements. *ACS Catal* 10:3580–3594. <https://doi.org/10.1021/acscatal.9b04655>
- Vovchok D, Zhang C, Hwang S et al (2020) Deciphering dynamic structural and mechanistic complexity in Cu/CeO₂/ZSM-5 catalysts for the reverse water-gas shift reaction. *ACS Catal* 10:10216–10228. <https://doi.org/10.1021/acscatal.0c01584>
- Fernández-García S, Collins SE, Tinoco M et al (2019) Influence of 111 nanofaceting on the dynamics of CO adsorption and oxidation over Au supported on CeO₂ nanocubes: an operando DRIFT insight. *Catal Today* 336:90–98. <https://doi.org/10.1016/j.cattod.2019.01.078>
- Daly H, Ni J, Thompsett D, Meunier F (2008) On the usefulness of carbon isotopic exchange for the operando analysis of metal–carbonyl bands by IR over ceria-containing catalysts. *J Catal* 254:238–243. <https://doi.org/10.1016/j.jcat.2007.12.013>

18. Yang C, Yu X, Heibler S et al (2017) Surface faceting and reconstruction of ceria nanoparticles. *Angew Chemie Int Ed* 56:375–379. <https://doi.org/10.1002/anie.201609179>
19. Wöll C (2020) Structure and chemical properties of oxide nanoparticles determined by surface-ligand IR spectroscopy. *ACS Catal* 10:168–176. <https://doi.org/10.1021/acscatal.9b04016>
20. Lustemberg PG, Plessow PN, Wang Y et al (2020) Vibrational frequencies of cerium-oxide-bound CO: a challenge for conventional DFT methods. *Phys Rev Lett* 125:256101. <https://doi.org/10.1103/PhysRevLett.125.256101>
21. Manzoli M, Boccuzzi F, Chiorino A et al (2007) Spectroscopic features and reactivity of CO adsorbed on different Au/CeO₂ catalysts. *J Catal* 245:308–315. <https://doi.org/10.1016/j.jcat.2006.10.021>
22. del Río E, Collins SE, Aguirre A et al (2014) Reversible deactivation of a Au/Ce_{0.62}Zr_{0.38}O₂ catalyst in CO oxidation: a systematic study of CO₂-triggered carbonate inhibition. *J Catal* 316:210–218. <https://doi.org/10.1016/j.jcat.2014.05.016>
23. Song W, Hensen EJM (2013) A computational DFT study of CO oxidation on a Au nanorod supported on CeO₂(110): on the role of the support termination. *Catal Sci Technol* 3:3020. <https://doi.org/10.1039/c3cy00319a>
24. Baurecht D, Fringeli UP (2001) Quantitative modulated excitation Fourier transform infrared spectroscopy. *Rev Sci Instrum* 72:3782–3792. <https://doi.org/10.1063/1.1400152>
25. Müller P, Hermans I (2017) Applications of modulation excitation spectroscopy in heterogeneous catalysis. *Ind Eng Chem Res* 56:1123–1136. <https://doi.org/10.1021/acs.iecr.6b04855>
26. Aguirre A, Barrios CE, Aguilar-Tapia A et al (2016) In-Situ DRIFT study of Au–Ir/ceria catalysts: activity and stability for CO oxidation. *Top Catal* 59:347–356. <https://doi.org/10.1007/s11244-015-0425-6>
27. Aguirre A, Zanella R, Barrios C et al (2019) Gold stabilized with iridium on ceria-niobia catalyst: activity and stability for CO oxidation. *Top Catal* 62:977–988. <https://doi.org/10.1007/s11244-019-01185-y>
28. Ziemba M, Hess C (2020) Influence of gold on the reactivity behaviour of ceria nanorods in CO oxidation: combining operando spectroscopies and DFT calculations. *Catal Sci Technol* 10:3720–3730. <https://doi.org/10.1039/D0CY00392A>
29. Schilling C, Ganduglia-Pirovano MV, Hess C (2018) Experimental and theoretical study on the nature of adsorbed oxygen species on shaped ceria nanoparticles. *J Phys Chem Lett* 9:6593–6598. <https://doi.org/10.1021/acs.jpcc.8b02728>
30. Schilling C, Hofmann A, Hess C, Ganduglia-Pirovano MV (2017) Raman spectra of polycrystalline CeO₂: a density functional theory study. *J Phys Chem C* 121:20834–20849. <https://doi.org/10.1021/acs.jpcc.7b06643>
31. Ziemba M, Weyel J, Hess C (2022) Elucidating the mechanism of the reverse water–gas shift reaction over Au/CeO₂ catalysts using operando and transient spectroscopies. *Appl Catal B Environ* 301:120825. <https://doi.org/10.1016/j.apcatb.2021.120825>
32. Schilling C, Hess C (2017) CO oxidation on ceria supported gold catalysts studied by combined operando raman/UV–Vis and IR spectroscopy. *Top Catal* 60:131–140. <https://doi.org/10.1007/s11244-016-0732-6>
33. Perdew JP, Burke K, Ernzerhof M (1996) Generalized gradient approximation made simple. *Phys Rev Lett* 77:3865–3868. <https://doi.org/10.1103/PhysRevLett.77.3865>
34. Blöchl PE (1994) Projector augmented-wave method. *Phys Rev B* 50:17953–17979. <https://doi.org/10.1103/PhysRevB.50.17953>
35. Monkhorst HJ, Pack JD (1976) Special points for Brillouin-zone integrations. *Phys Rev B* 13:5188–5192. <https://doi.org/10.1103/PhysRevB.13.5188>
36. Yang C, Yin LL, Bebensee F et al (2014) Chemical activity of oxygen vacancies on ceria: a combined experimental and theoretical study on CeO₂(111). *Phys Chem Chem Phys* 16:24165–24168. <https://doi.org/10.1039/c4cp02372b>
37. Bozon-Verduraz F, Bensalem A (1994) IR studies of cerium dioxide: influence of impurities and defects. *J Chem Soc Faraday Trans* 90:653. <https://doi.org/10.1039/ft9949000653>
38. Hemmingsson F, Schaefer A, Skoglundh M, Carlsson P-A (2020) CO₂ methanation over Rh/CeO₂ studied with infrared modulation excitation spectroscopy and phase sensitive detection. *Catalysts* 10:601. <https://doi.org/10.3390/catal10060601>
39. Ziemba M, Ganduglia-Pirovano MV, Hess C (2021) Insight into the mechanism of the water–gas shift reaction over Au/CeO₂ catalysts using combined operando spectroscopies. *Faraday Discuss* 229:232–250. <https://doi.org/10.1039/C9FD00133F>
40. Ghosh P, Farnesi Camellone M, Fabris S (2013) Fluxionality of Au clusters at ceria surfaces during CO oxidation: relationships among reactivity, size, cohesion, and surface defects from DFT simulations. *J Phys Chem Lett* 4:2256–2263. <https://doi.org/10.1021/jz4009079>
41. Liu J-C, Wang Y-G, Li J (2017) Toward rational design of oxide-supported single-atom catalysts: atomic dispersion of gold on ceria. *J Am Chem Soc* 139:6190–6199. <https://doi.org/10.1021/jacs.7b01602>
42. Liu Y, Li H, Yu J et al (2015) Electronic storage capacity of ceria: role of peroxide in Aux supported on CeO₂(111) facet and CO adsorption. *Phys Chem Chem Phys* 17:27758–27768. <https://doi.org/10.1039/c5cp03394b>
43. Han Z-K, Gao Y (2015) A 2D–3D structure transition of gold clusters on CeO_{2-x}(111) surfaces and its influence on CO and O₂ adsorption: a comprehensive DFT + U investigation. *Nanoscale* 7:308–316. <https://doi.org/10.1039/C4NR03346A>
44. Thang HV, Maleki F, Tosoni S, Pacchioni G (2021) Vibrational properties of CO adsorbed on a single atom catalysts on TiO₂(101), ZrO₂(101), CeO₂(111), and LaFeO₃(001) surfaces: a DFT study. *Top Catal* 1:3. <https://doi.org/10.1007/s11244-021-01514-0>
45. Penschke C, Paier J, Sauer J (2013) Oligomeric vanadium oxide species supported on the CeO₂(111) surface: structure and reactivity studied by density functional theory. *J Phys Chem C* 117:5274–5285. <https://doi.org/10.1021/jp400520j>
46. Penschke C, Paier J, Sauer J (2018) Vanadium oxide oligomers and ordered monolayers supported on CeO₂(111): structure and stability studied by density functional theory. *J Phys Chem C* 122:9101–9110. <https://doi.org/10.1021/acs.jpcc.8b01998>
47. Crossley King AD (1980) Adsorbate island dimensions and interaction energies from vibrational spectra: CO on Pt{001} and Pt{111}. *Surf Sci* 95:131–155. [https://doi.org/10.1016/0039-6028\(80\)90132-6](https://doi.org/10.1016/0039-6028(80)90132-6)
48. González SR, Aymonino PJ, Piro OE (1984) Spectroscopic evidence of vibrational dipole–dipole coupling between nitrosyl groups in some nitroprussides. *J Chem Phys* 81:625–628. <https://doi.org/10.1063/1.447735>
49. Hollins P (1985) Influence of dipole coupling on the infrared spectra of adsorbed species and its significance for the interpretation of transmission spectra from supported metal catalysts. *Adsorpt Sci Technol* 2:177–193. <https://doi.org/10.1177/026361748500200304>
50. Camellone MF, Fabris S (2009) Reaction mechanisms for the CO oxidation on Au/CeO₂ catalysts: activity of substitutional Au³⁺/Au⁺ cations and deactivation of supported Au⁺ adatoms. *J Am Chem Soc* 131:10473–10483. <https://doi.org/10.1021/ja902109k>

Publisher's Note Springer Nature remains neutral with regard to jurisdictional claims in published maps and institutional affiliations.

Insight into the mechanism of the water–gas shift reaction over Au/CeO₂ catalysts using combined *operando* spectroscopies†

Marc Ziemba, ^a M. Verónica Ganduglia-Pirovano ^b
and Christian Hess ^{*a}

Received 9th December 2019, Accepted 22nd January 2020

DOI: 10.1039/c9fd00133f

The mechanism of the low-temperature water–gas shift (LT-WGS) reaction over Au/CeO₂ catalysts with different ceria terminations, *i.e.*, (111), (110), and (100) facets, was investigated. Using combined *operando* Raman and UV-Vis spectroscopy as well as isotope exchange experiments, we are able to draw conclusions about the reducibility behaviour and the exchange of surface oxygen. Additional density functional theory (DFT) calculations facilitate the vibrational bands assignments and enhance the interpretation of the results on a molecular level. A facet-dependent role of gold is observed with respect to the oxygen dynamics, since for the CeO₂(111) facet the presence of gold is required to exchange surface oxygen, whereas the CeO₂(110) facet requires no gold, as rationalized by the low defect formation energy of this facet. This behaviour suggests that surface properties (termination, stepped surface) may have a strong effect on the reactivity. While the reduction of the support accompanies the reaction, its extent does not directly correlate with activity, highlighting the importance of other properties, such as the dissociative adsorption of water and/or CO₂/H₂ desorption. The results of our facet-dependent study are consistent with a redox mechanism, as underlined by H₂¹⁸O isotopic exchange experiments demonstrating the ready exchange of surface oxygen.

Introduction

Supported-metal (Au, Pt) ceria-based catalysts have been considered as promising candidates for the low-temperature water–gas shift (LT-WGS) reaction,^{1–4} which is important for steam reforming to increase the amount of hydrogen and reduce that of carbon monoxide.⁵ Furthermore, this reaction is of practical importance in fuel cell applications.^{6,7} In this context, the influence of the support properties on

^aEduard-Zintl-Institut für Anorganische und Physikalische Chemie, Technische Universität Darmstadt, Alarich-Weiss-Str. 8, 64287 Darmstadt, Germany. E-mail: christian.hess@tu-darmstadt.de

^bInstituto de Catálisis y Petroleoquímica – Consejo Superior de Investigaciones Científicas, Marie Curie 2, 28049 Madrid, Spain

† Electronic supplementary information (ESI) available. See DOI: 10.1039/c9fd00133f

the reactivity behaviour is of particular interest. Firstly, the choice of the support material leads to differences in the reactivity of the catalyst,⁸ and secondly, the surface termination of the support itself influences the reactivity.^{9–12} Among the ceria surfaces, the most stable CeO₂(111) facet has been studied, both experimentally and theoretically, as a bare support,^{13–15} but also as a gold-loaded sample in the context of LT-WGS.³ The other two terminations, *i.e.*, CeO₂(110) and CeO₂(100), have been used in just a few studies as a support for Au/CeO₂ catalysts for LT-WGS.^{11,12} To this end, it has been reported that bare ceria polyhedra, which terminate mainly with CeO₂(111) facets, show the lowest activity for the WGS reaction, whereas the thermodynamically less stable CeO₂(110) and CeO₂(100) surfaces, which occur on rods and cubes, are more active.¹² These differences in reactivity are related to the thermodynamic stability of the various surface terminations and their different defect formation energies. Additionally, gold interacts differently with the individual surface terminations, the interaction with the CeO₂(100) surface being strongest and that with the CeO₂(111) surface weakest, as has been shown in previous theoretical studies.^{16–19} Moreover, according to experimental studies using X-ray photoelectron spectroscopy (XPS) or environmental transmission electron microscopy (ETEM), the interaction at Au–ceria is different for the individual facets, which has been related to the observed catalytic activity.^{11,20} Despite these studies, and growing interest in the shape effects on catalytic reactions,^{11,21–24} the detailed impact of the surface termination on the reactivity behaviour of Au/CeO₂ catalysts is not well understood and is a topic of current research.⁹

Regarding the mechanism of the LT-WGS reaction, two mechanisms have been proposed in the literature, which are referred to as the redox and associative mechanisms.^{1,25,26} In both mechanisms, the cleavage of O–H bonds has been considered to be a key step, but direct experimental evidence for the different ceria facets is scarce.³ There are several theoretical studies that consider the interaction of water with various ceria surface terminations.^{27–29} According to these studies, the interaction of water is lowest on the CeO₂(111) surface and strongest on the CeO₂(100) surface.^{27–29} Besides water, also CO was reported to interact differently with the individual facets, which may influence the catalytic activity.^{30–32} In fact, the CeO₂(110) or CeO₂(100) surfaces tend to form strongly adsorbed carbonates on the surface, which may block active sites for the WGS reaction.^{30,31,33}

In a previous publication, our group reported on the role of surface and bulk oxygen involved in the LT-WGS reaction over gold catalysts supported on polycrystalline ceria, which exposes mainly the CeO₂(111) surface.³ Our results are consistent with a redox mechanism, which has been previously proposed^{1,34} and discussed.³⁵ According to this mechanism (see Fig. 1), CO is adsorbed at gold sites and reacts with lattice oxygen of the ceria support to produce CO₂ accompanied by the formation of an oxygen vacancy, *i.e.*, the reduction of ceria. Subsequently, water dissociatively adsorbs onto this vacancy, leading to the formation of a hydroxide at the defect itself and a second hydroxide from the reaction of the hydrogen atom with surface oxygen near the defect. Finally, hydrogen from the hydroxides is transferred to the gold particle and recombines to molecular hydrogen. While this mechanism has been discussed in the context of catalysts based on polycrystalline ceria, for a detailed understanding, the influence of the ceria termination should also be considered. For example, the reaction of CO with

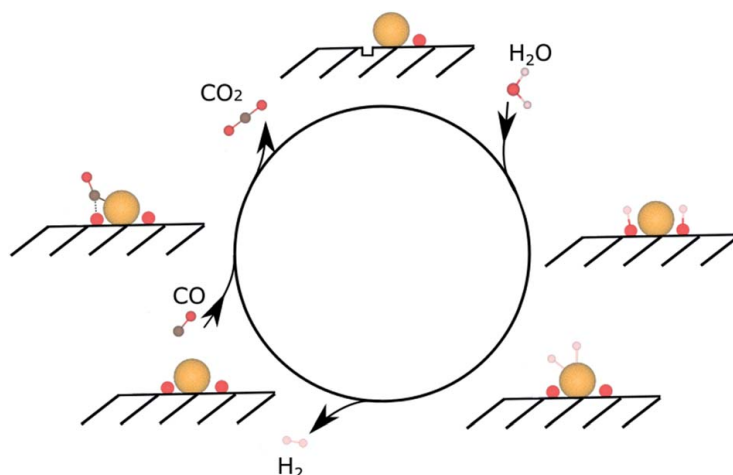


Fig. 1 Proposed mechanism for the WGS reaction over Au/CeO₂ catalysts. For details see text.

lattice oxygen requires an energy barrier to be overcome, which is expected to be different for each surface termination because of the different defect formation energies. Besides, as mentioned above, CO and H₂O interact differently with the individual facets, which may lead to differences in the activity behaviour.

In this contribution, new results on the effect of ceria faceting [(110), (100)] on the WGS reaction mechanism of Au/CeO₂ catalysts will be presented and discussed in the context of previous results on CeO₂(111). We will focus in particular on the oxygen dynamics by using *operando* Raman and UV-Vis spectroscopy, combined with isotope exchange experiments and supported by DFT+U (density functional theory plus Hubbard correction) calculations.

Experimental section

Catalyst preparation

CeO₂(111) was prepared by decomposition of Ce(NO₃)₃·6H₂O (Alfa Aesar, 99.5%) at 600 °C (6 °C min⁻¹) for 12 h. After cooling to room temperature the powder was sieved (200 μm) and calcined again using the same protocol.^{36,37}

The CeO₂[(110) + (100)] rods and CeO₂(100) cubes were prepared by hydrothermal synthesis of CeCl₃·7H₂O (Alfa Aesar, 99%) and Ce(NO₃)₃·6H₂O (Alfa Aesar, 99.5%) in a NaOH solution (98%, Grüssing GmbH). The concentration of the NaOH solution in water (electrical conductivity < 3 μS m⁻¹) was 9 M and 6 M for the rods and cubes, respectively.^{38,39} For both samples, 79 mL of the NaOH solution was added to 11 mL of precursor solution and stirred for 30 min. Then the solution was transferred to a PTFE (polytetrafluoroethylene, Teflon) autoclave with a volume of about 140 mL and thermally treated in an oven. After being heated to the final temperature at a rate of 1 °C min⁻¹, the rods were treated at 140 °C for 48 h and the cubes at 180 °C for 18 h. After cooling to room temperature, the resulting CeO₂ was centrifuged off, washed three times with deionized water, and dried at 85 °C for at least 24 h.

Gold was deposited onto CeO₂ *via* deposition precipitation,⁴⁰ using a 10⁻³ M HAuCl₄·3H₂O solution (Carl Roth, 99.9% (rods, cubes); Sigma Aldrich, 99.99% (polycrystalline ceria, sheets)) to yield total loadings of 0.5 wt% Au. The rods with

0.5 wt% Au (XPS) were obtained by loading the rods with 0.3 wt% Au (XPS) again. First, the ceria samples were dispersed in a ratio of 1 : 150 in deionized water, and the pH adjusted to 9 using a 0.1 M NaOH solution (98%, Grüssing GmbH). Subsequently, the chloroauric acid solution was set to pH 9 and added to the ceria dispersion to obtain the desired loading. After the addition, the pH value was checked again and adjusted to the pH value of 9 if necessary. Then, the reaction mixture was heated at 65 °C for 2 h and placed in an ultrasonic bath for 30 min after cooling. Finally, the residue was centrifuged, washed four times with deionized water, and dried at 85 °C for at least 24 h. The sheets were washed with a 0.25% ammonia solution before being washed with water.

Catalyst characterization

To determine the amount of gold, the catalysts were characterized by XPS on an SSX 100 ESCA spectrometer (Surface Science Laboratories Inc.). In this paper, the amount of gold is given in wt% at the surface, based on the results of the XPS analysis. Briefly, the X-radiation was generated by an Al K α monochromatic source (9 kV, 10 mA). The sample holder and the analyser were aligned at an angle of 55° to the horizontal. The X-ray beam had an angle of 35° with respect to the analyser horizontal and the sample was rotated by 16° with respect to the X-ray beam. The resolution of the XP spectrometer was 0.054 eV.

To ensure the comparability of the spectra, the u'' -signal of Ce(3d) was shifted to the literature value of 916.7 eV for all spectra.⁴¹ The spectra were deconvoluted by Gaussian–Lorentz functions with a 30/70 ratio, whereby the background was subtracted according to Shirley.⁴² For further details regarding the XP analysis, please refer to previous studies.⁴³ Contaminations caused by the synthesis, *e.g.* chlorine or nitrogen, can be excluded within the sensitivity of the XPS measurements.

Based on N₂ adsorption isotherms at 77 K and application of the BET (Brunauer–Emmett–Teller) model, the specific surface areas were determined to be 61 m² g⁻¹ for the sheets, 32 m² g⁻¹ for the cubes, and 88 m² g⁻¹ for the rods.

The samples were also characterized by transmission electron microscopy (TEM; JEOL JEM-2100F, Tokyo, Japan) to determine the surface termination and to check for potential changes of the surface termination induced by the WGS reaction. The microscope was equipped with a Schottky field emitter and operated at a nominal acceleration voltage of 200 kV. Sample preparation included dispersion in ethanol by means of an ultrasonic bath for 30 s, and placing a few drops on a carbon grid (Plano). After drying, the grid was coated with carbon (Bal-Tec MED010), preventing charging by the electron beam. Based on the TEM experiments, reaction-induced changes of the surface termination can be excluded. TEM images of the bare rods and cubes are shown in Fig. S1 of the ESI.† For the sheets, please refer to our previous work.^{44,45} TEM analysis confirms that the morphology and size of the particles do not change during the gold loading and exposure to reaction conditions (not shown).

Operando characterization

For the *operando* measurements, about 20–25 mg of the sample was placed in a stainless-steel sample holder (diameter: 8 mm; depth: 0.5 mm). Details of the setup have been described previously.³⁶ Briefly, Raman spectra were recorded on

a HL5R transmission spectrometer (Kaiser Optical) employing a frequency-doubled Nd:YAG laser (Cobolt) for excitation at 532 nm. The spectral resolution was specified as 5 cm^{-1} and the stability of the band positions was better than 0.3 cm^{-1} . The laser power at the position of the sample was set to a low value of 1 mW to prevent laser-induced changes. Cubes and sheets were measured by using an exposure time of 80 s and 5 accumulations, whereas for rods an exposure time of 250 s and 2 accumulations were used.

For all measurements an auto new dark and a cosmic ray filter were used. This means that, before each measurement, the background was recorded twice with a closed shutter to determine the background intensity. Furthermore, in each measurement, a second spectrum was recorded to allow for elimination of spikes caused by cosmic rays. As a result, the total measuring time amounted to about 1600 s for cubes and sheets, and about 2000 s for rods. All Raman spectra reported in this work were normalized to the highest intensity band, *i.e.*, the F_{2g} band. Given F_{2g} positions were determined by curve fitting using Lorentz functions.

The UV-Vis measurements were taken in diffuse reflection employing an AvaSpec ULS2048 spectrometer (Avantes), equipped with D_2 and halogen discharge lamps. The measuring time was 60 s, which is composed of an exposure time of 300 ms and 200 averages. Magnesium oxide powder (MgO, Sigma Aldrich), which shows no absorption between 170 and 1100 nm, was used as the white standard.

The sample temperature was determined by means of a Ni/Cr-Ni thermocouple (type K), which is located at the sample holder close to the sample. Sample temperatures deviated by a maximum of $2\text{ }^\circ\text{C}$ from the set temperatures.

The gases CO (99.997%, Air Liquide) and argon (99.996%, Westfalen) were dosed by digital mass flow controllers (MFCs, Bronkhorst). The dosage of $H_2^{16}O$ (electrical conductivity $< 3\text{ }\mu\text{S m}^{-1}$), $H_2^{18}O$ (97% + ^{18}O , Eurisotop), and $D_2^{16}O$ (99.9% D, Sigma Aldrich) was realized by a controlled evaporator mixer (CEM, Bronkhorst), and a liquid mass flow meter (LFM, Bronkhorst). In all experiments, the total flow rate was 100 mL min^{-1} . For quantitative analysis of the gas-phase composition, a FTIR spectrometer (Tensor 20, Bruker) was installed at the outlet of the cell. The spectral resolution was 4 cm^{-1} . The sampling time was set to 1 min, corresponding to the accumulation of 125 spectra. Using calibration curves, the concentrations of CO, $H_2^{16}O$, and CO_2 can be calculated. The catalytic activity is obtained by the quotient of the CO_2 and CO concentration in vol%. Because H_2 evolution is not accessible by FTIR, we examined the reactivity behaviour of the 0.6 wt% Au/CeO₂ sheets in a quartz reactor and an online mass spectrometer to detect H_2 .³ Based on these measurements, the evolution of H_2 is identical to that of CO_2 .

DFT calculations

To facilitate the assignment of vibrational bands, calculations on differently oriented ceria surfaces were performed using DFT+U (PBE+U/4.5 eV), as described in detail in a previous study.⁴⁶ All calculations were performed using the Vienna *Ab initio* Simulation Package (VASP, Version 5.3.5, <https://www.vasp.at/>), which includes the use of the GGA(PBE)+U approach (where GGA is the generalized gradient approximation to the exchange–correlation functional), with a parameterization by Perdew, Burke and Ernzerhof (PBE),⁴⁷ and a U_{eff} parameter of 4.5 eV

for the Ce 4f orbital (PBE+U/4.5 eV). Only valence electrons with a plane wave cutoff of 400 eV were considered. The Kohn–Sham equations were solved using the projector-augmented wave (PAW) method. Total energies and forces were calculated with a precision of 10^{-6} eV and 10^{-2} eV \AA^{-1} for electronic and force convergence, respectively. After having allowed for lattice relaxation, a normal mode analysis was performed, followed by the calculation of the Raman intensities of the vibrational modes using density functional perturbation theory (DFPT). For more detailed information please refer to our previous study⁴⁶ and to the ESI.†

Results

Catalytic activity

Fig. 2 depicts the steady-state catalytic activity during the LT-WGS reaction over gold-loaded ceria sheets, cubes, and rods upon exposure to a stream of $\text{H}_2\text{O}/\text{CO}/\text{Ar}$ (8% H_2O , 2% CO , Ar; 100 mL min^{-1}) at temperatures of $120 \text{ }^\circ\text{C}$ for sheets and $134 \text{ }^\circ\text{C}$ for all other samples. When applying identical conditions and the same measurement procedure the unloaded samples show no catalytic activity. As can be seen in Fig. 2, the sheets exhibit the highest activity and the cubes have a lower activity, despite the same amount of gold, followed by the rods, giving a first indication of the importance of the support properties, and more specifically, of the surface termination. Interestingly, the rods with the higher gold content (0.5 wt% Au) exhibit the lowest activity of all samples, illustrating the importance of the interaction between the support and gold for the catalytic activity, whereby the size of the gold particles is proposed to play a crucial role.⁴⁸ The fact that the sheets show the highest activity appears to contradict the expectations of

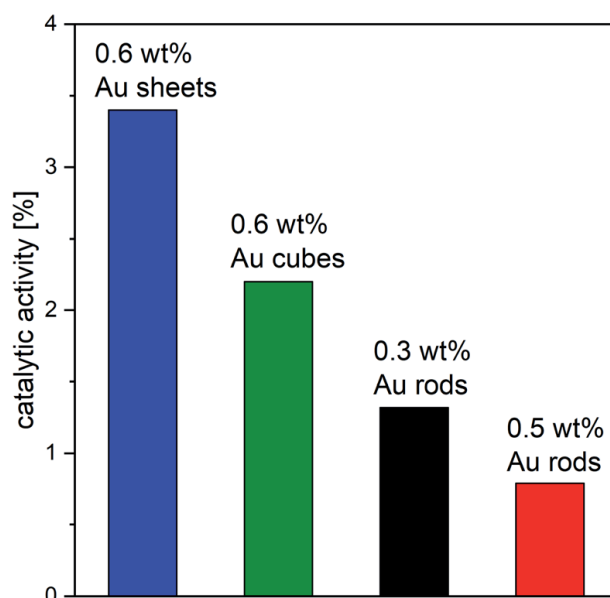


Fig. 2 Catalytic activity during LT-WGS reaction over 0.6 wt% Au/CeO₂ sheets (blue), 0.6 wt% Au/CeO₂ cubes (green), 0.3 wt% Au/CeO₂ rods (black), and 0.5 wt% Au/CeO₂ rods (red) upon exposure to a stream of $\text{H}_2\text{O}/\text{CO}/\text{Ar}$ (8% H_2O , 2% CO , Ar; 100 mL min^{-1}) at $120 \text{ }^\circ\text{C}$ for the sheets and at $134 \text{ }^\circ\text{C}$ for all other samples. The catalytic activity was measured after at least 1 h on stream.

a defined $\text{CeO}_2(111)$ terminating surface.^{11,12} However, previous TEM images of our polycrystalline ceria sample have shown the presence of stepped facets.^{44,45} Note that this sample was also used for the present work. These stepped sites may have a positive effect on activity during CO oxidation,⁴⁵ because of the changing surface properties, such as interactions with deposited gold, which in turn may result in different interactions with gas-phase molecules, or changes in the defect formation energy.^{49–51} To gain more detailed insight into the mechanism of the LT-WGS reaction over Au/CeO₂ catalysts, *operando* Raman and UV-Vis spectroscopy in combination with isotope exchange experiments was applied, as discussed in the following.

Operando UV-Vis spectroscopy

Fig. 3 depicts *operando* UV-Vis spectra of the Au/CeO₂ catalysts (solid lines) in comparison to spectra recorded in Ar flow (dashed lines). The UV-Vis spectra of the gold-loaded samples in Ar show absorption between 450 nm and 900 nm, in contrast to the bare ceria samples (see Fig. S2 in ESI†). It is noticeable that the sheets have the highest absorption and, despite a similar amount of gold, the absorption of the rods and cubes is lower. The absorption of the rods exhibits a strong dependence on the gold content. In fact, the rods loaded with 0.3 wt% Au show hardly any increase in absorption in comparison to the bare rods. Furthermore, upon closer inspection, differences in the profile of this band can be observed, *i.e.*, the band of the rods and cubes is significantly broader than that of the sheets. From these observations it can be concluded that the band is related to the gold loading, but that the amount of gold is not the only factor that has an influence. For this reason, given that the gold surface plasmons in this region

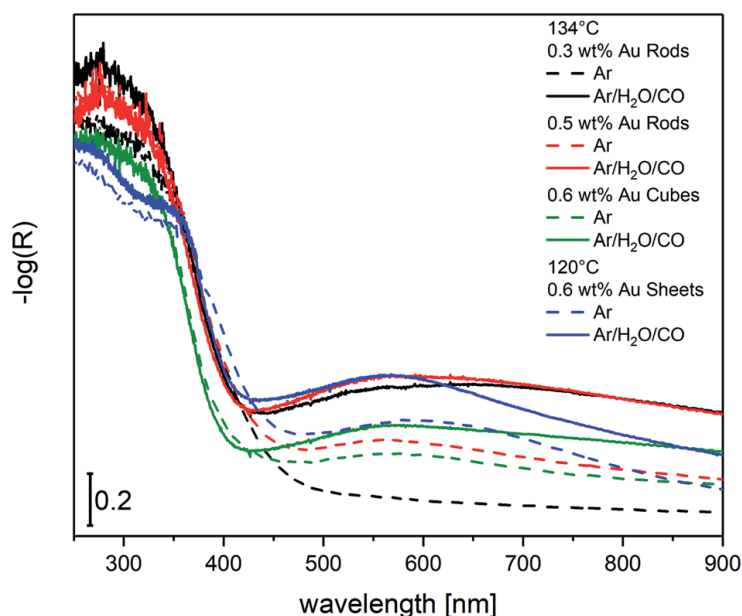


Fig. 3 *Operando* UV-Vis reflectance spectra of the Au/CeO₂ catalysts (solid lines) in comparison to spectra obtained under a stream of Ar prior to reaction (dashed lines). Reaction conditions consist of a feed of 8% H₂O/2% CO/Ar at a total flow of 100 mL min⁻¹, and a temperature of 120 °C for the sheets and 134 °C for all other samples. Spectra correspond to 0.6 wt% Au/CeO₂ sheets (blue), 0.6 wt% Au/CeO₂ cubes (green), 0.3 wt% Au/CeO₂ rods (black), and 0.5 wt% Au/CeO₂ rods (red).

originate from the presence of metallic gold, it can be said that the observed absorption is attributable to the fraction of metallic gold,^{52,53} which can be confirmed by XPS measurements. In fact, in our previous study, the Au 4f photoemission showed a fraction of metallic Au of 70% for the Au-loaded sheets.³ For all other samples, smaller Au⁰ contributions are observed (see Fig. S3 and S4 in ESI†): a Au⁰ fraction of 40% for the Au-loaded cubes, 63% for the 0.3 wt% Au rods, and 57% for the 0.5 wt% Au rods.

Switching from Ar to reaction conditions leads to a strong increase in absorption between 450 nm and 900 nm for all catalyst samples. The largest increase is observed for the rods loaded with 0.3 wt% Au, followed by the rods with 0.5 wt% Au loading. This behaviour can be explained by the easier reducibility of the rods, as they contain the CeO₂(110) facet, which has the lowest defect formation energy.⁵⁴ The reduction leads to a charge transfer from Ce³⁺ to Ce⁴⁺, which gives rise to absorption at around 570 nm.⁵⁵ In previous studies, such an increase in absorption has also been observed on bare ceria samples in the presence of hydrogen at elevated temperatures (200–700 °C).^{41,56} Summarizing, the absorption in the range between 450 nm and 900 nm originates from gold surface plasmons and a charge transfer between Ce³⁺ and Ce⁴⁺.

UV-Vis spectra recorded in a stream of H₂O/Ar after exposure to reaction conditions show a decrease in the absorption in the range 450–900 nm (see Fig. S5 in ESI†), but the initial state in Ar is not reached again, neither in H₂O/Ar nor by cooling the sample under Ar atmosphere. The observed behaviour indicates an agglomeration of the gold particles, leading to an enrichment of neutral gold, as has also been shown in earlier studies.^{53,57–59}

Operando Raman spectroscopy

To gain insight into the structural dynamics of the catalysts and the presence of adsorbates, Raman spectroscopy was applied. Fig. 4A shows *operando* Raman spectra, obtained with 532 nm wavelength excitation, of the facet-dependent Au/CeO₂ catalysts under reaction conditions (2% CO/8% H₂O/Ar). The spectra are dominated by the F_{2g} band at around 450 cm⁻¹, which has been cut off to give an enlarged view of the other features. Please note that the F_{2g} band positions are given at the top right of the figure. As a reference, the spectra for the bare ceria samples are shown in the ESI (see Fig. S6†) with F_{2g} bands located at 451.3, 458.1, and 461.7 cm⁻¹ for the rods, cubes, and sheets, respectively, and defect bands located within the 540–590 cm⁻¹ range.

Owing to the presence of gold-induced fluorescence, the comparison of relative Raman intensities needs to be done with care. In contrast to the cubes and rods with 0.5 wt% Au, for the rods with 0.3 wt% Au and the sheets only a small background is observed. In this case, we consider a comparison of the defect-related bands acceptable. In this context the Au-loaded rods show more intense defect bands at 540 cm⁻¹ and 590 cm⁻¹. Besides, it is noticeable that the F_{2g} band of the Au-loaded rods is located at 448.5 cm⁻¹ and that of the Au-loaded sheets at 456.4 cm⁻¹. Note that the F_{2g} red-shifts, that occur under reaction conditions, originate from an expansion of the unit cell on the basis of the greater ionic radius of the Ce³⁺ formed upon ceria reduction and can be related to the number of oxygen vacancies in ceria, as discussed previously.⁶⁰ These two observations clearly indicate a greater extent of reduction of the Au-loaded rods.

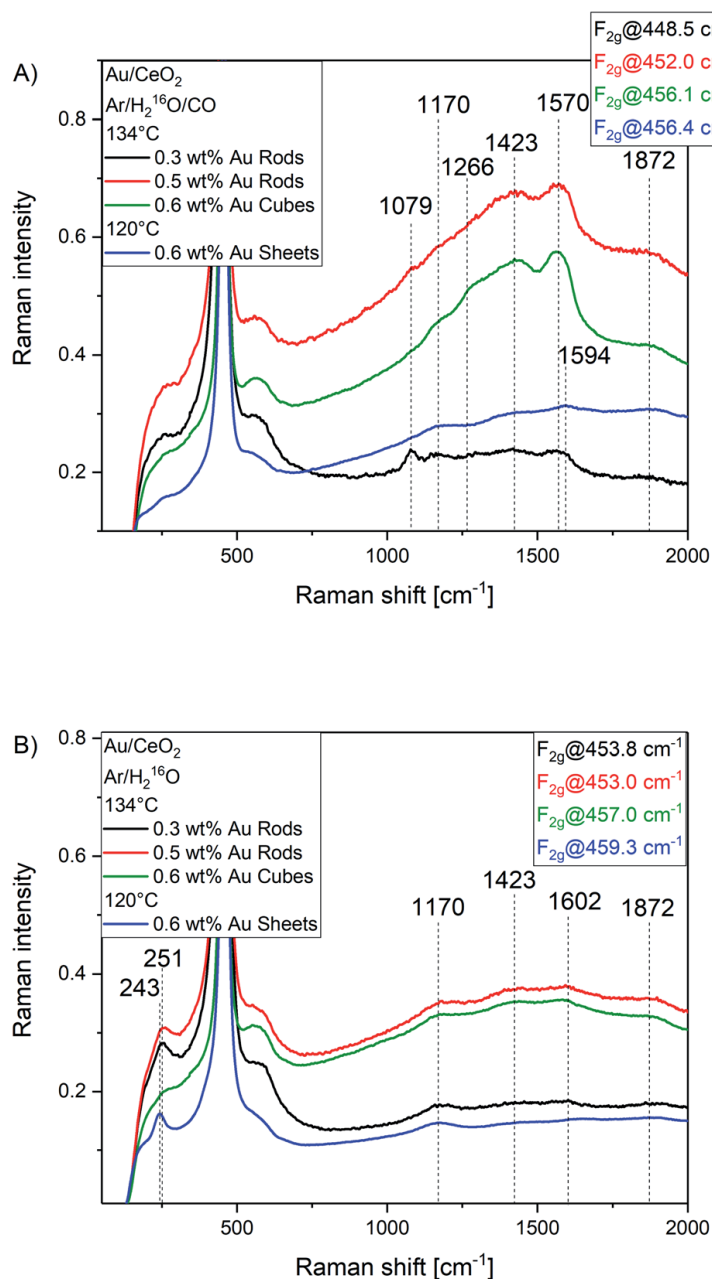


Fig. 4 (A) *Operando* Raman spectra of the Au/CeO₂ catalysts recorded under reaction conditions (2% CO/8% H₂O/Ar). (B) *In situ* Raman spectra recorded in 8% H₂O/Ar after reaction. The total flow rate is 100 mL min⁻¹. The temperature is 120 °C for the sheets and 134 °C for all other samples. The F_{2g} bands have been cut off for clarity; the F_{2g} band positions are given at the top right. Spectra correspond to 0.6 wt% Au/CeO₂ sheets (blue), 0.6 wt% Au/CeO₂ cubes (green), 0.3 wt% Au/CeO₂ rods (black), and 0.5 wt% Au/CeO₂ rods (red). Spectra were recorded at 532 nm excitation.

In the region of oxygen adsorbates, a Raman band is observed at 1079 cm⁻¹ in the case of the Au-loaded rods, which is hardly or not at all detected for the other samples. Interestingly, this band can only be observed under reaction conditions and is much more intense for the 0.3 wt% Au sample. Additionally, a band at around 1266 cm⁻¹ is detected for the Au-loaded cubes, whereas bands at 1423 cm⁻¹ and 1570 cm⁻¹ were observed for Au-loaded cubes and rods. The band at around 1594 cm⁻¹ originates from a formate species adsorbed at the CeO₂(111)

facet,³ whereas the weak band at around 1872 cm^{-1} can be assigned to molecular water. To explore the nature of the unassigned bands, including the feature at 1079 cm^{-1} , we performed isotope exchange experiments combined with DFT calculations, as will be discussed below.

Fig. 4B shows *in situ* Raman spectra of the Au/CeO₂ catalysts, recorded in 8% H₂O/Ar atmosphere after reaction. A comparison of the spectra under reaction conditions (see Fig. 4A) with those taken after reaction (H₂O/Ar) shows that the 2TA overtone at 251 cm^{-1} almost completely disappears under reaction conditions and reappears in H₂O/Ar. Besides, the 2LO-overtone at 1170 cm^{-1} is more pronounced in the H₂O/Ar atmosphere. This behaviour may originate from the strong change of the electronic structure under reaction conditions (see Fig. 3), leading to a decrease in intensity and signal-to-noise ratio. Note that the Au-loaded sheets show an additional band in the region of the 2TA overtone at 243 cm^{-1} , which is attributed to the longitudinal mode of surface oxygen, as previously discussed.⁴⁶ The loss of intensity of this band under reaction conditions can be explained by the reaction or removal of surface oxygen. The regeneration of defects is consistent with a blue-shift in the F_{2g} band of 2.9 cm^{-1} when switching from reaction conditions to H₂O/Ar atmosphere. Such a regeneration is observed for all samples and is most pronounced for the rods with 0.3 wt% Au loading, as reflected in a 5.8 cm^{-1} shift of the F_{2g} band. For the other two samples, the blue-shift is less pronounced, and amounts to about 1 cm^{-1} .

Under H₂O/Ar atmosphere, the band at 1423 cm^{-1} becomes more prominent for the Au-loaded cubes and rods with 0.5 wt% Au loading. Furthermore, the broad band at 1570 cm^{-1} disappears, and a small feature at 1602 cm^{-1} is detected. Note that owing to the width of the 1570 cm^{-1} band we cannot exclude the presence of the 1602 cm^{-1} feature under reaction conditions.

In summary, the Raman data demonstrates a significant difference in the reducibility of the samples and their interactions with molecules from the gas phase. As a prominent example of facet-dependent adsorption behaviour, the Au-loaded rods show a band at 1079 cm^{-1} under reaction conditions.

Isotope exchange experiments

To explore the nature of the observed bands, isotope exchange experiments were performed using H₂¹⁸O and D₂¹⁶O. Fig. 5 depicts the *operando* Raman spectra of the 0.3 wt% Au/CeO₂ rods under reaction conditions. As discussed in the following, several isotope shifts were observed. The use of H₂¹⁸O leads to a red-shift of the band located at 1079 cm^{-1} to 1025 cm^{-1} , which is not observed for D₂¹⁶O. This clearly shows that this vibrational mode involves oxygen but not hydrogen. Considering the spectral region, the presence of several vibrations related to carbonate and molecular oxygen adsorbates may be feasible. To facilitate the band assignment, DFT calculations were performed (see Fig. S7 and Table S1†), which help to readily exclude Raman active carbonate stretching vibrations (ν_{CO_3}) due to their mostly excessive shifts (based on the harmonic approximation). On the other hand, the observed behaviour would be consistent with the O–O stretching vibration of a superoxide. In fact, DFT calculations (see Fig. S8 and Table S2†) support the assignment of the 1079 cm^{-1} band to superoxide adsorbed on a CeO₂(110) facet, which occurs at significantly lower wavenumber than on the previously studied CeO₂(111) or CeO₂(100) facets.⁶¹ Due to

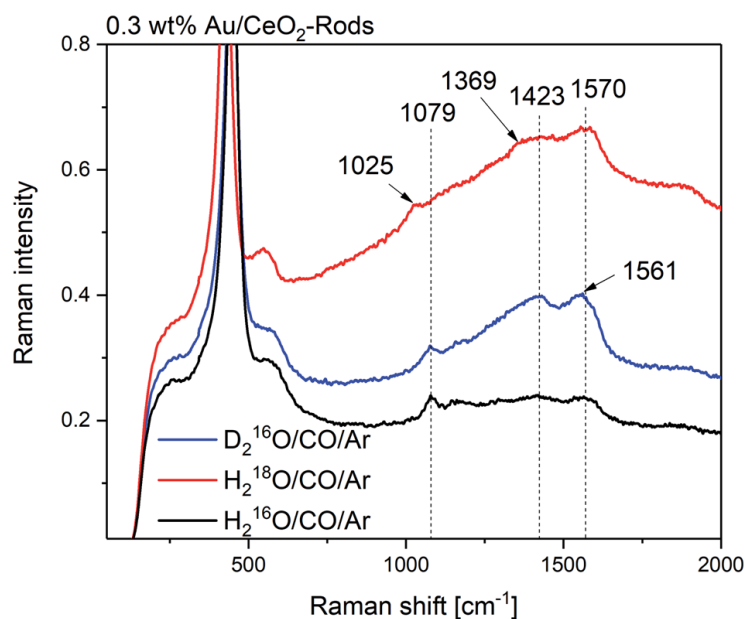


Fig. 5 *Operando* Raman spectra of the 0.3 wt% Au/CeO₂ rods. Obtained under reaction conditions (2% CO/8% H₂O/Ar) at 134 °C and at a total flow rate of 100 mL min⁻¹ using the water isotopes D₂¹⁶O (blue), H₂¹⁸O (red), and H₂¹⁶O (black). Raman spectra were recorded at 532 nm excitation.

the exclusive occurrence of the 1079 cm⁻¹ band under reaction conditions, which have been shown to lead to ceria reduction (see Fig. 4A), we can attribute the Raman band at 1079 cm⁻¹ to superoxide adsorbed on a reduced CeO₂(110) surface.

As can be seen in Fig. 5, the use of H₂¹⁸O induces a red-shift of the band at 1423 cm⁻¹ to 1369 cm⁻¹. The same behaviour is also observed in the case of the Au-loaded cubes (not shown). These bands may be assigned to vibrations of carbonate species on CeO₂(100) based on DFT calculations and the lack of an isotope shift when D₂O is used.⁶² Upon exposure to D₂¹⁶O, the band at 1570 cm⁻¹ shows a slight shift to 1561 cm⁻¹. Based on the position and observed isotope exchange behaviour, this feature is assigned to a formate species. In this context it is worth mentioning that, according to previous DFT calculations, replacing the lattice oxygen by ¹⁸O has no influence on the OCO vibrations.³

Dynamical behaviour under WGS reaction conditions

In the following, the dynamical behaviour of the facet-dependent Au/CeO₂ catalysts will be discussed by relating the catalytic activity to the spectroscopic changes (see Fig. 6). As spectroscopic properties the shift of the F_{2g} position (from Raman spectra) and the change in absorbance at 570 nm (from UV-Vis spectra) will be considered. In the course of the experiments, the catalysts were first exposed to Ar before the switch to reaction conditions (2% CO/8% H₂O/Ar) occurred, followed by exposure to 8% H₂O/Ar, and a final cooling phase to 48 °C in Ar. In general, all samples show the same trends in the variation of the absorption and the F_{2g} shift. Regarding the absorption behaviour, a strong increase upon exposure to reaction conditions and a smaller decrease when switching to 8% H₂O/Ar atmosphere is observed, but none of the samples return

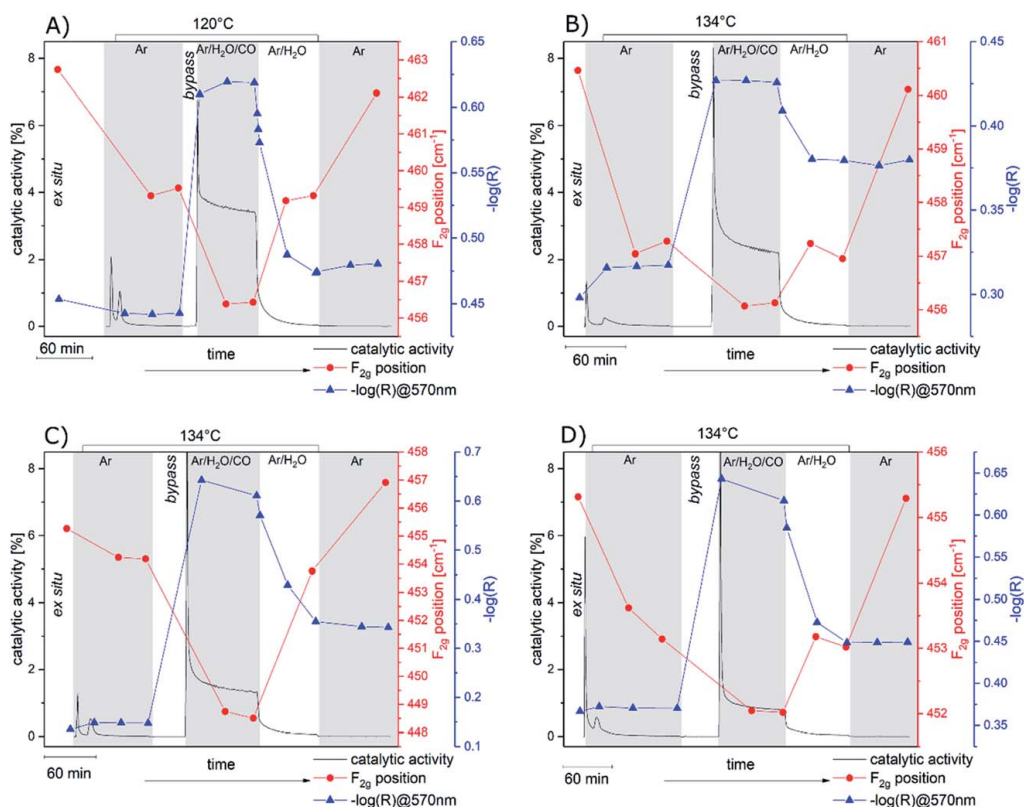


Fig. 6 Operando Raman (red) and UV-Vis (blue) results shown together with the catalytic activity (black) of (A) 0.6 wt% Au/CeO₂ sheets, (B) 0.6 wt% Au/CeO₂ cubes, (C) 0.3 wt% Au/CeO₂ rods, and (D) 0.5 wt% Au/CeO₂ rods at 120 °C (sheets) or 134 °C (cubes, rods) during WGS reaction (2% CO/8% H₂O/Ar) at a total flow rate of 100 mL min⁻¹. Raman spectra were recorded at 532 nm wavelength excitation. Prior to reaction the catalyst was exposed to Ar; after reaction the catalyst was exposed to Ar/H₂O (8% H₂O) and then cooled to 48 °C in Ar.

to their initial state. Among the Au/CeO₂ samples, the Au-loaded rods show the biggest and the Au-loaded cubes the smallest change in absorption when the feed is switched from Ar to reaction conditions. For comparison, for the unloaded samples, only very small or no changes were observed in this spectral range. Changes in absorption are related to gold surface plasmons and a reduction of the support, leading to Ce³⁺-Ce⁴⁺ transitions. When comparing the absolute absorption changes with the activity of the Au/CeO₂ catalysts, no correlation is recognizable at this point. Anyway, the activity is related to an increase in absorption, but the extent of the absolute change does not play a crucial role for the catalytic activity. These observations related to the activity indicate that reducibility alone is not decisive for the activity. This is apparent from a comparison of activity data in Fig. 2 and the absolute changes of the F_{2g} position and the absorption at 570 nm in Fig. 6. In the following, the oxygen dynamics of the bare samples are discussed, which further emphasizes the last statement.

To this end, details of the subsurface oxygen dynamics, as measured by the F_{2g} band position, are depicted in Fig. 7 following the experimental protocol discussed above (see Fig. 6), including a comparison of loaded with unloaded ceria samples. Furthermore, the F_{2g} band positions recorded during H₂¹⁸O exposure are shown. As a result of oxygen isotope exchange, large amounts of ¹⁸O are

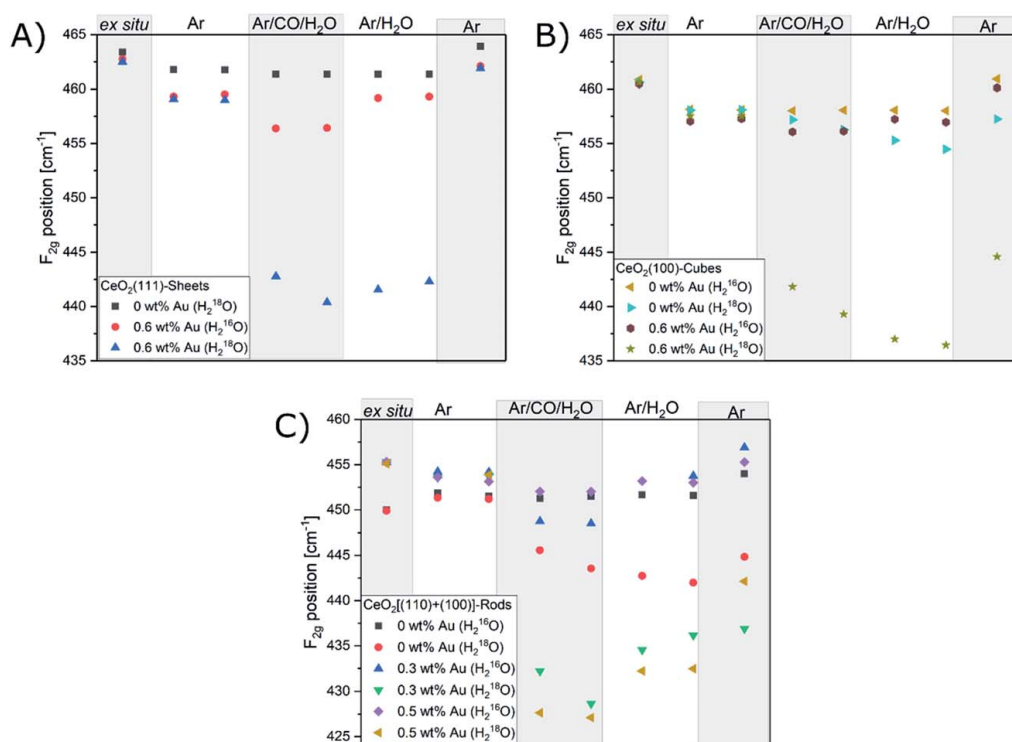


Fig. 7 Oxygen dynamics based on the Raman F_{2g} position for (A) 0.6 wt% Au/CeO₂ sheets, (B) 0.6 wt% Au/CeO₂ cubes, and (C) Au/CeO₂ rods in comparison to the bare ceria samples. The Au loadings for the rods were 0.3 wt% Au and 0.5 wt% Au; experiments were performed using H₂¹⁶O and H₂¹⁸O. The experimental conditions correspond to those given in the caption of Fig. 6.

detected in the ceria subsurface, indicating the facile dissociation of water at the catalyst surface and subsequent oxygen transfer from the surface to deeper layers. Interestingly, this behaviour is facet dependent, with CeO₂[(110)+(100)] rods showing the strongest dynamics, which is also present in the absence of gold. In contrast, in the case of CeO₂(111) facets, gold is required to induce a substitution of lattice oxygen.

Upon closer inspection, further differences between the samples can be seen, as discussed in the following. As shown in Fig. 7A, the bare sheets undergo only small changes, in contrast to the dynamics exhibited by the Au-loaded sheets. Thus, it appears that the gold loading significantly reduces the defect formation energy, so that an increase in temperature is sufficient to reduce the material. The largest change in F_{2g} position within the sequence of steps is observed under reaction conditions, and if H₂¹⁸O is employed, a further F_{2g} red-shift occurs, originating from the replacement of lattice oxygen by ¹⁸O. This latter (isotope-induced) red-shift is 16 cm^{-1} , in comparison to the calculated F_{2g} shift of 24 cm^{-1} for complete substitution.³ When CO is switched off, the catalyst regenerates, as indicated by a slight blue-shift of the F_{2g} band. If the feed is switched to pure Ar and the sample cooled down, the F_{2g} position returns to its initial value for both water isotopes, which can be explained by the dilution of subsurface ¹⁸O by ¹⁶O from the bulk in the absence of H₂¹⁸O, as discussed previously.³

For the cubes, lower initial F_{2g} positions are observed, indicating a higher oxygen defect concentration. This can be rationalized by the lower defect

formation energy of the CeO₂(100) facet compared to the CeO₂(111) facet. During the treatments the bare cubes show small F_{2g} shifts, which are attributed to temperature-related mode softening.^{63,64} In the presence of gold the extent of the F_{2g} shifts slightly increases, as a result of an easier reduction of the material due to a decrease in defect formation energy.⁶⁵ Unlike the sheets, the bare cubes show a further red-shift of the F_{2g} band after reaction conditions when H₂¹⁸O is used, indicating that an exchange of lattice oxygen can take place in the absence of any catalytic activity. The fact that a further exchange of oxygen is observed upon exposure to H₂¹⁸O/Ar suggests that water adsorbs more extensively in the absence of CO in the feed (thus avoiding other adsorbates). In contrast, for the CeO₂(111) sheets, no such behaviour is detected, owing to the lower interaction of water with the CeO₂(111) surface.^{27–29}

In the case of the Au-loaded cubes, a ready exchange of lattice oxygen under reaction conditions is observed, as indicated by the F_{2g} red-shift of 17 cm⁻¹. While the magnitude of the shift is similar to that of the Au-loaded sheets, the behaviour after reaction conditions is different, *i.e.*, the F_{2g} band shows a further red-shift, similar to the bare cubes. Thus, the exchange of lattice oxygen continues, even without any WGS activity. The maximum of the shift corresponds to 20.5 cm⁻¹ and is close to the value for complete substitution of 22.6 cm⁻¹, which we obtained by DFT calculations. When the sample is cooled down in Ar, a blue-shift is observed, but the F_{2g} band does not return to its original position, in contrast to the behaviour observed for the Au-loaded sheets. The observation that in the case of the Au-loaded cubes the initial state is only partially recovered can be explained by an equilibration of subsurface O¹⁸ with O¹⁶ from the bulk, which is not completed on the timescale of the experiment. This behaviour is consistent with that of the Au-loaded sheets (see above), considering the different extent of isotope exchange for the cube- and sheet-based samples.

Finally, the subsurface oxygen dynamics of the rods is depicted in Fig. 7C, which includes data for both gold loadings as well as the bare rods. Generally, the F_{2g} positions of the rods are significantly lower than those of the cubes and sheets. For the unloaded rods the F_{2g} band is located at 450 cm⁻¹, which corresponds to a red-shift of more than 13 cm⁻¹ compared to the sheets. One reason for this behaviour is the easier reducibility of the CeO₂(100) and CeO₂(110) facets of the rods. Interestingly, in the presence of H₂¹⁶O/CO/Ar, the sample with 0.3 wt % Au shows a distinct shift of 5.7 cm⁻¹, whereas the 0.5 wt% Au sample shows only a minor shift, comparable to that of the bare rods. On switching to H₂¹⁶O/Ar and Ar, defect regeneration occurs, as indicated by the F_{2g} band positions resembling the initial values.

In the presence of H₂¹⁸O, even the unloaded rods show a red-shift of the F_{2g} band that is larger than that of the cubes. Unlike for the gold-loaded samples, the F_{2g} band shifts further to the red when the conditions are switched from reaction to H₂¹⁸O/Ar atmosphere. Moreover, cooling in Ar induces only a small recovery, which clearly indicates that the isotope exchange of lattice oxygen penetrates deeper into the subsurface/bulk of rods in comparison to the cubes and sheets. In the case of the gold-loaded samples, very strong red-shifts of 25.1 cm⁻¹ and 26.8 cm⁻¹ are observed under reaction conditions for the 0.3 wt% Au and 0.5 wt% Au samples, respectively, followed by blue-shifts of 7.6 cm⁻¹ and 5.4 cm⁻¹ after reaction. This behaviour can be explained by the strongly reduced state of the samples created under reaction conditions, which leads to (at least) partial

regeneration after the reaction. It is worth mentioning that the 0.3 wt% Au sample undergoes larger shifts despite its lower WGS activity. This suggests that the amount of gold plays an important role in the exchange of lattice oxygen, but not necessarily with respect to the activity.

In summary, our findings show that for the reducibility behaviour of the samples, as measured by the red-shift of the F_{2g} band upon switching from Ar to reactive atmosphere, the surface termination is not the only decisive factor. This statement is justified by a comparison of the cubes and sheets (see Table 1), according to which the sheets are subject to larger shifts. As a consequence, the sheets are more strongly reduced than the cubes, despite their $CeO_2(111)$ termination. This behaviour can be rationalized by the initially higher defect concentrations of the cubes, and/or by a lowering of the defect formation energy at stepped surfaces.⁴⁹

Furthermore, by comparing Table 1 with Fig. 2, it is also evident that there is no correlation between the extent of the F_{2g} red-shift and the catalytic activity. This is direct proof that the activity depends not only on the defect formation energy but also on other parameters, such as the desorption energy of CO_2 and/or the activation of H_2O . In this context it has previously been shown that the interaction of CO_2 and H_2O with $CeO_2(110)$ and $CeO_2(100)$ facets is stronger than with the $CeO_2(111)$ facet. On one hand, this may lead to an easier activation of the above molecules, but on the other hand, more strongly adsorbed species may be formed, which may have a negative effect on catalytic activity.^{27–31} Previous studies reported a lowering of the CO_2 desorption energy at stepped sites by 0.85 eV (comparison between Au/ CeO_2 (ref. 66) and Au/ CeO_2 -U (ref. 49)). Based on the detailed TEM analysis of our $CeO_2(111)$ -based Au/ CeO_2 catalyst providing clear evidence for the presence of stepped sites,⁴⁴ we may therefore attribute the increased WGS activity of the Au-loaded sheets, as compared to the rod- and cube-based catalysts, to these stepped sites.⁴⁹

Insight into the reaction mechanism

Our findings strongly indicate that beside the amount of gold, support properties such as the type of facets and the presence of steps play an important role regarding the reactivity behaviour of Au/ CeO_2 catalysts in the WGS reaction. In particular, the defect formation energy alone, which differs for the individual surface terminations, is not decisive for a high activity, and we do not observe a correlation of activity with the number of defects, as proposed in the literature.⁶⁷ However, there are other aspects, such as the desorption energy of CO_2 and the

Table 1 Absolute F_{2g} shifts of the Au-loaded samples when switching from Ar to reaction conditions ($CO/H_2^{16}O/Ar$) and from reaction conditions to $H_2^{16}O/Ar$. Shifts of the bare ceria samples are always smaller than 0.1 cm^{-1} . The experimental conditions correspond to those in Fig. 6

Sample	$\Delta_{(Ar \rightarrow CO/H_2O/Ar)} [\text{cm}^{-1}]$	$\Delta_{(CO/H_2O/Ar \rightarrow H_2O/Ar)} [\text{cm}^{-1}]$
Au/sheets	3.1	2.9
Au/cubes	1.1	0.8
0.3 wt% Au/rods	5.7	5.3
0.5 wt% Au/rods	1.1	1.0

activation of H₂O, that need to be considered. Regarding H₂O activation it has been shown for Cu/CeO₂ catalysts that water dissociation may be rate-determining for the WGS reaction.⁶⁸ According to the literature, the interaction of water on the clean surface is lowest for CeO₂(111) and strongest for CeO₂(100).^{27–29} It should, however, be mentioned that the dissociation of water is more preferred on oxygen vacancies than on the clean surface^{69,70} and in the presence of oxygen vacancies the adsorption is weakest for CeO₂(111) and strongest for CeO₂(100).²⁸ Therefore, it will be important to investigate the interaction of water with different surface terminations in great detail in the future.

Turning now to the proposed mechanism for the WGS reaction (see Fig. 1), we see that our spectroscopic findings for Au/CeO₂ catalysts are consistent with a redox mechanism, independent of the surface termination. The isotope exchange experiments also show that the proposed dissociative adsorption of water involves an oxygen vacancy, as evidenced by the regeneration after reaction conditions in a stream of H₂O/Ar and by the replacement of ¹⁶O by ¹⁸O.

Conclusions

Our results demonstrate the potential of combining *operando* spectroscopies with isotope experiments to monitor the facet-dependent dynamics of different surface and bulk oxygen species in Au/CeO₂ catalysts during WGS conditions. Supported by DFT calculations, new insights into the reaction mechanism were obtained. Under reaction conditions a reduction of the ceria support materials takes place, which also involves subsurface oxygen. While all catalysts show reduction during reaction conditions, there is no correlation of the extent of reduction with the catalytic activity. As a result of the particularly strong reduction of the rods with 0.3 wt% Au loading during WGS reaction, a superoxide band is observed at 1079 cm⁻¹, in agreement with theoretical calculations. The reduction of the Au/CeO₂ samples is also responsible for the ready dissociation of water, a crucial step in the WGS reaction. The observed red-shift of the F_{2g} band and exchange of oxygen using H₂¹⁸O are consistent with a redox-type mechanism.

We found the WGS reaction to be strongly facet-dependent and to depend not only on the surface termination but also on other factors, such as the presence of stepped sites. In fact, based on our results, gold loaded on a stepped CeO₂(111), as in the case of the sheets, shows the highest WGS activity. The two less-stable surfaces, *i.e.*, CeO₂(110) and CeO₂(100), are able to adsorb CO as carbonate species, which may block active sites and lead to lower CO conversion, as indicated by the presence of carbonate bands at 1423 cm⁻¹ in the Raman spectra during reaction conditions (see Fig. 4).

Conflicts of interest

There are no conflicts to declare.

Acknowledgements

The DFT calculations were conducted on the Lichtenberg high performance computer of the TU Darmstadt. Jochen Rohrer and Karsten Albe are

acknowledged for support with the VASP code. We thank Stefan Lauterbach and Hans-Joachim Kleebe for TEM measurements, Martin Brodrecht for BET measurements, and Karl Kopp for technical support as well as for XPS measurements. M. V. G. P. thanks the support by the MINECO and MICINN-Spain (CTQ2015-71823-R and RTI2018-101604-B-I00, respectively).

References

- 1 Q. Fu, H. Saltsburg and M. Flytzani-Stephanopoulos, *Science*, 2003, **301**, 935–938.
- 2 C. M. Kalamaras, I. D. Gonzalez, R. M. Navarro, J. L. G. Fierro and A. M. Efstathiou, *J. Phys. Chem. C*, 2011, **115**, 11595–11610.
- 3 C. Schilling and C. Hess, *ACS Catal.*, 2019, **9**, 1159–1171.
- 4 A. Luengnaruemitchai, S. Osuwan and E. Gulari, *Catal. Commun.*, 2003, **4**, 215–221.
- 5 C. Ratnasamy and J. P. Wagner, *Catal. Rev.*, 2009, **51**, 325–440.
- 6 J. M. Zalc and D. G. Löffler, *J. Power Sources*, 2002, **111**, 58–64.
- 7 D. L. Trimm, *Appl. Catal., A*, 2005, **296**, 1–11.
- 8 P. Panagiotopoulou and D. I. Kondarides, *Catal. Today*, 2006, **112**, 49–52.
- 9 A. Trovarelli and J. Llorca, *ACS Catal.*, 2017, **7**, 4716–4735.
- 10 T. Montini, M. Melchionna, M. Monai and P. Fornasiero, *Chem. Rev.*, 2016, **116**, 5987–6041.
- 11 R. Si and M. Flytzani-Stephanopoulos, *Angew. Chem., Int. Ed.*, 2008, **47**, 2884–2887.
- 12 S. Agarwal, L. Lefferts, B. L. Mojet, D. A. J. M. Ligthart, E. J. M. Hensen, D. R. G. Mitchell, W. J. Erasmus, B. G. Anderson, E. J. Olivier, J. H. Neethling and A. K. Datye, *ChemSusChem*, 2013, **6**, 1898–1906.
- 13 Z. Wu and S. H. Overbury, *Catalysis by Materials with Well-Defined Structures*, 2015.
- 14 J. Paier, C. Penschke and J. Sauer, *Chem. Rev.*, 2013, **113**, 3949–3985.
- 15 M. V. Ganduglia-Pirovano, A. Hofmann and J. Sauer, *Surf. Sci. Rep.*, 2007, **62**, 219–270.
- 16 A. Chutia, D. J. Willock and C. R. A. Catlow, *Faraday Discuss.*, 2018, **208**, 123–145.
- 17 K.-J. Zhu, Y.-J. Yang, J.-J. Lang, B.-T. Teng, F.-M. Wu, S.-Y. Du and X.-D. Wen, *Appl. Surf. Sci.*, 2016, **387**, 557–568.
- 18 C. Zhang, A. Michaelides and S. J. Jenkins, *Phys. Chem. Chem. Phys.*, 2011, **13**, 22–33.
- 19 M. Nolan, *J. Chem. Phys.*, 2012, **136**, 134703.
- 20 N. Ta, J. Liu and W. Shen, *Chin. J. Catal.*, 2013, **34**, 838–850.
- 21 Z. A. Qiao, Z. Wu and S. Dai, *ChemSusChem*, 2013, **6**, 1821–1833.
- 22 J. Han, H. J. Kim, S. Yoon and H. Lee, *J. Mol. Catal. A: Chem.*, 2011, **335**, 82–88.
- 23 L. Liu, Z. Yao, Y. Deng, F. Gao, B. Liu and L. Dong, *ChemCatChem*, 2011, **3**, 978–989.
- 24 Z. Wu, V. Schwartz, M. Li, A. J. Rondinone and S. H. Overbury, *J. Phys. Chem. Lett.*, 2012, **3**, 1517–1522.
- 25 Y. Chen, J. Cheng, P. Hu and H. Wang, *Surf. Sci.*, 2008, **602**, 2828–2834.
- 26 S. Aranifard, S. C. Ammal and A. Heyden, *J. Catal.*, 2014, **309**, 314–324.
- 27 T. Kropp, J. Paier and J. Sauer, *J. Phys. Chem. C*, 2017, **121**, 21571–21578.

- 28 M. Molinari, S. C. Parker, D. C. Sayle and M. S. Islam, *J. Phys. Chem. C*, 2012, **116**, 7073–7082.
- 29 D. Fernández-Torre, K. Kośmider, J. Carrasco, M. V. Ganduglia-Pirovano and R. Pérez, *J. Phys. Chem. C*, 2012, **116**, 13584–13593.
- 30 M. Huang and S. Fabris, *J. Phys. Chem. C*, 2008, **112**, 8643–8648.
- 31 M. Nolan and G. W. Watson, *J. Phys. Chem. B*, 2006, **110**, 16600–16606.
- 32 M. Nolan, S. C. Parker and G. W. Watson, *Surf. Sci.*, 2006, **600**, 175–178.
- 33 Z. Wu, M. Li and S. H. Overbury, *J. Catal.*, 2012, **285**, 61–73.
- 34 T. Bunluesin, R. J. Gorte and G. W. Graham, *Appl. Catal., B*, 1998, **15**, 107–114.
- 35 Y. Chen, H. Wang, R. Burch, C. Hardacre and P. Hu, *Faraday Discuss.*, 2011, **152**, 121–133.
- 36 C. Schilling and C. Hess, *Top. Catal.*, 2017, **60**, 131–140.
- 37 A. Filtschew, K. Hofmann and C. Hess, *J. Phys. Chem. C*, 2016, **120**, 6694–6703.
- 38 Q. Wu, F. Zhang, P. Xiao, H. Tao, X. Wang, Z. Hu and Y. Lü, *J. Phys. Chem. C*, 2008, **112**, 17076–17080.
- 39 H.-X. Mai, L.-D. Sun, Y.-W. Zhang, R. Si, W. Feng, H.-P. Zhang, H.-C. Liu and C.-H. Yan, *J. Phys. Chem. B*, 2005, **109**, 24380–24385.
- 40 U. R. Pillai and S. Deevi, *Appl. Catal., A*, 2006, **299**, 266–273.
- 41 A. Laachir, V. Perrichon, A. Badri, J. Lamotte, E. Catherine, J. C. Lavalley, J. El Fallah, L. Hilaire, F. Le Normand, E. Quéméré, G. N. Sauvion and O. Touret, *J. Chem. Soc., Faraday Trans.*, 1991, **87**, 1601–1609.
- 42 D. A. Shirley, *Phys. Rev. B: Solid State*, 1972, **5**, 4709–4714.
- 43 C. T. Nottbohm and C. Hess, *Catal. Commun.*, 2012, **22**, 39–42.
- 44 C. Schilling and C. Hess, *J. Phys. Chem. C*, 2018, **122**, 2909–2917.
- 45 M. Tinoco, S. Fernandez-Garcia, M. Lopez-Haro, A. B. Hungria, X. Chen, G. Blanco, J. A. Perez-Omil, S. E. Collins, H. Okuno and J. J. Calvino, *ACS Catal.*, 2015, **5**, 3504–3513.
- 46 C. Schilling, A. Hofmann, C. Hess and M. V. Ganduglia-Pirovano, *J. Phys. Chem. C*, 2017, **121**, 20834–20849.
- 47 J. P. Perdew, K. Burke and M. Ernzerhof, *Phys. Rev. Lett.*, 1996, **77**, 3865–3868.
- 48 T. Tabakova, F. Boccuzzi, M. Manzoli, J. W. Sobczak, V. Idakiev and D. Andreeva, *Appl. Catal., B*, 2004, **49**, 73–81.
- 49 H. Y. Kim and G. Henkelman, *J. Phys. Chem. Lett.*, 2013, **4**, 216–221.
- 50 S. Fuente, M. M. Branda and F. Illas, *Theor. Chem. Acc.*, 2012, **131**, 1190.
- 51 J.-C. Liu, Y.-G. Wang and J. Li, *J. Am. Chem. Soc.*, 2017, **139**, 6190–6199.
- 52 S. Link and M. A. El-Sayed, *J. Phys. Chem. B*, 1999, **103**, 8410–8426.
- 53 J. A. Hernández, S. A. Gómez, T. A. Zepeda, J. C. Fierro-González and G. A. Fuentes, *ACS Catal.*, 2015, **5**, 4003–4012.
- 54 M. Nolan, J. Fearon and G. Watson, *Solid State Ionics*, 2006, **177**, 3069–3074.
- 55 C. W. M. Castleton, J. Kullgren and K. Hermansson, *J. Chem. Phys.*, 2007, **127**, 244704.
- 56 Y. Gao, R. Li, S. Chen, L. Luo, T. Cao and W. Huang, *Phys. Chem. Chem. Phys.*, 2015, **17**, 31862–31871.
- 57 N. Ta, J. Liu, S. Chenna, P. A. Crozier, Y. Li, A. Chen and W. Shen, *J. Am. Chem. Soc.*, 2012, **134**, 20585–20588.
- 58 N. Yi, R. Si, H. Saltsburg and M. Flytzani-Stephanopoulos, *Energy Environ. Sci.*, 2010, **3**, 831.
- 59 X.-P. Fu, L.-W. Guo, W.-W. Wang, C. Ma, C.-J. Jia, K. Wu, R. Si, L.-D. Sun and C.-H. Yan, *J. Am. Chem. Soc.*, 2019, **141**(11), 4613–4623.

- 60 Y. Lee, G. He, A. J. Akey, R. Si, M. Flytzani-Stephanopoulos and I. P. Herman, *J. Am. Chem. Soc.*, 2011, **133**, 12952–12955.
- 61 C. Schilling, M. V. Ganduglia-Pirovano and C. Hess, *J. Phys. Chem. Lett.*, 2018, **9**, 6593–6598.
- 62 G. N. Vayssilov, M. Mihaylov, P. S. Petkov, K. I. Hadjiivanov and K. M. Neyman, *J. Phys. Chem. C*, 2011, **115**, 23435–23454.
- 63 Z. V. Popović, Z. Dohčević-Mitrović, M. J. Konstantinović and M. Šćepanović, *J. Raman Spectrosc.*, 2007, **38**, 750–755.
- 64 Z. Dohčević-Mitrović, Z. V. Popović and M. Šćepanović, *Acta Phys. Pol., A*, 2009, **116**, 36–41.
- 65 M. Nolan, V. S. Verdugo and H. Metiu, *Surf. Sci.*, 2008, **602**, 2734–2742.
- 66 H. Y. Kim and G. Henkelman, *J. Phys. Chem. Lett.*, 2012, **3**, 2194–2199.
- 67 Q. Fu, A. Weber and M. Flytzani-Stephanopoulos, *Catal. Lett.*, 2001, **77**, 87–95.
- 68 A. A. Gokhale, J. A. Dumesic and M. Mavrikakis, *J. Am. Chem. Soc.*, 2008, **130**, 1402–1414.
- 69 M. B. Watkins, A. S. Foster and A. L. Shluger, *J. Phys. Chem. C*, 2007, **111**, 15337–15341.
- 70 J. Vecchietti, A. Bonivardi, W. Xu, D. Stacchiola, J. J. Delgado, M. Calatayud and S. E. Collins, *ACS Catal.*, 2014, **4**, 2088–2096.

Proceedings

Combined DFT and *Operando* Spectroscopic Study of the Water-Gas Shift Reaction over Ceria-Based Catalysts: The Role of the Noble Metal and Ceria Faceting †

Marc Ziemba, Danny Stark and Christian Hess *

Eduard-Zintl-Institute of Inorganic and Physical Chemistry, Technical University of Darmstadt, Alarich-Weiss-Str. 8, 64287 Darmstadt, Germany; marc.ziemba@tu-darmstadt.de (M.Z.); danny.stark@stud.tu-darmstadt.de (D.S.)

* Correspondence: christian.hess@tu-darmstadt.de

† Presented at the 1st International Electronic Conference on Catalysis Sciences, 10–30 November 2020; Available online: <https://eccs2020.sciforum.net>.

Published: 9 November 2020

Abstract: Ceria loaded with noble metals (Cu, Au) is a highly active material for the low-temperature water-gas shift reaction (LT-WGSR), but nevertheless details of the metal support interaction as well as the role of the ceria surface termination and the metal loading are still unclear. Using *operando* Raman and UV/Vis spectroscopy combined with theoretical density functional theory (DFT) calculations, we aim at a molecular-level understanding of LT-WGSR catalysts. In particular, by using this combined approach, we are able to draw conclusions about the reducibility state of the ceria support during reaction conditions. Our results show that the defect formation energy of the support does not play a major role for the WGSR, but rather other reaction steps such as the dissociation of water or the desorption of CO₂.

Keywords: ceria; supported metals; surface termination; water-gas shift; *operando* spectroscopy; density functional theory

1. Introduction

In the low-temperature (<200 °C) water-gas shift reaction (LT-WGSR), which is important for increasing the amount of hydrogen and reducing that of carbon monoxide in fuel cell applications, supported metals such as gold or copper on active supports such as ceria have been proven to be good alternatives to the conventional copper-zinc oxide catalysts used in industry [1–4]. According to the current state of research, the role of the metal and the ceria faceting during reaction remain unclear [3,5,6]. In our previous studies we could already demonstrate that for polycrystalline Au/CeO₂(111) catalysts, surface and bulk oxygen is involved in the reaction mechanism [4]. Thus, these results are consistent with a previously proposed and discussed redox mechanism [7–9]. In a very recent study, we evaluated the influence of the surface termination of Au/CeO₂ catalysts, and could show that CeO₂(111) is best suited for LT-WGSR [6].

In this study, we address gold and copper loaded ceria polyhedra and sheets as well as cubes with CeO₂(111) and CeO₂(100) surface terminations, respectively, to gain new insight into the structural dynamics during reaction and the associated significance of the metal and surface termination. For this purpose, we apply an *operando* spectroscopic approach, which combines Raman and UV/Vis spectroscopy. In addition, density functional theory (DFT) is used to calculate the vibrational frequencies, Raman activities and adsorption energies of possible reaction intermediates.

2. Methods

Ceria cubes were prepared by hydrothermal synthesis (for details see Ref. [10]), ceria polyhedra were obtained commercially (Sigma Aldrich, <25 nm (BET)), and ceria sheets were synthesized by thermal decomposition of $\text{Ce}(\text{NO}_3)_3 \cdot 6\text{H}_2\text{O}$ at 600 °C (for details see Ref. [4]). The gold loading was realized by means of an electrolyte deposition, which is described in more detail in Ref. [10]. Copper was loaded by incipient wetness impregnation using $\text{Cu}(\text{NO}_3)_2 \cdot 3\text{H}_2\text{O}$ as precursor and calcination at 500 °C. The target for all metal loadings was 0.5 wt% Au or Cu, respectively.

Operando Raman (532 nm) and UV/Vis spectra in combination with activity measurements using gas-phase FT-IR spectroscopy were recorded using an experimental setup that has been described previously [4,6,10–12]. All measurements were carried out at approx. 130 °C at the sample. Before reaction conditions (2% CO and 8% H₂O balanced in Ar) the sample was heated at the same temperature for about 1h in Ar. After applying reaction conditions, CO is switched off and 8% water is passed over the sample. The total flow rate was always 100 mL/min.

3. Results and Discussion

Figure 1 shows the catalytic activities of various CeO₂-based catalysts loaded with 0.5 wt% gold or copper. Comparison of the copper and gold catalysts shows that all gold loaded ones have a higher catalytic activity. It is worth mentioning that samples without noble metal loading do not show any conversion of CO. Furthermore, the Au-sheets show the highest activity; likewise, among the copper catalysts the sheets are the most active, although the polyhedra also possess a CeO₂(111) termination. In this context, comparison of the polyhedra and sheets shows that it is not only the surface termination of the support that matters, but also the particle shape. To this end, our previous studies have shown the presence of steps on ceria sheets [12]. These steps may have an influence on the catalytic activity, in fact earlier theoretical studies have demonstrated the increased activity of a stepped CeO₂(111) facet during CO oxidation [13]. These results underline that beside the metal and the metal support interaction, also the support properties may have a strong influence on the reaction process.

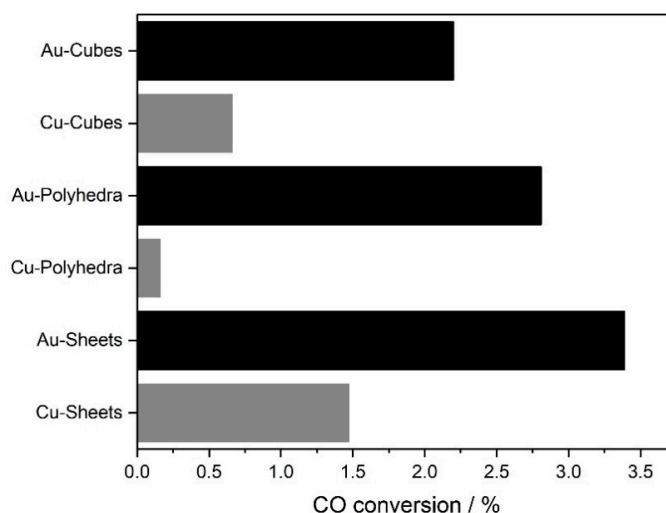


Figure 1. CO conversions (in %) during LT-WGS reaction of gold (black) and copper (gray) loaded (0.5 wt%) ceria catalysts with different morphologies. The catalytic activity was measured after at least 1 h on stream at about 130 °C under 2% CO and 8% H₂O balanced in Ar (total flow: 100 mL/min).

To better understand these catalytic activities, we will now take a closer look at the Au/CeO₂ catalysts using Raman spectroscopy, since these are expected to show larger variations in their properties due to their higher catalytic activities as compared to the copper samples. To this end, Figure 2a depicts Raman spectra of the gold loaded cubes, sheets, and polyhedra during WGS

conditions, while Figure 2b shows their spectra immediately after reaction conditions in a 8% H₂O stream. All samples show red-shifts of the F_{2g} band, which is a measure for near-surface oxygen defects [14], when switching from Ar atmosphere to reaction conditions (not shown). The observed red-shift is highest for the sheets (3.2 cm⁻¹), followed by the polyhedra (1.7 cm⁻¹) and the cubes (1.2 cm⁻¹), which correlates with the catalytic activity, i.e., sheets show the highest activity etc. This is also consistent with the UV/Vis results (not shown), which are characterized by an increase in absorption in the range above 450 nm (Ce³⁺ → Ce⁴⁺ charge transfer transitions) [12], when switching to reaction conditions, and an decrease under 8% H₂O after reaction conditions. However, the reduction of the support (see F_{2g} shifts and UV/Vis results) is not consistent with the oxygen defect formation energies, which is lowest on the CeO₂(100) facet [15]. These mentioned significant differences between sheets and polyhedra despite the same surface termination must be related to the presence of a stepped CeO₂(111) surface on the sheets. Hence, the defect formation energy of the support is not decisive for a high catalytic activity, but rather other factors such as the dissociation of water or the desorption of CO₂. In this context, previous studies have already shown that water dissociation is the rate-limiting step for Cu/CeO₂ catalysts during LT-WGSR [16] and that a stepped CeO₂(111) surface can reduce the CO₂ desorption energy [13]. Based on these observations, the above results are consistent with a redox mechanism that was confirmed in our previous studies [4]. In addition to the shift of the F_{2g} band, changes in the longitudinal and transversal surface modes of CeO₂(111) at 243 cm⁻¹ and 402 cm⁻¹ [14] disappear almost completely under WGSR conditions and reappear after switching to 8% H₂O for sheets and polyhedra. This can be explained by the removal of lattice oxygen under reaction conditions, thereby creating oxygen vacancies, which can be filled in the presence of H₂O and in the absence of CO. Furthermore, changes in the defect bands (540 and 590 cm⁻¹) are observed, which decrease again after switching from reaction conditions to 8% H₂O, which is also consistent with a blue-shift of the F_{2g} band.

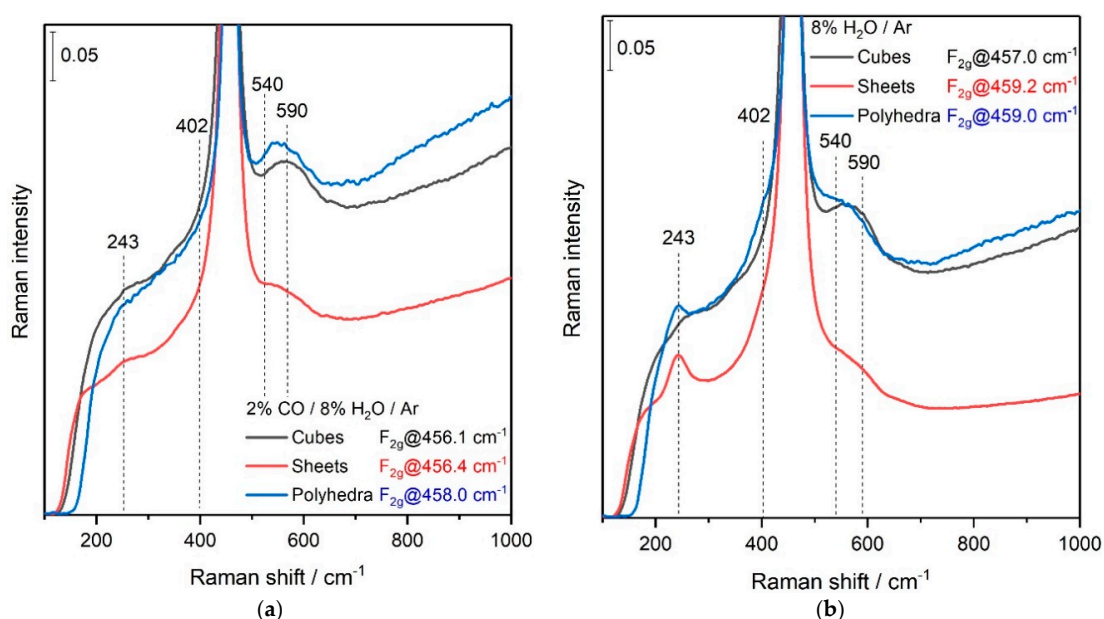


Figure 2. (a) *Operando* Raman spectra (532 nm) of ceria cubes (black), sheets (red), and polyhedra (blue) during WGSR conditions (2% CO/8% H₂O/Ar) and at a total flow rate of 100 mL/min. (b) In situ Raman spectra (532 nm) of ceria cubes (black), sheets (red), and polyhedra (blue) in 8% H₂O balanced in Ar after WGSR conditions (total flow: 100 mL/min).

4. Conclusions

In summary, based on the above data, CeO₂ catalysts loaded with gold are more suitable for LT-WGSR than those loaded with copper. Furthermore, using a ceria support with a stepped CeO₂(111) facet yields the best catalytic performance. *Operando* Raman spectra are consistent with a redox

mechanism involving lattice oxygen and therefore a Mars-van-Krevelen type mechanism. By examining different ceria facets, we could show that a low defect formation energy is not sufficient for high catalytic activities and that rather other aspects such as the water dissociation, the desorption of CO₂ or the metal support interaction play a major role. In conclusion, the combination of *operando* Raman and UV/Vis spectroscopy is a powerful tool for studying LT-WGSR over different metal ceria catalysts.

Author Contributions: Formal analysis and investigation, M.Z. and D.S.; data curation and original draft preparation, M.Z.; review and editing, M.Z., D.S., and C.H.; original idea, supervision, project administration, and funding acquisition, C.H. All authors have read and agreed to the published version of the manuscript.

Funding: This research received no external funding.

Acknowledgments: The DFT calculations were conducted on the Lichtenberg high performance computer of the TU Darmstadt. Jochen Rohrer and Karsten Albe are acknowledged for support with the VASP code. We thank Stefan Lauterbach and Hans-Joachim Kleebe for TEM measurements, Martin Brodrecht for BET measurements, M. Verónica Ganduglia Pirovano for support in theory and Karl Kopp for technical support.

Conflicts of Interest: The authors declare no conflict of interest.

References

1. Ratnasamy, C.; Wagner, J.P. Water Gas Shift Catalysis. *Catal. Rev.* **2009**, *51*, 325–440, doi:10.1080/01614940903048661.
2. Trimm, D.L. Minimisation of carbon monoxide in a hydrogen stream for fuel cell application. *Appl. Catal. A Gen.* **2005**, *296*, 1–11, doi:10.1016/j.apcata.2005.07.011.
3. Ren, Z.; Peng, F.; Li, J.; Liang, X.; Chen, B. Morphology-dependent properties of Cu/CeO₂ catalysts for the water-gas shift reaction. *Catalysts* **2017**, *7*, doi:10.3390/catal7020048.
4. Schilling, C.; Hess, C. Elucidating the Role of Support Oxygen in the Water–Gas Shift Reaction over Ceria-Supported Gold Catalysts Using Operando Spectroscopy. *ACS Catal.* **2019**, *9*, 1159–1171, doi:10.1021/acscatal.8b04536.
5. Trovarelli, A.; Llorca, J. Ceria Catalysts at Nanoscale: How Do Crystal Shapes Shape Catalysis? *ACS Catal.* **2017**, *7*, 4716–4735, doi:10.1021/acscatal.7b01246.
6. Ziemba, M.; Ganduglia-Pirovano, V.; Hess, C. Insight into the mechanism of the water-gas shift reaction over Au/CeO₂ catalysts using combined operando spectroscopies. *Faraday Discuss.* **2020**, doi:10.1039/C9FD00133F.
7. Fu, Q.; Saltsburg, H.; Flytzani-Stephanopoulos, M. Active nonmetallic Au and Pt species on ceria-based water-gas shift catalysts. *Science* **2003**, *301*, 935–938, doi:10.1126/science.1085721.
8. Bunluesin, T.; Gorte, R.J.; Graham, G.W. Studies of the water-gas-shift reaction on ceria-supported Pt, Pd, and Rh: Implications for oxygen-storage properties. *Appl. Catal. B Environ.* **1998**, *15*, 107–114, doi:10.1016/S0926-3373(97)00040-4.
9. Chen, Y.; Wang, H.; Burch, R.; Hardacre, C.; Hu, P. New insight into mechanisms in water-gas-shift reaction on Au/CeO₂(111): A density functional theory and kinetic study. *Faraday Discuss.* **2011**, *152*, 121–133, doi:10.1039/c1fd00019e.
10. Ziemba, M.; Hess, C. Influence of gold on the reactivity behaviour of ceria nanorods in CO oxidation: Combining operando spectroscopies and DFT calculations. *Catal. Sci. Technol.* **2020**, *10*, 3720–3730, doi:10.1039/D0CY00392A.
11. Nottbohm, C.T.; Hess, C. Investigation of ceria by combined Raman, UV–vis and X-ray photoelectron spectroscopy. *Catal. Commun.* **2012**, *22*, 39–42, doi:10.1016/j.catcom.2012.02.009.
12. Schilling, C.; Hess, C. Real-Time Observation of the Defect Dynamics in Working Au/CeO₂ Catalysts by Combined Operando Raman/UV–Vis Spectroscopy. *J. Phys. Chem. C* **2018**, *122*, 2909–2917, doi:10.1021/acs.jpcc.8b00027.
13. Kim, H.Y.; Henkelman, G. CO Oxidation at the Interface of Au Nanoclusters and the Stepped-CeO₂(111) Surface by the Mars–van Krevelen Mechanism. *J. Phys. Chem. Lett.* **2013**, *4*, 216–221, doi:10.1021/jz301778b.
14. Schilling, C.; Hofmann, A.; Hess, C.; Ganduglia-Pirovano, M.V. Raman Spectra of Polycrystalline CeO₂: A Density Functional Theory Study. *J. Phys. Chem. C* **2017**, *121*, 20834–20849, doi:10.1021/acs.jpcc.7b06643.

15. Nolan, M.; Parker, S.C.; Watson, G.W. The electronic structure of oxygen vacancy defects at the low index surfaces of ceria. *Surf. Sci.* **2005**, *595*, 223–232, doi:10.1016/j.susc.2005.08.015.
16. Gokhale, A.A.; Dumesic, J.A.; Mavrikakis, M. On the Mechanism of Low-Temperature Water Gas Shift Reaction on Copper. *J. Am. Chem. Soc.* **2008**, *130*, 1402–1414, doi:10.1021/ja0768237.

Publisher's Note: MDPI stays neutral with regard to jurisdictional claims in published maps and institutional affiliations.



© 2020 by the authors. Licensee MDPI, Basel, Switzerland. This article is an open access article distributed under the terms and conditions of the Creative Commons Attribution (CC BY) license (<http://creativecommons.org/licenses/by/4.0/>).

Approaching C1 Reaction Mechanisms Using Combined *Operando* and Transient Analysis: A Case Study on Cu/CeO₂ Catalysts during the LT-Water–Gas Shift Reaction

Marc Ziemba, Jakob Weyel, and Christian Hess*

Cite This: *ACS Catal.* 2022, 12, 9503–9514

Read Online

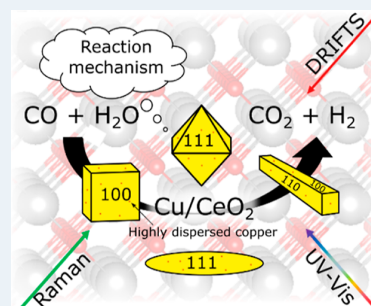
ACCESS |

Metrics & More

Article Recommendations

Supporting Information

ABSTRACT: The elucidation of reaction mechanisms is an essential part of catalysis research, providing approaches to improve catalysts or, ultimately, to design catalysts based on a profound understanding of their mode of operation. In the context of C1 processes, redox and/or associative mechanisms have been proposed in the literature, but their critical assessment has been a major challenge. Here, we highlight the importance of applying a combination of techniques suited to address both the redox properties and intermediate/adsorbate dynamics in a targeted manner. We illustrate our approach by exploring the mechanism of LT-WGS over low-loaded Cu/CeO₂ catalysts using different ceria morphologies (sheets, polyhedra, cubes, and rods) to study the influence of the surface termination. While the results from *operando* Raman and UV–vis spectroscopy are consistent with a redox mechanism, there is no direct correlation of activity with reducibility. Probing the subsurface/bulk oxygen dynamics using *operando* Raman F_{2g} analysis coupled with H₂¹⁸O highlights the importance of transport properties and the availability of oxygen at the surface. Transient IR spectra reveal the presence of different surface carbonates, none of which are directly involved in the reaction but rather act as spectator species, blocking active sites, as supported by the facet-dependent analysis. From transient IR spectroscopy there is no indication of the involvement of copper, suggesting that the catalytic effect of copper is mainly based on electronic effects. The results from the *operando* and transient analysis unequivocally support a redox mechanism for LT-WGS over Cu/CeO₂ catalysts and demonstrate the potential of our combined spectroscopic approach to distinguish between redox and associative mechanisms in oxide-supported metal catalysts.



KEYWORDS: mechanism, Cu/CeO₂, water–gas shift, *operando* spectroscopy, transient spectroscopy, Raman, DRIFTS, UV–vis

1. INTRODUCTION

Hydrogen plays a central role in the production of fine chemicals and in the energy sector. As its main source is the reforming of hydrocarbons,¹ it will be essential to use alternative sources, such as water splitting and the conversion of water in the framework of the water–gas shift (WGS) reaction, in the future. In addition, the WGS reaction plays an important role in adjusting the amount of hydrogen and carbon monoxide for fuel cell applications.² It is therefore of great importance to find efficient and cost-effective WGS catalysts that run efficiently even at low temperatures (<200 °C). Metal-loaded ceria has been proven to be a good alternative to the conventional copper–zinc oxide catalysts used in industry,^{3–6} but important aspects such as the reaction mechanism, the role of the metal, and the influence of the ceria support properties are still a matter of debate.

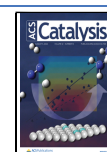
Redox and/or associative mechanisms have been proposed in the literature not only in the context of the WGS reaction but also for C1 processes (e.g., reverse WGS, RWGS). In the redox mechanism, adsorbed CO is oxidized to CO₂ by lattice oxygen from the support, leading to oxygen vacancy formation. The latter is replenished by water after O–H bond cleavage,

while hydrogen atoms combine to H₂. Associative mechanisms are based on the formation of surface intermediate species, starting from adsorbed CO and support hydroxyl groups, and their decomposition to CO₂ and hydrogen. As intermediates, formate,^{7–9} carbonate,^{10,11} carboxyl/carboxylate,^{12–15} and hydroxycarbonyl¹⁶ species have been proposed. In an earlier work on ceria-supported noble metals (Pt, Pd, Rh, and Au), a redox mechanism was proposed,^{17,18} while later, by use of IR spectroscopy, an associative formate-based mechanism was suggested¹⁹ and critically discussed.²⁰ Based on steady-state isotopic transient kinetic analysis on Pt catalysts, formate was excluded from being an important intermediate.⁸ Water dissociation was reported to be energetically important for the WGS reaction,^{8,13,21–24} but not rate-limiting, as shown for

Received: May 4, 2022

Revised: July 11, 2022

Published: July 20, 2022



Pt¹⁴ and Au²⁵ catalysts. Regarding Cu/CeO₂ catalysts, in particular, the interaction of metallic copper with oxygen vacancies (O_{vac}) was reported to enhance the reactivity,²⁶ as supported by studies on the inverse CeO₂/CuO–Cu system, where defect-rich ceria was proposed to be mainly responsible for water dissociation and metallic copper for providing adsorbed CO for the reaction.²⁷ In later studies, carbonates were proposed as intermediates using *operando* SSITKA-DRIFTS²⁸ (steady-state isotropic transient kinetic analysis–diffuse reflectance Fourier transform spectroscopy) and in situ DRIFTS,²⁹ but in the latter study, stationary measurements in helium as background were performed, therefore not allowing a definite statement on the mechanism. Thus, in the literature, two main mechanisms are currently being discussed for supported metal oxide catalysts, namely, the redox and associative mechanisms, and which mechanism is ultimately the more important and dominant one is not yet fully resolved.^{30,31}

Cu/CeO₂ catalysts have recently received increasing attention, showing good conversions in low-temperature (LT-)WGS.^{29,32–34} According to literature reports, the catalytic activity increases with the Cu loading,^{35,36} therefore, most studies have focused on highly loaded catalysts.^{29,33,37} However, normalized to the Cu content, the low-loaded catalysts show higher conversions.³⁶ Nevertheless, there are no detailed mechanistic studies on the loading dependence of the mechanism itself. In addition, it is worth mentioning that the method of loading copper onto the support has great influence on the catalytic activity, as it can affect the copper dispersion and particle size.^{34,37} For example, it has been shown that mesoporous copper–cerium–titania composites prepared by chemisorption–hydrolysis exhibit a higher activity than those prepared by incipient wetness impregnation (IWI) due to the presence of finely dispersed CuO particles.³⁸ In this context it is worth mentioning that our previous studies on Au/CeO₂ catalysts, exhibiting highly dispersed Au particles, have demonstrated facet-dependent agglomeration of gold during the reaction, limiting the WGS activity.^{39,40}

Previous literature studies on Cu/CeO₂ catalysts have highlighted the importance of the copper oxidation state,^{26,34,36,41} which depends on both the gas-phase environment and the loading.^{36,42,43} On the one hand, the interaction of metallic copper with oxygen vacancies (O_{vac}) was reported to enhance the reactivity,²⁶ while on the other, copper was shown to have an oxidation state of +1 at the interface and to participate in the reaction,⁴⁴ as supported by other studies, demonstrating the stability of oxidized copper under reductive conditions.⁴⁵ In addition, a strong dependence of the state of copper on the gas phase at 180 °C was observed for 20 wt % Cu/CeO₂, that is, mainly Cu⁰ was detected during CO exposure and Cu⁺ in the subsequent exposure to an inert gas.⁴² At low loadings, for example, 1 wt % Cu/CeO₂, the catalyst behaves differently, as rather Cu⁺ is observed under a CO atmosphere, which is then further oxidized to Cu²⁺ on switching to He,⁴³ indicative of electronic metal–support interactions.

Another important parameter for the Cu–ceria interaction and the reactivity behavior is the selection of the ceria facet. To this end, theoretical studies have revealed a dependence on the strength of the interaction of Cu with the low-index surface facets,^{34,46} which is also reflected in the catalytic activity.^{29,32–34,47} For 5 wt % Cu/CeO₂ catalysts, octahedra were found to exhibit the highest WGS activity at ≥200 °C,

followed by rods and cubes, by providing the best Cu dispersion, the largest amount of moderately active copper oxide, and the strongest Cu–support interaction.²⁹ To summarize previous literature findings, the state of copper when supported by ceria strongly depends on the copper loading, and so far a major focus has been placed on highly loaded catalysts. Thus, various aspects, such as the dependence of the mechanism on copper loading, oxygen/defect dynamics during reaction, and the role of copper and its state, are not sufficiently clarified.

In this study, we address the WGS reaction mechanism of low-loaded Cu/CeO₂ catalysts. To this end, it is important to develop approaches that enable the redox properties to be monitored on the one hand and the surface intermediate dynamics on the other. Thus, we combined *operando* Raman and UV–vis spectroscopy as well as isotopic labeling by H₂¹⁸O to probe (sub)surface properties. Modulation excitation (ME-)DRIFTS measurements with its increased sensitivity toward adsorbates,⁴⁸ complemented by quasi in situ XPS, allowed us to study the support and (transient) adsorbate dynamics as well as the surface state of Cu/CeO₂ catalysts in an integrated manner. Besides the mechanistic aspects, we address the role of ceria surface facets, highlighting the importance of the support properties, and compare our findings with those obtained previously for Au/CeO₂ catalysts,^{25,39,40} underlining the role of the supported metal.

2. EXPERIMENTAL SECTION

2.1. Catalyst Preparation. Polycrystalline ceria sheets were prepared by thermal decomposition of Ce(NO₃)₃·6H₂O (Alfa Aesar, 99.5%) at 600 °C as described in our previous studies.^{49,50} Ceria cubes and rods were prepared by the hydrothermal synthesis of CeCl₃·7H₂O (Alfa Aesar, 99%) and Ce(NO₃)₃·6H₂O (Alfa Aesar, 99.5%) in a NaOH solution (98%, Grüssing GmbH) as described in our previous studies.^{39,51} Ceria polyhedra or octahedra were purchased from Sigma-Aldrich [<25 nm (BET)].

Copper was loaded onto ceria via deposition–precipitation (DP) using a 10^{−3} M CuCl₂·2H₂O solution (Sigma-Aldrich, ≥99.5%), by first redispersing the ceria samples in a ratio of 1:150 in deionized water and adjusting the pH to 9 using a 0.1 M NaOH solution (98%, Grüssing GmbH). Subsequently, the copper chloride solution was set to pH 8 and added to the ceria suspension to obtain the desired loading. After the addition, the pH value was checked again and adjusted to 9. Then, the reaction mixture was heated at 65 °C for 2 h and placed in an ultrasonic bath for 30 min after cooling. Finally, the residue was centrifuged, washed four times with deionized water, and dried at 85 °C for at least 24 h.

2.2. Catalyst Characterization. **2.2.1. Transmission Electron Microscopy and Energy-Dispersive X-ray Measurements.** Transmission electron microscopy (TEM) measurements were performed on a JEOL JEM-2100F (Tokyo, Japan), which is equipped with a Schottky field emitter and operates at a nominal acceleration voltage of 200 kV. For preparation, the sample was dispersed in an ultrasonic bath for 30 s in ethanol and then placed on a carbon grid (Plano). After drying, the grid was coated with carbon (Bal-Tec MED010) to prevent charging by the electron beam. Energy-dispersive X-ray (EDX) spectra were recorded on an Oxford X-MAX 80 silicon drift detector (Oxford Instruments Nanoanalysis, High Wycombe, UK), which is attached to a JEOL JEM-2100F (Tokyo, Japan).

2.2.2. Operando Spectroscopy. The catalytic activity, *operando* Raman ($\lambda_{\text{ex}} = 532 \text{ nm}$) and UV–vis as well as quasi in situ XP measurements were performed using an experimental setup that has been described previously.^{25,39,50,52,53} Briefly, for the measurements, about 20–25 mg of the sample was placed in a stainless steel sample holder (8 mm diameter, 0.5 mm depth) and the catalyst temperature was set to 130 or 190 °C in all measurements. Due to the cell geometry and because the gases flow over the catalyst sample, the amount of catalyst has hardly any influence on the activity when the sample holder is fully covered. The gases CO (99.997%, Westfalen) and argon (99.996%, Westfalen) were dosed by digital mass flow controllers (MFCs, Bronkhorst), while H₂¹⁶O (electrical conductivity < 3 $\mu\text{S m}^{-1}$), H₂¹⁸O (97% + 18O, Eurisotop), and D₂¹⁶O (99.9% D, Sigma-Aldrich) were dosed by a controlled evaporator mixer (Bronkhorst) and a liquid mass flow meter (Bronkhorst). The total flow rate was set to 100 mL/min. All gas compositions were balanced in argon to keep the conversion low and eliminate the influence of possible transport effects, which allowed us to focus on the reaction mechanism. This also applies to the DRIFTS measurements, which will be described below.

The laser power for Raman measurements at the position of the sample was 1 mW, as measured with a power meter (Ophir). Spectra of the catalysts were recorded with an exposure time of 150 s and 3 accumulations. For all measurements, a cosmic ray filter and an auto new dark correction were applied, resulting in a total measuring time of about 1800 s for the Cu/CeO₂ catalysts. All Raman spectra reported in this work were normalized to the F_{2g} band, the position of which was determined by curve fitting using Lorentzian functions.

UV–vis spectra were taken before and after a Raman spectrum and the measuring time was 60 s, resulting from 200 runs with an exposure time of 300 ms each. As the white standard, magnesium oxide powder (MgO, Sigma-Aldrich) was employed, which shows no absorption between 170 and 1100 nm.

To analyze the gas phase and its composition, a Fourier transform infrared (FTIR) spectrometer (Tensor 20, Bruker) was installed at the outlet of the reaction cell. The resolution was 4 cm⁻¹, and the measurement time was 1 min, allowing for the accumulation of 125 spectra. Using calibration curves, the concentration of CO₂ was calculated to determine the conversion of CO. The catalytic activity is the ratio of the amount of CO₂, as measured by FTIR at the outlet of the cell, to the amount of dosed CO.

2.2.3. Quasi In Situ XPS. XP spectra were recorded on a modified LHS/SPECS EA200 MCD system using a Mg K α source (1253.6 eV, 168 W) as described previously.^{50,52,54} The calibration of the binding energy scale was performed with Au 4f_{7/2} = 84.0 eV and Cu 2p_{3/2} = 932.67 eV signals from foil samples. Prior to the measurements, the sample was treated successively with Ar, H₂O/CO/Ar, and H₂O/Ar at 190 °C, and the subsequent transfer of the sample into the analysis chamber was performed without air exposure (quasi in situ). To minimize partial charging, the sample was placed on a gold-coated stainless steel sample holder. Further sample charging was taken into account by setting the peak of the C 1s signal to 284.8 eV. Survey spectra were recorded at a resolution of 0.4 eV and detailed spectra at a resolution of 0.025 eV.

2.2.4. Modulation Excitation-DRIFTS. ME-DRIFTS was performed on an INVENIO spectrometer (Bruker) equipped

with a liquid nitrogen-cooled mercury cadmium telluride detector and a commercial reaction cell (Praying Mantis high temperature reaction chamber, Harrick Scientific Products) with infrared transparent ZnSe windows. Please note, a more detailed description of our basic DRIFTS setup has already been published,^{55,56} and the additionally needed MES setup (gas pipelines, communication channels, and data processing) is described in [ref 57].

In our measurements, 25–35 mg of the catalyst was placed in a stainless steel sample holder (8 mm \varnothing , 0.5 mm depth). The exact weight of the sample has hardly any influence on the catalytic activity due to the cell geometry and because the gas flows over the sample. In this context, our previous experiments on CO oxidation over Au/ceria catalysts have demonstrated a strong resemblance of the activities obtained in the Raman/UV–vis setup to those recorded in the DRIFTS setup, with regard to both absolute activities and temporal behavior.⁵⁶ As background, the catalyst itself was used after 15 min pretreatment in either H₂O atmosphere (100 mL min⁻¹ of 8 vol % H₂O in argon), D₂O atmosphere (100 mL min⁻¹ of 8 vol % D₂O in argon), or CO atmosphere (100 mL min⁻¹ of 2 vol % CO in argon) at the reaction temperature of 190 °C and a subsequent gas-phase modulation procedure (identical to the desired experiment), which ensures a reproducible state of the sample. The atmosphere during the background measurement was the same as in the respective pretreatment. For our measurements, we used the rapid scan mode extension of the spectrometer software OPUS 8.5. Spectra were measured from 850 to 4000 cm⁻¹ with a resolution of 0.2 cm⁻¹, an aperture of 6 mm, and a mirror speed of 120 kHz. A Valco Instruments 4/2 valve (model E2CA, version ED), communicating with the INVENIO, is used to rapidly switch the gas flows, which are set via digital MFCs (Bronkhorst).

During ME-DRIFTS, the sample is constantly exposed to one of the three feeds already described for the pretreatment. Whereas in the case of constant H₂O and D₂O (both kept at 8 vol %), at the same time a flux of CO is pulsed over the sample, changing from 0 to 2 vol %, and in the case of constant CO (kept at 2 vol %), a flux of H₂O or D₂O is pulsed, changing from 0 to 8 vol %. In all cases, the total flow rate is 100 mL min⁻¹ balanced with Ar. Switching the valve position initially resulted in a square wave modulation behavior of the modulation gas (CO or H₂O or D₂O) concentration, but due to the residence time behavior of the setup, it is better fitted by a sine wave, as already discussed in our previous work.⁵⁷

One measurement series consisted of 20 periods, with a duration of 292 s each. For each spectrum, five consecutive interferograms were averaged, so that one spectrum is acquired approximately every 3.7 s. This value is also used to approximate the experimental uncertainties of the time values derived from phase-sensitive detection (PSD). For further investigations on the stability of identical successive measurements, please refer to our previous work.⁵⁷

3. RESULTS AND DISCUSSION

3.1. Catalyst Characterization and Performance.

Regarding the characterization of the ceria samples, we refer to our previous studies.^{39,40,50,51} Briefly, the specific surface areas of sheets, polyhedra, cubes, and rods are 57, 36, 32, and 88 m² g⁻¹, respectively. TEM images of the corresponding particles are provided in ref 40 (cf. Figure 1). The copper loading was determined by inductively coupled plasma–optical

emission spectrometry to be 0.42, 0.46, 0.46, and 0.45 wt % for the sheets, polyhedra, cubes, and rods, respectively. Furthermore, no copper was detected by TEM in exemplary measurements on sheets and cubes before and after the reaction at 190 °C, the detection of which would be an indication of larger copper clusters (not shown). However, EDX verifies the presence of copper on the entire particles, for both large and small measuring areas (see Figure S1). Hence, the combined electron microscopy results point to the presence of highly dispersed copper on the surface of the ceria particles, in good agreement with the N₂O–CO temperature-programmed desorption (TPD) results of a previous study on similarly prepared Cu/CeO₂ catalysts, which revealed a copper dispersion of 100% at a loading of 1.9 wt %.⁵⁸

Figure 1 summarizes WGS activities at 130 and 190 °C for the different Cu/CeO₂ catalysts. At both temperatures, the

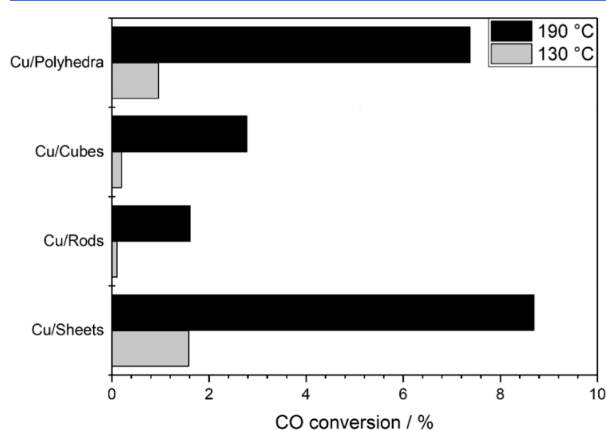


Figure 1. Percentage CO conversion during LT-WGS of Cu/CeO₂ catalysts with different morphologies at 130 and 190 °C. The catalytic activity was measured after at least 1 h on stream in 2 vol % CO/8 vol % H₂O/Ar (total flow rate: 100 mL/min).

same trend in conversion is observed: sheets > polyhedra > cubes > rods. Under these conditions, the bare ceria samples show no significant WGS activity. Interestingly, the activities are very different from those of Cu/CeO₂ catalysts prepared by

IWI,⁵⁹ which is expected to result in lower copper dispersions than the DP method. According to Figure 1, polyhedra- and sheet-based catalysts gave by far the highest conversions, while for the catalysts in ref 59 prepared by IWI, the cubes were more active than the polyhedra, which is consistent with literature results on 5 wt % Cu/CeO₂ catalysts prepared by the DP method.²⁹ It needs to be mentioned, however, that for the catalysts used in this study, the copper loading was about 10 times smaller and thus on average smaller copper clusters are expected to be present on the surface.²⁹ In any case, the observed differences in reactivity behavior highlight that, besides the preparation method and copper loading, which may both affect the copper dispersion, also the ceria surface termination plays a major role regarding the WGS activity of Cu/CeO₂ catalysts. In this study, we will focus on samples prepared by DP because these samples show slightly higher conversions. In the following, mostly *operando* measurements at 190 °C will be presented to illustrate the largest possible structural changes.

3.2. Copper State: Dependence on Gas Exposure. To characterize the copper state, we employed quasi in situ XP and *operando* UV–vis spectroscopy. XP spectra were recorded after pretreatment in an argon reaction atmosphere and H₂O at 190 °C (see Figure S2). Due to the small copper loading, only the Cu 2p_{3/2} photoemission gave an acceptable signal-to-noise (S/N) ratio. While the binding energies of Cu⁰ and Cu⁺ hardly differ, the presence of Cu²⁺ can be identified via its slightly shifted binding energy and a shake-up structure, as discussed previously in the context of reference substances (Cu foil, Cu₂O, CuO).⁶⁰ Our samples contain finely dispersed copper on ceria, which may show significantly shifted binding energies as a result of metal–support interactions.⁶¹ Additionally, the copper coverage may have an influence on the position of the Cu 2p_{3/2} signal.⁶² Nevertheless, shake-up structures, which are indicative of Cu²⁺, are evident at 943 eV, especially for the sheets and polyhedra. In the absence of the reaction mixture, electronic metal–support interactions occur, which are expected to oxidize metallic copper.^{42,43} Previous studies have also shown that at low loadings (1 wt % Cu), no metallic copper is present on the surface, even during CO treatment.⁴³ We therefore attribute the observed Cu 2p_{3/2} photoemission to Cu⁺ and/or Cu²⁺, which is underlined by our UV–vis results

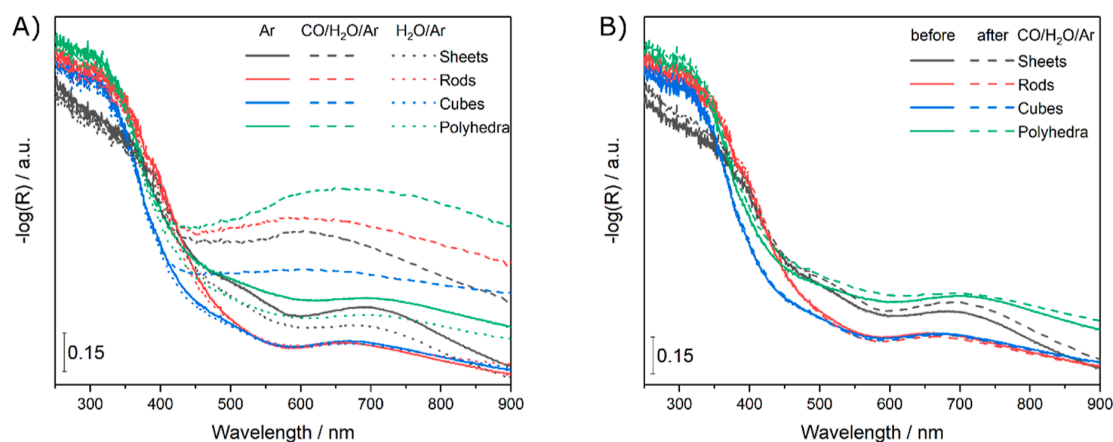


Figure 2. In situ/*operando* UV–vis reflectance spectra of Cu/CeO₂ sheets (black), rods (red), cubes (blue), and polyhedra (green) at 190 °C (A) for different gas exposures, (B) before and after reaction conditions.

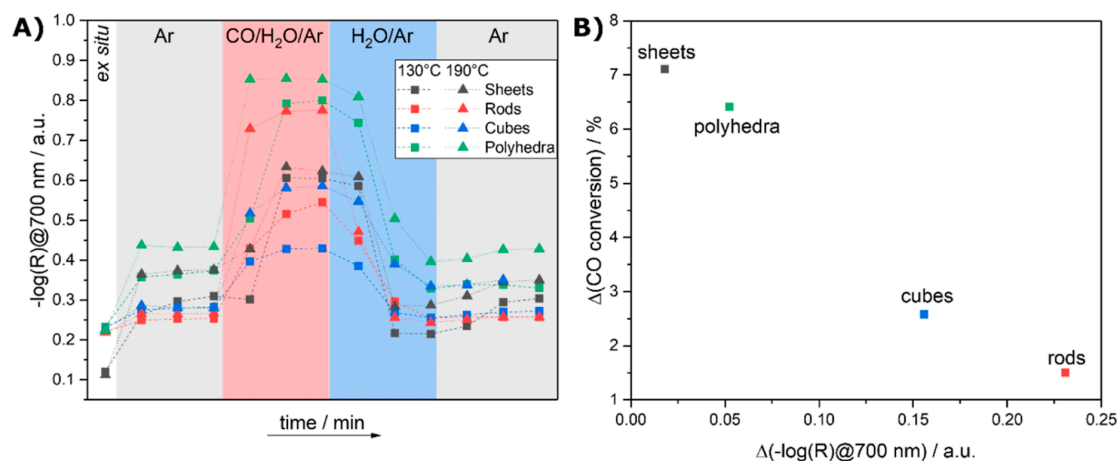


Figure 3. (A) In situ/operando UV-vis results for Cu/CeO₂ catalysts recorded during the indicated gas exposures at 130 °C (square) and 190 °C (triangle) and at a total flow rate of 100 mL/min, except for the ex situ spectra, which were taken at 25 °C. Spectra were recorded at the beginning, after about 30 min, and after about 1 h of exposure to the indicated gas phases. (B) Correlation of the difference in CO conversion at 190 and 130 °C with the difference in absorbance at 700 nm, determined approximately 1 h after beginning to apply reaction conditions.

discussed next, which allow changes to be detected when switching between different gas environments.

The *operando* UV-vis spectra in Figure 2 were recorded at 190 °C, successively in argon, reaction atmosphere, water, and argon. All UV-vis spectra show a dynamical absorption behavior in the visible region, which is generally characterized by Ce⁴⁺–Ce³⁺ charge transfer transitions (broad),⁶³ absorption bands of Cu⁺ and/or [Cu₂O]²⁺ species (400–470 nm), and d–d Cu²⁺ transitions (600–850 nm).^{64–66} Besides, copper surface plasmons may contribute to the signal (520–580 nm), providing evidence of larger metallic copper domains (Cu_n),^{67,68} while highly dispersed metallic copper may not be detectable by UV-vis.

The samples show clear differences in their absorption behavior (see Figure 2), but it is difficult to make quantitative statements, owing to the width of the bands. The sheets and polyhedra (see Figure 2A) show a significantly higher absorption for wavelengths >450 nm in argon, which speaks for the presence of Cu⁺ and/or [Cu₂O]²⁺ species. In addition, all samples show a band at about 700 nm, which is most pronounced for the sheets but has the highest (and broadest) absorption for the polyhedra. Because previous studies provided no evidence of metallic copper on low-loaded Cu/CeO₂,⁴³ this band can be assigned to Cu²⁺.⁶⁵ The observations indicate significant differences in the copper species under argon, whereby the 111 surfaces possess the highest fraction of Cu⁺ and Cu²⁺ on the surface, consistent with our XPS results.

When switching to reaction conditions, all samples show a broad increase in absorbance at wavelengths above 450 nm, indicating a reduction of the support. When CO is switched off, this absorption feature decreases again; in the case of the polyhedra and sheets, it becomes even lower than that detected in the argon phase prior to reaction conditions. The width of the feature may suggest that the sheets and polyhedra are more oxidized than in the initial argon phase, in contrast to the rods and cubes, which do not show any significant changes in the spectral profile.

To check the stability of the catalysts, we compared the UV-vis spectra in argon before and after applying reaction conditions. Figure 2B reveals that the rods and cubes do not undergo any changes, while the sheets and polyhedra show a

slightly higher absorption over the entire visible range. Especially for the sheets, this is noticeable in the region around 700 nm and may be indicative of an increase in Cu²⁺ species. Interestingly, in a direct comparison with our previous results on Au/CeO₂ catalysts with similar noble metal loadings, where the increase in vis absorption from one argon phase to the other correlated negatively with the activity,^{39,40} the Cu/CeO₂ samples show an inverse behavior (see also below). In the case of the gold samples, we could attribute the observed behavior to gold agglomeration. For the copper samples, agglomeration is unlikely, as it would lead to lower activities over time, which is not consistent with our results. We therefore attribute the observed UV-vis behavior to an increase in the amount of Cu⁺ and Cu²⁺ surface species.

3.3. Structural Dynamics under Reaction Conditions.

For better visualization of the dynamic changes in the UV-vis spectra, Figure 3A shows the absorbances at 700 nm under different gas atmospheres at 130 and 190 °C. There is a clear dependence on the gas-phase composition and temperature. All samples reach their maximum absorption under reaction atmosphere and show a reversible behavior in H₂O or argon, as already indicated in Figure 2.

At 190 °C, the absolute increases are slightly higher than at 130 °C, but vary significantly between the samples. Figure 3B depicts the negative correlation between the differences in CO conversion and the absorbances under reaction conditions at the two temperatures, showing a near-linear behavior. As mentioned above, the broad increase in absorption is mainly due to the reduction of the support materials. Considering that there is no relation between the CO conversions and specific surface areas, we can conclude that defects are only a minor factor in determining the catalytic activity; thus, a surface too rich in defects (e.g., rods) may not be beneficial for WGS over Cu/CeO₂. This is further supported by the observation that the absolute change in absorption upon switching from argon to reaction conditions does not correlate with the WGS activity, consistent with previous results on CO oxidation, which have shown that the Ce³⁺ fraction is not correlated with activity and that the state of copper is of greater importance.⁴²

Next, the results from Raman spectroscopy at 532 nm excitation will be discussed. In the context of ceria-based

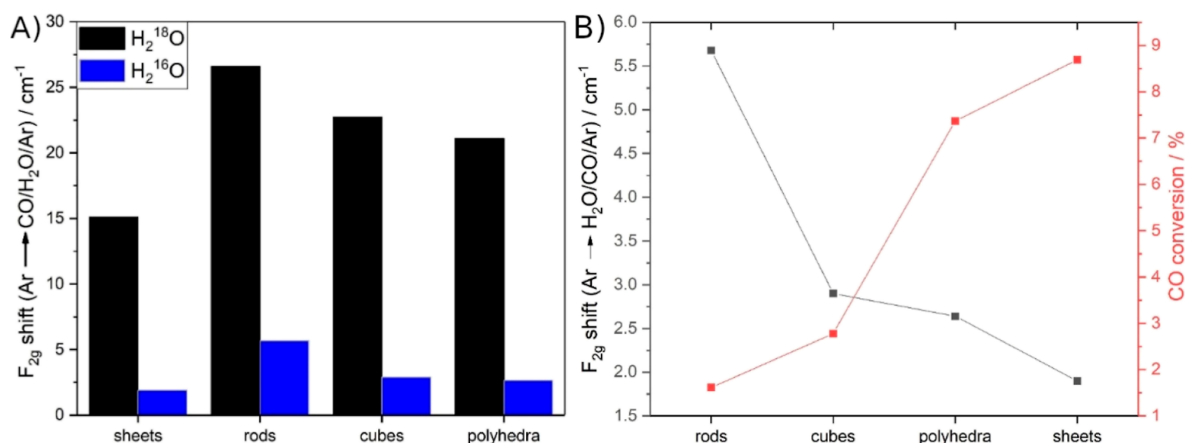


Figure 4. In situ/operando Raman spectroscopic results (532 nm) showing the (A) F_{2g} shifts of Cu/CeO₂ catalysts when switching from the argon atmosphere to reaction conditions (CO/H₂O/Ar; flow rate: 100 mL/min) using H₂¹⁶O (blue) and H₂¹⁸O (black), (B) correlation between F_{2g} shifts and CO conversion.

catalysts, the F_{2g} band provides important information about the oxygen dynamics, as shown previously.^{39,50,53} Figure 4A depicts the F_{2g} shifts when switching from the first argon to the reaction phase. In addition, as part of the measurements, isotope labeling by H₂¹⁸O was used to follow the exchange of lattice oxygen by H₂O. As discussed previously, at constant temperature, the F_{2g} shift allows changes in the defect density of the support to be monitored.⁵⁰ The gas-phase-dependent F_{2g} positions (see Figure S3) show a behavior similar to that described in the context of the UV–vis data in Figure 3. However, absolute changes differ from those in the UV–vis spectra. For example, the polyhedra show the highest absorption in the UV–vis measurements, while the F_{2g} red shift is lowest after the sheets. This behavior may be explained either by additional copper contributions to the UV–vis spectra, which dominate the Ce⁴⁺–Ce³⁺ charge transfer transitions, or by the different penetration depths of the two methods. Closer inspection of the F_{2g} shifts in Figure 4A when using H₂¹⁶O under reaction conditions (blue bar) reveals the following trend regarding the F_{2g} red shift: sheets < polyhedra < cubes < rods. Thus, the sheets are reduced the least, while the rods are reduced the most. As the same trend is also observed for H₂¹⁸O (black bar), the same applies to the replacement of lattice oxygen by ¹⁸O. Interestingly, the absolute F_{2g} shifts at 130 °C (not shown) are identical to those at 190 °C despite the lower activity, which is a clear indication that the catalytic activity is not linked to the support reducibility. This is further supported by the negative correlation of the F_{2g} shifts with the CO conversions, shown in Figure 4B. Based on the above findings from in situ/operando Raman spectroscopy, we can exclude a mechanism that is only linked to the reducibility, fully consistent with the UV–vis results.

From the Raman spectra during reaction conditions and H₂¹⁶O exposure (see Figure S4) it is difficult to extract further information besides the F_{2g} position owing to self-absorption (see UV–vis results) and fluorescence effects. An exception is the detection of a feature at around 1560 cm⁻¹ for the polyhedra and cubes, which becomes even more obvious at 130 °C (see Figure S5) and may indicate the presence of carbonates. For unloaded samples this band is not observed

(not shown). Adsorbate signals will be discussed in more detail below in the context of the DRIFTS measurements.

An important aspect regarding the functioning of ceria-based catalysts is the mobility of lattice oxygen and/or oxygen vacancies. To this end, it should be pointed out that all samples exhibit an F_{2g} blue-shift when switching from reaction conditions to H₂¹⁶O (see Figure S3), demonstrating that the support is oxidized by water. Interestingly, for H₂¹⁸O, a different behavior is observed. This is illustrated by Figure 5,

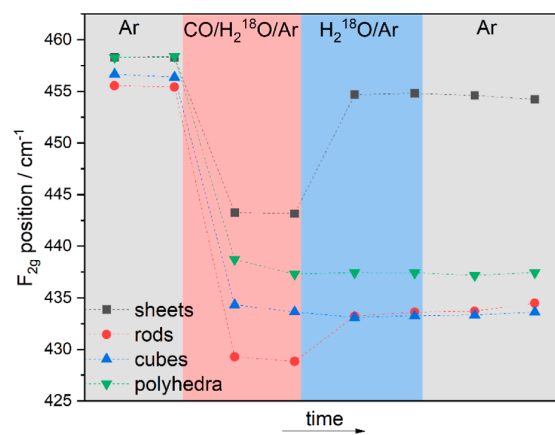


Figure 5. In situ/operando Raman F_{2g} positions for Cu/CeO₂ catalysts exposed to the indicated gas environments at 190 °C using H₂¹⁸O (total flow rate: 100 mL/min). The underlying spectra were recorded at 532 nm excitation and after gas-phase exposure for about 30 min and 1 h.

which depicts the F_{2g} positions during the different gas phases at 190 °C. It is noticeable that polyhedra and cubes do not undergo any changes in the F_{2g} position after reaction conditions, while the F_{2g} positions of the sheets and rods show blue shifts of 11.7 and 4.8 cm⁻¹, respectively. Compared with the blue shifts detected after reaction conditions in the case of H₂¹⁶O, these shifts are significantly larger for the sheets (3.0 cm⁻¹) and slightly smaller for the rods (5.4 cm⁻¹). Before discussing the observed behavior, we will briefly summarize the different contributions to the F_{2g} shifts. The reduction of the

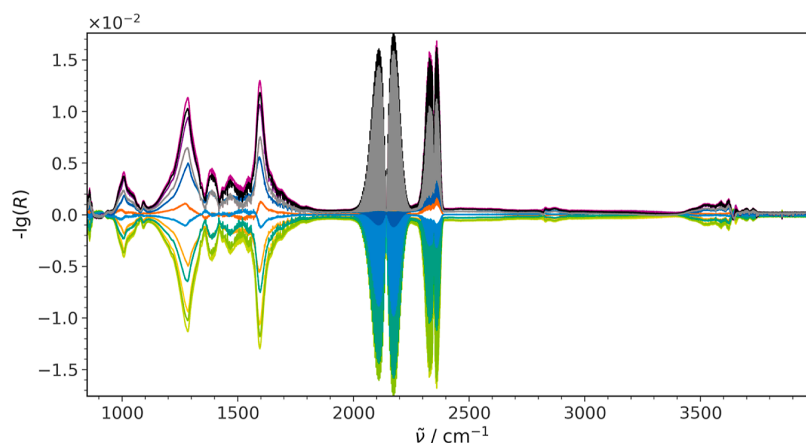


Figure 6. PSD spectra of Cu/CeO₂ sheets at 190 °C. The gas-phase composition was periodically changed from 8 vol % H₂O/Ar to 2 vol % CO/8 vol % H₂O/Ar.

support and the exchange of ¹⁶O by ¹⁸O lead to a red shift, while the opposite processes, that is, the oxidation or the exchange of ¹⁸O by ¹⁶O, lead to blue shifts. Because each sample undergoes oxidation (accompanied by a blue shift) upon switching from reaction conditions to H₂¹⁶O flow, there must be a further exchange of ¹⁶O with ¹⁸O by H₂¹⁸O for the polyhedra and cubes, which compensates the blue shift due to support oxidation. For the rods, a blue shift is observed, which may originate from oxidation and/or diffusion of ¹⁶O from the bulk to the (sub)surface. We propose that in the case of the rods, further exchange of ¹⁶O with ¹⁸O (from H₂¹⁸O) plays a minor role in contrast to the cubes and polyhedra because the difference in the comparison of the use of H₂¹⁶O and H₂¹⁸O and the absolute shift between reaction conditions and the subsequent H₂O phase is less than 1 cm⁻¹. For the sheets, the blue shift is by 8.7 cm⁻¹ larger than that detected as a result of oxidation during the H₂¹⁶O experiments. Remarkably, this behavior reveals that the ceria sheets facilitate the transport of ¹⁶O from the bulk to the (sub)surface. In this context, it should be pointed out that the red shift under reaction conditions is smallest for the sheets and thus most of the ¹⁶O is still present. In contrast, the polyhedra, which come closest to the sheets regarding the F_{2g} shifts, exhibit a completely different behavior, as mentioned above. Thus, the ceria sheets are the only support material that shows a high mobility of lattice oxygen and/or oxygen vacancies, probably contributing to its high activity, while surface area related effects can be excluded because, for example, the rods have a larger surface area than the sheets.

ME-DRIFTS experiments were conducted to explore the adsorbate dynamics and to assess the possibility of an associative mechanism. As potential adsorbates participating in the reaction, carbonates (850–1800 cm⁻¹), CO adsorbates (2000–2200 cm⁻¹), and hydroxyls (3400–3800 cm⁻¹) may be expected. Figure 6 depicts the complete PSD spectra of a CO pulse experiment (i.e., switching between 0 and 2 vol %) with a constant flow of 8 vol % H₂O/Ar over Cu/CeO₂ sheets. The same type of experiments was also performed for the other Cu/CeO₂ samples as well as the bare supports (see Figures S6 and S7), revealing a similar overall behavior despite differences in the spectral profiles. In Figure 6, the carbonate region is characterized by signals at 1009, 1285, 1388, 1434, 1470, 1547, and 1597 cm⁻¹. The most intense signals, at 1285 and 1597

cm⁻¹, are attributed to the presence of bidentate carbonate,^{50,69} while the residual features originate from other carbonate-like species, for example, bridged formate species.^{69,70} Notably, in the CO region, no signals are detected, except the contributions of gaseous CO (see Figure S8). To this end, our previous studies have demonstrated that the sensitive detection of adsorbed CO is not limited by the presence of the gas-phase CO signature.⁵⁷ Thus, based on our findings from transient ME-DRIFTS-PSD, a major contribution of CO adsorbates to the WGS reaction can be ruled out. This is in accordance to an in situ (steady state) DRIFTS study on low-loaded Cu/CeO₂, which did not report any CO adsorbates above 150 °C.³⁶ Even enhancing the time resolution in another series of experiments, in which spectra were recorded every 0.5 s, did not lead to the appearance of any CO-related adsorbate signals. Inverting the modulation sequence by switching H₂O (between 0 and 8 vol %) at a constant flow of 2 vol % CO/Ar reveals a minor signal at around 2109 cm⁻¹, which is characteristic of Cu⁺–CO species (see Figure S8 for enlarged view and Table S1).⁷¹ Considering that the signal is small and only appears in modulation experiments favoring its presence, we propose CO adsorbates to have a negligible (if any) role in the WGS reaction. To further clarify this behavior, we also performed steady-state DRIFTS measurements on the sheets (see Figure S11). These clearly show that a band is visible at 2109 cm⁻¹ under CO/Ar, but decreases significantly under reaction conditions. The electronic contribution⁷² at 2025 cm⁻¹ remains constant, which is why it does not appear in the ME-DRIFTS experiments. Thus, the steady-state results are fully consistent with our ME-DRIFTS results.

The hydroxyl region contains signals at 3530, 3622, 3642, and 3653 cm⁻¹, as well as contributions of combination bands of gaseous CO₂ centered at about 3610 and 3710 cm⁻¹.⁷³ The hydroxyl feature at 3620 cm⁻¹ is attributed to a triply bonded OH group (type III),⁷⁴ while those at 3642 and 3653 cm⁻¹ are associated with OH (type II-B) and OH (type II*-B),⁷⁵ which may mutually transform into each other (see below). The assignment of the 3530 cm⁻¹ feature is less obvious. Previously, OH features within 3520–3660 cm⁻¹ have been assigned to bi- and tri-coordinated species,⁷⁶ also consistent with our other hydroxyl assignments.

From the PSD spectra, time values were determined, which show the sequence of signals within one (modulation) period, thus yielding important mechanistic information (see Table 1).

Table 1. Results from Transient IR-PSD Analysis of Cu/CeO₂ Sheets^a

position/cm ⁻¹	t(Cu/CeO ₂)/s	assignment
3653	73	OH (II*-B)
3642	46 (-)	OH (II-B)
3622	45	OH (III)
3530	45	OH (type III)
2361	40	CO ₂ (g)
2064	23	CO (g)
1597	45	bidentate carbonate
1547	50	carbonate species
1470	48	carbonate species
1434	49	carbonate species
1388	50	carbonate species
1285	45	bidentate carbonate
1009	46	bidentate carbonate

^aTime values correspond to the signal onset, and signals of decreasing bands are marked with (-). Refer to Figure 6 for the underlying PSD spectra.

The first two signals that appear correspond to the CO reactant (~23 s) and the product CO₂ (~40 s), while the signals within the carbonate region show larger time values (45–50 s), as do the hydroxides at 3530 and 3622 cm⁻¹. The OH signal at 3653 cm⁻¹ (II*-B) increases and that at 3642 cm⁻¹ (II-B) decreases in the more reductive phase (i.e., during CO pulsing), as would be expected (see Table 1). On the other hand, as these signals are expected to mutually transform into each other, it appears surprising at first that they do not appear at exactly the same time value (with opposite sign). The observed deviation may originate from their overlap with other signals, thereby mixing up their time values, as has been discussed in more detail previously.⁵⁷

Taking into account the experimental uncertainty of 3.7 s for the time values, none of the species observed in the carbonate and hydroxide region may take part in the initial formation of the product CO₂.

To identify signals of catalytically active species, we follow a routine comprising three main steps. In the first step, spectator signals are removed by subtracting a background spectrum of a catalyst that has already undergone several modulation periods prior to the actual modulation experiment and by applying a PSD to the recorded data set. In the second step, we characterize the species that appear in the PSD spectra as a result of the periodic (precursor) concentration changes according to their temporal behavior. For a consistent picture, the comparison of PSD spectra from different reactant modulation schemes is crucial, as catalytically active species are expected to appear in both data sets and at comparable times.

Following our routine, additional ME-DRIFTS experiments were performed, in which now the 2 vol % CO/Ar flow was kept constant and water was periodically pulsed, thus switching from 0 to 8 vol % share of the total flow (see Figure S9). A comparison of the spectra obtained with both modulation approaches (pulsing CO or H₂O) is shown in Figure S10. At this point, it should be noted that both cases lead to similar CO₂ conversions because both modulation conditions result in

the same (dynamic) conditions that enable the WGS reaction. Temporal analysis reveals that all of the detected signals appear or disappear more or less at the same time as the pulsed H₂O component, except those of CO₂ or weakly adsorbed H₂O, which are delayed by ~3–5 s (see Table S1). In the hydroxyl region, clear signals are missing (see Figure S10), suggesting that there are no actively participating hydroxyls involved in H₂ formation. It should be mentioned, however, that weak hydroxyl signals may be masked by contributions from gaseous and weakly adsorbed water in that spectral region. Besides, the possibility of a highly labile and fast-reacting hydroxyl species, as suggested previously, cannot be excluded.³⁶ When comparing the combined results from the modulation experiments, there is no spectroscopic evidence that would unambiguously point toward an associative mechanism. Although some adsorbate signals are observable in the spectra of both modulation experiments (see Figure S10), the temporal analysis reveals that all adsorbate signals in the CO modulation experiment are observed after product formation (see Table 1), while in the case of H₂O modulation, signals appear slightly earlier than product formation (see Table S1). Therefore, the observed behavior may be described by adsorption/desorption processes taking place when the respective reactant CO or H₂O is pulsed over the surface, rather than a direct participation in the reaction.

The bidentate carbonate pattern observed in Figure 6 did not appear when H₂O was pulsed (see Figure S9), which was further confirmed by D₂O pulsing experiments aiming at a carbonate region less crowded by gaseous water. Although these experiments cleared the view for the carbonate region, the findings from our H₂O measurements were confirmed, that is, that there is no signal of an active species that might be attributed to CO₂ formation.

4. DISCUSSION OF THE REACTION MECHANISM

In the literature, two main mechanisms have been proposed for the WGS reaction over metal-supported oxide catalysts: a redox mechanism and an associative one. The latter proceeds via intermediates, for example, carbonates, formates, or hydroxides.^{30,31,77} Furthermore, theoretical studies on pure CeO₂(111) show a combined redox–associative route.⁷⁸ It has been challenging to find *operando* approaches that enable a critical assessment of the reaction mechanism. Here, we propose a spectroscopic approach based on the combination of *operando* and transient methods. In this context it should be mentioned that the type of mechanism depends on the properties of the catalyst system as well as on the temperature.

Based on our spectroscopic findings, we identified several catalyst properties that may be related to the activity of the catalyst. These include the reducibility, whose dynamics could be followed by means of *operando* Raman and UV–vis measurements; the mobility of lattice oxygen, which could be detected by the H₂¹⁸O Raman experiments; and the tendency to form stable adsorbates (e.g., surface carbonates), which may block active sites. The last property is of particular relevance for the 110 and 100 surface (rods and cubes), as demonstrated previously by CO-TPD for bare octahedra, cubes, and rods,⁷⁹ and by Raman/UV–vis spectroscopy for low-loaded Au/CeO₂.³⁹ In addition, from our transient spectra, there is no evidence for the presence of intermediates on either the support or copper, which would have supported an associative mechanism. Instead, our results are in agreement with a redox

mechanism, consistent with our previous studies on Au/CeO₂ catalysts.^{25,39}

The *operando* Raman results have revealed a negative correlation of the F_{2g} shift with the conversion (see Figure 4B), demonstrating that the reducibility is not directly responsible for the activity. Based on the assumption of a redox mechanism, this finding may be related to the fact that oxygen must be available at the surface to allow for facile oxidation of CO. To this end, the isotope experiments have shown that in the case of sheets, oxygen is readily supplied to the surface for CO oxidation. We therefore propose the superior LT-WGS performance of the sheet-based catalysts to be related to the availability of surface oxygen. In fact, for the less active polyhedra, a significantly lower diffusion of oxygen (vacancies) from bulk to surface was observed (see Figure 5). For the cubes and rods, on the other hand, the reducibility is too high, leading to an enhanced reactivity toward CO₂ and the formation of surface carbonates, which may block active sites.

The comparison of loaded and unloaded samples clearly shows that the presence of copper plays a major role because none of the ceria supports exhibit any LT-WGS activity. To this end, besides the specification of the copper oxidation state, the role of copper in the mechanism is of importance. Starting with the last point, our transient DRIFTS measurements provide no indication for an active involvement of copper in the reaction. While we cannot exclude hydrogen recombination occurring so rapidly that it cannot be detected despite the use of a transient method, we rather propose copper to change the electronic properties. This is supported by the *operando* UV–vis spectra because, for example, the unloaded sheets and polyhedra (not shown) do not show any significant changes in the visible range in contrast to the loaded samples. Thus, the presence of even small loadings of copper significantly changes the reduction properties. This is also supported by the Raman spectra, which do not show significant F_{2g} red shifts under reaction conditions.³⁹

Regarding the oxidation state of copper, our UV–vis and XPS results suggest that the surface termination plays a role. In particular, the 111 surfaces were found to exhibit a larger fraction of Cu²⁺ on the surface, which we postulate as a possible reason for the higher activities of the polyhedra and sheets.

In summary, our results are consistent with a redox mechanism in which oxidation occurs by water, with oxygen being incorporated into the crystal lattice. This process is so fast that no intermediates are observed. Finally, reduction takes place by CO, which immediately reacts to CO₂.

5. CONCLUSIONS

In this work, we demonstrate the use of a combined *operando*/transient spectroscopic approach to investigate the redox properties and the intermediate/adsorbate dynamics on supported metal catalysts. We address low-loaded Cu/CeO₂ catalysts during the LT-WGS reaction, providing first evidence for a pure redox mechanism using coupled *operando* Raman and UV–vis spectroscopy, which in turn is supported by transient ME-DRIFTS experiments. Thus, information about bulk CeO₂ can be obtained using Raman and UV–vis spectroscopy, while UV–vis spectra provide additional information about dispersed copper species. ME-DRIFTS measurements are used to identify surface intermediates. To explore the facet-dependent behavior, ceria sheets (111, steps), polyhedra (111), cubes (100), and rods (110, 100) are studied.

Summarizing the key findings, there is no direct correlation between activity and reducibility based on the conversion data and the *operando* Raman and UV–vis results, while the use of H₂¹⁸O experiments underlines the importance of transport properties and the availability of oxygen at the surface. Regarding surface processes, our transient DRIFTS measurements do not show any active participation of copper or adsorbates in the WGS reaction; while the presence of various surface carbonates is observed, temporal analysis reveals their role as spectator species. However, it should be noted, that highly reactive surface intermediates cannot be completely excluded, despite the also previously shown high sensitivity of ME-DRIFTS.^{50,57}

With respect to copper, we can conclude that its participation in the catalysis is mainly based on electronic effects. Such observations have also been reported in previous studies on Cu/CeO₂ catalysts for various reactions.⁴¹ Even small amounts of copper (<0.5 wt %) affect the support properties, inducing significant catalytic activities resulting from metal–support interactions. In contrast to our earlier RWGS study over Au/CeO₂, no intermediates (e.g., carbonates, hydroxides, and formates) are involved in the reaction. Furthermore, unlike our gold catalysts from previous studies, Cu/CeO₂ is expected to be more stable, as *operando* Raman and UV–vis did not give any indication of copper agglomeration. Thus, while gold catalysts may show a somewhat higher activity, they are more expensive and suffer from instabilities.

Our combination of *operando* Raman/UV–vis spectroscopy and ME-DRIFTS is a powerful tool to investigate a wide range of metal-supported oxide catalysts and to provide a detailed understanding of their functioning, for example, in C1 processes such as RWGS. In particular, our approach allows us to distinguish between redox and associative mechanisms and to investigate their respective weight, which is of great importance to provide new approaches toward better catalysts and, ultimately, to design catalysts based on a profound knowledge of their structural behavior under working conditions.

■ ASSOCIATED CONTENT

SI Supporting Information

The Supporting Information is available free of charge at <https://pubs.acs.org/doi/10.1021/acscatal.2c02216>.

Additional characterization data, in situ/*operando* Raman results, quasi in situ XPS spectra, and additional ME-DRIFTS as well as steady-state DRIFTS data (PDF)

■ AUTHOR INFORMATION

Corresponding Author

Christian Hess – Eduard Zintl Institute of Inorganic and Physical Chemistry, Technical University of Darmstadt, 64287 Darmstadt, Germany; orcid.org/0000-0002-4738-7674; Email: christian.hess@tu-darmstadt.de

Authors

Marc Ziemba – Eduard Zintl Institute of Inorganic and Physical Chemistry, Technical University of Darmstadt, 64287 Darmstadt, Germany; orcid.org/0000-0001-8075-2322

Jakob Weyel – Eduard Zintl Institute of Inorganic and Physical Chemistry, Technical University of Darmstadt, 64287 Darmstadt, Germany

Complete contact information is available at:
<https://pubs.acs.org/10.1021/acscatal.2c02216>

Notes

The authors declare no competing financial interest.

ACKNOWLEDGMENTS

We thank Stefan Lauterbach and Hans-Joachim Kleebe for TEM and EDX measurements, Martin Brodrecht for BET measurements, and Karl Kopp for technical support and helpful discussions on the XPS results. J.W. gratefully acknowledges a scholarship from the Fonds der Chemischen Industrie im Verband der Chemischen Industrie e.V.

REFERENCES

- (1) Staffell, I.; Scamman, D.; Velazquez Abad, A.; Balcombe, P.; Dodds, P. E.; Ekins, P.; Shah, N.; Ward, K. R. The Role of Hydrogen and Fuel Cells in the Global Energy System. *Energy Environ. Sci.* **2019**, *12*, 463–491.
- (2) Trimm, D. L. Minimisation of Carbon Monoxide in a Hydrogen Stream for Fuel Cell Application. *Appl. Catal., A* **2005**, *296*, 1–11.
- (3) Ratnasamy, C.; Wagner, J. P. Water Gas Shift Catalysis. *Catal. Rev.* **2009**, *51*, 325–440.
- (4) Rodriguez, J. A.; Grinter, D. C.; Liu, Z.; Palomino, R. M.; Senanayake, S. D. Ceria-Based Model Catalysts: Fundamental Studies on the Importance of the Metal-Ceria Interface in CO Oxidation, the Water-Gas Shift, CO₂ Hydrogenation, and Methane and Alcohol Reforming. *Chem. Soc. Rev.* **2017**, *46*, 1824–1841.
- (5) Xu, J.; Yang, W.; Song, S.; Zhang, H. Ultra-Small Noble Metal Ceria-Based Catalytic Materials: From Synthesis to Application. *Eur. J. Inorg. Chem.* **2021**, 689–701.
- (6) Abdel-Mageed, A. M.; Chen, S.; Fauth, C.; Häring, T.; Bansmann, J. Fundamental Aspects of Ceria Supported Au Catalysts Probed by In Situ/Operando Spectroscopy and TAP Reactor Studies. *ChemPhysChem* **2021**, *22*, 1302–1315.
- (7) Shido, T.; Iwasawa, Y. Regulation of Reaction Intermediate by Reactant in the Water-Gas Shift Reaction on CeO₂, in Relation to Reactant-Promoted Mechanism. *J. Catal.* **1992**, *136*, 493–503.
- (8) Kalamaras, C. M.; Dionysiou, D. D.; Efstathiou, A. M. Mechanistic Studies of the Water-Gas Shift Reaction over Pt/Ce_xZr_{1-x}O₂ Catalysts: The Effect of Pt Particle Size and Zr Dopant. *ACS Catal.* **2012**, *2*, 2729–2742.
- (9) Leppelt, R.; Schumacher, B.; Plzak, V.; Kinne, M.; Behm, R. Kinetics and Mechanism of the Low-Temperature Water-Gas Shift Reaction on Au/CeO₂ Catalysts in an Idealized Reaction Atmosphere. *J. Catal.* **2006**, *244*, 137–152.
- (10) Goguet, A.; Meunier, F. C.; Tibiletti, D.; Breen, J. P.; Burch, R. Spectrokinetic Investigation of Reverse Water-Gas-Shift Reaction Intermediates over a Pt/CeO₂ Catalyst. *J. Phys. Chem. B* **2004**, *108*, 20240–20246.
- (11) Meunier, F. C.; Tibiletti, D.; Goguet, A.; Reid, D.; Burch, R. On the Reactivity of Carbonate Species on a Pt/CeO₂ Catalyst under Various Reaction Atmospheres: Application of the Isotopic Exchange Technique. *Appl. Catal., A* **2005**, *289*, 104–112.
- (12) Mudiyansele, K.; Senanayake, S. D.; Feria, L.; Kundu, S.; Baber, A. E.; Graciani, J.; Vidal, A. B.; Agnoli, S.; Evans, J.; Chang, R.; Axnanda, S.; Liu, Z.; Sanz, J. F.; Liu, P.; Rodriguez, J. A.; Stacchiola, D. J. Importance of the Metal-Oxide Interface in Catalysis: In Situ Studies of the Water-Gas Shift Reaction by Ambient-Pressure X-ray Photoelectron Spectroscopy. *Angew. Chem., Int. Ed.* **2013**, *52*, 5101–5105.
- (13) Chen, Y.; Wang, H.; Burch, R.; Hardacre, C.; Hu, P. New Insight into Mechanisms in Water-Gas-Shift Reaction on Au/CeO₂(111): A Density Functional Theory and Kinetic Study. *Faraday Discuss.* **2011**, *152*, 121–133.
- (14) Vecchiotti, J.; Bonivardi, A.; Xu, W.; Stacchiola, D.; Delgado, J. J.; Calatayud, M.; Collins, S. E. Understanding the Role of Oxygen Vacancies in the Water Gas Shift Reaction on Ceria-Supported Platinum Catalysts. *ACS Catal.* **2014**, *4*, 2088–2096.
- (15) Liu, Z.-P.; Jenkins, S. J.; King, D. A. Origin and Activity of Oxidized Gold in Water-Gas-Shift Catalysis. *Phys. Rev. Lett.* **2005**, *94*, 196102.
- (16) Bobadilla, L. F.; Santos, J. L.; Ivanova, S.; Odriozola, J. A.; Urakawa, A. Unravelling the Role of Oxygen Vacancies in the Mechanism of the Reverse Water-Gas Shift Reaction by Operando DRIFTS and Ultraviolet-Visible Spectroscopy. *ACS Catal.* **2018**, *8*, 7455–7467.
- (17) Fu, Q.; Saltsburg, H.; Flytzani-Stephanopoulos, M. Active Nonmetallic Au and Pt Species on Ceria-Based Water-Gas Shift Catalysts. *Science* **2003**, *301*, 935–938.
- (18) Bunluesin, T.; Gorte, R. J.; Graham, G. W. Studies of the Water-Gas-Shift Reaction on Ceria-Supported Pt, Pd, and Rh: Implications for Oxygen-Storage Properties. *Appl. Catal., B* **1998**, *15*, 107–114.
- (19) Shido, T.; Iwasawa, Y. Reactant-Promoted Reaction Mechanism for Water-Gas Shift Reaction on Rh-Doped CeO₂. *J. Catal.* **1993**, *141*, 71–81.
- (20) Burch, R.; Goguet, A.; Meunier, F. C. A Critical Analysis of the Experimental Evidence for and against a Formate Mechanism for High Activity Water-Gas Shift Catalysts. *Appl. Catal., A* **2011**, *409–410*, 3–12.
- (21) Chen, Y.; Cheng, J.; Hu, P.; Wang, H. Examining the Redox and Formate Mechanisms for Water-Gas Shift Reaction on Au/CeO₂ Using Density Functional Theory. *Surf. Sci.* **2008**, *602*, 2828–2834.
- (22) Tibiletti, D.; Amieiro-Fonseca, A.; Burch, R.; Chen, Y.; Fisher, J. M.; Goguet, A.; Hardacre, C.; Hu, P.; Thompsett, D. DFT and in Situ EXAFS Investigation of Gold/Ceria-Zirconia Low-Temperature Water Gas Shift Catalysts: Identification of the Nature of the Active Form of Gold. *J. Phys. Chem. B* **2005**, *109*, 22553–22559.
- (23) Rodriguez, J. A.; Liu, P.; Hrbek, J.; Evans, J.; Pérez, M. Water Gas Shift Reaction on Cu and Au Nanoparticles Supported on CeO₂(111) and ZnO(0001): Intrinsic Activity and Importance of Support Interactions. *Angew. Chem., Int. Ed.* **2007**, *46*, 1329–1332.
- (24) Amieiro Fonseca, A.; Fisher, J. M.; Ozkaya, D.; Shannon, M. D.; Thompsett, D. Ceria-Zirconia Supported Au as Highly Active Low Temperature Water-Gas Shift Catalysts. *Top. Catal.* **2007**, *44*, 223–235.
- (25) Schilling, C.; Hess, C. Elucidating the Role of Support Oxygen in the Water-Gas Shift Reaction over Ceria-Supported Gold Catalysts Using Operando Spectroscopy. *ACS Catal.* **2019**, *9*, 1159–1171.
- (26) Wang, X.; Rodriguez, J. A.; Hanson, J. C.; Gamarra, D.; Martínez-Arias, A.; Fernández-García, M. In Situ Studies of the Active Sites for the Water Gas Shift Reaction over Cu-CeO₂ Catalysts: Complex Interaction between Metallic Copper and Oxygen Vacancies of Ceria. *J. Phys. Chem. B* **2006**, *110*, 428–434.
- (27) Barrio, L.; Estrella, M.; Zhou, G.; Wen, W.; Hanson, J. C.; Hungria, A. B.; Hornés, A.; Fernández-García, M.; Martínez-Arias, A.; Rodriguez, J. A. Unraveling the Active Site in Copper-Ceria Systems for the Water-Gas Shift Reaction: In Situ Characterization of an Inverse Powder CeO_{2-x}/CuO-Cu Catalyst. *J. Phys. Chem. C* **2010**, *114*, 3580–3587.
- (28) López Cámara, A.; Chansai, S.; Hardacre, C.; Martínez-Arias, A. The Water-Gas Shift Reaction over CeO₂/CuO: Operando SSITKA-DRIFTS-Mass Spectrometry Study of Low Temperature Mechanism. *Int. J. Hydrogen Energy* **2014**, *39*, 4095–4101.
- (29) Ren, Z.; Peng, F.; Li, J.; Liang, X.; Chen, B. Morphology-Dependent Properties of Cu/CeO₂ Catalysts for the Water-Gas Shift Reaction. *Catalysts* **2017**, *7*, 48.
- (30) Chen, Y.; Lin, J.; Wang, X. Noble-Metal Based Single-Atom Catalysts for the Water-Gas Shift Reaction. *Chem. Commun.* **2022**, *58*, 208–222.

- (31) Chen, W.-H.; Chen, C.-Y. Water Gas Shift Reaction for Hydrogen Production and Carbon Dioxide Capture: A Review. *Appl. Energy* **2020**, *258*, 114078.
- (32) Ning, J.; Zhou, Y.; Shen, W. Atomically Dispersed Copper Species on Ceria for the Low-Temperature Water-Gas Shift Reaction. *Sci. China Chem.* **2021**, *64*, 1103–1110.
- (33) Lykaki, M.; Stefa, S.; Carabineiro, S.; Soria, M.; Madeira, L.; Konsolakis, M. Shape Effects of Ceria Nanoparticles on the Water-Gas Shift Performance of Cu_x/CeO₂ Catalysts. *Catalysts* **2021**, *11*, 753.
- (34) Zhou, Y.; Chen, A.; Ning, J.; Shen, W. Electronic and Geometric Structure of the Copper-Ceria Interface on Cu/CeO₂ Catalysts. *Sci. China Chem.* **2020**, *41*, 928–937.
- (35) Ning, J.; Zhou, Y.; Chen, A.; Li, Y.; Miao, S.; Shen, W. Dispersion of Copper on Ceria for the Low-Temperature Water-Gas Shift Reaction. *Catal. Today* **2020**, *357*, 460 No. June, 1–8.
- (36) Vovchok, D.; Guild, C. J.; Llorca, J.; Xu, W.; Jafari, T.; Toloueinia, P.; Kriz, D.; Waluyo, I.; Palomino, R. M.; Rodriguez, J. A.; Suib, S. L.; Senanayake, S. D. Cu Supported on Mesoporous Ceria: Water Gas Shift Activity at Low Cu Loadings through Metal-Support Interactions. *Phys. Chem. Chem. Phys.* **2017**, *19*, 17708–17717.
- (37) Ahn, S. Y.; Na, H. S.; Jeon, K. W.; Lee, Y. L.; Kim, K. J.; Shim, J. O.; Roh, H. S. Effect of Cu/CeO₂ Catalyst Preparation Methods on Their Characteristics for Low Temperature Water-gas Shift Reaction: A Detailed Study. *Catal. Today* **2020**, *352*, 166–174.
- (38) Tsoncheva, T.; Mileva, A.; Issa, G.; Henych, J.; Tolasz, J.; Dimitrov, M.; Kovacheva, D.; Atanasova, G.; Štengl, V. Mesoporous Copper-Ceria-Titania Ternary Oxides as Catalysts for Environmental Protection: Impact of Ce/Ti Ratio and Preparation Procedure. *Appl. Catal., A* **2020**, *595*, 117487.
- (39) Ziemba, M.; Ganduglia-Pirovano, M. V.; Hess, C. Insight into the Mechanism of the Water-Gas Shift Reaction over Au/CeO₂ Catalysts Using Combined Operando Spectroscopies. *Faraday Discuss.* **2021**, *229*, 232–250.
- (40) Ziemba, M.; Schilling, C.; Ganduglia-Pirovano, M. V.; Hess, C. Toward an Atomic-Level Understanding of Ceria-Based Catalysts: When Experiment and Theory Go Hand in Hand. *Acc. Chem. Res.* **2021**, *54*, 2884–2893.
- (41) Konsolakis, M. The Role of Copper-Ceria Interactions in Catalysis Science: Recent Theoretical and Experimental Advances. *Appl. Catal., B* **2016**, *198*, 49–66.
- (42) Kang, L.; Wang, B.; Güntner, A. T.; Xu, S.; Wan, X.; Liu, Y.; Marlow, S.; Ren, Y.; Gianolio, D.; Tang, C. C.; Murzin, V.; Asakura, H.; He, Q.; Guan, S.; Velasco-Vélez, J. J.; Pratsinis, S. E.; Guo, Y.; Wang, F. R. The Electrophilicity of Surface Carbon Species in the Redox Reactions of CuO-CeO₂ Catalysts. *Angew. Chem.* **2021**, *133*, 14541–14549.
- (43) Kang, L.; Wang, B.; Bing, Q.; Zalibera, M.; Büchel, R.; Xu, R.; Wang, Q.; Liu, Y.; Gianolio, D.; Tang, C. C.; Gibson, E. K.; Danaie, M.; Allen, C.; Wu, K.; Marlow, S.; Sun, L.; He, Q.; Guan, S.; Savitsky, A.; Velasco-Vélez, J. J.; Callison, J.; Kay, C. W. M.; Pratsinis, S. E.; Lubitz, W.; Liu, J.; Wang, F. R. Adsorption and Activation of Molecular Oxygen over Atomic Copper(I/II) Site on Ceria. *Nat. Commun.* **2020**, *11*, 4008.
- (44) Chen, A.; Yu, X.; Zhou, Y.; Miao, S.; Li, Y.; Kuld, S.; Sehested, J.; Liu, J.; Aoki, T.; Hong, S.; Camellone, M. F.; Fabris, S.; Ning, J.; Jin, C.; Yang, C.; Nefedov, A.; Wöll, C.; Wang, Y.; Shen, W. Structure of the Catalytically Active Copper-Ceria Interfacial Perimeter. *Nat. Catal.* **2019**, *2*, 334–341.
- (45) Yu, W.-Z.; Wu, M.-Y.; Wang, W.-W.; Jia, C.-J. In Situ Generation of the Surface Oxygen Vacancies in a Copper-Ceria Catalyst for the Water-Gas Shift Reaction. *Langmuir* **2021**, *37*, 10499–10509.
- (46) Ren, Z.; Liu, N.; Chen, B.; Li, J.; Mei, D. Nucleation of Cu_n (n = 1–5) Clusters and Equilibrium Morphology of Cu Particles Supported on CeO₂ Surface: A Density Functional Theory Study. *J. Phys. Chem. C* **2018**, *122*, 27402–27411.
- (47) Yao, S. Y.; Xu, W. Q.; Johnston-Peck, A. C.; Zhao, F. Z.; Liu, Z. Y.; Luo, S.; Senanayake, S. D.; Martínez-Arias, A.; Liu, W. J.; Rodriguez, J. A. Morphological Effects of the Nanostructured Ceria Support on the Activity and Stability of CuO/CeO₂ Catalysts for the Water-Gas Shift Reaction. *Phys. Chem. Chem. Phys.* **2014**, *16*, 17183–17195.
- (48) Müller, P.; Hermans, I. Applications of Modulation Excitation Spectroscopy in Heterogeneous Catalysis. *Ind. Eng. Chem. Res.* **2017**, *56*, 1123–1136.
- (49) Filtschew, A.; Hofmann, K.; Hess, C. Ceria and Its Defect Structure: New Insights from a Combined Spectroscopic Approach. *J. Phys. Chem. C* **2016**, *120*, 6694–6703.
- (50) Ziemba, M.; Weyel, J.; Hess, C. Elucidating the Mechanism of the Reverse Water-Gas Shift Reaction over Au/CeO₂ Catalysts Using Operando and Transient Spectroscopies. *Appl. Catal., B* **2022**, *301*, 120825.
- (51) Ziemba, M.; Hess, C. Influence of Gold on the Reactivity Behaviour of Ceria Nanorods in CO Oxidation: Combining Operando Spectroscopies and DFT Calculations. *Catal. Sci. Technol.* **2020**, *10*, 3720–3730.
- (52) Nottbohm, C. T.; Hess, C. Investigation of Ceria by Combined Raman, UV-Vis and X-Ray Photoelectron Spectroscopy. *Catal. Commun.* **2012**, *22*, 39–42.
- (53) Schilling, C.; Hess, C. Real-Time Observation of the Defect Dynamics in Working Au/CeO₂ Catalysts by Combined Operando Raman/UV-Vis Spectroscopy. *J. Phys. Chem. C* **2018**, *122*, 2909–2917.
- (54) Ziemba, M.; Schumacher, L.; Hess, C. Reduction Behavior of Cubic In₂O₃ Nanoparticles by Combined Multiple In Situ Spectroscopy and DFT. *J. Phys. Chem. Lett.* **2021**, *12*, 3749–3754.
- (55) Schilling, C.; Ziemba, M.; Hess, C.; Ganduglia-Pirovano, M. V. Identification of Single-Atom Active Sites in CO Oxidation over Oxide-Supported Au Catalysts. *J. Catal.* **2020**, *383*, 264–272.
- (56) Schilling, C.; Hess, C. CO Oxidation on Ceria Supported Gold Catalysts Studied by Combined Operando Raman/UV-Vis and IR Spectroscopy. *Top. Catal.* **2017**, *60*, 131–140.
- (57) Weyel, J.; Ziemba, M.; Hess, C. Elucidating Active CO-Au Species on Au/CeO₂(111): A Combined Modulation Excitation DRIFTS and Density Functional Theory Study. *Top. Catal.* **2022**.
- (58) Li, A.; Yao, D.; Yang, Y.; Yang, W.; Li, Z.; Lv, J.; Huang, S.; Wang, Y.; Ma, X. Active Cu⁰-Cu⁺ Sites for the Hydrogenation of Carbon-Oxygen Bonds over Cu/CeO₂ Catalysts. *ACS Catal.* **2022**, *12*, 1315–1325.
- (59) Ziemba, M.; Stark, D.; Hess, C. Combined DFT and Operando Spectroscopic Study of the Water-Gas Shift Reaction over Ceria Based Catalysts: The Role of the Noble Metal and Ceria Faceting. *Chem. Proc.* **2020**, *2*, 23.
- (60) Briggs, D.; Seah, M. P. *Practical Surface Analysis by Auger and X-ray Photoelectron Spectroscopy*; Wiley, 1983.
- (61) Monte, M.; Munuera, G.; Costa, D.; Conesa, J. C.; Martínez-Arias, A. Near-Ambient XPS Characterization of Interfacial Copper Species in Ceria-Supported Copper Catalysts. *Phys. Chem. Chem. Phys.* **2015**, *17*, 29995–30004.
- (62) Szabová, L.; Skála, T.; Matolínová, I.; Fabris, S.; Farnesi Camellone, M.; Matolín, V. Copper-Ceria Interaction: A Combined Photoemission and DFT Study. *Appl. Surf. Sci.* **2013**, *267*, 12–16.
- (63) Castleton, C. W. M.; Kullgren, J.; Hermansson, K. Tuning LDA +U for Electron Localization and Structure at Oxygen Vacancies in Ceria. *J. Chem. Phys.* **2007**, *127*, 244704.
- (64) Zabilskiy, M.; Djinović, P.; Tchernychova, E.; Tkachenko, O. P.; Kustov, L. M.; Pintar, A. Nanoshaped CuO/CeO₂ Materials: Effect of the Exposed Ceria Surfaces on Catalytic Activity in N₂O Decomposition Reaction. *ACS Catal.* **2015**, *5*, 5357–5365.
- (65) Praliaud, H. Surface and Bulk Properties of Cu-ZSM-5 and Cu/Al₂O₃ Solids during Redox Treatments. Correlation with the Selective Reduction of Nitric Oxide by Hydrocarbons. *Appl. Catal., B* **1998**, *16*, 359–374.
- (66) Pestryakov, A. N.; Petranovskii, V. P.; Kryazhkov, A.; Ozhereliev, O.; Pfänder, N.; Knop-Gericke, A. Study of Copper Nanoparticles Formation on Supports of Different Nature by UV-Vis Diffuse Reflectance Spectroscopy. *Chem. Phys. Lett.* **2004**, *385*, 173–176.

- (67) Chan, G. H.; Zhao, J.; Hicks, E. M.; Schatz, G. C.; Van Duyne, R. P. Plasmonic Properties of Copper Nanoparticles Fabricated by Nanosphere Lithography. *Nano Lett.* **2007**, *7*, 1947–1952.
- (68) Bu, Y.; Niemantsverdriet, J. W. H.; Fredriksson, H. O. A. Cu Model Catalyst Dynamics and CO Oxidation Kinetics Studied by Simultaneous in Situ UV–Vis and Mass Spectroscopy. *ACS Catal.* **2016**, *6*, 2867–2876.
- (69) Romero-Sarria, F.; Martínez T, L. M.; Centeno, M. A.; Odriozola, J. A. Surface Dynamics of Au/CeO₂ Catalysts during CO Oxidation. *J. Phys. Chem. C* **2007**, *111*, 14469–14475.
- (70) Vayssilov, G. N.; Mihaylov, M.; Petkov, P. S.; Hadjiivanov, K. I.; Neyman, K. M. Reassignment of the Vibrational Spectra of Carbonates, Formates, and Related Surface Species on Ceria: A Combined Density Functional and Infrared Spectroscopy Investigation. *J. Phys. Chem. C* **2011**, *115*, 23435–23454.
- (71) Yang, S.-C.; Pang, S. H.; Sulmonetti, T. P.; Su, W.-N.; Lee, J.-F.; Hwang, B.-J.; Jones, C. W. Synergy between Ceria Oxygen Vacancies and Cu Nanoparticles Facilitates the Catalytic Conversion of CO₂ to CO under Mild Conditions. *ACS Catal.* **2018**, *8*, 12056–12066.
- (72) Daly, H.; Ni, J.; Thompsett, D.; Meunier, F. C. On the Usefulness of Carbon Isotopic Exchange for the Operando Analysis of Metal-Carbonyl Bands by IR over Ceria-Containing Catalysts. *J. Catal.* **2008**, *254*, 238–243.
- (73) Isokoski, K.; Poteet, C. A.; Linnartz, H. Highly Resolved Infrared Spectra of Pure CO₂ Ice (15–75 K). *Astron. Astrophys.* **2013**, *555*, A85.
- (74) Laachir, A.; Perrichon, V.; Badri, A.; Lamotte, J.; Catherine, E.; Lavalley, J. C.; El Fallah, J.; Hilaire, L.; Le Normand, F.; Quéméré, E.; Sauvion, G. N.; Touret, O. Reduction of CeO₂ by Hydrogen. Magnetic Susceptibility and Fourier-Transform Infrared, Ultraviolet and X-Ray Photoelectron Spectroscopy Measurements. *J. Chem. Soc. Faraday. Trans.* **1991**, *87*, 1601–1609.
- (75) Badri, A.; Binet, C.; Lavalley, J. An FTIR Study of Surface Ceria Hydroxy Groups during a Redox Process with H₂. *J. Chem. Soc. Faraday. Trans.* **1996**, *92*, 4669.
- (76) Bera, P.; Cámara, A. L.; Hornés, A.; Martínez-Arias, A. Comparative in Situ DRIFTS-MS Study of ¹²CO- and ¹³CO-TPR on CuO/CeO₂ Catalyst. *J. Phys. Chem. C* **2009**, *113*, 10689–10695.
- (77) Gao, X.; Lin, X.; Xie, X.; Li, J.; Wu, X.; Li, Y.; Kawi, S. Modification Strategies of Heterogeneous Catalysts for Water–Gas Shift Reactions. *React. Chem. Eng.* **2022**, *7*, 551–565.
- (78) Salcedo, A.; Irigoyen, B. Unraveling the Origin of Ceria Activity in Water–Gas Shift by First-Principles Microkinetic Modeling. *J. Phys. Chem. C* **2020**, *124*, 7823–7834.
- (79) Wu, Z.; Li, M.; Overbury, S. H. On the Structure Dependence of CO Oxidation over CeO₂ Nanocrystals with Well-Defined Surface Planes. *J. Catal.* **2012**, *285*, 61–73.



Contents lists available at ScienceDirect

Applied Catalysis B: Environmental

journal homepage: www.elsevier.com/locate/apcatb

Elucidating the mechanism of the reverse water–gas shift reaction over Au/CeO₂ catalysts using *operando* and transient spectroscopies

Marc Ziemba¹, Jakob Weyel¹, Christian Hess^{*}

Eduard-Zintl-Institute of Inorganic and Physical Chemistry, Technical University of Darmstadt, Alarich-Weiss-Str. 8, 64287 Darmstadt, Germany

ARTICLE INFO

Keywords:

Gold-based catalyst
CeO₂
Reverse water–gas shift
CO₂ activation
Operando spectroscopy

ABSTRACT

The reaction mechanism of the reverse water–gas shift reaction (rWGSR) over Au/ceria catalysts was investigated by monitoring the catalyst dynamics and reaction intermediates using *operando* and transient spectroscopies, as well as by DFT calculations. Combined *operando* Raman and UV-Vis spectroscopic analysis allows establishing a correlation between subsurface oxygen vacancies and catalytic activity. Comparison of different ceria support materials, i.e., polyhedra and polycrystalline sheets, reveals that the defect concentration is not rate-determinant. Using transient DRIFTS, we are able to identify individual steps of hydrogen dissociation on supported gold and to gain detailed insight into the reduction of CO₂ via formate and carbonate formation. It is demonstrated that CO₂ reduction is influenced by the surface pretreatment. Considering all spectroscopic findings, we propose an associative mechanism via carbonate and formate intermediates as the main route for the rWGSR over Au/ceria(111) catalysts, while a redox mechanism plays only a minor role.

1. Introduction

The ever-increasing levels of CO₂ emissions [1] and the resulting impact of the greenhouse effect are the main reasons for the importance of dealing with CO₂, while solutions to stop its further release into the atmosphere continue to be sought after. In an increasing number of CO₂ capture technologies, its activation and use as a C1 source is an attractive strategy [2]. It is of particular interest to use CO₂ as a non-fossil source for the production of syngas, owing to its versatility and relevance for a multitude of applications. In this context the reverse water–gas shift reaction (rWGSR) plays an important role in the energy sector, allowing CO₂ to be converted first to CO and then to liquid fuels via CO hydrogenation (Fischer–Tropsch process).

While noble metal–loaded CeO₂ catalysts have been shown to be active for the rWGSR [3,4], their mode of operation (redox vs associative mechanism) is still a matter of debate. For example, previous studies on Pt/CeO₂ catalysts have shown that intermediates such as carbonates or formates play an important role in the reaction, pointing to an associative mechanism [5,6]. In contrast, the water–gas shift reaction at 300 °C proceeds largely via a redox mechanism [7]. Considerable catalytic activity as well as the appearance of intermediates such as formates or bidentate carbonates was also reported for Cu/CeO₂ catalysts

[8]. In this context, a facet dependence of the ceria support was reported, with the CeO₂(110) surface showing a much higher activity than the CeO₂(111) surface [8]. In contrast, experiments on the bare supports, which become active at temperatures >550 °C [9], have shown that the effect of the surface termination is much smaller [9], highlighting the importance of the metal–support interaction.

Regarding other supports, recent *operando* studies of the rWGSR over gold-loaded catalysts, comparing a redox active (Au/TiO₂) with an inactive (Au/Al₂O₃) support, are of interest in the context of the present study [10]. In particular, the reaction over Au/Al₂O₃ is shown to occur via intermediates such as formates, while for the Au/TiO₂ catalyst a redox mechanism involving the formation of hydroxycarbonyls has been postulated, following earlier studies on copper- and gold-loaded TiO₂(110) catalysts during the water–gas shift reaction [11]. With increasing temperature, the associative mechanism is found to contribute more strongly, due to more facile decomposition of adsorbates such as carbonates and formates, thereby releasing CO [10].

This study will focus on Au/CeO₂ catalysts that are known to be active for the rWGSR [12,13] and water–gas shift reaction (WGSR) [14–17]. While previous studies have demonstrated that Au/CeO₂ catalysts [12] as well as bare ceria [18,19] can be re-oxidized by CO₂, indicating a redox mechanism, the role of adsorbates/reaction

^{*} Corresponding author.

E-mail address: christian.hess@tu-darmstadt.de (C. Hess).

¹ These authors contributed equally.

<https://doi.org/10.1016/j.apcatb.2021.120825>

Received 23 August 2021; Received in revised form 6 October 2021; Accepted 12 October 2021

Available online 18 October 2021

0926-3373/© 2021 Elsevier B.V. All rights reserved.

intermediates has not been clarified yet. In this context, it is of particular interest to explore the role of gold during the re-oxidation process and its contribution during rWGS. For LT-WGS and CO oxidation it has previously been shown that the gold/ceria interface and size distribution have an influence on the catalytic activity [20,21]. Using XAS and DRIFTS during LT-WGS gold was found to be metallic [22], but under reductive conditions or in long-term studies agglomeration of surface gold atoms to small gold particles can occur [23]. Applying *operando* SSITKA-mass spectrometry-DRIFTS to the LT-WGS over a 0.5 wt% Pt/Ce_{1-x}La_xO_{2-δ} catalyst has revealed that the active species is not only formed on the Pt particle but also in its environment [24], which again underlines the importance of the metal-support interaction. In addition, previous studies have shown that hydrogen dissociation on stoichiometric ceria, which leads to the formation of two surface hydroxides, requires temperatures > 400 °C [25]. However, surface oxygen defects significantly affect the H₂ adsorption, giving rise to increased heterolytic dissociation (Ce-H and OH) [25,26]. On Au/CeO₂ catalysts, heterolytic dissociation is feasible at 150 °C, leading to a hydroxide and a gold hydride species [27]. Furthermore, studies on different gold supported materials have shown that an increase in the gold loading results in a higher surface hydroxide concentration, thus providing direct evidence for a gold-catalyzed H₂ dissociation [28].

To elucidate the rWGS reaction mechanism in detail, we employed combined *operando* Raman and UV-Vis as well as transient DRIFTS measurements, supplemented by quasi *in situ* XPS, enabling us to address the support and (transient) adsorbate dynamics, as well as the surface state of Au/CeO₂ catalysts, in an integrated manner. We obtain insight into the role of the support by using ceria with two different particle shapes, i.e., polycrystalline ceria and ceria polyhedra. While polyhedra terminate exclusively with the CeO₂(111) surface, the polycrystalline ceria, which resembles sheets, also contains stepped sites. Previous studies have shown a positive effect of stepped sites on the activity during CO oxidation over Au/CeO₂ catalysts [29].

2. Experimental section

2.1. Catalyst preparation

Polycrystalline ceria sheets were prepared by decomposition of cerium nitrate as described in previous studies [15,30]. Briefly, Ce(NO₃)₃·6H₂O (Alfa Aesar, 99.5%) was calcined at 600 °C (6 °C/min) for 12 h. After cooling to room temperature, the powder was sieved (200 μm) and calcined again using the same protocol. Ceria polyhedra were obtained commercially (Sigma Aldrich, <25 nm (BET)). Gold was loaded onto ceria by electrolyte deposition using a 10⁻³ M HAuCl₄·3H₂O solution (Carl Roth, 99.9%), as described in detail elsewhere [15,30].

2.2. Catalyst characterization

2.2.1. Operando spectroscopy

Combined *operando* Raman and UV-Vis spectra as well as the catalytic activity were measured with a previously described experimental setup [14,15,31,32]. Briefly, for the *operando* measurements, about 20–25 mg of the sample was placed in a stainless steel sample holder (8 mm diameter, 0.5 mm depth). Due to the cell geometry and as the catalyst sample is overflowed by the gases, the amount of catalyst has hardly any influence on the activity. The sample temperature was determined by means of a Ni/Cr-Ni thermocouple (type K), which was located at the sample holder close to the catalyst. Measured temperatures deviated by a maximum of 3 °C from the set temperatures in a constant gas stream. The catalyst temperature was set to 250 °C in all measurements. Raman spectra were recorded with an HL5R transmission spectrometer (Kaiser Optical), using a frequency-doubled Nd:YAG laser (Cobolt) for excitation at 532 nm. The laser power at the position of the sample was 1 mW, as measured with a power meter (Ophir). The spectral resolution was specified as 5 cm⁻¹ and the band

position stability was better than 0.3 cm⁻¹. Spectra of the gold-loaded catalysts were recorded with an exposure time of 225 s and 2 accumulations and those of the bare samples with an exposure time of 150 s and 3 accumulations. For all measurements a cosmic ray filter and an auto new dark correction were applied, resulting in a total measuring time of about 1800 s for the bare and gold-loaded samples. All Raman spectra reported in this work were normalized to the band with the highest intensity, i.e., the F_{2g} band. The given F_{2g} positions were determined by curve fitting using Lorentzian functions.

UV-Vis spectra were recorded in diffuse reflection using an AvaSpec ULS2048 spectrometer (Avantes) equipped with a deuterium lamp and a halogen discharge lamp. Spectra were taken before and after a Raman spectrum. The total measuring time was 60 s, resulting from 200 runs with an exposure time of 300 ms each. As white standard, magnesium oxide powder (Sigma Aldrich) was employed, which shows no absorption within 170–1100 nm.

The gases CO₂ (99.999%, Westfalen), H₂ (99.999%, Westfalen), and argon (99.996%, Westfalen) were dosed by digital mass flow controllers (MFCs, Bronkhorst). Gas atmospheres of 10 vol% H₂/Ar, 2 vol% CO₂/Ar, and 4 vol% H₂/2 vol% CO₂/Ar for reactive conditions were applied at a total flow rate of 100 mL/min. All gas compositions are balanced in argon to keep the turnover low and to eliminate the influence of possible transport effects thus allowing to focus on the reaction mechanism. To analyze the gas phase and its composition, a Fourier transform infrared (FTIR) spectrometer (Tensor 20, Bruker) was installed at the outlet of the reaction cell. The resolution was 4 cm⁻¹, and the measurement time was 1 min, in which 125 spectra were accumulated. Using calibration curves, the concentration of CO was calculated, allowing the conversion of CO₂ to CO to be determined. The catalytic activity is the ratio of the amount of CO, as measured by FTIR at the outlet of the cell, to the amount of dosed CO₂. The activity of the empty cell, which showed a CO₂ conversion of 4.2%, was taken into account when calculating the catalyst activities given in the following. Please note that this background activity is a result of the cell specifications and has been shown to be reproducible.

2.2.2. Transient DRIFTS

Diffuse reflectance IR Fourier transform spectroscopy (DRIFTS) was performed on a Vertex 70 (Bruker) FTIR spectrometer equipped with a liquid nitrogen cooled mercury cadmium telluride (MCT) detector and a commercial reaction cell (Praying Mantis™ High Temperature Reaction Chamber, Harrick Scientific Products) with infrared transparent KBr windows, as described previously [30,33].

As background, the catalyst itself was employed after a 15-minute exposure at 250 °C to H₂ (4 mol%) or CO₂ (2 mol%) or the reaction mixture (4 mol% H₂ and 2 mol% CO₂, balanced with argon; total gas flow: 100 mL/min). For transient measurements we employed the rapid scan mode extension of Bruker's spectrometer software OPUS 7.2. Spectra were acquired within 850–3800 cm⁻¹, utilizing a resolution of 0.5 cm⁻¹ and an aperture of 8 mm. The mirror speed was set to 40 kHz. A Valco Instruments 4/2 valve (Model E2CA, version ED), communicating with the Vertex 70, was employed to rapidly switch between gas flows.

In transient DRIFTS experiments, the gas phase was switched immediately after the background spectrum had been recorded, commencing the measurements. A spectrum was obtained every 5 s and consisted of an average of six individual spectra, each based on five interferograms. One measurement series took 6 min.

3. Results and discussion

3.1. Catalyst characterization and performance

The ceria nanoparticles were first characterized using BET and TEM (for details see Fig. 1 and SI, Figs. S1, and S2). The commercial sample contains particles in the form of polyhedra with a specific surface area of 36 m²/g and a pore volume of 0.08 cm³g⁻¹, whereas the sample

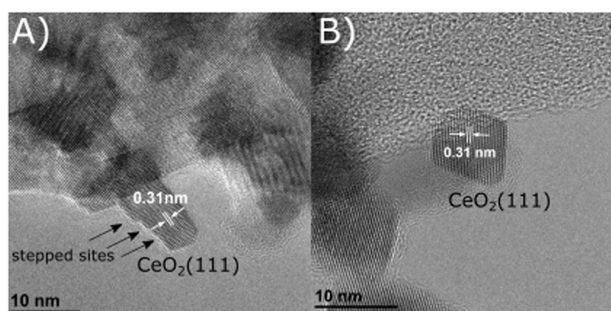


Fig. 1. Detailed TEM images of **A)** ceria sheets and **B)** ceria polyhedra. The white arrows indicate the separation of the lattice planes in the direction of the particle surface. Fig. 1A was modified from Ref [14].

prepared by decomposition of cerium nitrate, as described previously [14], contains particles with a sheet shape with a surface area of $57 \text{ m}^2/\text{g}$ and a pore volume of $0.17 \text{ cm}^3/\text{g}$. Both samples exhibit a $\text{CeO}_2(111)$ -terminated surface, but the sheets show additional stepped $\text{CeO}_2(111)$ sites (see Fig. 1) [14]. Using ICP-OES, the gold loading was determined as 0.31 wt% for the sheets and 0.27 wt% for the polyhedra. In our previous study on $\text{Au}/\text{CeO}_2(111)$ sheets, the CO-Au vibrations measured by DRIFTS showed a large dispersion of gold due to presence of single atoms and/or smaller clusters, which we assume to be the prepared state also in this study [33]. Contaminations caused by the synthesis, e.g. nitrogen or chlorine, can be excluded within the sensitivity of the XPS measurements.

As summarized in Table 1, both the bare and gold-loaded ceria samples show conversion of CO_2 upon exposure to reaction conditions (4% H_2 , 2% CO_2 , Ar; 100 mL/min) at 250 °C. For the unloaded polyhedra and sheets, activities of 2.2% and 1.6% were determined, respectively, while the gold-loaded samples showed significantly higher activities of 5.3% (Au/polyhedra) and 5.4% (Au/sheets). It is noteworthy that the polyhedra yield a higher CO_2 conversion despite their lower surface area. The activity of the gold-loaded samples, on the other hand, does not show a significant difference within the experimental error. In comparison to a previous study on 2.4 wt% Au/CeO_2 the activity is in the same range ($4.8 \times 10^{-8} \text{ mol}_{\text{CO}}/\text{s}$, 240 °C) as reported here [12], while compared to other ceria-based materials [4], our Au/CeO_2 catalysts show rather high activity considering the low temperature and higher CO_2 concentration. A 2% Pt/ CeO_2 catalyst (Johnson Matthey) has previously been reported to show a conversion of 13.7% at 225 °C, but it should be noted that a lower flow rate of 40 mL/min and a CO_2/H_2 ratio of 1:4 was used, thus preventing a direct comparison of the activity data [34].

3.2. Role of Au and CeO_2

Fig. 2 depicts combined Raman and UV-Vis data of bare and gold-loaded sheets and polyhedra, recorded at 250 °C for different gas atmospheres. As discussed below, the Raman F_{2g} positions and the change in UV-Vis absorption at 550 nm both reflect the reduction of the ceria support. In the following, we will first focus on the F_{2g} position, which

Table 1

Catalytic activity during rWGSR over bare ceria and gold-loaded ceria samples using a feed of $\text{H}_2/\text{CO}_2/\text{Ar}$ (4% H_2 , 2% CO_2 , Ar; 100 mL/min) at 250 °C. The catalytic activity was measured after at least 1 h time-on-stream.

Sample	CO ₂ conversion	
	%	mol _{CO} /s
CeO ₂ sheets	1.6	2.2×10^{-8}
CeO ₂ polyhedra	2.2	3.0×10^{-8}
0.31 wt% Au/CeO ₂ sheets	5.4	7.3×10^{-8}
0.27 wt% Au/CeO ₂ polyhedra	5.3	7.2×10^{-8}

has previously been shown to be a good indicator for subsurface oxygen defects [14,15,32]. Compared to the starting F_{2g} positions in argon, it is noticeable that the gold-loaded samples are red-shifted with respect to the unloaded samples, evidencing that the gold-loaded samples possess a larger number of oxygen defects. Based on this observation, one may expect the gold-loaded samples to be more reducible, which is confirmed by changing the gas phase to H_2 . In fact, for the gold-loaded samples a significantly larger redshift than for the unloaded samples is detected, whereby the shift is greatest for the sheets. This behavior demonstrates that polyhedra and sheets are characterized by a different defect formation energy, which is smaller for the sheets. When switching to reaction conditions, all samples show only slight changes, which are within the experimental error, which is why no conclusions should be drawn at this point. However, upon switching to argon, a blueshift is observed, which is indicative of an oxidation of the subsurface and can be explained by a diffusion of oxygen from the bulk to the surface. Such an oxygen diffusion was confirmed by H_2^{18}O experiments in our previous studies on the WGSR over Au/ceria catalysts [14,15]. Our results show that reaction intermediates formed during reaction conditions can decompose or desorb in argon, leaving a surface oxygen vacancy and thus promoting an oxygen diffusion from the bulk to the (sub)surface, which results in a F_{2g} blueshift.

The absorption increase at 550 nm, which can be attributed to a charge transfer from Ce^{3+} to Ce^{4+} [35], allows the change in the oxidation state of the support to be monitored, i.e., the extent of ceria reduction. Comparison of the unloaded and the gold-loaded samples reveals that gold-containing ceria shows a higher absorption at 550 nm already under ex situ conditions (see Fig. 2), which can be explained by the presence of metallic gold giving rise to surface plasmons absorbing in this range [36]. Accordingly, the higher absorption of the gold-loaded polyhedra can be explained by their higher fraction of metallic gold, which is confirmed by the Au 4f photoemissions (see below) and the ex situ UV-Vis spectra (see Fig. S3). Upon heating to 250 °C under argon, the gold-loaded samples show an increase in absorption, indicating that the presence of gold can reduce the defect formation energy. When the feed is switched to hydrogen, all samples show an increase, consistent with the Raman results. Interestingly, this reduction-induced increase is also detected for the unloaded polyhedra, but was hardly detected in the Raman F_{2g} shift, which can be explained by the different information depths of the two methods. Upon exposure to reaction conditions, a slight decrease in absorption can be seen in all samples, resulting from ceria oxidation, whereas switching to argon leads to a more pronounced re-oxidation of the support, in agreement with the Raman results, except for the gold-loaded polyhedra. The UV-Vis behavior of the gold-loaded polyhedra may be explained by the higher fraction of metallic gold and its partial agglomeration during exposure to reducing conditions. Briefly summarizing, all unloaded and gold-loaded samples are subject to gas-phase-dependent oxygen dynamics. A comparison of the extent of ceria reduction, as observed by *operando* Raman and UV-Vis spectroscopy, with the rWGSR activity data shows that the role of the support reducibility for the reaction mechanism needs to be further explored.

To gain more detailed insight into the catalysts' vibrational and electronic structure under reductive, reactive, and oxidative conditions, Fig. 3 depicts Raman spectra (left panel) and UV-Vis spectra (right panel) of the gold-loaded samples during exposure to H_2/Ar , reaction conditions, and CO_2/Ar . In the Raman spectra, the band at 243 cm^{-1} , originating from the longitudinal mode of surface oxygen, and the oxygen defect-related band at 550 cm^{-1} are of particular interest [37]. The surface mode shows an increase in intensity during CO_2 exposure, which is more pronounced for the sheets, demonstrating that the surface of the sheets can be re-oxidized more efficiently under CO_2 atmosphere than that of the polyhedra. It is difficult to make statements about the intensity of the defect band as the background changes with the gas atmosphere and thus both re-oxidation and background changes are likely to have an effect on the intensity of the defect band. However, as can be seen from Fig. 3A, the 550 cm^{-1} band is more pronounced for the

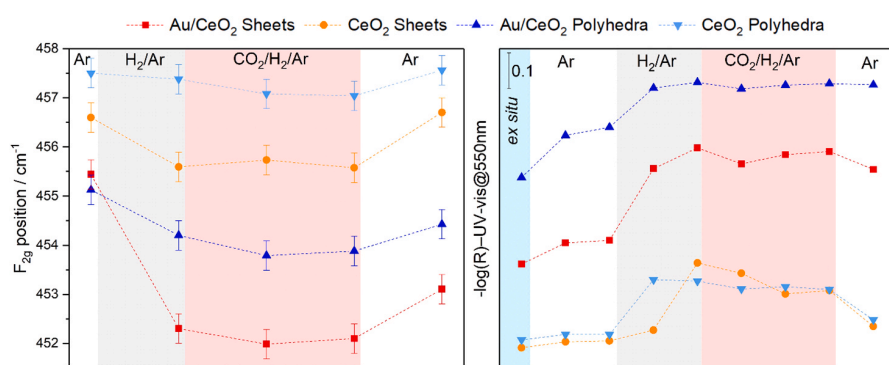


Fig. 2. *In situ* and *operando* Raman (left) and UV-Vis (right) results for Au/CeO₂ sheets and Au/CeO₂ polyhedra together with the corresponding bare support materials recorded during the indicated gas exposures at 250 °C and at a total flow rate of 100 mL/min, except for the *ex situ* spectra, which were taken at 25 °C. The measurement error for the F_{2g} position is indicated. The sample was exposed to each gas phase for about 30 min except for the reaction phase, which was present for 1 h. For details see text.

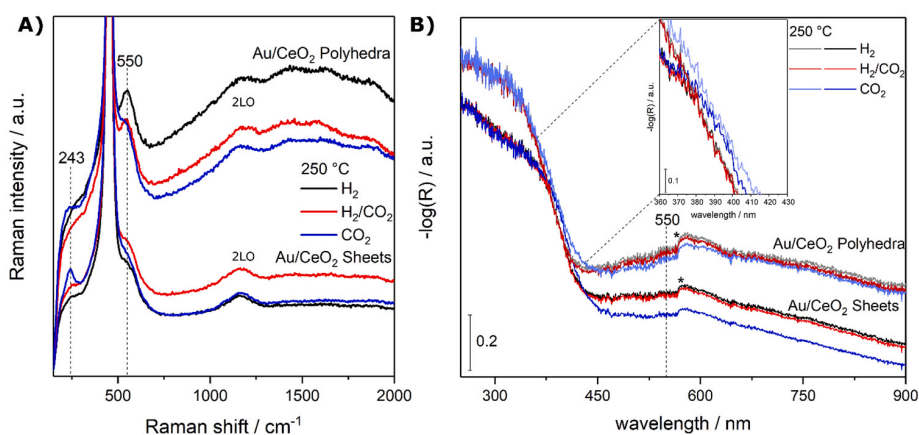


Fig. 3. *Operando* A) Raman and B) UV-Vis spectra of Au/CeO₂ sheets (bottom) and Au/CeO₂ polyhedra (top). The spectra were recorded at 250 °C, at a total flow rate of 100 mL/min, and during gas exposures to H₂ (10%), H₂/CO₂ (4%/2%) and CO₂ (2%). In the Raman spectra the high-intensity F_{2g} peak was cut off to allow an enlarged view of the other features. The inset in the right panel provides an enlarged view of the absorption within 360–430 nm.

polyhedra and its shape changes upon exposure to CO₂. The broad band at 1170 cm⁻¹ is caused by the 2LO overtone [37], whereas additional features above 1250 cm⁻¹ may originate from carbonaceous adsorbates. This aspect will be investigated in more detail using DRIFTS (see below).

The UV-Vis spectra in Fig. 3B show that under CO₂ atmosphere the absorption decreases from about 450 nm on. This effect is more pronounced for the sheets, which can be explained by more facile surface oxidation of the sheets, fully consistent with the intensity increase of the Raman longitudinal surface oxygen mode at 243 cm⁻¹ (see above). The increase in oxidation during exposure to CO₂ also influences the band edge. In fact, as shown in the inset of Fig. 3B, the absorption becomes wider due to the larger band gap, originating from the decrease in Ce³⁺ [35]. Upon switching from H₂ to reaction conditions no significant change in the gold surface plasmon region (~550 nm) was observed, indicating that about the same degree of gold agglomeration is present under both conditions. In this context, it should also be mentioned that previous studies on Au/CeO₂ have shown that H₂ treatment at 200 °C already reduces all cationic gold to metallic gold [38].

Next, the gold-loaded samples were alternately exposed to H₂, CO₂, and reaction conditions, and monitored by combined *operando* Raman and UV-Vis spectroscopy. The results for the F_{2g} position, the absorption at 550 nm, and the gas-phase IR signal are summarized in Fig. 4. The spectroscopic data clearly shows that CO₂ is able to re-oxidize pre-reduced gold-loaded ceria, which can then be reduced again by H₂. The simultaneous gas-phase analysis reveals the formation of H₂O during H₂ treatment, while subsequent treatment with CO₂ leads to CO and H₂O formation (see Fig. 4), demonstrating that hydrogen must still be present on the surface, e.g. as adsorbed water or hydroxide. This observation

will be confirmed by the DRIFTS data (see below). Likewise, after CO₂ treatment followed by exposure to H₂, CO and H₂O are formed (see Fig. 4), which shows the presence of surface carbon species, which only desorb when hydrogen is available. We can rule out residual H₂ or CO₂ as a potential source for the gas-phase signals, as the residence time is about 1 min but the effects continue for more than 10 min. Thus, the results so far would be consistent with a (combined) redox and associative mechanism.

In Fig. 4 it is noticeable that the changes in F_{2g} position and 550 nm absorption are larger for the sheets, underlining their higher redox activity. Interestingly, polyhedra and sheets are characterized by different reduction levels after H₂ treatment (see F_{2g} positions), but show the same F_{2g} position upon exposure to CO₂. This behavior may be an indication that reduced ceria can only be oxidized to a limited extent by using CO₂. Despite equal F_{2g} positions, different absorptions at 550 nm are observed, which can be explained by different fractions of metallic gold clusters.

In the following, we will examine more closely the effect of the pretreatment (H₂ or CO₂) on the reaction process. When the atmosphere is switched from H₂ to reaction conditions, the UV-Vis spectra show a slight decrease in 550 nm absorption and the Raman spectra a small F_{2g} redshift (see Figs. 4 and S4). However, these changes are too small to make a definitive statement. Nevertheless, the situation is different in the case of the CO₂ pretreatment, where the two samples show a pronounced reduction when the reaction conditions are switched on, as indicated by the F_{2g} redshift and the increase in 550 nm absorption, both of which are significantly higher for the sheets. Comparison of the activity data in Figs. 4 and S4 reveals that after pretreatment with CO₂

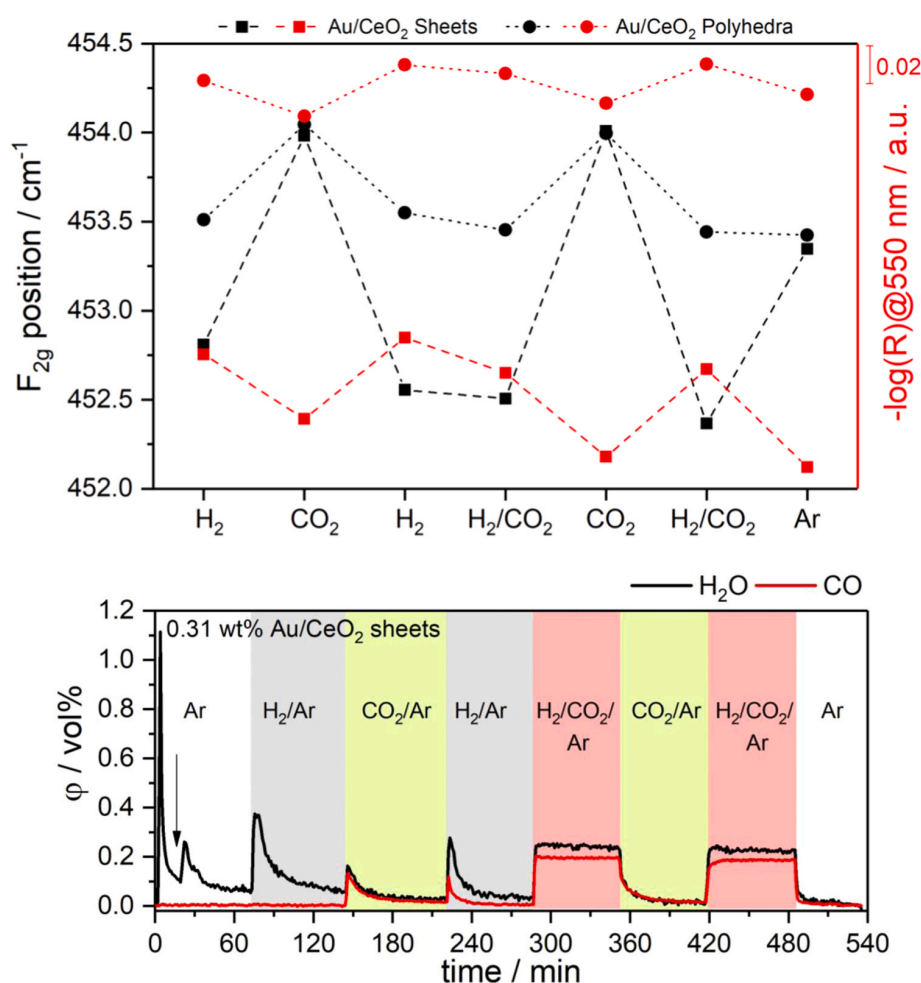


Fig. 4. Top: Operando Raman and UV-Vis results of Au/CeO₂ sheets and Au/CeO₂ polyhedra during exposure to H₂ (10%), CO₂ (2%), H₂/CO₂ (4%/2%), and argon at 250 °C and a total flow rate of 100 mL/min. The data were obtained by averaging two Raman spectra and three UV-Vis spectra per gas phase, except for argon, where the results from only one Raman spectrum and two UV-Vis spectra were used. Bottom: Gas-phase IR analysis of Au/sheets. The corresponding data for Au/polyhedra are shown in Fig. S4. The increased water concentration in the first few minutes is due to the purging of the cell. The cell was heated to 250 °C, starting after 19 min (see black arrow), leading to water desorption and thus an increase in the H₂O concentration.

both samples yield a 0.5% smaller conversion. This behavior suggests that the reaction occurs preferentially over a reduced surface and, as indicated by the F_{2g} shift, lattice oxygen is involved in the reaction mechanism. Another aspect that may affect the activity could be the formation of stable adsorbates during CO₂ treatment, thus blocking active sites. This aspect of the influence of pretreatment will be addressed later in the context of our transient measurements. After reaction conditions, the feed was switched to argon as in the previous measurements (see Fig. 2), which leads to a re-oxidation, whereby the observed changes are significantly larger for the sheets, again showing their increased oxygen mobility.

To investigate the changes in oxidation state of the surface after exposure to different gas atmospheres, *quasi in situ* XPS was applied. In these measurements, XPS spectra were recorded after synthesis, H₂ pretreatment, and reaction conditions without exposure to air when transferring the samples from the pre-treatment/reaction cell to the analysis chamber. It should be mentioned that XPS probes exclusively surface properties, in contrast to Raman and UV-Vis spectroscopy. First of all, XPS analysis did not reveal a significant increase in the surface carbon concentration after reaction conditions (not shown). Hence there is no indication for coking during reaction. As a measure of the surface oxidation state, Table 2 and Fig. S8 depict the O:Ce ratios of the gold-loaded samples, while the corresponding Au 4f photoemissions are shown in Fig. S9. Starting with the O:Ce ratios of the as-prepared samples, both Au/sheets and Au/polyhedra are characterized by approximately the same O:Ce ratio of 1.97. This is indicative of the presence of

Table 2

Surface O:Ce ratios as obtained from the XPS analysis of gold-loaded ceria sheets and polyhedra.

Pretreatment	O:Ce ratio
<i>0.31 wt% Au/CeO₂ sheets</i>	
None (as prepared)	1.97 ± 0.07
30 min H ₂ (10%), 250 °C	1.83 ± 0.08
1 h H ₂ /CO ₂ (4%/2%), 250 °C	1.75 ± 0.09
<i>0.27 wt% Au/CeO₂ polyhedra</i>	
None (as prepared)	1.97 ± 0.08
30 min H ₂ (10%), 250 °C	1.50 ± 0.08
1 h H ₂ /CO ₂ (4%/2%), 250 °C	1.39 ± 0.06

surface oxygen defects, and considering that adsorbates such as carbonates or water are still present after synthesis (see outgassing process in Fig. 4), the actual defect content after synthesis will be higher than this value suggests.

Upon treatment with 10% H₂ at 250 °C, a decrease in the O:Ce ratio is observed for both samples, which can readily be explained by a surface reduction due to water formation, as evident from the gas-phase IR measurements (see Fig. 4 and S4). This behavior is also consistent with the F_{2g} redshift and the 550 nm absorption increase discussed above (see Fig. 2). However, upon closer inspection, it can be seen that the stoichiometry change is smaller for the sheets than for the polyhedra, suggesting a lower defect concentration at the surface of the sheets.

At first glance, this observation seems to be in conflict with the Raman and UV-Vis measurements that probe the subsurface. However, the apparent contradiction can be resolved when taking into account the oxygen mobility between surface and subsurface and the fact that oxygen defects are first formed at the surface. In fact, according to the Raman and UV-Vis results, an exchange between surface and subsurface/bulk must have taken place upon switching from reactive to argon atmosphere, because all samples are subject to an F_{2g} blueshift and absorption decrease, despite the inert conditions (see Fig. 4). As these changes are always larger for the sheets, a larger mobility of lattice oxygen in sheets is expected than for the polyhedra. As a consequence of the more facile transfer of oxygen from the subsurface/bulk to the surface, the overall change in the O:Ce surface ratio is smaller for the sheets.

After analysis of the reduction treatment, the sample was transferred to the reaction chamber under absence of air and exposed to reaction conditions, followed by another XPS measurement. As shown in Table 2 and Fig. S8, a further decrease of the O:Ce ratio is detected, but these changes are within the error of the experiment. To this end, we cannot exclude the loss of adsorbates formed under reaction conditions when transferring the sample to the XPS analysis chamber under vacuum conditions. In fact, transient DRIFT spectra clearly show that reaction intermediates desorb immediately after the reaction conditions are stopped by switching off one reactant (see Fig. S6). For these reasons, the quasi *in situ* analysis after reaction conditions needs to be treated with caution.

Next, the state of gold will be addressed based on the Au 4f photoemissions. Due to the low gold loading, a quantitative analysis is challenging (see Fig. S9), but qualitative statements can still be made. Independent of the pretreatment and sample, the state of the gold does not change significantly and metallic or negatively charged gold is present independent of the pretreatment, since the central Au 4f_{7/2} binding energy never exceeds values of 84.5 eV. However, a comparison between polyhedra and sheets shows that the signals of polyhedra are at slightly lower binding energies (~0.4 eV), which could indicate more metallic gold, in agreement with the UV-Vis results. In this context, besides the state of gold the presence of potential gold adsorbates should be taken into account. The latter will be addressed by transient DRIFT spectra, as described in the following.

3.3. Transient surface analysis

To gain insight into possible adsorbates during the reaction, transient DRIFT spectra of unloaded and gold-loaded ceria catalysts were recorded, by using spectra of the catalysts under H₂ or CO₂ as background. As the background is measured either in H₂, CO₂ or H₂/CO₂, negative signals can occur due to non-stable intermediates. These negative signals are important indicators providing information about the reversibility as well as possible intermediates, which are only formed under reaction conditions. After the background had been recorded, CO₂ or H₂ was added to the constant feed of H₂ or CO₂, thus switching to reaction conditions, and transient DRIFT spectra were taken every 5 s to monitor the temporal evolution of the adsorbates. By recording the gas-phase composition together with transient DRIFT spectra we confirmed the formation of CO and H₂O under reaction conditions. Fig. 5 depicts transient DRIFT spectra recorded 6 min after switching on the H₂ (A) and CO₂ (B) flow. The same experiments were also performed in reverse, i.e., the catalysts were exposed to reaction conditions and then one reactant was removed (see Fig. S6). Both experiments give comparable results, with the difference that the latter measurements show an inverse trend for the same signals. This reversibility underlines that the corresponding adsorbate bands must be related to reaction intermediates. We also recorded transient DRIFTS after 2 h, largely resembling the behavior after 6 min, and performed modulation excitation (ME) DRIFTS (for details see SI), which show the same bands as our transient DRIFTS experiments, further supporting our claim that the observed bands are associated with reaction intermediates [39].

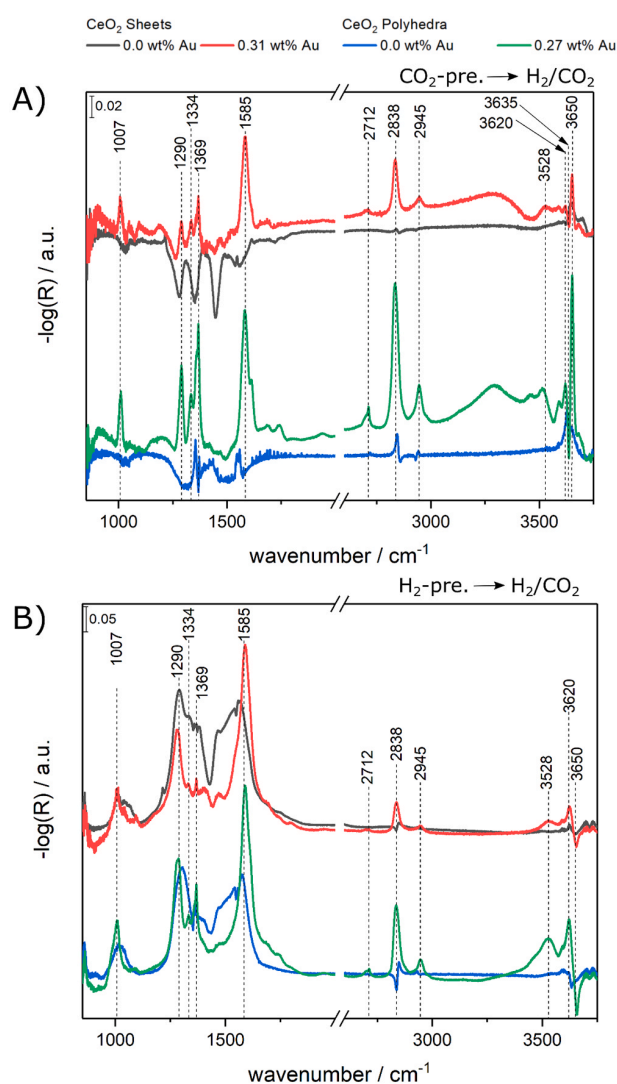


Fig. 5. Transient DRIFT spectra of bare and gold-loaded polyhedra and sheets. The spectra were recorded after pretreatment in H₂ (4 mol%) or CO₂ (2 mol%) balanced in argon at 250 °C at a total gas flow of 100 mL/min. Prior to the measurements A) the H₂ supply was switched on while CO₂ remained constant or B) the CO₂ supply was switched on while H₂ remained constant. Shown are only the last spectra of a measurement series with a duration of 6 min. As background, spectra of the catalyst after 15-minute exposure to either H₂ (4 mol%) or CO₂ (2 mol%) at 250 °C were employed.

When comparing the sheets and polyhedra in both experiments with and without gold loading, the same overall trends are observed. However, it is noticeable that the signals are sharper for the polyhedra, which contain only one clearly defined surface termination, i.e., CeO₂(111), thus limiting the number of possible adsorbates compared to the sheets which terminate mainly with the CeO₂(111) facet, but exhibit additional steps. Despite the latter differences, the similarities of the adsorbate bands detected for polyhedra and sheet samples point to a dominance of CeO₂(111)-related vibrational features. Therefore, the signals of ceria sheets and polyhedra that can be seen in Fig. 5 will be discussed together in the following.

To trace species related to the reaction, one needs to identify IR bands, which exhibit comparable intensity changes in both experiments, i.e., when either H₂ or CO₂ is switched on. Comparison of the spectra of the gold-loaded sheets and polyhedra in Fig. 5 reveals that this is obviously the case for the C-H stretching signal at 2838 cm⁻¹ as well as

its minor neighboring peaks at 2712 cm^{-1} and 2945 cm^{-1} , which are all assigned to bridged/bidentate formate species in agreement with the literature [40–43].

Further confirmation of the presence of formate species may arise from the identification of their complete vibrational pattern, including the region below 2000 cm^{-1} . In this region, signals appear at about 1007 cm^{-1} , 1290 cm^{-1} , 1334 cm^{-1} , 1369 cm^{-1} , and 1585 cm^{-1} in both experiments, which, except for the 1290 cm^{-1} feature, all coincide with the expectations for bridged formate species [40,41]. Regarding bare ceria, formate-related C-H signals can be detected unambiguously for polyhedra only. The identification of other formate bands, identified previously for gold-loaded samples, is hampered by the appearance of negative signals in the carbonate region for the bare samples when switching on H_2 (see Fig. 5A), as will be discussed below. When switching on CO_2 , besides the increasing C-H signal at 2848 cm^{-1} , a nearby negative signal at 2838 cm^{-1} is observed (see Fig. 5B). This indicates that a small part of the formate species may either undergo structural changes or may be subject to changing surroundings, possibly induced by the different redox properties of the reductive gas environment. Therefore, an additional experiment was performed, in which the gas phase was switched between reactive and reducing conditions (see Fig. S5). The observed 10 cm^{-1} redshift of the C-H signal at 2848 cm^{-1} upon reduction is fully consistent with the results in Fig. 5, thus confirming the above hypothesis, while the continuous shift behavior evidences the reversibility of the gas phase-induced changes.

Concerning gold-loaded ceria, the two signals at about 1007 cm^{-1} and 1585 cm^{-1} , together with the intense and characteristic band at 1290 cm^{-1} , suggest the presence of a carbonate species. However, the features at around 1007 cm^{-1} and 1585 cm^{-1} coincide with those of formate (see above). The latter feature furthermore exhibits a shoulder at around 1610 cm^{-1} in both experiments, which may indicate the presence of bidentate carbonates during the reaction. In the literature, bands at around 1610 cm^{-1} have been assigned to hydrogen carbonates or bidentate carbonate, but due to the lack of characteristic hydrogen carbonate bands at 1218 or 1393 cm^{-1} , their presence can be ruled out, thus pointing to the presence of bidentate carbonate [40,41,44].

Fig. 5 shows that for bare ceria the situation is more complex than for gold-loaded samples. When switching on CO_2 (see Fig. 5B), the overall trend of all signals in the carbonate region is positive, as in the case of the gold-loaded samples. In particular, in the region between the two intense bands at about 1290 and 1585 cm^{-1} the signals are broader, indicating the presence of more carbonate species during reaction as compared to gold-loaded ceria. In contrast, when switching from CO_2 atmosphere to reaction conditions (see Fig. 5A), the signals within $1000\text{--}1700\text{ cm}^{-1}$ show a general decrease in intensity, indicating decreased adsorption of CO_2 as carbonates onto the ceria surface. Especially for the sheets, hydrogen carbonates are also present, as evidenced by the characteristic $\delta(\text{COH})$ vibration at 1217 cm^{-1} , which is most clearly visible in Figs. 5B and S6B [33].

Important mechanistic conclusions can be drawn from the signal at 1943 cm^{-1} , which is only observed for the gold-loaded samples and increases weakly in both experiments, i.e., after switching on CO_2 and H_2 (see Fig. 6). Fig. 6 provides an enlarged view of the region around 1950 cm^{-1} , together with a spectrum of a Au/sheets sample with $0.62\text{ wt}\%$ gold, i.e., about doubled gold loading, showing an intensity increase of the 1943 cm^{-1} feature with increasing gold loading. The 1943 cm^{-1} feature is attributed to Au–H stretching modes of (partially) dissociatively adsorbed hydrogen, as confirmed by our DFT calculations, in which a hydrogen molecule was placed on a gold atom adsorbed on the (111) surface (see Fig. S17, structure B), corresponding to the most stable $\text{Au}_1/\text{CeO}_2(111)$ structure from our previous studies (see Fig. S17, structure A) [33]. In this case, the calculated H–H distance was 0.93 \AA , compared to a distance of 0.75 \AA for gas-phase H_2 . Based on our experimental observations and DFT results, we propose this state to be stable under reaction conditions only, while in the absence of CO_2 , proton transfer to the nearest oxygen atom takes place, leading to

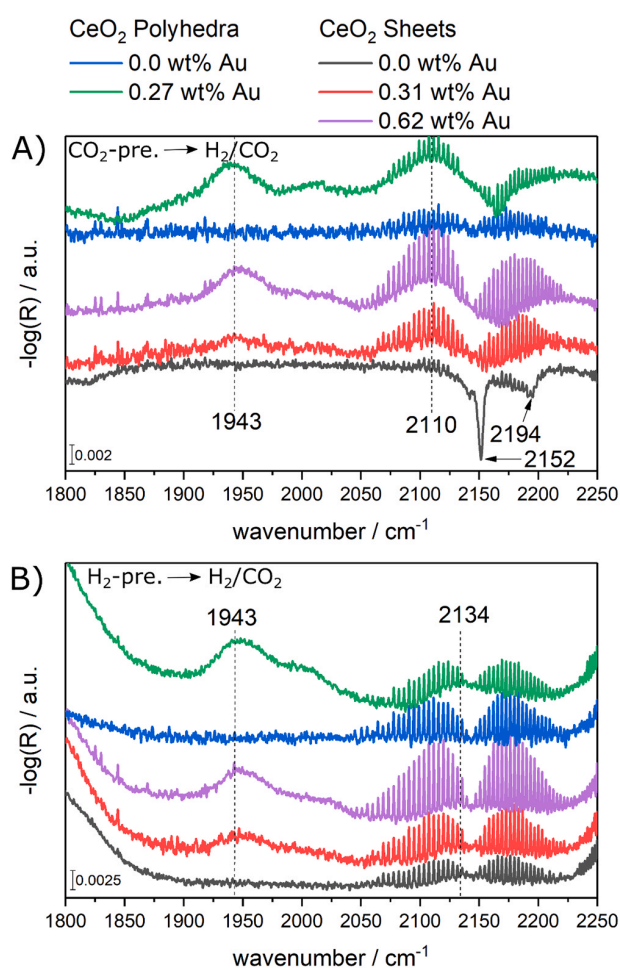


Fig. 6. Enlarged view of *in situ* DRIFT spectra from Fig. 5 showing the presence of adsorbed hydrogen. Spectra were taken A) after the H_2 supply was switched on while CO_2 remained constant, B) after the CO_2 supply was switched on while H_2 remained constant. Shown are only the last spectra of a measurement series with a duration of 6 min. For comparison, spectra of Au/CeO₂ sheets with $0.62\text{ wt}\%$ gold are shown.

immediate formation of a hydroxide and a Au–H species, since this state is energetically preferred by 1.33 eV (see Fig. S17, structure C). Such a scenario is fully consistent with the absence of the 1943 cm^{-1} band in H_2 atmosphere, i.e., without CO_2 being present (see Fig. S7). In this context, previous studies reported a Au–H species at 2134 cm^{-1} [27]. Remarkably, the 2134 cm^{-1} band is consistent with our DFT calculations and corresponds to a single H atom adsorbed on a gold atom (see Fig. S17, structure C), which is detected here for the gold-loaded sheets and polyhedra, lying underneath the signals of gaseous CO (see Fig. 6). For pretreatment in H_2 atmosphere the Au–H signal has its maximum at exactly 2134 cm^{-1} , whereas in the case of CO_2 pretreatment, the maximum is detected at about 2110 cm^{-1} . This redshift of the maximum may be induced by another signal with negative sign, located at about 2164 cm^{-1} , which may originate from adsorbed CO on CeO₂(111) [33]. This hypothesis is confirmed by spectra of the bare sheets, which show a contribution from CO adsorbates, as will be discussed below. To the best of our knowledge, we have demonstrated the intermediate step of H_2 adsorption on gold for the first time. It should be mentioned that we also performed isotope exchange experiments. However, the H_2 -Au species is not identifiable by D_2 isotope exchange as the bands shift into the carbonate/formate region and the H_2 -Au region is covered by C–D vibrations of formates (not shown). The theoretical H–D shifts are given in

Table S2.

Based on the DRIFT spectra in Fig. 6, there is no indication for CO adsorbed on gold, since the Au/polyhedra contain larger gold clusters (see above), which would result in IR signals of adsorbed CO below 2100 cm^{-1} [33], and the signals within $2050\text{--}2200\text{ cm}^{-1}$ are less pronounced after pretreatment with H_2 . The latter behavior can be explained by the fact that the signals in this region are assigned to H-Au species (see above), which already exist under the H_2 pretreatment and are thus subtracted by the background. It is noteworthy that the band at 1943 cm^{-1} is asymmetric towards higher wavenumbers, possessing a pronounced shoulder at around 2000 cm^{-1} . We propose this behavior to be caused by the presence of larger gold clusters. To confirm this hypothesis, we placed a hydrogen atom on the most stable $\text{Au}_4/\text{CeO}_2(111)$ structure from our previous DFT studies (see Fig. S17, structure H) [33]. The calculations reveal a characteristic band, which is blue shifted by 23 cm^{-1} compared to our single-site structure. Note that this process is endothermic, with an adsorption energy of 0.31 eV (see Table 2). Thus, this state is not preferred, but it is conceivable that the small energy barrier may be overcome at the elevated temperatures of our experiments and a spillover of hydrogen occurs. Further calculations show that H_2 interacts only weakly with the Au_4 cluster ($E_{\text{ads}} = -0.1\text{ eV}$), in contrast to the single-site adsorption energy of -1.08 eV discussed above (see Table S1). Thus, for larger clusters, no hydrogen dissociation on gold is expected; rather, this band is caused by H atoms from H_2 adsorption on single Au atoms migrating over the ceria surface. This behavior would also be consistent with experiment, as, based on UV-Vis spectra, the polyhedra contain more metallic gold and thus larger gold clusters (see Fig. S3), and these have the most pronounced asymmetry. Regarding the higher 1943 cm^{-1} signal of the polyhedra (despite the presence of larger gold clusters) we point out that, in general, the polyhedra show stronger DRIFTS signals than the sheets (see also Fig. 5). Possible reasons for this behavior may be the larger fraction of single Au atoms in the polyhedra, the higher porosity of the sheets, and/or crystal size/shape effects.

Closer inspection of the transient DRIFT spectra of the bare supports reveals that the sheets exhibit a decreasing feature at 2152 cm^{-1} , which is not detected for the polyhedra (see Fig. 6) and only visible after CO_2 pretreatment and addition of H_2 . The same behavior is also observed for the switching-off experiments (see Fig. S7), i.e., only the bare sheets show an increasing signal at 2152 cm^{-1} after exposure to reaction conditions and after subsequent switching-off of H_2 . This signal is assigned to CO adsorbed on $\text{CeO}_2(111)$, in agreement with the literature [45]. The fact that it is only detected for the ceria sheets suggests that CO adsorbs more strongly at steps than on the flat $\text{CeO}_2(111)$, while exhibiting a similar vibrational frequency. Another interesting observation is that it decreases when H_2 is switched on and increases when H_2 is switched off. Moreover, it remains invisible when CO_2 is switched on after pretreatment in H_2 atmosphere (see Fig. 6). Thus the respective surface species seems to be stable only in the absence of H_2 . Detailed analysis of the spectra in Figs. 5 and 6 reveals that the presence of this CO adsorbate signal correlates with low intensity formate signals in the C-H region at 2838 and 2945 cm^{-1} , in contrast to the ceria polyhedra, which have no adsorbed CO signal and whose formate signals are more intense at the same time. This behavior may indicate that formates are not needed as an intermediate in the rWGSR over bare ceria sheets, where stepped sites are present. So, instead of an associative mechanism including formates as intermediates, a redox mechanism involving only surface oxygen atoms may be operative.

Furthermore, at around 2200 cm^{-1} a broad band with increasing intensity is observed for the gold samples in the H_2 -on experiment (see Fig. 6A), which is not present in the CO_2 -on experiment (see Fig. 6B). The same inverse behavior for the intensities is also seen for the switching-off experiments (see Fig. S7). These observations suggest that these species are not involved in the reaction but are spectator species. In previous studies on Zeolite NaY, bands in this region have been attributed to Au^{3+} -CO species [46], and such oxidation states of gold are

also conceivable on $\text{CeO}_2(111)$ if gold occupies a cerium lattice site [47].

Regarding the bare samples, the sheets show a decreasing band at 2194 cm^{-1} , which is detected in the H_2 -on experiment (see Fig. 6A) but not in the switching-off experiments (see Fig. S7), implying that the related species is not involved in the reaction. Due to the decreasing intensity in the H_2 -on and the increasing intensity in the H_2 -off experiment, the band does probably not originate from CO adsorbates, which are formed during the reaction, but probably from weakly adsorbed CO_2 on the reduced surface, which has also been detected in the same range on other oxides such as MgO [48]. Its absence in case of the polyhedra suggests that this process may be influenced by steps.

Based on the transient DRIFTS shown in Fig. 5, OH species are involved in the reaction. For the gold-loaded samples, increasing O-H stretching signals are observed at about 3528 and 3620 cm^{-1} , and the latter show a stronger increase when the CO_2 feed is switched on. The 3620 cm^{-1} band can be assigned to a triply bonded OH group (type III) [49]. Bands at around 3510 cm^{-1} have previously been attributed to a residual oxy-hydroxide phase [50], but our band is sensitive to the different gas environments. Our DFT calculations have revealed that the dissociation of hydrogen on the gold atom leads to a hydroxide species (see above), which is characterized by a vibrational frequency of 3548 cm^{-1} (Fig. S17, structure C). For comparison to the bare support, we have recalculated the most stable hydroxide (H-NNN) from the literature [51] and obtained a vibrational frequency of 3732 cm^{-1} . Based on these findings, we propose the band at 3528 cm^{-1} to originate from hydroxides near gold atoms. Besides, DFT calculations on hydroxides adsorbed on reduced ceria gave significantly higher frequencies than observed here [50].

In contrast, the intense band at about 3650 cm^{-1} increases in intensity upon addition of H_2 (see Fig. 5A), and decreases when CO_2 is switched on (see Fig. 5B). This behavior supports previous assignments of this band to O-H stretching of bridged hydroxide in the presence of an oxygen defect on reduced ceria, which has been referred to as OH (II*-B) [50]. In addition, a feature at about 3635 cm^{-1} rises under oxidizing conditions (see Fig. 5B) and decreases under reducing ones (see Fig. 5A), which is consistent with the corresponding hydroxyl species on unreduced surfaces, i.e., OH (II-B) [50].

Water, the only other final product besides CO, might appear in a gaseous or weakly bound surface state. The spectra of bare ceria exhibit only very weak water-related signals due to rotationally resolved gaseous water between 1400 and 2000 cm^{-1} , as well as above 3500 cm^{-1} . For the gold-loaded catalysts, some gaseous water is visible in Fig. 5 A when H_2 is turned on, whereas weakly bound water can be found as a broad increasing signal, centered around 3300 cm^{-1} (see Fig. 5A). Upon addition of CO_2 , no weakly bound water is detected and the rotational bands of gaseous water are by far weaker (see Fig. 5B). The largely missing water signal may be a result of the pretreatment with hydrogen, which leads to the formation of water, that partially desorbs, thus making it invisible in the difference spectra [25].

From the transient DRIFT spectra in Fig. 5 it is apparent that the type of pretreatment has a pronounced influence on the relative intensities of the individual species. In particular, the formate signals gain considerable intensity upon CO_2 pretreatment (see Fig. 5B). On the other hand, the above activity results showed a lower conversion for CO_2 pretreatment than for H_2 pretreatment. Thus, we can already state at this point that the pretreatment has an influence on the reactivity behavior.

4. Discussion of the reaction mechanism

Comparing the degree of reduction obtained by the Raman and UV-Vis analysis with the CO_2 conversions, it is clear that the reducibility of the support does not play the leading role for the rWGSR activity. In particular, the polyhedra undergo smaller changes during the different gas exposures than the sheets, but exhibit an activity that is higher for the unloaded sample and about the same for the gold-loaded sample. Therefore, a major question concerns the mechanistic role of gold and

the ceria support in rWGS over Au/ceria catalysts. Our experimental results, especially the transient DRIFT spectra, show that a different mechanism prevails on the gold-loaded samples than on bare ceria. This is supported by the decreasing intensities of bare ceria in the range below 2000 cm^{-1} (see Fig. 5A) and the appearance of additional bands compared to the gold-loaded samples (in this range) when CO_2 is turned on (see Fig. 5B). A redox mechanism alone cannot explain this behavior. We rather propose that an associative mechanism can occur on the polyhedra even in the absence of gold, which is supported by the formate decomposition (see Fig. S6A). Such a behavior is not observed on the sheets. On the other hand, for the sheets, an additional CO-related band is observed at 2152 cm^{-1} , which is not visible for the polyhedra despite the same surface termination, strongly supporting the assumption of a different mechanism on the differently shaped particles. Based on these observations, we propose that on both ceria samples a redox mechanism predominates, but that on the polyhedra also an associative mechanism occurs. In particular, we associate the occurrence of the redox mechanism with the better reducibility of the sheets, originating from the steps. The occurrence of a redox mechanism on both samples is also supported by Fig. S14, which shows an increase of CO in the IR gas phase data when switching from H_2 to CO_2 . At the same time, the switch from CO_2 to H_2 also shows a slight increase in the CO signal for the polyhedra, which is related to the decomposition of remaining carbonaceous adsorbates and thus indicates a reaction pathway via intermediates.

For the gold-loaded samples, an associative mechanism dominates on both samples and is probably facilitated by the easier activation of H_2 in the presence of gold. Nevertheless, on the gold-loaded samples a redox mechanism also takes place, as is apparent from switching between oxidizing and reducing conditions, which evidenced the oxidation or reduction of the surface, leading to CO or H_2O formation (see Fig. 4 and S4). For the rWGS over Au/ TiO_2 catalysts a mechanism involving hydroxycarbonyls has been suggested, which we however exclude for Au/ceria, since we do not detect any CO adsorbed on gold, which is essential for the formation of hydroxycarbonyls. Besides, characteristic carboxylate bands are absent [52], which would indicate the activation of CO_2 on gold. By combining all spectroscopic and theoretical findings of this study, we developed an overall picture of the associative

mechanism on the gold-loaded samples, as summarized in Fig. 7: Starting with a reduced ceria surface (1), the adsorption of CO_2 , facilitated by an oxygen vacancy, leads to carbonate formation (2). Next, carbonate decomposes by release of CO and healing of an oxygen vacancy (3). Reaction of H_2 with surface oxygen results in the formation of water, thereby reducing the surface, while another hydrogen molecule is activated on gold. This activation proceeds in two steps (4). First, a hydrogen molecule dissociatively adsorbs on gold (see Fig. S17, structure B), followed by a spillover onto ceria, forming a hydroxide (see Fig. S17, structure C), as shown by our combination of experiment and theory. Next, a CO_2 molecule adsorbing onto ceria in the vicinity of gold as carbonate (again facilitated by vacancies), is transformed into formate by hydrogen transport from gold to ceria (5). Finally, formate reacts with a neighboring hydroxide, leading to water and CO formation, thus closing the catalytic cycle. The individual reaction steps are summarized in Fig. S16.

We point out that there are two routes by which CO_2 can be activated, i.e., via carbonates or formates/hydroxycarbonyls [53,54]. Theoretical studies [53] indicate that the route via hydroxycarbonyls (COOH) is more competitive than that via formates (HCOO), but based on the absence of specific hydroxycarbonyls bands [55] in our IR experiments, the route via COOH appears to play a minor role. Furthermore, H_2 pretreatment leads to a reduced surface and supports the dissociation of CO_2 to CO via carbonates [53], which is consistent with our observation of higher activities after H_2 pretreatment and the lower C-H signals in Fig. 5B. This step is also proposed to be rate-determining, since the healing of defects by CO_2 via the release of CO ($\text{CeO}_2(111)$ without gold) is endothermic by 0.98 eV. Based on our findings, the formate and carbonate formation steps (5, 2) cannot be explicitly separated from each other, thus these steps may run independently of each other. For example, by omitting steps 2 and 3, the reaction may proceed directly to step 4. This is also consistent with the higher C-H intensities in the measurements with CO_2 pretreatment (see Fig. 5A), which are starting from a more oxidized surface compared to the H_2 pretreatment. Studies during methane dry reforming over ^{18}O labeled Ni/ CeO_2 have shown, that lattice oxygen is involved in the formation of CO [56]. However, in the reaction discussed here, no coking of the catalyst can be detected, so the involvement of lattice oxygen in CO

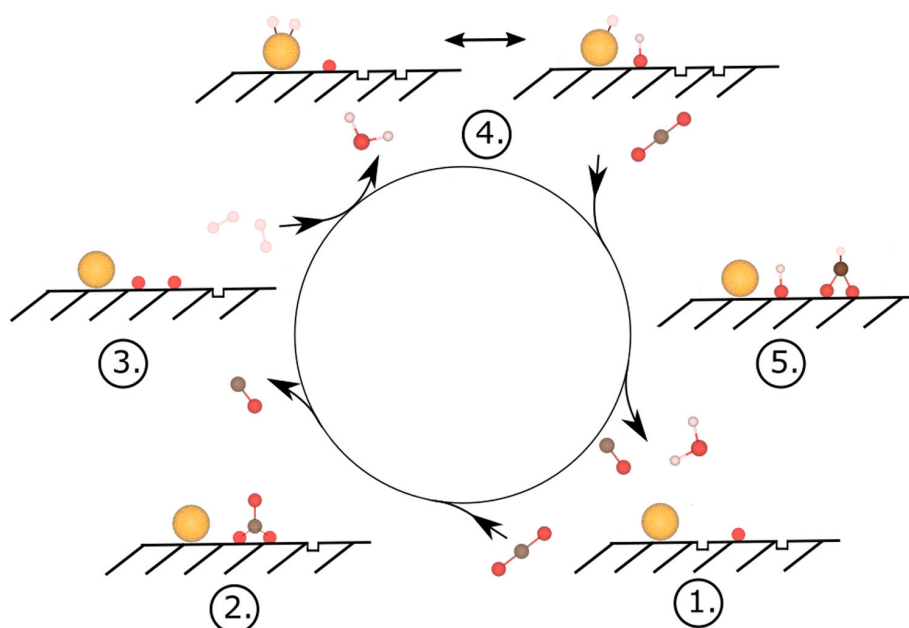


Fig. 7. Proposed mechanism for the reverse water-gas shift reaction (rWGS) over Au/ $\text{CeO}_2(111)$ catalysts. For clarity, only the reaction pathway mediated by a gold single site is shown. Atoms correspond to oxygen (red), carbon (brown), hydrogen (white) and gold (gold).

formation similar to methane dry reforming is improbable. Nevertheless, such studies could support the involvement of lattice oxygen in the formation of H₂O. In summary, the CO₂ reduction pathway depends on the concentration of defects and/or hydroxides, which in turn depend on the pretreatment (see also Fig. S13). Thus, on a defect-rich surface (H₂ pretreatment), the path via carbonates is preferred, while on the other hand, on a surface with fewer defects, the path via formates will dominate.

5. Conclusions

Based on the *operando* Raman and UV-Vis spectroscopic observations, the ability to form defects plays a minor role in the conversion of CO₂ within the rWGS. Indeed, when the reducibility of the gold-loaded samples is compared, sheets undergo significantly larger changes under reducing (H₂) or reaction conditions (see Fig. 3), while their activity is very similar to that of the polyhedra (see Table 1). These observations are evidence of the fact that defect formation is not essential for the reaction pathway and that the route via intermediates (formates, carbonates, hydroxides) is more important. However, detailed analysis reveals that the pretreatment (H₂, CO₂) has an influence on the reaction pathway and on the catalytic activity. To this end, CO₂ reduction over a reduced ceria surface favors carbonate intermediates, while over a low-defect surface a reduction via formates is preferred; besides, starting from a highly reduced surface (H₂ pretreatment) leads to higher activities.

In contrast to bare ceria, a pure redox mechanism loses importance on Au/ceria catalysts at lower temperatures (<250 °C). This is attributed to the activation of hydrogen on gold atoms, whereas hydrogen interacts in its molecular form only very weakly with the bare CeO₂(111) surface [51]. In this context, using transient DRIFTS in combination with DFT calculations, we were able to elucidate for the first time the individual steps of H₂ activation over Au/CeO₂(111), which is shown to proceed in two steps (see Fig. 7). Based on our findings, we propose gold atoms to be essential for an associative mechanism.

Our study clearly reveals that multiple techniques, sampling both subsurface and surface properties, are required to elucidate the mechanism of the rWGS over Au/CeO₂ catalysts. In particular, the use of *operando* and transient approaches in combination with theory is shown to enable a detailed analysis, including spectroscopic features not reported in the literature.

CRedit authorship contribution statement

Marc Ziemba, Jakob Weyel: Investigation, Methodology, Software, Validation, Formal analysis, Data curation, Visualization, Writing – original draft. **Christian Hess:** Conceptualization, Visualization, Supervision, Project Administration, Funding acquisition, Writing – review & editing.

Declaration of Competing Interest

The authors declare that they have no known competing financial interests or personal relationships that could have appeared to influence the work reported in this paper.

Acknowledgement

We thank Stefan Lauterbach and Hans-Joachim Kleebe for TEM measurements, Martin Brodrecht for BET measurements, M. Verónica Ganduglia-Pirovano for support in theory, and Karl Kopp for technical support and helpful discussions on the XPS results. Calculations for this research were conducted on the Lichtenberg high performance computer of the TU Darmstadt. Jakob Weyel gratefully acknowledges a scholarship from the Fonds der Chemischen Industrie im Verband der

Chemischen Industrie e.V.

Appendix A. Supporting information

Supplementary data associated with this article can be found in the online version at [doi:10.1016/j.apcatb.2021.120825](https://doi.org/10.1016/j.apcatb.2021.120825).

References

- [1] J. Jiang, B. Ye, J. Liu, Research on the peak of CO₂ emissions in the developing world: current progress and future prospect, *Appl. Energy* 235 (2019) 186–203, <https://doi.org/10.1016/j.apenergy.2018.10.089>.
- [2] X. Chen, Y. Chen, C. Song, P. Ji, N. Wang, W. Wang, L. Cui, Recent advances in supported metal catalysts and oxide catalysts for the reverse water-gas shift reaction, *Front. Chem.* 8 (2020) 1–21, <https://doi.org/10.3389/fchem.2020.00709>.
- [3] M. Boaro, S. Colussi, A. Trovarelli, Ceria-based materials in hydrogenation and reforming reactions for CO₂ valorization, *Front. Chem.* 7 (2019) 28, <https://doi.org/10.3389/fchem.2019.00028>.
- [4] K. Chang, H. Zhang, M. Cheng, Q. Lu, Application of ceria in CO₂ conversion catalysis, *ACS Catal.* 10 (2020) 613–631, <https://doi.org/10.1021/acscatal.9b03935>.
- [5] G. Jacobs, B.H. Davis, Reverse water-gas shift reaction: steady state isotope switching study of the reverse water-gas shift reaction using in situ DRIFTS and a Pt/ceria catalyst, *Appl. Catal. A Gen.* 284 (2005) 31–38, <https://doi.org/10.1016/j.apcata.2005.01.013>.
- [6] F.C. Meunier, D. Tibiletti, A. Goguet, D. Reid, R. Burch, On the reactivity of carbonate species on a Pt/CeO₂ catalyst under various reaction atmospheres: Application of the isotopic exchange technique, *Appl. Catal. A Gen.* 289 (2005) 104–112, <https://doi.org/10.1016/j.apcata.2005.04.018>.
- [7] C.M. Kalamaras, S. Americanou, A.M. Efstathiou, “Redox” vs “associative formate with –OH group regeneration” WGS reaction mechanism on Pt/CeO₂: Effect of platinum particle size, *J. Catal.* 279 (2011) 287–300, <https://doi.org/10.1016/j.jcat.2011.01.024>.
- [8] L. Lin, S. Yao, Z. Liu, F. Zhang, N. Li, D. Vovchok, A. Martínez-Arias, R. Castañeda, J. Lin, S.D. Senanayake, D. Su, D. Ma, J.A. Rodriguez, In situ characterization of Cu/CeO₂ nanocatalysts for CO₂ hydrogenation: morphological effects of nanostructured ceria on the catalytic activity, *J. Phys. Chem. C* 122 (2018) 12934–12943, <https://doi.org/10.1021/acs.jpcc.8b03596>.
- [9] Y. Liu, Z. Li, H. Xu, Y. Han, Reverse water-gas shift reaction over ceria nanocube synthesized by hydrothermal method, *Catal. Commun.* 76 (2016) 1–6, <https://doi.org/10.1016/j.catcom.2015.12.011>.
- [10] L.F. Bobadilla, J.L. Santos, S. Ivanova, J.A. Odriozola, A. Urakawa, Unravelling the role of oxygen vacancies in the mechanism of the reverse water-gas shift reaction by *operando* DRIFTS and ultraviolet–visible spectroscopy, *ACS Catal.* 8 (2018) 7455–7467, <https://doi.org/10.1021/acscatal.8b02121>.
- [11] J.A. Rodríguez, J. Evans, J. Graciani, J.-B. Park, P. Liu, J. Hrbek, J.F. Sanz, High water–gas shift activity in TiO₂(110) supported Cu and Au nanoparticles: role of the oxide and metal particle size, *J. Phys. Chem. C* 113 (2009) 7364–7370, <https://doi.org/10.1021/jp900483u>.
- [12] L.C. Wang, M. Tahvildar Khazaneh, D. Widmann, R.J. Behm, TAP reactor studies of the oxidizing capability of CO₂ on a Au/CeO₂ catalyst – a first step toward identifying a redox mechanism in the reverse water–gas shift reaction, *J. Catal.* 302 (2013) 20–30, <https://doi.org/10.1016/j.jcat.2013.02.021>.
- [13] L.C. Wang, D. Widmann, R.J. Behm, Reactive removal of surface oxygen by H₂, CO and CO/H₂ on a Au/CeO₂ catalyst and its relevance to the preferential CO oxidation (PROX) and reverse water gas shift (RWGS) reaction, *Catal. Sci. Technol.* 5 (2015) 925–941, <https://doi.org/10.1039/C4CY01030B>.
- [14] C. Schilling, C. Hess, Elucidating the role of support oxygen in the water–gas shift reaction over ceria-supported gold catalysts using *operando* spectroscopy, *ACS Catal.* 9 (2019) 1159–1171, <https://doi.org/10.1021/acscatal.8b04536>.
- [15] M. Ziemba, M.V. Ganduglia-Pirovano, C. Hess, Insight into the mechanism of the water–gas shift reaction over Au/CeO₂ catalysts using combined *operando* spectroscopies, *Faraday Discuss.* 229 (2021) 232–250, <https://doi.org/10.1039/C9FD00133F>.
- [16] X. Fu, L. Guo, W. Wang, C. Ma, C. Jia, K. Wu, R. Si, L.-D. Sun, C.-H. Yan, Direct identification of active surface species for the water–gas shift reaction on a gold–ceria catalyst, *J. Am. Chem. Soc.* 141 (2019) 4613–4623, <https://doi.org/10.1021/jacs.8b09306>.
- [17] A.M. Efstathiou, *Catalysis*, Royal Society of Chemistry, Cambridge, 2016, <https://doi.org/10.1039/9781782626855>.
- [18] T. Staudt, Y. Lykhach, N. Tsud, T. Skála, K.C. Prince, V. Matolín, J. Libuda, Ceria reoxidation by CO₂: a model study, *J. Catal.* 275 (2010) 181–185, <https://doi.org/10.1016/j.jcat.2010.07.032>.
- [19] S. Ackermann, L. Sauvin, R. Castiglioni, J.L.M. Rupp, J.R. Scheffe, A. Steinfeld, Kinetics of CO₂ reduction over nonstoichiometric ceria, *J. Phys. Chem. C* 119 (2015) 16452–16461, <https://doi.org/10.1021/acs.jpcc.5b03464>.
- [20] J.A. Rodríguez, D.C. Grinter, Z. Liu, R.M. Palomino, S.D. Senanayake, Ceria-based model catalysts: fundamental studies on the importance of the metal–ceria interface in CO oxidation, the water-gas shift, CO₂ hydrogenation, and methane and alcohol reforming, *Chem. Soc. Rev.* 46 (2017) 1824–1841, <https://doi.org/10.1039/c6cs00863a>.

- [21] J.H. Carter, G.J. Hutchings, Recent advances in the gold-catalysed low-temperature water-gas shift reaction, *Catalysts* 8 (2018) 627, <https://doi.org/10.3390/catal8120627>.
- [22] A.M. Abdel-Mageed, G. Kucérova, J. Bansmann, R.J. Behm, Active Au species during the low-temperature water gas shift reaction on Au/CeO₂: a time-resolved operando XAS and DRIFTS study, *ACS Catal.* 7 (2017) 6471–6484, <https://doi.org/10.1021/acscatal.7b01563>.
- [23] J.H. Carter, X. Liu, Q. He, S. Althahban, E. Nowicka, S.J. Freakley, L. Niu, D. J. Morgan, Y. Li, J.W.H. Niemantsverdriet, S. Golunski, C.J. Kiely, G.J. Hutchings, Activation and deactivation of gold/ceria-zirconia in the low-temperature water-gas shift reaction, *Angew. Chem. Int. Ed.* 56 (2017) 16037–16041, <https://doi.org/10.1002/anie.201709708>.
- [24] (a) A.M. Efstathiou, K.C. Petalidou, Reply to the Letter to the Editor concerning the comments of Dr. F. Meunier to the article, *Appl. Catal. B: Environ.* 136–137 (2013) 225–238; (b) Kalamaras, et al., titled “The effect of La³⁺-doping of CeO₂ support on the water-gas shift re”, *Appl. Catal. B Environ.* 152–153 (2014) 439–443, <https://doi.org/10.1016/j.apcatb.2014.01.064>.
- [25] D. Schweke, L. Shelly, R. Ben David, A. Danon, N. Kostirya, S. Hayun, Comprehensive study of the ceria-H₂ system: effect of the reaction conditions on the reduction extent and intermediates, *J. Phys. Chem. C* 124 (2020) 6180–6187, <https://doi.org/10.1021/acs.jpcc.9b11975>.
- [26] Z. Wu, Y. Cheng, F. Tao, L. Daemen, G.S. Foo, L. Nguyen, X. Zhang, A. Beste, A. J. Ramirez-Cuesta, Direct neutron spectroscopy observation of cerium hydride species on a cerium oxide catalyst, *J. Am. Chem. Soc.* 139 (2017) 9721–9727, <https://doi.org/10.1021/jacs.7b05492>.
- [27] R. Juárez, S.F. Parker, P. Concepción, A. Corma, H. García, Heterolytic and heterotopic dissociation of hydrogen on ceria-supported gold nanoparticles. Combined inelastic neutron scattering and FT-IR spectroscopic study on the nature and reactivity of surface hydrogen species, *Chem. Sci.* 1 (2010) 731, <https://doi.org/10.1039/c0sc00336k>.
- [28] D. Ren, L. He, L. Yu, R.-S. Ding, Y.-M. Liu, Y. Cao, H.-Y. He, K.-N. Fan, An unusual chemoselective hydrogenation of quinoline compounds using supported gold catalysts, *J. Am. Chem. Soc.* 134 (2012) 17592–17598, <https://doi.org/10.1021/ja3066978>.
- [29] H.Y. Kim, G. Henkelman, CO Oxidation at the interface of Au nanoclusters and the stepped-CeO₂(111) surface by the Mars-van Krevelen mechanism, *J. Phys. Chem. Lett.* 4 (2013) 216–221, <https://doi.org/10.1021/jz301778b>.
- [30] C. Schilling, C. Hess, CO Oxidation on ceria supported gold catalysts studied by combined operando Raman/UV-Vis and IR spectroscopy, *Top. Catal.* 60 (2017) 131–140, <https://doi.org/10.1007/s11244-016-0732-6>.
- [31] C. Schilling, M.V. Ganduglia-Pirovano, C. Hess, Experimental and theoretical study on the nature of adsorbed oxygen species on shaped ceria nanoparticles, *J. Phys. Chem. Lett.* 9 (2018) 6593–6598, <https://doi.org/10.1021/acs.jpcclett.8b02728>.
- [32] M. Ziemba, C. Hess, Influence of gold on the reactivity behaviour of ceria nanorods in CO oxidation: combining operando spectroscopies and DFT calculations, *Catal. Sci. Technol.* 10 (2020) 3720–3730, <https://doi.org/10.1039/D0CY00392A>.
- [33] C. Schilling, M. Ziemba, C. Hess, M.V. Ganduglia-Pirovano, Identification of single-atom active sites in CO oxidation over oxide-supported Au catalysts, *J. Catal.* 383 (2020) 264–272, <https://doi.org/10.1016/j.jcat.2020.01.022>.
- [34] A. Goguet, F.C. Meunier, D. Tibiletti, J.P. Breen, R. Burch, Spectrokinetic investigation of reverse water-gas-shift reaction intermediates over a Pt/CeO₂ catalyst, *J. Phys. Chem. B* 108 (2004) 20240–20246, <https://doi.org/10.1021/jp047242w>.
- [35] C.W.M. Castleton, J. Kullgren, K. Hermansson, Tuning LDA+U for electron localization and structure at oxygen vacancies in ceria, *J. Chem. Phys.* 127 (2007), 244704, <https://doi.org/10.1063/1.2800015>.
- [36] J.A. Hernández, S.A. Gómez, T.A. Zepeda, J.C. Fierro-González, G.A. Fuentes, Insight into the deactivation of Au/CeO₂ catalysts studied by in situ spectroscopy during the CO-PROX reaction, *ACS Catal.* 5 (2015) 4003–4012, <https://doi.org/10.1021/acscatal.5b00739>.
- [37] C. Schilling, A. Hofmann, C. Hess, M.V. Ganduglia-Pirovano, Raman spectra of polycrystalline CeO₂: a density functional theory study, *J. Phys. Chem. C* 121 (2017) 20834–20849, <https://doi.org/10.1021/acs.jpcc.7b06643>.
- [38] A.M. Abdel-Mageed, G. Kucérova, J. Bansmann, R.J. Behm, Active Au species during the low-temperature water gas shift reaction on Au/CeO₂: a time-resolved operando XAS and DRIFTS study, *ACS Catal.* 7 (2017) 6471–6484, <https://doi.org/10.1021/acscatal.7b01563>.
- [39] V. Marchionni, D. Ferri, O. Kröcher, A. Wokaun, Increasing the sensitivity to short-lived species in a modulated excitation experiment, *Anal. Chem.* 89 (2017) 5801–5809, <https://doi.org/10.1021/acs.analchem.6b04939>.
- [40] G.N. Vayssilov, M. Mihaylov, P.S. Petkov, K.I. Hadjiivanov, K.M. Neyman, Reassignment of the vibrational spectra of carbonates, formates, and related surface species on ceria: a combined density functional and infrared spectroscopy investigation, *J. Phys. Chem. C* 115 (2011) 23435–23454, <https://doi.org/10.1021/jp208050a>.
- [41] F. Romero-Sarria, L.M. Martínez T, M.A. Centeno, J.A. Odriozola, Surface dynamics of Au/CeO₂ catalysts during CO oxidation, *J. Phys. Chem. C* 111 (2007) 14469–14475, <https://doi.org/10.1021/jp073541k>.
- [42] D. Vovchok, C. Zhang, S. Hwang, L. Jiao, F. Zhang, Z. Liu, S.D. Senanayake, J. A. Rodriguez, Deciphering dynamic structural and mechanistic complexity in Cu/CeO₂/ZSM-5 catalysts for the reverse water-gas shift reaction, *ACS Catal.* 10 (2020) 10216–10228, <https://doi.org/10.1021/acscatal.0c01584>.
- [43] W.O. Gordon, Y. Xu, D.R. Mullins, S.H. Overbury, Temperature evolution of structure and bonding of formic acid and formate on fully oxidized and highly reduced CeO₂(111), *Phys. Chem. Chem. Phys.* 11 (2009) 11171–11183, <https://doi.org/10.1039/b913310k>.
- [44] Y. Denkwitz, A. Karpenko, V. Plzak, R. Leppelt, B. Schumacher, R.J. Behm, Influence of CO₂ and H₂ on the low-temperature water-gas shift reaction on Au/CeO₂ catalysts in idealized and realistic reformat, *J. Catal.* 246 (2007) 74–90, <https://doi.org/10.1016/j.jcat.2006.11.012>.
- [45] C. Wöll, Structure and chemical properties of oxide nanoparticles determined by surface-ligand IR spectroscopy, *ACS Catal.* (2019), <https://doi.org/10.1021/acscatal.9b04016>.
- [46] M.Y. Mihaylov, J.C. Fierro-Gonzalez, H. Knözinger, B.C. Gates, K.I. Hadjiivanov, Formation of nonclassical carbonyls of Au³⁺ in zeolite NaY: characterization by infrared spectroscopy, *J. Phys. Chem. B* 110 (2006) 7695–7701, <https://doi.org/10.1021/jp057426q>.
- [47] M.F. Camellone, S. Fabris, Reaction mechanisms for the CO oxidation on Au/CeO₂ catalysts: activity of substitutional Au³⁺/Au⁺ cations and deactivation of supported Au⁺ adatoms, *J. Am. Chem. Soc.* 131 (2009) 10473–10483, <https://doi.org/10.1021/ja902109k>.
- [48] I.M. Hill, S. Hanspal, Z.D. Young, R.J. Davis, DRIFTS of Probe molecules adsorbed on magnetite, zirconia, and hydroxyapatite catalysts, *J. Phys. Chem. C* 119 (2015) 9186–9197, <https://doi.org/10.1021/jp509889j>.
- [49] A. Laachir, V. Perrichon, A. Badri, J. Lamotte, E. Catherine, J.C. Lavalley, J. El Fallah, L. Hilaire, F. Le Normand, E. Quéméré, G.N. Sauvion, O. Touret, Reduction of CeO₂ by hydrogen. Magnetic susceptibility and Fourier-transform infrared, ultraviolet and X-ray photoelectron spectroscopy measurements, *J. Chem. Soc. Faraday Trans. 87* (1991) 1601–1609, <https://doi.org/10.1039/FT9918701601>.
- [50] A. Badri, C. Binet, J. Lavalley, An FTIR study of surface ceria hydroxy groups during a redox process with H₂, *J. Chem. Soc. Faraday Trans.* 92 (1996) 4669, <https://doi.org/10.1039/ft9969204669>.
- [51] D. Fernández-Torre, J. Carrasco, M.V. Ganduglia-Pirovano, R. Pérez, Hydrogen activation, diffusion, and clustering on CeO₂(111): A DFT+U study, *J. Chem. Phys.* 141 (2014), 014703, <https://doi.org/10.1063/1.4885546>.
- [52] E.T. Saw, U. Oemar, M.L. Ang, H. Kus, S. Kawi, High-temperature water gas shift reaction on Ni-Cu/CeO₂ catalysts: effect of ceria nanocrystal size on carboxylate formation, *Catal. Sci. Technol.* 6 (2016) 5336–5349, <https://doi.org/10.1039/C5CY01932J>.
- [53] X. Lu, W. Wang, S. Wei, C. Guo, Y. Shao, M. Zhang, Z. Deng, H. Zhu, W. Guo, Initial reduction of CeO₂ on perfect and O-defective CeO₂(111) surfaces: towards CO or COOH? *RSC Adv.* 5 (2015) 97528–97535, <https://doi.org/10.1039/c5ra17825h>.
- [54] Y. Yang, S. Wang, Y. Jiang, X. Wu, C. Xia, R. Peng, Y. Lu, CO₂ Activation and reduction on Pt-CeO₂-based catalysts, *J. Phys. Chem. C* 123 (2019) 17092–17101, <https://doi.org/10.1021/acs.jpcc.9b02878>.
- [55] O. Pozdnyakova, D. Teschner, A. Wootsch, J. Krohnert, B. Steinhauer, H. Sauer, L. Toth, F. Jentoft, A. Knopgericke, A. Knopgericke, Z. Paal, Preferential CO oxidation in hydrogen (PROX) on ceria-supported catalysts, part I: oxidation state and surface species on Pt/CeO₂ under reaction conditions, *J. Catal.* 237 (2006) 1–16, <https://doi.org/10.1016/j.jcat.2005.10.014>.
- [56] C.M. Damaskinos, J. Zavašnik, P. Djinić, A.M. Efstathiou, Dry reforming of methane over Ni/Ce_{0.8}Ti_{0.2}O_{2-δ}: the effect of Ni particle size on the carbon pathways studied by transient and isotopic techniques, *Appl. Catal. B Environ.* 296 (2021), 120321, <https://doi.org/10.1016/j.apcatb.2021.120321>.

Reduction Behavior of Cubic In_2O_3 Nanoparticles by Combined Multiple *In Situ* Spectroscopy and DFT

Marc Ziemba, Leon Schumacher, and Christian Hess*



Cite This: *J. Phys. Chem. Lett.* 2021, 12, 3749–3754



Read Online

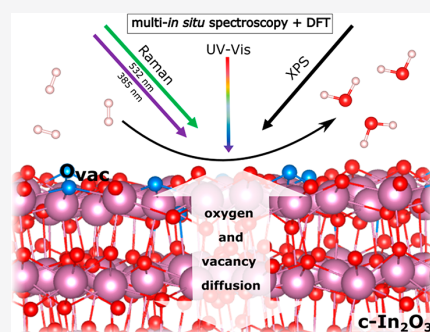
ACCESS |

Metrics & More

Article Recommendations

Supporting Information

ABSTRACT: Indium oxide (In_2O_3) has emerged as a highly active catalyst for methanol synthesis by CO_2 hydrogenation. In this work we elucidate the reduction behavior and oxygen dynamics of cubic In_2O_3 nanoparticles by *in situ* Raman and UV–vis spectra in combination with density functional theory (DFT) calculations. We demonstrate that application of UV and visible Raman spectroscopy enables, first, a complete description of the In_2O_3 vibrational structure fully consistent with theory and, second, the first theoretical identification of the nature of defect-related bands in reduced In_2O_3 . Combining these findings with quasi *in situ* XPS and *in situ* UV–vis measurements allows the temperature-dependent structural dynamics of In_2O_3 to be unraveled. While the surface of a particle is not in equilibrium with its bulk at room temperature, oxygen exchange between the bulk and the surface occurs at elevated temperatures, leading to an oxidation of the surface and an increase in oxygen defects in the bulk. Our results demonstrate the potential of combining different *in situ* spectroscopic methods with DFT to elucidate the complex redox behavior of In_2O_3 nanoparticles.



Cubic indium oxide (In_2O_3 , $Ia\bar{3}$) shows high catalytic activity for a variety of reactions, such as CO_2 hydrogenation to methanol or the reverse water gas shift reaction.^{1–6} To gain insight into the mode of operation of In_2O_3 catalysts, a detailed understanding of their redox behavior, including the associated oxygen dynamics and the In_2O_3 defect structure, will be required. In this context, oxygen vacancies could be identified as active sites during methanol synthesis or the reverse water gas shift reaction, since CO_2 is activated over $\text{In}_2\text{O}_{3-x}$ sites formed by H_2 .^{2,7–9} Furthermore, selective hydrogen combustion by In_2O_3 has recently been shown to be an essential part of tandem catalysts for propane to propylene conversion.¹⁰ Since both processes involve oxygen vacancies, there is a need for a detailed understanding of their formation and dynamics. In this context, previous studies have shown that at elevated temperatures (300 °C) and under reducing conditions metallic indium is formed and defect-related Raman bands occur.^{11,12} However, the nature of these bands and the interplay of surface and subsurface/bulk processes, which is of great importance for catalysis, are still not clarified, despite previous work on the vibrational analysis of In_2O_3 .^{13–19}

In this study, we investigate catalytically interesting In_2O_3 nanoparticles with respect to their structural behavior under oxidative and reductive conditions, both experimentally and theoretically. By use of multiwavelength *in situ* Raman spectroscopy and, in particular, selective resonance enhancement at 385 nm excitation, a profound description of In_2O_3 -related vibrational modes is provided. Furthermore, we explore the oxygen dynamics at the surface and in the bulk, using a

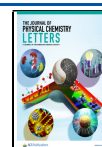
combination of UV–vis and X-ray photoelectron (XP) spectroscopy, as well as X-ray diffraction (XRD).

After synthesis by precipitation of indium(III) nitrate hydrate, the In_2O_3 particles were first characterized by N_2 adsorption at 77 K, XRD, transmission electron microscopy (TEM), and XPS (for details see Supporting Information). By use of N_2 adsorption and the Brunauer–Emmett–Teller (BET) model, the specific surface area was determined as 39 m^2/g (for isotherms see Figure S1). The XRD results show that only cubic ($Ia\bar{3}$) In_2O_3 is present (see Figure S2) and, by means of the Scherrer equation, the size of the particles was calculated to be 19 nm. These results are consistent with the TEM images (see Figure S3), which additionally show that the particles are present as sheets terminating with a $\text{In}_2\text{O}_3(222)$ surface, based on the observed distances between the lattice planes of 0.29 nm.²⁰ XPS analysis reveals an O:In ratio of 1.47 (see Table S1; see Supporting Information for details on the calculation), indicating that oxygen defects are already present in the as-prepared state. However, it should be noted that detailed analysis of the C 1s photoemission reveals a shoulder at higher binding energies (~ 289 eV), indicating the presence of oxygen containing adsorbates, e.g., carbonates (see Figure

Received: March 19, 2021

Accepted: April 5, 2021

Published: April 12, 2021



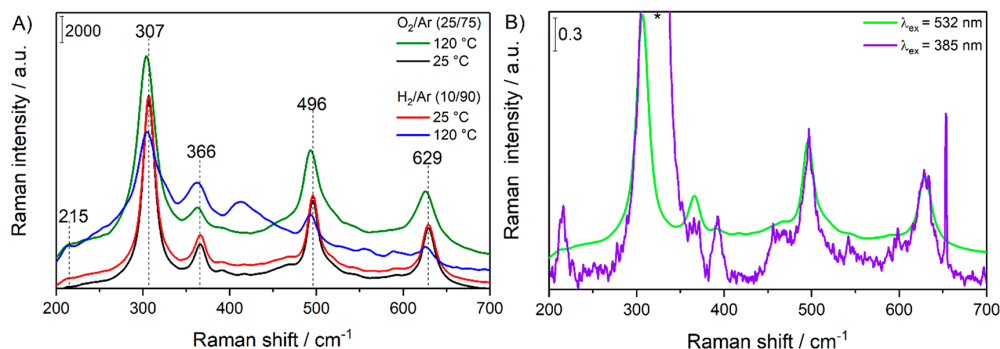


Figure 1. (A) *In situ* Raman spectra ($\lambda_{\text{ex}} = 532$ nm) of In_2O_3 nanoparticles. Spectra were recorded at the indicated temperatures at a total flow rate of 100 mL/min and by applying a feed of 25% O_2/Ar for oxidative and of 10% H_2/Ar for reductive conditions. (B) Comparison of two *in situ* Raman spectra, at 532 nm (green) and 385 nm (violet) excitation. Both spectra were recorded at 25 °C after pretreatment in O_2/Ar at 120 °C for 1 h. For better comparability, both spectra were normalized to the band at 629 cm^{-1} . The asterisk (*) marks a band originating from the CaF_2 window ($\lambda_{\text{ex}} = 385$ nm), while the sharp feature at 650 cm^{-1} results from cosmic rays.

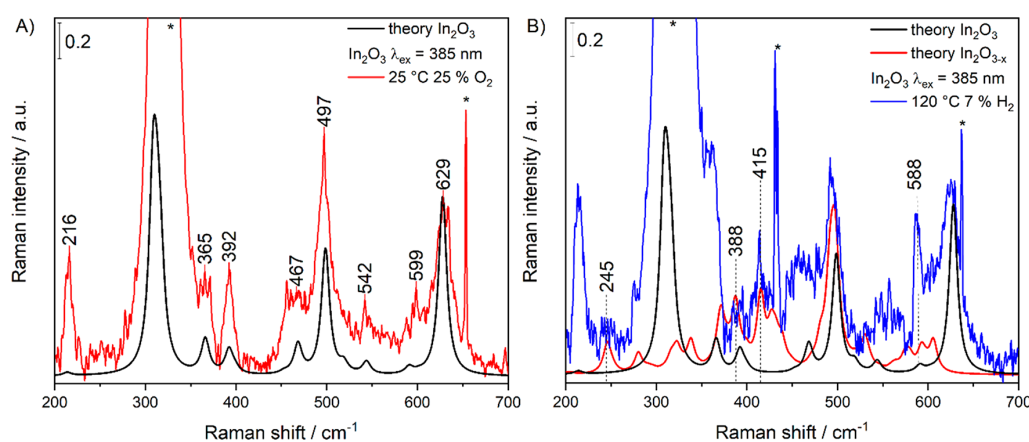


Figure 2. (A) Theoretical (DFT) Raman spectrum of a nondefective primitive In_2O_3 ($Ia\bar{3}$) cell (black) compared to the *in situ* 385 nm Raman spectrum (red) of In_2O_3 recorded at 25 °C in 25% O_2/He (pretreatment: 1 h, 120 °C, 25% O_2/He , 50 mL/min). (B) Theoretical (DFT) Raman spectrum of a defective primitive $\text{In}_2\text{O}_{3-x}$ ($Ia\bar{3}$) cell (red) compared to the *in situ* 385 nm Raman spectrum (blue) of In_2O_3 recorded at 120 °C in 7% H_2/He (for more details see Supporting Information). The total flow rate was always 50 mL/min. The asterisks (*) mark bands originating from the CaF_2 window, while the sharp feature at around 430 and 650 cm^{-1} results from cosmic rays. For better comparability, all spectra except the theoretical $\text{In}_2\text{O}_{3-x}$ spectrum are normalized to the 628 cm^{-1} band. The theoretical $\text{In}_2\text{O}_{3-x}$ spectrum was normalized and scaled (factor: 1.05) to the band at 495 cm^{-1} .

S4),²¹ which increase the O:In ratio. We can therefore conclude that there are significantly more defects present on the surface than *ex situ* XPS reveals.

In the following, we will first discuss the results from multiwavelength Raman spectroscopy. Figure 1A shows *in situ* Raman spectra of In_2O_3 at 532 nm laser excitation. Under O_2/Ar flow the Raman spectra are characterized by four strong bands at 307, 366, 496, and 629 cm^{-1} , which can readily be assigned to $\delta(\text{InO}_6)$, $\nu(\text{InO}_6)$, In–O–In, and $\nu(\text{InO}_6)$ vibrations of cubic In_2O_3 , in accordance with the literature.^{16,22} Comparison of the temperature-dependent O_2/Ar spectra (black and green) reveals a red shift and a change in full width at half-maximum (fwhm) at 120 °C, which originate from a temperature effect, as the spectra of reduced In_2O_3 (blue) show the same positions. In summary, it can be said that a low degree of reduction has no influence on the Raman positions, just the temperature does, since at 120 °C the spectra in O_2/Ar and H_2/Ar show the same positions. After oxygen treatment at 25 °C, hydrogen was passed over the sample at 25 °C but did

not lead to detectable changes in the Raman spectrum. In contrast, at 120 °C in H_2/Ar flow, the overall intensity decreased and the phonon ratios changed significantly. Furthermore, new Raman features appeared at 254, 413, 555, and 589 cm^{-1} ; the broad band at 413 cm^{-1} had already been observed in earlier studies, but its exact nature has not been clarified yet.¹¹ As part of this study, measurements were also performed at 250 °C, but under these conditions Raman spectra are hampered by increased absorption (see Figure 3) and fluorescence and are therefore not shown. For this reason, the sample was subsequently cooled to 25 °C under argon and another spectrum was recorded (see Figure S6). Again, the spectrum is dominated by the increased absorption (see yellow spectrum in Figure 3A), but the In_2O_3 phonons are visible; however defect-related features remain hidden by the higher background. A significant feature of the band positions is that they exhibit a red shift in contrast to the spectra at 120 °C under H_2 . This highlights the fact that the bands shift red at higher defect concentrations. In addition, we see bands at 1499

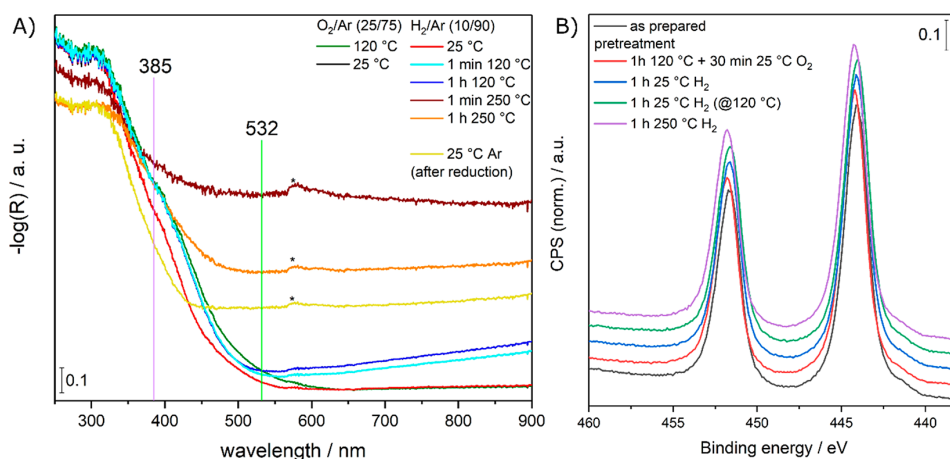


Figure 3. (A) *In situ* UV/vis spectra of In_2O_3 nanoparticles. Spectra were recorded at the indicated temperatures at a total flow rate of 100 mL/min and by applying a feed of 25% O_2/Ar for oxidative and 10% H_2/Ar for reductive conditions. After reduction at 250 °C, the sample was cooled down to 25 °C in Ar (yellow). Spectra were recorded after about 1 h of equilibration. In addition, for H_2/Ar flow at higher temperatures (>25 °C), spectra are shown after 1 min of equilibration. The asterisks (*) mark a measurement artifact of the spectrometer. Note that the spectra under O_2 and H_2 at 25 °C overlap. Note that no changes between the spectra at 25 °C in O_2 (black) and H_2 (red) occur. (B) In 3d photoemission of In_2O_3 nanoparticles. Spectra were normalized to the In $3d_{5/2}$ signal. Spectra were recorded directly after synthesis (black), after O_2 (25%) pretreatment (red), after H_2 (10%) pretreatment at 25 °C (blue, green), and after H_2 pretreatment at 250 °C (violet). All spectra were recorded at 25 °C except the green one, which was recorded at 120 °C. Spectra in (B) are offset for clarity.

and 1554 cm^{-1} (see Figure S7), which may be attributed to In–H vibrations.^{23–26} The intensity ratio of these bands changes with the gas-phase composition; i.e., the band at 1499 cm^{-1} increases upon exposure to hydrogen, indicating the activation of H_2 . The chemical environment appears to have a strong influence on the band position, as for example In–H species on CHA zeolites have been shown to exhibit bands within $1700\text{--}1800\text{ cm}^{-1}$.²⁷ In contrast, OH-related Raman bands show only temperature-related changes and completely disappear upon treatment at 250 °C in H_2 flow (see Figure S8).

As an additional laser wavelength for Raman spectroscopy, we used 385 nm excitation, which minimizes fluorescence and, due to an electronic resonance with In_2O_3 , enables selective resonance enhancement of In_2O_3 -related modes. A comparison of the two excitation wavelengths shows (see Figure 1B) that the 385 nm Raman spectrum reveals additional phonons, which were not detectable or only very difficult to detect with 532 nm excitation.

In order to understand the nature of these bands, we employed DFT to calculate Raman spectra (for details see Supporting Information). Figure 2A shows a comparison of a calculated Raman spectrum of a primitive In_2O_3 cell with an experimental spectrum (385 nm) recorded in O_2/Ar at 25 °C. The theoretical spectrum was scaled to the band at 629 cm^{-1} (factor 1.09). It is noticeable that the theoretical band positions are in excellent agreement with experiment. Furthermore, the Raman spectrum of the unit cell shows the same positions as that of the primitive cell for symmetry reasons (see Figure S11). In addition to the bands detected at 532 nm excitation, new features appear at 392, 467, 542, and 599 cm^{-1} , which can be assigned to vibrations with F_{2g}/E_g (392 cm^{-1}), F_{2g} (467 cm^{-1}), F_{2g} (542 cm^{-1}), and E_g (599 cm^{-1}) symmetry, based on our DFT results and in accordance with the literature.¹⁴

In summary, the above results show that Raman spectra of In_2O_3 can be fully described by DFT. Since a combined

experimental and theoretical approach may thus be expected to facilitate the understanding of more complex systems, it was applied to bulk oxygen vacancies in defective In_2O_3 . The defect formation in bulk In_2O_3 corresponds to 3.58 eV in the primitive cell and 3.40 eV in the unit cell, which can be attributed to a 50% lower defect concentration in the unit cell, in agreement with the literature.^{28–30} In the following, only the primitive cell will be discussed. In this case, our DFT calculations show that the oxygen defect formation energy and the Raman active modes do not differ between the removed oxygen atoms, since all oxygen atoms are equal and possess C_1 symmetry. Thus, no particular oxygen defect is preferred in bulk In_2O_3 .

Figure 2B shows a theoretically calculated Raman spectrum of a defective primitive cell ($\text{In}_2\text{O}_{3-x}$; red), which is compared with a nondefective cell (black), and an experimental Raman spectrum ($\lambda_{\text{ex}} = 385\text{ nm}$; blue), which was recorded in hydrogen at 120 °C. Again, the theoretical spectrum is in good agreement with the experimental results. In fact, it can be clearly seen by comparison of the two theoretical spectra that the Raman features at 245 cm^{-1} , at around 400 cm^{-1} , and at 588 cm^{-1} are defect-related. To this end, a direct comparison of the experimental spectra of In_2O_3 and reduced In_2O_3 is shown in Figure S9 for clarity. In addition, theory also shows that the spectrum of $\text{In}_2\text{O}_{3-x}$ is dominated by accumulations of closely spaced bands. As a consequence, an exact assignment of the symmetry of the individual bands is difficult and of no use experimentally, since the symmetry is lost due to the presence of the defect in the crystal lattice. Hence the detected bands are composed of several nondegenerate vibrations with similar energy, which explains their width, as illustrated for the broad band at around 413 cm^{-1} (see Figure 1A). This feature can be better resolved at 385 nm excitation due to resonance effects, as shown in Figure 2B. The experimental band shape agrees well with that obtained by DFT calculations. According to theory, its width originates from more than 10 nondegenerate vibrations with similar symmetry (mostly $\delta(\text{InO}_3)$ character).

In summary, unlike defect-free In_2O_3 , no degeneracy occurs in defect-rich In_2O_3 .

A comparison of the two experimental Raman spectra in Figure 2 reveals that in reduced indium oxide the band at 392 cm^{-1} loses its intensity, new bands appear in the region around 400 cm^{-1} , the band at around 550 cm^{-1} loses its asymmetry and becomes wider, and the band at 587 cm^{-1} is more intense. The observed vibrational signature of reduced indium oxide is fully consistent with the simultaneous presence of In_2O_3 and $\text{In}_2\text{O}_{3-x}$, based on the combination of the corresponding theoretical spectra (see black and red spectra in Figure 2B). Therefore, hydrogen treatment at $120\text{ }^\circ\text{C}$ does not lead to complete reduction. Similar to reduced In_2O_3 , the oxygen-treated In_2O_3 shows a feature at 245 cm^{-1} (see Figure 2A,B), which originates from a $\delta(\text{InO}_5)$ vibration of $\text{In}_2\text{O}_{3-x}$ (see Figure 2B), revealing that the oxygen-pretreated In_2O_3 contains oxygen defects.

At $250\text{ }^\circ\text{C}$ in H_2/Ar flow, acceptable Raman spectra were not accessible at either excitation wavelength. Therefore, we recorded a spectrum at $25\text{ }^\circ\text{C}$ in helium after treatment at $250\text{ }^\circ\text{C}$ in H_2 flow (see Figure S9), which shows that the defect-related bands become more intense. The aspects that are responsible for the difficult accessibility of the spectra at $250\text{ }^\circ\text{C}$ and H_2 will now be considered in more detail, since in contrast to 532 nm , at 385 nm only small changes in the absorption and hence the electronic structure of the particles were detected (see Figure 3A). The observed Raman behavior must therefore be related to other effects. In this context, XRD measurements (see Figure S2) show that during reduction with hydrogen at $250\text{ }^\circ\text{C}$ metallic indium (particle size: 67 nm) is formed and that the particle size of the In_2O_3 particles increases from 19 to 29 nm . To understand this behavior in more detail, we explored the changes in the electronic structure and the properties of the surface and bulk by using XP and UV–vis spectroscopy. Note that by means of XPS, only surface properties are detected. In contrast, all other methods used in this study probe properties of the whole particle, based on the penetration depth and the size of the particles, which will be referred to as bulk in the following.

Figure 3A depicts *in situ* UV–vis spectra of indium oxide, which were recorded analogously to the Raman spectra in Figure 1. These spectra clearly show that the sample undergoes significant changes during reduction and oxidation. First, it is noticeable that all spectra are characterized by strong absorption in the UV range, originating from directly allowed transitions into O $2p$ valence bands.^{31,32} In O_2 atmosphere, the absorption between 250 and 450 nm is observed to increase and broaden at $120\text{ }^\circ\text{C}$ compared to $25\text{ }^\circ\text{C}$. This behavior is related to an increase of the band gap with rising temperature, as a result of the increased carrier density caused by the Burstein–Moss effect.^{33,34} Upon exposure to hydrogen at $25\text{ }^\circ\text{C}$, no changes are detected, consistent with the 532 nm Raman spectra (see Figure 1A). Subsequent heating to $120\text{ }^\circ\text{C}$ leads again to a broadening of the absorption within 250 – 450 nm , indicative of a band-gap increase. In contrast to the spectrum recorded in oxygen ($120\text{ }^\circ\text{C}$), the absorption is somewhat lower, suggesting a slightly lower band gap. This behavior can be explained by the formation of defects, which can act as donors, thus creating new energy levels in the near-band-gap region.³⁵ Furthermore, Figure 3A shows an increase in absorption in the visible range ($>500\text{ nm}$). In contrast to lower temperatures ($<120\text{ }^\circ\text{C}$), the absorption continues to grow after 1 h of treatment. Upon switching to $250\text{ }^\circ\text{C}$, it

reaches a maximum after 1 min and decreases during the following 59 min . The origin of these changes in vis absorption can be explained by the presence of defects located at or near the surface.³⁵ Besides, at $250\text{ }^\circ\text{C}$ in hydrogen, the formation of metallic indium is conceivable, as evidenced by XRD measurements after treatment (see Figure S2). However, the absorption of indium surface plasmons is not as broad as the defect-induced absorption.^{36,37} We therefore attribute the observed changes in absorption to a combination of the two effects.

The time-dependent dynamics can be explained by a balance between bulk oxygen and surface vacancies. As a consequence, at a high concentration of surface defects a transfer of oxygen from the bulk to the surface takes place until an equilibrium state is reached. Such a scenario is supported by quasi *in situ* XPS measurements (for details see Supporting Information), which show that, despite indium oxide reduction, the oxygen concentration on the surface slightly increases (see O:In ratios in Table S1). Thus, starting at $120\text{ }^\circ\text{C}$, there is an exchange of oxygen between the bulk and defects at the surface. This can also be demonstrated by heating the sample to $120\text{ }^\circ\text{C}$ in the XPS analysis chamber after the same H_2 pretreatment at $25\text{ }^\circ\text{C}$ as mentioned before (see Figure 1A) while simultaneously recording mass spectra showing the release of CO_2 and H_2O . The XP spectrum recorded at $120\text{ }^\circ\text{C}$ reveals an increase in the surface O:In ratio compared to $25\text{ }^\circ\text{C}$, despite desorption of CO_2 and H_2O (see Table S1).

Returning to the XRD results, which showed formation of metallic indium, we performed XPS measurements of the sample after the same pretreatment ($250\text{ }^\circ\text{C}$, $10\%\text{ H}_2$). These spectra show a higher amount of oxygen than during reduction at lower temperatures. On the other hand, there is no evidence of metallic indium or indium in oxidation states other than In^{3+} (see Figure 3B). This clearly demonstrates that at higher temperatures ($>120\text{ }^\circ\text{C}$) oxygen is transported from the bulk to the surface. Thus, despite the lower defect energy on the surface,³⁸ defects in the bulk seem to be preferred. In this context, it has previously been shown that oxygen vacancies are the predominant donor in In_2O_3 and are responsible for the oxygen self-diffusion process.³⁹ These results are also underlined by theoretical studies that propose that oxygen vacancies are already mobile at temperatures of about 400 K .⁴⁰

Summarizing, in this study we elucidated the oxygen dynamics of oxidized and reduced cubic In_2O_3 nanoparticles by a combination of spectroscopic techniques supported by theoretical calculations. We have shown that surface oxygen defects are in equilibrium with the bulk at temperatures above $120\text{ }^\circ\text{C}$ and that in the equilibrium state bulk defects are preferred over surface defects, resulting in a lower defect formation on the surface. We furthermore demonstrated that experimental vibrational Raman spectra of In_2O_3 and $\text{In}_2\text{O}_{3-x}$ are in excellent agreement with those calculated by DFT. By exploitation of resonance effects, for example, at 385 nm excitation, and facilitation by theoretical calculations, new insight into the nature of vibrational bands was provided, such as the band at 245 cm^{-1} , which was assigned to a $\delta(\text{InO}_5)$ vibration in defective In_2O_3 . Finally, while our findings highlight the potential of combining multiple *in situ* spectroscopic and theoretical analyses to unravel the redox dynamics of cubic In_2O_3 , such an approach may be of great interest for other reducible oxide materials as well for their structural characterization under catalytic conditions.

■ ASSOCIATED CONTENT

SI Supporting Information

The Supporting Information is available free of charge at <https://pubs.acs.org/doi/10.1021/acs.jpcllett.1c00892>.

Detailed information on experimental and theoretical methods as well as additional experimental data (PDF)

■ AUTHOR INFORMATION

Corresponding Author

Christian Hess – *Eduard Zintl Institute of Inorganic and Physical Chemistry, Technical University of Darmstadt, 64287 Darmstadt, Germany*; orcid.org/0000-0002-4738-7674; Email: christian.hess@tu-darmstadt.de

Authors

Marc Ziemba – *Eduard Zintl Institute of Inorganic and Physical Chemistry, Technical University of Darmstadt, 64287 Darmstadt, Germany*

Leon Schumacher – *Eduard Zintl Institute of Inorganic and Physical Chemistry, Technical University of Darmstadt, 64287 Darmstadt, Germany*

Complete contact information is available at: <https://pubs.acs.org/doi/10.1021/acs.jpcllett.1c00892>

Notes

The authors declare no competing financial interest.

■ ACKNOWLEDGMENTS

The DFT calculations were conducted using the Lichtenberg high performance computer of the TU Darmstadt. We thank Stefan Lauterbach and Hans-Joachim Kleebe for TEM measurements, Martin Brodrecht for nitrogen adsorption/desorption experiments, Kathrin Hofmann for XRD analysis, M. Verónica Ganduglia-Pirovano for helpful discussions, and Karl Kopp for technical support.

■ REFERENCES

- (1) Sun, Q.; Ye, J.; Liu, C.; Ge, Q. In₂O₃ as a Promising Catalyst for CO₂ Utilization: A Case Study with Reverse Water Gas Shift over In₂O₃. *Greenhouse Gases: Sci. Technol.* **2014**, *4* (1), 140–144.
- (2) Wang, J.; Liu, C.-Y.; Senfle, T. P.; Zhu, J.; Zhang, G.; Guo, X.; Song, C. Variation in the In₂O₃ Crystal Phase Alters Catalytic Performance toward the Reverse Water Gas Shift Reaction. *ACS Catal.* **2020**, *10* (5), 3264–3273.
- (3) Wang, W.; Zhang, Y.; Wang, Z.; Yan, J.; Ge, Q.; Liu, C. Reverse Water Gas Shift over In₂O₃ – CeO₂ Catalysts. *Catal. Today* **2016**, *259* (Part 2), 402–408.
- (4) Tsoukalou, A.; Abdala, P. M.; Stoian, D.; Huang, X.; Willinger, M. G.; Fedorov, A.; Müller, C. R. Structural Evolution and Dynamics of an In₂O₃ Catalyst for CO₂ Hydrogenation to Methanol: An Operando XAS-XRD and in Situ TEM Study. *J. Am. Chem. Soc.* **2019**, *141* (34), 13497–13505.
- (5) Frei, M. S.; Capdevila-Cortada, M.; García-Muelas, R.; Mondelli, C.; López, N.; Stewart, J. A.; Curulla Ferré, D.; Pérez-Ramírez, J. Mechanism and Microkinetics of Methanol Synthesis via CO₂ Hydrogenation on Indium Oxide. *J. Catal.* **2018**, *361* (1), 313–321.
- (6) Ye, J.; Liu, C.; Mei, D.; Ge, Q. Active Oxygen Vacancy Site for Methanol Synthesis from CO₂ Hydrogenation on In₂O₃(110): A DFT Study. *ACS Catal.* **2013**, *3* (6), 1296–1306.
- (7) Wang, J.; Zhang, G.; Zhu, J.; Zhang, X.; Ding, F.; Zhang, A.; Guo, X.; Song, C. CO₂ Hydrogenation to Methanol over In₂O₃-Based Catalysts: From Mechanism to Catalyst Development. *ACS Catal.* **2021**, *11* (3), 1406–1423.

- (8) Qin, B.; Li, S. First Principles Investigation of Dissociative Adsorption of H₂ during CO₂ Hydrogenation over Cubic and Hexagonal In₂O₃ Catalysts. *Phys. Chem. Chem. Phys.* **2020**, *22*, 3390–3399.

- (9) Rui, N.; Zhang, F.; Sun, K.; Liu, Z.; Xu, W.; Stavitski, E.; Senanayake, S. D.; Rodriguez, J. A.; Liu, C.-J. Hydrogenation of CO₂ to Methanol on a Au^{δ+}-In₂O_{3-x} Catalyst. *ACS Catal.* **2020**, *10* (19), 11307–11317.

- (10) Yan, H.; He, K.; Samek, I. A.; Jing, D.; Nanda, M. G.; Stair, P. C.; Notestein, J. M. Tandem In₂O₃-Pt/Al₂O₃ Catalyst for Coupling of Propane Dehydrogenation to Selective H₂ Combustion. *Science* **2021**, *371* (6535), 1257–1260.

- (11) Bielz, T.; Lorenz, H.; Jochum, W.; Kaindl, R.; Klausner, F.; Klötzer, B.; Penner, S. Hydrogen on In₂O₃: Reducibility, Bonding, Defect Formation, and Reactivity. *J. Phys. Chem. C* **2010**, *114* (19), 9022–9029.

- (12) Gervasini, A.; Perdigon-Melon, J. A.; Guimon, C.; Auroux, A. An In-Depth Study of Supported In₂O₃ Catalysts for the Selective Catalytic Reduction of NO_x: The Influence of the Oxide Support. *J. Phys. Chem. B* **2006**, *110* (1), 240–249.

- (13) García-Domene, B.; Ortiz, H. M.; Gomis, O.; Sans, J. A.; Manjón, F. J.; Muñoz, A.; Rodríguez-Hernández, P.; Achary, S. N.; Errandonea, D.; Martínez-García, D.; Romero, A. H.; Singhal, A.; Tyagi, A. K. High-Pressure Lattice Dynamical Study of Bulk and Nanocrystalline In₂O₃. *J. Appl. Phys.* **2012**, *112* (12), 123511.

- (14) Kranert, C.; Schmidt-Grund, R.; Grundmann, M. Raman Active Phonon Modes of Cubic In₂O₃. *Phys. Status Solidi RRL* **2014**, *8* (6), 554–559.

- (15) Berengue, O. M.; Rodrigues, A. D.; Dalmaschio, C. J.; Lanfredi, A. J. C.; Leite, E. R.; Chiquito, A. J. Structural Characterization of Indium Oxide Nanostructures: A Raman Analysis. *J. Phys. D: Appl. Phys.* **2010**, *43* (4), No. 045401.

- (16) Wang, C. Y.; Dai, Y.; Pezoldt, J.; Lu, B.; Kups, T.; Cimalla, V.; Ambacher, O. Phase Stabilization and Phonon Properties of Single Crystalline Rhombohedral Indium Oxide. *Cryst. Growth Des.* **2008**, *8* (4), 1257–1260.

- (17) Panneerdoss, I. J.; Jeyakumar, S. J.; Ramalingam, S.; Jothibas, M. Characterization of Prepared In₂O₃ Thin Films: The FT-IR, FT-Raman, UV-Visible Investigation and Optical Analysis. *Spectrochim. Acta, Part A* **2015**, *147*, 1–13.

- (18) Ramsteiner, M.; Feldl, J.; Galazka, Z. Signatures of Free Carriers in Raman Spectra of Cubic In₂O₃. *Semicond. Sci. Technol.* **2020**, *35* (1), No. 015017.

- (19) Gan, J.; Lu, X.; Wu, J.; Xie, S.; Zhai, T.; Yu, M.; Zhang, Z.; Mao, Y.; Wang, S. C. I.; Shen, Y.; Tong, Y. Oxygen Vacancies Promoting Photoelectrochemical Performance of In₂O₃ Nanocubes. *Sci. Rep.* **2013**, *3* (1), 1021.

- (20) Wang, X.; Zhang, M.; Liu, J.; Luo, T.; Qian, Y. Shape- and Phase-Controlled Synthesis of In₂O₃ with Various Morphologies and Their Gas-Sensing Properties. *Sens. Actuators, B* **2009**, *137* (1), 103–110.

- (21) Sun, Y.; Murphy, C. J.; Reyes-Gil, K. R.; Reyes-García, E. A.; Lilly, J. P.; Raftery, D. Carbon-Doped In₂O₃ Films for Photoelectrochemical Hydrogen Production. *Int. J. Hydrogen Energy* **2008**, *33* (21), 5967–5974.

- (22) Elouali, S.; Bloor, L. G.; Binions, R.; Parkin, I. P.; Carmalt, C. J.; Darr, J. A. Gas Sensing with Nano-Indium Oxides (In₂O₃) Prepared via Continuous Hydrothermal Flow Synthesis. *Langmuir* **2012**, *28* (3), 1879–1885.

- (23) Andrews, L.; Wang, X. Infrared Spectra of Indium Hydrides in Solid Hydrogen and of Solid Indane. *Angew. Chem.* **2004**, *116* (13), 1738–1741.

- (24) Wang, X.; Andrews, L. Infrared Spectra of Indium Hydrides in Solid Hydrogen and Neon. *J. Phys. Chem. A* **2004**, *108* (20), 4440–4448.

- (25) Fontcuberta i Morral, A.; Zahler, J. M.; Griggs, M. J.; Atwater, H. A.; Chabal, Y. J. Spectroscopic Studies of the Mechanism for Hydrogen-Induced Exfoliation of InP. *Phys. Rev. B: Condens. Matter Mater. Phys.* **2005**, *72* (8), No. 085219.

- (26) Liu, N.; Kuech, T. F. Interfacial Chemistry of InP/GaAs Bonded Pairs. *J. Electron. Mater.* **2007**, *36* (3), 179–190.
- (27) Maeno, Z.; Yasumura, S.; Wu, X.; Huang, M.; Liu, C.; Toyao, T.; Shimizu, K. Isolated Indium Hydrides in CHA Zeolites: Speciation and Catalysis for Nonoxidative Dehydrogenation of Ethane. *J. Am. Chem. Soc.* **2020**, *142* (10), 4820–4832.
- (28) Walsh, A.; Catlow, C. R. A.; Sokol, A. A.; Woodley, S. M. Physical Properties, Intrinsic Defects, and Phase Stability of Indium Sesquioxide. *Chem. Mater.* **2009**, *21* (20), 4962–4969.
- (29) Walsh, A.; Sokol, A. A.; Catlow, C. R. A. Free Energy of Defect Formation: Thermodynamics of Anion Frenkel Pairs in Indium Oxide. *Phys. Rev. B: Condens. Matter Mater. Phys.* **2011**, *83* (22), 224105.
- (30) Agoston, P.; Erhart, P.; Klein, A.; Albe, K. Geometry, Electronic Structure and Thermodynamic Stability of Intrinsic Point Defects in Indium Oxide. *J. Phys.: Condens. Matter* **2009**, *21* (45), 455801.
- (31) Novkovski, N.; Tanusevski, A. Origin of the Optical Absorption of In₂O₃ Thin Films in the Visible Range. *Semicond. Sci. Technol.* **2008**, *23* (9), No. 095012.
- (32) Schleife, A.; Neumann, M. D.; Esser, N.; Galazka, Z.; Gottwald, A.; Nixdorf, J.; Goldhahn, R.; Feneberg, M. Optical Properties of In₂O₃ from Experiment and First-Principles Theory: Influence of Lattice Screening. *New J. Phys.* **2018**, *20* (5), No. 053016.
- (33) Burstein, E. Anomalous Optical Absorption Limit in InSb. *Phys. Rev.* **1954**, *93* (3), 632–633.
- (34) Moss, T. S. The Interpretation of the Properties of Indium Antimonide. *Proc. Phys. Soc., London, Sect. B* **1954**, *67* (10), 775–782.
- (35) Gu, F.; Li, C.; Han, D.; Wang, Z. Manipulating the Defect Structure (V_O) of In₂O₃ Nanoparticles for Enhancement of Formaldehyde Detection. *ACS Appl. Mater. Interfaces* **2018**, *10* (1), 933–942.
- (36) Cingarapu, S.; Yang, Z.; Sorensen, C. M.; Klabunde, K. J. Synthesis of Indium Nanoparticles: Digestive Ripening under Mild Conditions. *Inorg. Chem.* **2011**, *50* (11), 5000–5005.
- (37) Khanna, P. K.; Jun, K.-W.; Hong, K. B.; Baeg, J.-O.; Chikate, R. C.; Das, B. K. Colloidal Synthesis of Indium Nanoparticles by Sodium Reduction Method. *Mater. Lett.* **2005**, *59* (8–9), 1032–1036.
- (38) Walsh, A. Surface Oxygen Vacancy Origin of Electron Accumulation in Indium Oxide. *Appl. Phys. Lett.* **2011**, *98* (26), 261910.
- (39) Tang, A.; Mei, Z.; Huo, W.; Du, X. Self-Diffusion Measurements in In₂O₃ Isotopic Heterostructures: Oxygen Vacancy Energetics. *Sci. China: Phys., Mech. Astron.* **2018**, *61* (11), 117321.
- (40) Agoston, P.; Albe, K. Ab Initio Modeling of Diffusion in Indium Oxide. *Phys. Rev. B: Condens. Matter Mater. Phys.* **2010**, *81* (19), 195205.

CO₂ HydrogenationHow to cite: *Angew. Chem. Int. Ed.* **2022**, *61*, e202209388

International Edition: doi.org/10.1002/anie.202209388

German Edition: doi.org/10.1002/ange.202209388

Elucidating CO₂ Hydrogenation over In₂O₃ Nanoparticles using Operando UV/Vis and Impedance Spectroscopies

Marc Ziemba, Mariusz Radtke, Leon Schumacher, and Christian Hess*

Abstract: In₂O₃ has emerged as a promising catalyst for CO₂ activation, but a fundamental understanding of its mode of operation in CO₂ hydrogenation is still missing, as the application of operando vibrational spectroscopy is challenging due to absorption effects. In this mechanistic study, we systematically address the redox processes related to the reverse water-gas shift reaction (rWGS) over In₂O₃ nanoparticles, both at the surface and in the bulk. Based on temperature-dependent operando UV/Vis spectra and a novel operando impedance approach for thermal powder catalysts, we propose oxidation by CO₂ as the rate-determining step for the rWGS. The results are consistent with redox processes, whereby hydrogen-containing surface species are shown to exhibit a promoting effect. Our findings demonstrate that oxygen/hydrogen dynamics, in addition to surface processes, are important for the activity, which is expected to be of relevance not only for In₂O₃ but also for other reducible oxide catalysts.

Introduction

Catalysts based on cubic In₂O₃ (c-In₂O₃, Ia $\bar{3}$) are known for their excellent properties in the context of CO₂ activation, such as for methanol synthesis,^[1–6] direct liquid fuel production using bifunctional catalysts,^[7] or the reverse water-gas shift reaction (rWGS).^[8–12] The latter reaction is of great relevance for the energy sector and the chemical industry, since CO₂ can be converted to CO, which can then be hydrogenated to liquid fuels (via the Fischer–Tropsch process) or used as feedstock for chemical processes. Such an approach would allow the increasing energy demand to be met while reducing the large amounts of CO₂ emitted by burning fossil fuels.

Theoretical studies have addressed CO₂ hydrogenation over In₂O₃, highlighting the importance of oxygen

vacancies,^[8] where H₂ dissociation is thermodynamically and kinetically favored.^[13] More specifically, a frustrated Lewis pair (FLP) on the In₂O_{3–x}(OH)_y(111) surface has been proposed to be responsible for H₂ dissociation as well as for CO₂ reduction, with the latter being the rate-limiting step.^[14,15] Another theoretical (density functional theory, DFT) study^[6] on possible reaction pathways reports that the protonation of a bent CO₂ adsorbate (bt-CO₂^{*}) to a carboxylate intermediate (COOH^{*}) is the rate-limiting step for CO formation, which is followed by COOH^{*} decomposition into CO and hydroxide on the surface.^[6] In a combined in situ spectroscopic and DFT study, the temperature-dependent reduction behavior of c-In₂O₃ was investigated.^[16]

On the experimental side, surface indium oxo species have been proposed to be responsible for the heterolytic dissociation of hydrogen on alumina-supported c-In₂O₃, which is associated with the formation of surface indium hydrides and hydroxyl groups.^[17] Other studies on In₂O₃-CeO₂ catalysts highlight the importance of oxygen vacancies in In₂O₃ for CO₂ conversion.^[9] Cubic In₂O₃ has been shown to be more suitable for rWGS than hexagonal In₂O₃, by enhancing the dissociative adsorption of H₂, facilitating the formation of oxygen vacancies and increasing the ability to adsorb and activate CO₂.^[8] Defect-rich In₂O₃ has been employed as a photocatalyst for rWGS,^[18–20] exhibiting high activities at ≤200 °C, whereas at higher temperatures the difference between photochemical and thermal activities became smaller.^[18]

Mechanistic data on In₂O₃ during the thermal rWGS (≥200 °C) is still very limited, in particular on the surface chemistry and subsurface/bulk dynamics, which may be related to experimental challenges for IR and Raman spectroscopy resulting from the In₂O₃ absorption properties.^[16,21,22] In fact, to the best of our knowledge, so far no operando studies on the rWGS over In₂O₃ catalysts have been reported. Nevertheless, (sub)surface/bulk processes seem to play an important role in c-In₂O₃ catalysts, as our previous study^[16] has shown an exchange of oxygen vacancies between bulk and (sub)surface at elevated temperatures. Besides, diffusion of hydrogen may be of relevance by affecting the electronic structure^[23–25] or the formation of hydrogenated intermediates (e.g. COOH^{*}),^[6,26] thereby influencing the catalytic activity. Impedance measurements were employed to gain mechanistic insight in the context of methanol steam reforming and (r)WGS,^[12] but further analysis using equivalent-circuit fitting or operando monitoring was not performed. In summary, it appears that in the literature both a regenerative redox mechanism

[*] M. Ziemba, M. Radtke, L. Schumacher, C. Hess
 Eduard Zintl Institute of Inorganic and Physical Chemistry,
 Technical University of Darmstadt
 Alarich-Weiss-Str. 8, 64287 Darmstadt (Germany)
 E-mail: christian.hess@tu-darmstadt.de

© 2022 The Authors. Angewandte Chemie International Edition published by Wiley-VCH GmbH. This is an open access article under the terms of the Creative Commons Attribution License, which permits use, distribution and reproduction in any medium, provided the original work is properly cited.

(without the occurrence of reaction intermediates like e.g., carbonates, COOH*) and the reaction via intermediates are postulated, whereby the simultaneous occurrence is also conceivable.^[3,6,8,21,26]

In this mechanistic study, we employ (quasi) in situ and operando spectroscopies (Raman, UV/Vis, X-ray photoelectron spectroscopy (XPS)) to explore the surface and subsurface dynamics of In₂O₃ during rWGSR. Bulk properties are directly probed by operando impedance spectroscopy supported by ex situ X-ray diffraction (XRD) analysis. We demonstrate, on one hand, the readiness of the In₂O₃ surface for reduction by H₂ and oxidation by CO₂, and, on the other, the participation of the subsurface/bulk in the reaction, thus enhancing the understanding of the mechanism, in particular, the CO₂ activation process, the role of oxygen vacancies, and the participation of hydrogen-related adsorbates.

Results and Discussion

Details of the characterization of the In₂O₃ sample used in this study have already been published.^[16] Briefly, the particles have a specific surface area of 39 m² g⁻¹ and our ex situ XRD results show that only cubic (*Ia* $\bar{3}$) In₂O₃ is present. In addition, transmission electron microscopy (TEM) measurements show that the particles are present as sheets terminating with an In₂O₃(222) surface. Contaminations caused by the synthesis, e.g. nitrogen, can be excluded within the sensitivity of our XPS measurements.

First, the In₂O₃ was analyzed for its activity as a function of temperature, while we simultaneously monitored the electronic structure using operando UV/Vis spectroscopy. Our previous UV/Vis studies on In₂O₃ during 10 vol % H₂ exposure have revealed a strong dependence of the absorption in the visible range on the oxygen defect density.^[16] The bottom panel of Figure 1 depicts the temporal evolution of the absorbance at 700 nm as an indicator for oxygen defects upon exposure to different gas phases or temperatures. Starting at 130 °C, switching from O₂ to H₂ leads to an increase in absorbance in the visible range and H₂O formation in the gas phase, which illustrates that In₂O₃ undergoes reduction even at just 130 °C. Exposure to reaction conditions shows a further increase in absorbance, resulting from the longer residence time under H₂ flow, since CO₂ is not yet activated at this temperature, as evidenced by the absence of CO in the gas phase (not shown).

Increasing the temperature to 160 °C leads to a strong increase in absorbance, which continues even after 160 °C is reached. This behavior can be explained by a strong reduction of the catalyst, as supported by the absence of CO but increasing concentration of H₂O in the gas phase. In this context, H₂-temperature programmed desorption (TPD) experiments from previous studies^[21] have shown that a large fraction of adsorbed hydrogen is already desorbed at these temperatures thus does not remain on the surface.

Starting at a temperature of 190 °C, the catalyst becomes active towards CO₂ conversion and shows only a weak

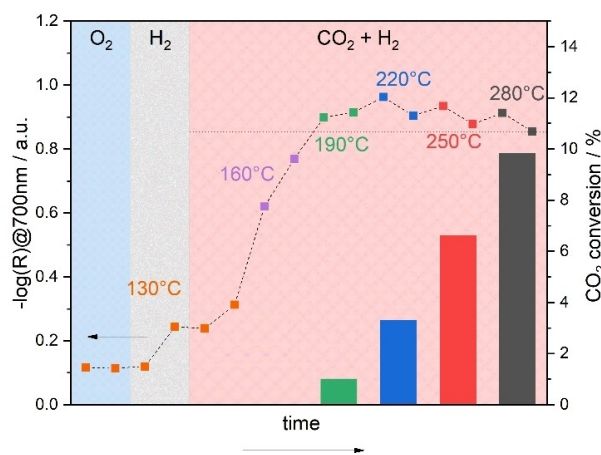


Figure 1. In situ/operando UV/Vis results for In₂O₃ sheets recorded during O₂ and H₂ exposures at 130 °C and reaction conditions (CO₂:H₂, 2:4) ranging from 130 to 280 °C in 30 °C steps. From 190 °C on, the sample becomes active in terms of conversion of CO₂, which is shown by bars (right axis). At lower temperatures, the conversion is within the experimental uncertainty. The exposure time before the conditions were changed was \approx 30 min. The horizontal dotted line helps to illustrate the change in absorbance in the reaction phase.

increase or even a decrease in visible absorption. The absorption reaches its maximum during the first measurement at 220 °C and then decreases again over the next 30 min at 220 °C. The changes in absorption behavior can be explained in terms of counteracting contributions to the indium reduction state from temperature-dependent reduction and CO₂ conversion leading to oxidation. At 220 °C the maximum degree of reduction is reached under reaction conditions but at this temperature CO₂ is significantly converted, which oxidizes the surface and thus results in an overall decrease in visible absorption. With time, a stationary state is established by balancing the contributions from reduction by H₂ and oxidation by CO₂. At temperatures >190 °C, a similar absorption behavior is observed, consisting of an initial increase and a subsequent decrease in absorption, which clearly shows that reduction by H₂ is faster than oxidation by CO₂. Comparison of the different equilibrated states reveals that the absorption is at its highest at 190 °C and decreases with temperature, strongly suggesting that the oxidation of the catalyst by CO₂ increases with temperature while the reduction remains at about the same level, because the maximum amount of oxygen vacancies has been reached. This could be a first indication that CO₂ activation with subsequent formation of CO is the rate-determining step. The same experiment was performed with a CO₂ to H₂ ratio of 4:2 (see Figure S1). The results are similar, but the reduction is much slower due to the lower H₂ content, which is why the further reduction of the material ends only after 250 °C. These findings underline our previous results.

The activities we measured compare favorably to those of previous studies on polycrystalline In₂O₃,^[9,11] which is likely to terminate with the 111 surface due to the method

of synthesis (thermal decomposition of $\text{In}(\text{NO}_3)_3$) and the fact that it is the most thermally stable. However, this should be viewed with caution, as previously lower flow rates were used, resulting in higher residence times, and higher reactant concentrations in the gas feed. For this reason, we will refrain from a more detailed comparison of the activities. Other factors leading to higher conversions may be the smaller crystallite size and thus the larger specific surface area of the In_2O_3 particles used here. Besides, the particle shape or the surface termination may have an influence on the activity, as has been shown in the context of CO oxidation,^[27] while differences in H_2 or CO_2 activation over $\text{In}_2\text{O}_3(111)$ or $\text{In}_2\text{O}_3(110)$ have been demonstrated by theoretical studies (DFT).^[6,13,28,29]

Next, we performed operando UV/Vis measurements at 250 °C while systematically varying the gas phase between oxidative/reactive and reductive conditions. Figure 2 shows the absorbances at 532 nm and 700 nm (see Figure S2 for the corresponding UV/Vis spectra), where the former mainly resembles the self-absorption in our Raman experi-

ments, which were recorded at 532 nm (see below). In these experiments we first pretreated the catalyst with O_2 to start from an oxidized state. During heating to 250 °C under O_2 exposure, desorption of H_2O and CO_2 was observed (not shown), indicating that the surface is being cleaned from adsorbates. Upon exposure to O_2 flow, the absorption at 532 nm increased significantly (see Figure 2). Since this wavelength is located within the absorption edge, the observed behavior can be explained by an increase in the band edge, originating from the temperature increase (Burstein–Moss effect) and/or from oxidation.^[16]

On switching to H_2 , the absorption at 532 and 700 nm increases significantly, which is mainly attributed to a reduction of the (sub)surface and possibly also to an increase in reflectivity through small metallic indium domains. This is supported by the strong presence of H_2O in the gas phase. Since the same trends in absorption can be observed at both wavelengths (and the entire remaining visible range), only the absorption at 700 nm will be discussed in the following.

Upon exposure to CO_2 , there is again a strong decrease in absorption, which is in the range of the absorption in O_2 , demonstrating that the sample can be oxidized again by CO_2 and that the process of reduction seems to be completely reversible on the basis of UV/Vis spectra and their penetration depth. At the same time, the gas phase initially shows a small increase in CO (see Figure 2, bottom panel), implying surface oxidation by CO_2 , thereby releasing CO. Such a reversibility with respect to the oxidation state in the absence of H_2 could indicate that hydrogen is not required for CO_2 reduction.

On switching to H_2 afterwards, the detected CO signal is significantly lower, which shows that only small amounts of CO_2 in the form of carbonates or other carbonaceous adsorbates remain on the surface in the CO_2 phase. In contrast, the H_2O signal increases, which in turn is associated with the reduction of the surface, as can be seen by the increase in absorbance.

Exposure to reaction conditions (H_2/CO_2) induces a decrease in absorption despite the same H_2 concentration, which, however, does not reach the level detected in CO_2 . This behavior confirms the findings of Figure 1, i.e., that the reduction and oxidation processes must be in equilibrium, with the reduction still predominating. Interestingly, the two reaction phases are characterized by the same absorption (see Figure 2, top panel) and CO evolution (see Figure 2, bottom panel), despite the completely different initial states. This clearly demonstrates that the pretreatment has no influence on the reaction and suggests that certain intermediates only form under reaction conditions, since the CO release under reaction conditions is significantly higher than when switching from H_2 to CO_2 or vice versa. In this context, previous photocatalytic studies have shown that the surface hydroxide concentration is also higher under reaction conditions than under pure H_2 .^[18] As can be seen in Figure 2, switching off CO_2 after reaction conditions leads to a renewed increase in absorption and thus a reduction of the surface.

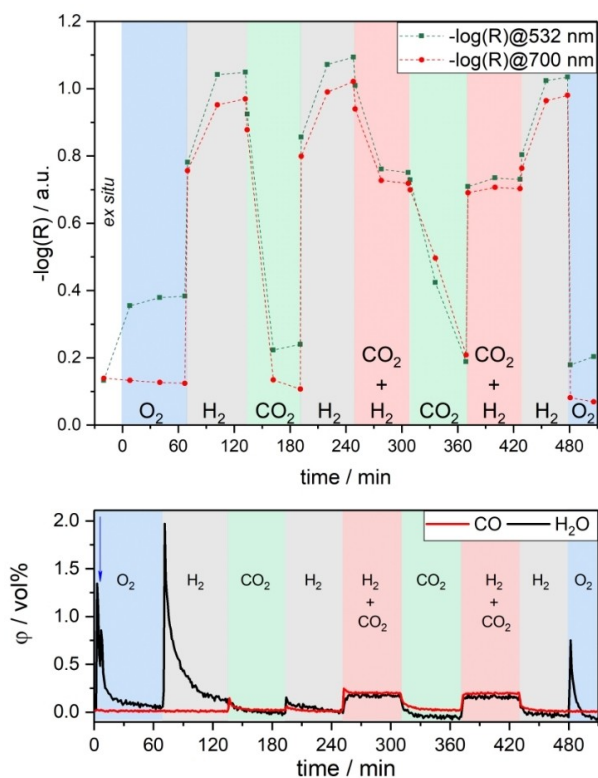


Figure 2. Top: In situ/operando UV/Vis results for In_2O_3 sheets recorded during the indicated gas exposures at 250 °C and at a total flow rate of 100 mL min^{-1} , except for the ex situ spectra, which were taken at 25 °C. The exposure time in each gas phase was about 1 h with the exception of the last O_2 phase (30 min). Bottom: Gas-phase IR analysis during the UV/Vis measurements. The increased water concentration in the first few minutes is due to the purging of the cell. Starting after 6 min (see blue arrow) the cell was heated to 250 °C, leading to water desorption and thus an increase in the H_2O concentration. For details see text.

Finally, In_2O_3 is exposed to O_2 flow to check the reversibility of the system. The gas-phase data reveals a strong H_2O signal decaying with time, which implies the presence/formation of hydroxides/adsorbed hydrogen during H_2 exposure. During this O_2 exposure, the absorbance is lower than during the first O_2 phase, and major differences were detected for 532 nm absorption, which is located in the absorption edge. Since in both cases the experimental conditions were the same, we attribute the observed drop in absorption to a decrease in the band gap resulting from a larger crystallite size. To test this hypothesis, we performed ex situ XRD measurements after different gas exposures until the first reaction phase, which clearly show that the crystallite size increases from 12 nm after the first O_2 phase to 27 nm after the subsequent H_2 (for diffractograms, see Figure S3). Note that all following gas atmospheres have no significant influence on the crystallite size. Notably, after the second H_2 exposure, additional reflections are detected, which originate from metallic indium (JCPDS 85-1409), showing that metallic indium is formed during reduction with 4 vol % H_2 at 250 °C. To this end, it should be noted that small domains of metallic indium, formed during the first H_2 phase and under reaction conditions, may have oxidized back under air exposure and thus cannot be excluded by the present ex situ XRD analysis.

To further probe the reducibility behavior of In_2O_3 , we recorded the XRD pattern after CO exposure (4 vol %) after a prior oxygen treatment, analogous to the other measurements. For CO exposure, significantly more metallic indium was formed and the crystallite size grew only to 21 nm, in contrast to the observed 27 nm for H_2 . Thus, hydrogen is a weaker reducing agent towards In_2O_3 than CO, which is consistent with the literature.^[12] Furthermore, hydrogen must have an additional effect on the sample, since the crystallite size increases significantly more compared to CO. To gain insight into the electronic structure changes during CO reduction, we recorded in situ UV/Vis spectra (see Figure S4), which reveal a higher absorption in the visible region during CO exposure, implying a better reduction by CO. We also highlight the fact that the presence of CO strongly contributes to the enhanced electronic inductive effects in the impedance spectra in the Figure 3B compared to the purely reductive H_2 treatment (Figure S6, Table S2). Interestingly, the sample absorbance almost returns to its original value (measured in O_2) on subsequent exposure to CO_2 . Thus, In_2O_3 can be re-oxidized by CO_2 , releasing CO regardless of the reducing agent (H_2 or CO). Moreover, no surface hydrogen species are required for the oxidation by CO_2 , indicating that no hydrogen-containing intermediates are involved in the re-oxidation process.

To elucidate the charge and mass transport in In_2O_3 nanoparticles, operando potentiostatic electrochemical impedance spectroscopy (p-EIS) spectra were acquired. It should be mentioned that due to the sample shape (no pellet) a Mott-Schottky analysis is disturbed by gas inclusion and an increased number of grain boundaries and is not completely reproducible. For this reason, such an analysis was not performed in this work. The non-uniform sample

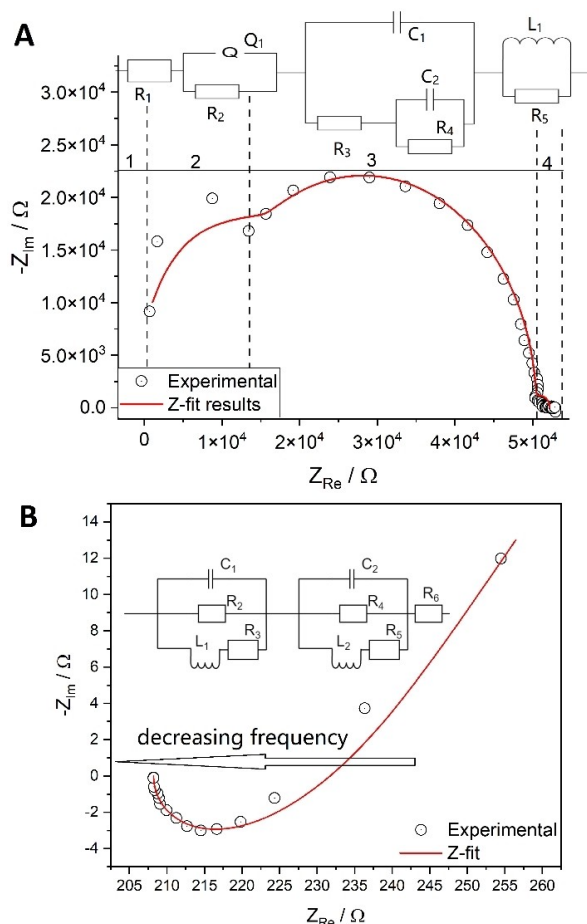


Figure 3. Nyquist plots based on operando p-EIS of In_2O_3 , shown together with fits according to the corresponding equivalent circuits. A) During CO_2 gas treatment (2 vol %; total flow: 50 mL min^{-1}) at 250 °C with the different areas in the Nyquist plot and the corresponding assignment in the equivalent circuit. Region 1: electrode bulk resistance; region 2: vacancy reorganization; region 3: capacitive behavior of the non-reduced In_2O_3 ; region 4: gas diffusion into In_2O_3 nanoparticles. B) During CO_2/H_2 treatment (2 vol % CO_2 , 4 vol % H_2 ; total flow rate: 50 mL min^{-1}) at 250 °C. The experimental data shows a reversed behavior, with high-frequency points located on the right. R: resistance, C: capacitance, L: inductance, Q: non-ideal capacitance. The values resulting from the fit analysis are summarized in Table S2.

distribution also has an impact on the p-EIS spectra, which deviate from ideal behavior by ca. 10 %, as validated by Kramers-Kronig-relations (see Supporting Information). All spectra (see Figure 3 and Figures S5–S11) were recorded under the same gas sequence and composition as in Figure 2. A considerable impact of the gas phase on the impedance spectra was found for all treatments, which is reflected in the profile of the Nyquist plots. However, as there are no fundamental differences between spectra taken under the same gas atmosphere, only the spectra of the first treatment with a specific gas phase will be discussed, starting with the spectrum under O_2 exposure (see Figure S5).

As In_2O_3 is a semiconductor with a band gap of approximately 3 eV,^[30] accumulation of charged surface oxygen due to polarization is expected.^[31] The polarization manifests itself in a sharp and vertical increase of the impedance in the Nyquist plot, and both imaginary and real parts of the impedance reach values in the megohm range (see Figure S5), which speaks for very limited to no conductivity of In_2O_3 during the oxygen treatment. The spectrum in O_2 atmosphere may therefore be treated as a response of bare In_2O_3 nanoparticles and will serve as a reference for the discussion of changes observed during the following gas treatments.

Regarding surface charging, a similar behavior was previously observed for CeO_2 at room temperature.^[32] The presence of a limited diffusion region results from the hindered oxygen accumulation on the In_2O_3 surface. The voltage applied to the sample causes external polarization due to the non-conductive character of In_2O_3 at room temperature, and the activation energy from the temperature dependent conductivity behavior of 137 kJ mol^{-1} will not be reached by simple polarization but requires elevated temperatures.^[33]

The major reduction of In_2O_3 was observed during the hydrogen treatment (see Figure S6). The pronounced contribution of the inductive part ($L=2.03 \times 10^{-5} \text{ H}$ during the first H_2 treatment) observed in the operando p-EIS spectrum is attributed to the percolation of In_2O_3 nanoparticles with hydrogen species,^[34] referring here to the penetration of these species into the solid. This is in agreement with previous IR and DFT studies on In_2O_3 , which have demonstrated the diffusion of interstitial hydrogen to increase conductivity.^[23–25] Thereby, hydrogen percolates into the bulk of a nanoparticle and creates an inductive response of the EIS spectrum, typical for gas diffusion in the bulk of a material.^[34] The reduction of the In_2O_3 nanoparticles is proposed to proceed according to the reaction $\text{In}_2\text{O}_3 + 3 \text{H}_2 \rightarrow 2 \text{In}^0 + 3 \text{H}_2\text{O}$. Thus, the first two H_2 phases show a purely resistive behavior at the beginning of the Nyquist plot, indicating the formation of metallic indium. In the third phase, this behavior is less pronounced, but this is also consistent with our UV/Vis results (lowest absorption at 532 nm).

The decomposition of H_2 into protons within In_2O_3 was speculated to occur by a homolytic or a heterolytic splitting process, as discussed by García-Melchor and López.^[35] In this context, theoretical studies have shown that both scenarios are conceivable, but strongly depend on the degree of reduction.^[13] Under our conditions, owing to the high degree of indium oxide reduction, heterolytic dissociation is more likely.^[13] To describe the spectrum in Figure S6, a considerable contribution of the Warburg element is necessary (see Table S2), which speaks for the distribution of hydrogen gas on the surface. The Warburg element is commonly used to describe mass transport processes, therefore, coupling it with inductive parts will deliberately lead to the description of a gaseous contribution to the impedance response.^[36]

Following the hydrogen treatment, In_2O_3 was exposed to CO_2 and an operando p-EIS spectrum was recorded (see

Figure 3A). The equivalent circuit shown in Figure 3A is divided into four parts. The first part represents the electrode bulk resistance (R_1), which was found to be in the ohm range (see Table S2), speaking for improved conductivity compared to the pristine material (with R_1 in the megohm range); nevertheless, remaining vacancies induced by the H_2 phase remain active, judging by our Raman spectra below. In the second part, the reorganization of vacancies occurs.^[37] The third part contributes mostly to the p-EIS spectrum and is assigned to non-reduced In_2O_3 , while at low frequencies (L_1R_3 region) gas diffusion takes place, as, for example, observed for polycrystalline tin oxide.^[38,39] The regions are assigned based on the frequency domains where impedance data was recorded, starting from the high-frequency region and bulk impedance, followed by the internal electronic structure in the middle-frequency region and ending on the diffusion response within low-frequency regions.^[40]

During reaction conditions (see Figure 3B), the hydrogen flow, penetrating the interior of the In_2O_3 , carries the CO_2 gas with it, as judged by the inductance contribution ($L=1.03 \times 10^{-5} \text{ H}$), which differs from the value obtained for the first H_2 treatment ($L=2.03 \times 10^{-5} \text{ H}$). The reaction occurs in the bulk due to gas percolation, rather than on the surface as in the case of pure CO_2 exposure. In this context, we propose that the higher inductance is caused by the reaction $\text{CO}_2 + \text{H}_2 \rightarrow \text{CO} + \text{H}_2\text{O}$ and thus by the presence of CO , which is also detected in the gas phase. Therefore, the respective parts of the triple equivalent circuits of Figure 3B correspond to the interaction of In_2O_3 with H_2 (right part of the circuit) and CO_2 (left part of the circuit). Please note that the EIS spectrum is reversed compared to what it was in the case of H_2 treatment, implying that the high frequency points are in the region of high imaginary and real impedances, originating from gas percolation and the induction of the gas impedance.^[34] In contrast to pure hydrogen, there is no pure resistance behavior at the beginning of the spectrum, indicating that no metallic indium is formed under reaction conditions. This is corroborated by our operando UV/Vis results, which show a significantly lower absorption in the visible region than under H_2 atmosphere.

Figure 4 depicts quasi in situ Raman spectra of In_2O_3 , recorded under argon at 50°C after treatment with O_2 , H_2 , H_2/CO_2 , and CO_2 . The bands at 306, 366, 495 and 629 cm^{-1} can be assigned to $\delta(\text{InO}_6)$, $\nu(\text{InO}_6)$, In-O-In , and $\nu(\text{InO}_6)$ vibrations of cubic In_2O_3 , respectively, which is in accordance with the literature.^[16,41] These bands become broader with increasing number of defects (see H_2 and H_2/CO_2 treatment, Figure 4), consistent with previous studies.^[42] The feature at 595 cm^{-1} also originates from cubic In_2O_3 and is attributed to a vibration with E_g symmetry.^[43] It shows a red-shift under reaction conditions and H_2 , as a result of defect formation, consistent with our previous study.^[16] All other features (415, 531, and 559 cm^{-1}) are related to oxygen defects, as confirmed by DFT.^[16] Notably, the band at 306 cm^{-1} shows a shoulder towards larger wavenumbers, which is caused by reduction and was also observed in previous studies.^[21,42,44]

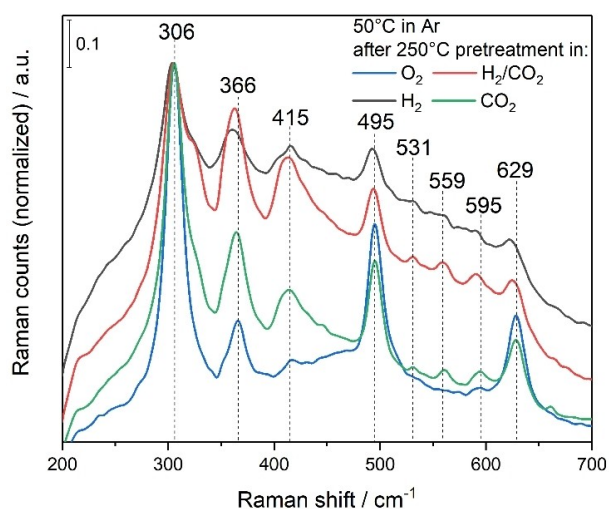


Figure 4. Quasi in situ Raman spectra recorded in argon at 50 °C after the indicated gas exposures at 250 °C and at a total flow rate of 100 mL min⁻¹. The spectra were normalized to the band with the highest intensity at around 306 cm⁻¹. The spectra were recorded sequentially in the order O₂, H₂, H₂/CO₂, and CO₂. The sample was cooled to 50 °C under argon.

Comparison of the different gas phases reveals a significantly higher background for H₂ and reaction conditions, which is caused by fluorescence, self-absorption of the laser, and an increased reflectivity by metallic indium (as also detected by p-EIS, see flat line for Z_{Re} between 240 and 220 Ω in Figure S6). Nevertheless, closer inspection of the spectra recorded after O₂ and CO₂ exposure shows that the 415 cm⁻¹ band is less pronounced for O₂, implying that re-oxidation by CO₂ is not as efficient as by oxygen. This behavior is in agreement with previous impedance studies,^[12] which show that In₂O₃ is best re-oxidized with O₂, followed by H₂O and CO₂. In the UV/Vis measurements such a difference was not observed due to the lower penetration depth, implying that the surface is completely oxidized, but the bulk is not. Thus, a certain number of defects remain present even under O₂.

The high-wavenumber region of the Raman spectra shows bands at 3647 and 3675 cm⁻¹ (see Figure S12), which originate from bridging hydroxyl groups^[44,45] and reappear after exposure to reaction conditions after being consumed in the reducing atmosphere. Interestingly, after reaction conditions, a new band is detected at 2867 cm⁻¹, which is assigned to the C–H stretching vibration of a formate-like species.^[44] This shows that under reaction conditions a stable adsorbate is formed, which involves atoms from both reactants. However, in this context it is important to note that this observation does not imply the presence of a reaction intermediate, as the detected band may be due to an observer species. At this point it should be noted that we cannot exclude the presence of other intermediates. Future operando Raman experiments may possibly clarify the role of formate or other species, but this is currently hampered by the large background (see introduction).

In order to obtain additional surface information, XPS and ultraviolet photoelectron spectroscopy (UPS) was applied (for XPS data and discussion see Supporting Information). Figure 5 depicts the UP spectra of In₂O₃ using He I radiation after exposure to the different gas atmospheres, analogous to the XP spectra. All UP spectra show the typical valence band features at 4.4, 6.1 and 8.7 eV.^[46,47] For all gas atmospheres, the features at 5.7, 8.7, and 10.5 eV increase in intensity compared to the spectrum after O₂ exposure, but most prominently for exposure to CO₂ and reaction conditions. Previous studies have proposed the contributions at 5.7 and 10.5 eV to be determined by modified valence band (VB) states subjected to adsorption of molecules.^[46] In our case, in principle, hydroxides and/or carbonaceous adsorbates (e.g., carbonates, formates) may contribute to the spectral changes compared to the O₂ spectrum, but the presence of carbonaceous adsorbates appears to be more likely, considering the increased intensity after exposure to CO₂ and the reaction phase. This is further supported by the IR gas-phase measurements, which show the presence of hydrogen-containing adsorbates on the surface after H₂ treatment (see Figure 2). In this context, in a previous near-ambient-pressure (NAP) UPS study on In₂O₃ during rWGSR, it was shown that the temperature as well as the CO₂:H₂ ratio have a strong influence on the valence region,^[48] which is reflected in line broadening. This is in agreement with our findings that the surface is strongly influenced by the gas environment, where a greater CO₂ content leads to greater changes, which indicates the presence of carbonaceous adsorbates.

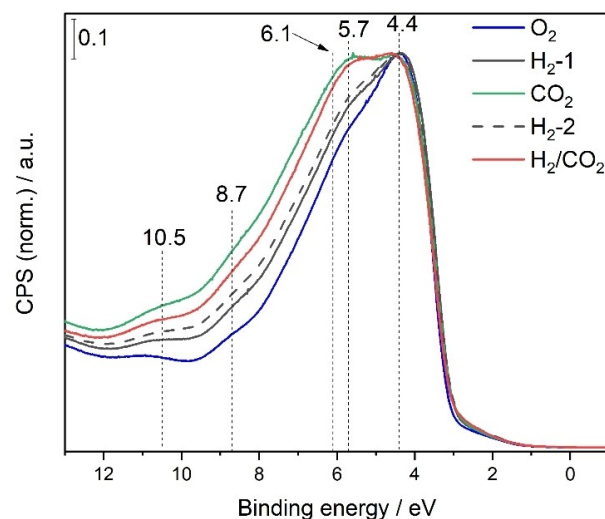


Figure 5. Valence band photoelectron spectra recorded quasi in situ after exposure to the indicated gas atmospheres at 250 °C and at a total flow rate of 100 mL min⁻¹. The blue spectrum was obtained after O₂ (25%) pretreatment, the gray ones after H₂ (4%) pretreatment, the green one after CO₂ (2%) pretreatment, and the red one after H₂/CO₂ (4%/2%) pretreatment. The gas sequence corresponds to that of the UV/Vis experiments in Figure 2 up to the first reaction phase and the hyphenated number indicates the order of the gas sequence. The source was He I ($h\nu = 21.2$ eV).

Summarizing the findings from the combined surface analysis by Raman, XP and UP spectroscopies, there is a clear indication of variations in the surface composition, the indium state, and the number of oxygen vacancies when switching between oxidative, reductive, and reactive gas atmospheres. The indium and support surface state after exposure to reaction conditions largely follows a behavior expected within the limits of oxidative (CO₂) and reductive (H₂) atmospheres, while the overall changes in the adsorbate species (e.g. OH, formate) are rather distinct, somewhat resembling the observed subsurface/bulk behavior (see Figure 2). By combining these findings with the operando UV/Vis and impedance results, the active state of the catalyst can be specified as reduced, i.e., oxygen-defect containing (but non-metallic) In₂O₃, percolated with reactant and product gases, and exhibiting surface species, such as hydroxides, hydrides, and carbonaceous adsorbates. Although the redox processes can occur separately, the simultaneous presence of H₂ and CO₂ clearly provides synergistic effects towards CO₂ conversion. Our results emphasize, in particular, the importance of subsurface/bulk dynamics for the activity in reducible oxide catalysts, besides surface processes.

Conclusion

In this study, we have generated a deeper understanding of the mechanism of rWGS over c-In₂O₃ catalysts by applying operando UV/Vis spectroscopy and (in the context of thermal catalysis) newly developed operando impedance spectroscopy, as well as quasi in situ spectroscopies (Raman, XPS, UPS). The new mechanistic insight into the In₂O₃ mode of operation was supported by a systematic investigation of the related reduction and oxidation processes and their comparison to reaction conditions. For example, our study shows that despite surface reduction, diffusion of oxygen vacancies leads to bulk reduction. While reduced c-In₂O₃ nanoparticles can be re-oxidized by CO₂ on the surface, complete oxidation of the bulk is only possible with O₂. This behavior is independent of the reducing agent (H₂ or CO), although CO leads to stronger In₂O₃ reduction.

Based on temperature-dependent UV/Vis analysis under reaction conditions, oxidation by CO₂ is identified as the rate-determining step for the rWGS, which is supported by operando impedance spectra, showing a predominance of the hydrogen contribution. The significant evolution of CO and H₂O, also after separate treatment with CO₂ or H₂, is fully consistent with redox processes but because conversions are somewhat higher under reaction conditions, hydrogen-containing surface species (e.g. hydroxides, hydrides) are proposed to have a promoting effect on CO₂ conversion and/or hydrogen containing intermediates (e.g. COOH*) may play a role. Such a behavior would be in accordance with results from theoretical studies, which associate CO₂ conversion with frustrated Lewis pairs.^[14,15]

The above analysis of the (sub)surface and bulk properties during the rWGS demonstrates that the entire In₂O₃ nanoparticle is involved in the reaction, which is only

accessible by using complementary in situ/operando techniques. Combining our new experimental findings with results from theory allows us to develop a consistent mechanistic picture of rWGS over c-In₂O₃. Our findings are of immediate relevance for a detailed understanding of CO₂ hydrogenation and other related catalytic processes over In₂O₃, but they are also expected to be of more general impact, considering the growing importance of catalysts based on reducible oxide materials.

Acknowledgements

We thank Stefan Lauterbach and Hans-Joachim Kleebe for TEM measurements, Martin Brodrecht for nitrogen adsorption/desorption experiments, Kathrin Hofmann for XRD analysis, and Karl Kopp for technical support and helpful discussions on the XPS results. Open Access funding enabled and organized by Projekt DEAL.

Conflict of Interest

The authors declare no conflict of interest.

Data Availability Statement

The data that support the findings of this study are available from the corresponding author upon reasonable request.

Keywords: CO₂ Activation · In₂O₃ · Operando Spectroscopy · Reaction Mechanism · Reverse Water-Gas Shift

- [1] A. Tsoukalou, P. M. Abdala, D. Stoian, X. Huang, M.-G. Willinger, A. Fedorov, C. R. Müller, *J. Am. Chem. Soc.* **2019**, *141*, 13497–13505.
- [2] M. S. Frei, M. Capdevila-Cortada, R. García-Muelas, C. Mondelli, N. López, J. A. Stewart, D. Curulla Ferré, J. Pérez-Ramírez, *J. Catal.* **2018**, *361*, 313–321.
- [3] J. Wang, G. Zhang, J. Zhu, X. Zhang, F. Ding, A. Zhang, X. Guo, C. Song, *ACS Catal.* **2021**, *11*, 1406–1423.
- [4] N. Rui, F. Zhang, K. Sun, Z. Liu, W. Xu, E. Stavitski, S. D. Senanayake, J. A. Rodriguez, C.-J. Liu, *ACS Catal.* **2020**, *10*, 11307–11317.
- [5] N. Rui, K. Sun, C. Shen, C. J. Liu, *J. CO₂ Util.* **2020**, *42*, 101313.
- [6] B. Qin, Z. Zhou, S. Li, P. Gao, *J. CO₂ Util.* **2021**, *49*, 101543.
- [7] P. Gao, S. Li, X. Bu, S. Dang, Z. Liu, H. Wang, L. Zhong, M. Qiu, C. Yang, J. Cai, et al., *Nat. Chem.* **2017**, *9*, 1019–1024.
- [8] J. Wang, C.-Y. Liu, T. P. Senftle, J. Zhu, G. Zhang, X. Guo, C. Song, *ACS Catal.* **2020**, *10*, 3264–3273.
- [9] W. Wang, Y. Zhang, Z. Wang, J. Yan, Q. Ge, C. Liu, *Catal. Today* **2016**, *259*, 402–408.
- [10] J.-I. Makiura, T. Higo, Y. Kurosawa, K. Murakami, S. Ogo, H. Tsuneki, Y. Hashimoto, Y. Sato, Y. Sekine, *Chem. Sci.* **2021**, *12*, 2108–2113.
- [11] Q. Sun, J. Ye, C. Liu, Q. Ge, *Greenhouse Gas Sci. Technol.* **2014**, *4*, 140–144.
- [12] T. Bielz, H. Lorenz, P. Amann, B. Klötzer, S. Penner, *J. Phys. Chem. C* **2011**, *115*, 6622–6628.

- [13] B. Qin, S. Li, *Phys. Chem. Chem. Phys.* **2020**, *22*, 3390–3399.
- [14] M. Ghoussoub, S. Yadav, K. K. Ghuman, G. A. Ozin, C. V. Singh, *ACS Catal.* **2016**, *6*, 7109–7117.
- [15] K. K. Ghuman, T. E. Wood, L. B. Hoch, C. A. Mims, G. A. Ozin, C. V. Singh, *Phys. Chem. Chem. Phys.* **2015**, *17*, 14623–14635.
- [16] M. Ziemba, L. Schumacher, C. Hess, *J. Phys. Chem. Lett.* **2021**, *12*, 3749–3754.
- [17] A. I. Serykh, *J. Phys. Chem. C* **2016**, *120*, 21436–21440.
- [18] J. Y. Y. Loh, N. P. Kherani, *Molecules* **2019**, *24*, 3818.
- [19] J. Y. Y. Loh, Y. Ye, N. P. Kherani, *ACS Appl. Mater. Interfaces* **2020**, *12*, 2234–2242.
- [20] L. Wang, Y. Dong, T. Yan, Z. Hu, A. A. Jelle, D. M. Meira, P. N. Duchesne, J. Y. Y. Loh, C. Qiu, E. E. Storey, et al., *Nat. Commun.* **2020**, *11*, 2432.
- [21] T. Bielz, H. Lorenz, W. Jochum, R. Kaindl, F. Klauser, B. Klötzer, S. Penner, *J. Phys. Chem. C* **2010**, *114*, 9022–9029.
- [22] N. Siedl, P. Gügel, O. Diwald, *J. Phys. Chem. C* **2013**, *117*, 20722–20729.
- [23] Y. Qin, P. Weiser, K. Villalta, M. Stavola, W. B. Fowler, I. Biaggio, L. Boatner, *J. Appl. Phys.* **2018**, *123*, 161506.
- [24] S. Limpijumong, P. Reunchan, A. Janotti, C. G. Van de Walle, *Phys. Rev. B* **2009**, *80*, 193202.
- [25] W. Yin, K. Smithe, P. Weiser, M. Stavola, W. B. Fowler, L. Boatner, S. J. Pearton, D. C. Hays, S. G. Koch, *Phys. Rev. B* **2015**, *91*, 075208.
- [26] Y. Qi, L. Song, S. Ouyang, X. Liang, S. Ning, Q. Zhang, J. Ye, *Adv. Mater.* **2020**, *32*, 1903915.
- [27] W. J. Kim, D. Pradhan, Y. Sohn, *J. Mater. Chem. A* **2013**, *1*, 10193.
- [28] A. Posada-Borbón, H. Grönbeck, *Phys. Chem. Chem. Phys.* **2020**, *22*, 16193–16202.
- [29] A. Posada-Borbón, H. Grönbeck, *Phys. Chem. Chem. Phys.* **2019**, *21*, 21698–21708.
- [30] A. Walsh, J. L. F. Da Silva, S.-H. Wei, C. Körber, A. Klein, L. F. J. Piper, A. DeMasi, K. E. Smith, G. Panaccione, P. Torelli, et al., *Phys. Rev. Lett.* **2008**, *100*, 167402.
- [31] V. Balasubramani, S. Chandraleka, T. S. Rao, R. Sasikumar, M. R. Kuppusamy, T. M. Sridhar, *J. Electrochem. Soc.* **2020**, *167*, 037572.
- [32] M. M. El-Nahass, A. M. Hassanien, A. A. Atta, E. M. A. Ahmed, A. A. Ward, *J. Mater. Sci. Mater. Electron.* **2017**, *28*, 1501–1507.
- [33] M. Radtke, C. Hess, *J. Mater. Eng. Perform.* **2022**, <https://doi.org/10.1007/s11665-022-06653-3>.
- [34] S. Cruz-Manzo, R. Chen, P. Rama, *J. Fuel Cell Sci. Technol.* **2012**, *9*, 051002.
- [35] M. García-Melchor, N. López, *J. Phys. Chem. C* **2014**, *118*, 10921–10926.
- [36] J. Huang, Y. Gao, J. Luo, S. Wang, C. Li, S. Chen, J. Zhang, *J. Electrochem. Soc.* **2020**, *167*, 166503.
- [37] T.-M. Pan, Y.-S. Huang, J.-L. Her, *Sci. Rep.* **2018**, *8*, 12902.
- [38] M. Labeau, U. Schmatz, G. Delabougliuse, J. Roman, M. Vallet-Regi, A. Gaskov, *Sens. Actuators B* **1995**, *26*, 49–52.
- [39] T. Yang, J. Liu, H. Finklea, S. Lee, W. K. Epting, R. Mahbub, T. Hsu, P. A. Salvador, H. W. Abernathy, G. A. Hackett, *Int. J. Hydrogen Energy* **2018**, *43*, 15445–15456.
- [40] J. Stankiewicz, M. P. Lozano, F. Villuendas, *Phys. Rev. B* **2012**, *85*, 125306.
- [41] S. Elouali, L. G. Bloor, R. Binions, I. P. Parkin, C. J. Carmalt, J. A. Darr, *Langmuir* **2012**, *28*, 1879–1885.
- [42] F. Gu, C. Li, D. Han, Z. Wang, *ACS Appl. Mater. Interfaces* **2018**, *10*, 933–942.
- [43] C. Kranert, R. Schmidt-Grund, M. Grundmann, *Phys. Status Solidi RRL* **2014**, *8*, 554–559.
- [44] S. Sänze, C. Hess, *J. Phys. Chem. C* **2014**, *118*, 25603–25613.
- [45] A. N. Kharlanov, O. A. Turakulova, V. V. Lunin, *Kinet. Catal.* **2004**, *45*, 260–265.
- [46] V. Brinzari, G. Korotcenkov, M. Ivanov, V. Nehasil, V. Matolin, K. Mašek, M. Kamei, *Surf. Sci.* **2007**, *601*, 5585–5594.
- [47] V. Brinzari, G. Korotcenkov, V. Matolin, *Appl. Surf. Sci.* **2005**, *243*, 335–344.
- [48] N. B. Mhamane, S. Chetry, R. Ranjan, T. Raja, C. S. Gopinath, *ACS Sustainable Chem. Eng.* **2022**, *10*, 3521–3531.

Manuscript received: June 27, 2022

Accepted manuscript online: July 14, 2022

Version of record online: August 18, 2022

5 Ausblick

In dieser Arbeit wurden CeO_2 und In_2O_3 basierte Katalysatoren während der CO-Oxidation, der WGS und der rWGS Reaktion charakterisiert. Dennoch bleiben offene Fragen, wie beispielsweise der Metallzustand unter *operando* Bedingungen auf den mit Gold oder Kupfer beladenen CeO_2 Katalysatoren. Diese Eigenschaften könnten zukünftig mittels NAP-XPS oder *operando* XAS charakterisiert werden, jedoch stellen die geringen Beladungen eine Herausforderung dar. Aus diesem Grund sollten auch beladungsabhängige Studien in Betracht gezogen werden.

Für In_2O_3 könnten NAP-XPS oder *operando* XAS ebenfalls von Interesse sein, da unter reduktiven Bedingungen metallisches Indium gebildet wird, welches mittels XPS an der Oberfläche und mittels XAS integral quantifiziert werden könnte. Die jetzigen Ergebnisse deuten jedoch darauf hin, dass metallisches Indium nicht in die Reaktion involviert ist, weshalb es von Interesse wäre, diese Bildung zu unterdrücken. Dies wäre ebenfalls von Bedeutung für die Charakterisierung mittels schwingungsspektroskopischer Methoden, da sich die Bildung von metallischem Indium negativ auf die Qualität der Spektren auswirkt. Um dies und die Absorptionseffekte zu umgehen, wäre eventuell die Nutzung eines Fourier-Transform-Raman-Aufbaus mit einer Wellenlänge von 1064 nm von Interesse. Dies könnte ein Weg sein, In_2O_3 Partikel auch unter *operando* Bedingungen mittels Raman Spektroskopie zu charakterisieren. Eine andere Möglichkeit wäre die Detektion von Phononen mittels IR Spektroskopie im fernen IR Bereich. Aufgrund der vermeintlich negativen Eigenschaften des metallischen Indiums und der zu starken Reduktionseigenschaften von In_2O_3 wäre es jedoch von Bedeutung, diese Eigenschaften vollkommen zu unterdrücken. Dies könnte beispielsweise durch die Abscheidung weniger Schichten In_2O_3 auf ZrO_2 geschehen, was mittels Atomlagenabscheidung (ALD) realisiert werden könnte. In diesem Kontext konnten theoretische Studien von $\text{In}_2\text{O}_3/\text{ZrO}_2$ bereits die Steigerung der Defektbildungsenergie in Abhängigkeit der In_2O_3 Schichtdicke zeigen.[74] Ein anderer Ansatz könnte über die In_2O_3 Nanopartikel selbst gehen, indem die Oberflächenterminierung gesteuert wird. In diesem Zusammenhang wären ebenfalls facettenabhängige Studien von Interesse, da hier beispielsweise im Rahmen der CO-Oxidation schon Unterschiede in der Aktivität beobachtet wurden.[75] In Hinblick auf die Oberfläche könnten auch 2D- In_2O_3 oder ultradünne Schichten von Interesse sein, da so Absorptionseffekte unterdrückt werden könnten. Letztere konnten beispielsweise schon mittels Hydrothermalsynthese hergestellt werden.[76] Zuletzt wäre auch eine Verdünnung von In_2O_3 mittels CeO_2 denkbar. Pures CeO_2 ist für die rWGS Reaktion zwar kaum aktiv, kleine Mengen an In_2O_3 haben jedoch einen erheblichen Einfluss auf die Aktivität.[77]

Abgesehen von der (r)WGS Reaktion wäre natürlich auch interessant, die Methanolsynthese durch Hydrierung von CO_2 zu betrachten, da diese mithilfe von erneuerbaren Energien einen attraktiven Weg zur Nutzung des Treibhausgases CO_2 darstellt. In diesem Kontext wären Studien an den CeO_2 basierten sowie den In_2O_3 Katalysatoren von Interesse. Allerdings würden für In_2O_3 auch Metallbeladungen in Frage kommen, da es so eventuell möglich ist, die Selektivität in Richtung Methanol zu lenken. In diesem Kontext konnte schon ein positiver Einfluss von Gold sowohl auf die Aktivität als auch auf die Selektivität beobachtet werden.[78] Es gibt jedoch noch offene Fragen und Herausforderungen in diesem Bereich, wie z. B. die Rolle des Trägers, da die Charakterisierung durch schwingungsspektroskopische Methoden aufgrund der zusätzlichen elektronischen Effekte, die Gold mit sich bringt, erschwert werden könnte.

Eine weitere nachhaltige Reaktion wäre das Dry Reforming mit der Nutzung von Biogas als Quelle. Hierbei

könnten beispielsweise CeO_2 und In_2O_3 in Verbindung mit Nickel interessante Ergebnisse liefern. Andere Katalysatoren aus dieser Studie könnten zusätzlich auf deren Aktivität geprüft werden. So wäre es möglich, die CO_2 Aktivierung besser zu verstehen, da lediglich die Wasserstoffquelle (hier CH_4 statt H_2) ausgetauscht werden würde.

Abschließend lässt sich sagen, dass es im komplexen Themenfeld der beladenen Metalloxide in der Katalyse durchaus noch offene Fragen gibt. Dennoch konnte diese Arbeit zu mindestens einen kleinen Beitrag zur Aufklärung von Reaktionsmechanismen für die CO-Oxidation und die (r)WGS Reaktion leisten.

Literaturverzeichnis

- [1] W. Reschetilowski, *Einführung in die Heterogene Katalyse, Bd. 1999*, Springer Berlin Heidelberg, Berlin, Heidelberg, **2015**.
- [2] A. Trovarelli, J. Llorca, *ACS Catal.* **2017**, *7*, 4716–4735.
- [3] Z.-A. Qiao, Z. Wu, S. Dai, *ChemSusChem* **2013**, *6*, 1821–1833.
- [4] H.-X. Mai, L.-D. Sun, Y.-W. Zhang, R. Si, W. Feng, H.-P. Zhang, H.-C. Liu, C.-H. Yan, *J. Phys. Chem. B* **2005**, *109*, 24380–24385.
- [5] Z. Liu, X. Li, M. Mayyas, P. Koshy, J. N. Hart, C. C. Sorrell, *CrystEngComm* **2017**, *19*, 4766–4776.
- [6] C. Yang, X. Yu, S. Heißler, P. G. Weidler, A. Nefedov, Y. Wang, C. Wöll, T. Kropp, J. Paier, J. Sauer, *Angew. Chem. Int. Ed.* **2017**, *56*, 16399–16404.
- [7] C. Schilling, M. V. Ganduglia-Pirovano, C. Hess, *J. Phys. Chem. Lett.* **2018**, *9*, 6593–6598.
- [8] P. Pérez-Bailac, P. G. Lustemberg, M. V. Ganduglia-Pirovano, *J. Phys. Condens. Matter* **2021**, *33*, 504003.
- [9] C. Song, *Catal. Today* **2002**, *77*, 17–49.
- [10] D. Trimm, *Appl. Catal. A: Gen.* **2005**, *296*, 1–11.
- [11] H. Ha, S. Yoon, K. An, H. Y. Kim, *ACS Catal.* **2018**, *8*, 11491–11501.
- [12] L.-W. Guo, P.-P. Du, X.-P. Fu, C. Ma, J. Zeng, R. Si, Y.-Y. Huang, C.-J. Jia, Y.-W. Zhang, C.-H. Yan, *Nat. Commun.* **2016**, *7*, 13481.
- [13] Y.-G. Wang, D. Mei, V.-A. Glezakou, J. Li, R. Rousseau, *Nat. Commun.* **2015**, *6*, 6511.
- [14] I. Staffell, D. Scamman, A. V. Abad, P. Balcombe, P. E. Dodds, P. Ekins, N. Shah, K. R. Ward, *Energy Environ. Sci.* **2019**, *12*, 463–491.
- [15] J. A. Rodriguez, D. C. Grinter, Z. Liu, R. M. Palomino, S. D. Senanayake, *Chem. Soc. Rev.* **2017**, *46*, 1824–1841.
- [16] J. Xu, W. Yang, S. Song, H. Zhang, *Eur. J. Inorg. Chem.* **2021**, *2021*, 689–701.
- [17] J. Jiang, B. Ye, J. Liu, *Appl. Energy* **2019**, *235*, 186–203.
- [18] X. Chen, Y. Chen, C. Song, P. Ji, N. Wang, W. Wang, L. Cui, *Front. Chem.* **2020**, *8*, 1–21.
- [19] J. Wang, C.-Y. Liu, T. P. Senftle, J. Zhu, G. Zhang, X. Guo, C. Song, *ACS Catal.* **2020**, *10*, 3264–3273.
- [20] J. Wang, G. Zhang, J. Zhu, X. Zhang, F. Ding, A. Zhang, X. Guo, C. Song, *ACS Catal.* **2021**, *11*, 1406–1423.
- [21] X.-Y. Meng, C. Peng, J. Jia, P. Liu, Y.-L. Men, Y.-X. Pan, *J. CO₂ Util.* **2022**, *55*, 101844.
- [22] F. Wang, J. Jiang, B. Wang, *Catalysts* **2019**, *9*, 477.
- [23] M. A. Bañares, I. E. Wachs, *J. Raman Spectrosc.* **2002**, *33*, 359–380.

-
- [24] M. A. Bañares, M. O. Guerrero-Pérez, J. L. G. Fierro, G. G. Cortez, *J. Mater. Chem.* **2002**, *12*, 3337–3342.
- [25] M. O. Guerrero-Pérez, M. A. Bañares, *ChemComm* **2002**, *2*, 1292–1293.
- [26] J. W. Ward, *J. Catal.* **1968**, *11*, 259–260.
- [27] M. Banares, L. Dauphin, V. Calvoperez, T. Fehlner, E. Wolf, *J. Catal.* **1995**, *152*, 396–409.
- [28] A. Chakrabarti, M. E. Ford, D. Gregory, R. Hu, C. J. Keturakis, S. Lwin, Y. Tang, Z. Yang, M. Zhu, M. A. Bañares, I. E. Wachs, *Catal. Today* **2017**, *283*, 27–53.
- [29] A. M. Abdel-Mageed, S. Chen, C. Fauth, T. Häring, J. Bansmann, *ChemPhysChem* **2021**, *22*, 1302–1315.
- [30] C. Schilling, C. Hess, *Top. Catal.* **2017**, *60*, 131–140.
- [31] C. Schilling, C. Hess, *J. Phys. Chem. C* **2018**, *122*, 2909–2917.
- [32] E. Smith, G. Dent, *Modern Raman Spectroscopy - A Practical Approach*, Bd. 5, John Wiley & Sons, Ltd, **2004**.
- [33] P. Vandenabeele, *Practical Raman Spectroscopy - An Introduction*, John Wiley & Sons, Ltd, **2013**.
- [34] C. Hess, *Chem. Soc. Rev.* **2021**, *50*, 3519–3564.
- [35] C. Schilling, A. Hofmann, C. Hess, M. V. Ganduglia-Pirovano, *J. Phys. Chem. C* **2017**, *121*, 20834–20849.
- [36] Y. Lee, G. He, A. J. Akey, R. Si, M. Flytzani-Stephanopoulos, I. P. Herman, *J. Am. Chem. Soc.* **2011**, *133*, 12952–12955.
- [37] S. Loridant, *Catal. Today* **2021**, *373*, 98–111.
- [38] T. A. X. Nijhuis, S. J. Tinnemans, T. Visser, B. M. Weckhuysen, *Phys. Chem. Chem. Phys.* **2003**, *5*, 4361–4365.
- [39] J. J. H. B. Sattler, A. M. Mens, B. M. Weckhuysen, *ChemCatChem* **2014**, *6*, 3139–3145.
- [40] A. M. Beale, A. M. J. van der Eerden, K. Kervinen, M. A. Newton, B. M. Weckhuysen, *Chem. Comm.* **2005**, 3015.
- [41] C. W. M. Castleton, J. Kullgren, K. Hermansson, *J. Chem. Phys.* **2007**, *127*, 244704.
- [42] T. Bielz, H. Lorenz, W. Jochum, R. Kaindl, F. Klauser, B. Klötzer, S. Penner, *J. Phys. Chem. C* **2010**, *114*, 9022–9029.
- [43] A. Schleife, M. D. Neumann, N. Esser, Z. Galazka, A. Gottwald, J. Nixdorf, R. Goldhahn, M. Feneberg, *New J. Phys.* **2018**, *20*, 053016.
- [44] N Novkovski, A Tanuševski, *Semicond. Sci. Technol.* **2008**, *23*, 095012.
- [45] C. Kranert, R. Schmidt-Grund, M. Grundmann, *Phys. Status Solidi RRL* **2014**, *8*, 554–559.
- [46] D. Baurecht, U. P. Fringeli, *Rev. Sci. Instrum.* **2001**, *72*, 3782–3792.
- [47] V. Marchionni, D. Ferri, O. Kröcher, A. Wokaun, *Anal. Chem.* **2017**, *89*, 5801–5809.
- [48] P. Müller, I. Hermans, *Ind. Eng. Chem. Res.* **2017**, *56*, 1123–1136.
- [49] A. R. C. Bredar, A. L. Chown, A. R. Burton, B. H. Farnum, *ACS Appl. Energy Mater.* **2020**, *3*, 66–98.
- [50] M. Höber, P. Wachter, B. Königshofer, F. Mütter, H. Schröttner, C. Hochenauer, V. Subotić, *Fuel* **2022**, *324*, 124256.
- [51] X. Vendrell, Y. Kubyshin, L. Mestres, J. Llorca, *ChemCatChem* **2020**, *12*, 5926–5931.

-
- [52] T. Bielz, H. Lorenz, P. Amann, B. Klötzer, S. Penner, *J. Phys. Chem. C* **2011**, *115*, 6622–6628.
- [53] L. Nguyen, F. F. Tao, Y. Tang, J. Dou, X.-J. Bao, *Chem. Rev.* **2019**, *119*, 6822–6905.
- [54] S. Bhandari, S. Rangarajan, M. Mavrikakis, *Acc. Chem. Res.* **2020**, *53*, 1893–1904.
- [55] W. Koch, M. C. Holthausen, *A Chemist's Guide to Density Functional Theory, Bd. 2*, Wiley, Weinheim, FRG, **2001**.
- [56] J. Kohanoff, *Electronic Structure Calculations for Solids and Molecules*, Cambridge University Press, Cambridge, **2006**.
- [57] D. Püschner, *Quantitative Rechenverfahren der Theoretischen Chemie*, Springer Fachmedien Wiesbaden, Wiesbaden, **2017**.
- [58] P. E. Blöchl, *Phys. Rev. B* **1994**, *50*, 17953–17979.
- [59] H. J. Monkhorst, J. D. Pack, *Phys. Rev. B* **1976**, *13*, 5188–5192.
- [60] J. P. Perdew, K. Burke, M. Ernzerhof, *Phys. Rev. Lett.* **1996**, *77*, 3865–3868.
- [61] S. L. Dudarev, G. A. Botton, S. Y. Savrasov, C. J. Humphreys, A. P. Sutton, *Phys. Rev. B* **1998**, *57*, 1505–1509.
- [62] J. L. F. Da Silva, M. V. Ganduglia-Pirovano, J. Sauer, V. Bayer, G. Kresse, *Phys. Rev. B* **2007**, *75*, 045121.
- [63] G. Kresse, P. Blaha, J. L. F. Da Silva, M. V. Ganduglia-Pirovano, *Phys. Rev. B* **2005**, *72*, 237101.
- [64] D. Porezag, M. R. Pederson, *Phys. Rev. B* **1996**, *54*, 7830–7836.
- [65] M. Lazzeri, F. Mauri, *Phys. Rev. Lett.* **2003**, *90*, 036401.
- [66] A. Fonari, S. Stauffer, Python program to evaluate off-resonance Raman activity using VASP code as the backend. **2013**, <https://github.com/raman-sc/VASP/>.
- [67] Q. Wu, F. Zhang, P. Xiao, H. Tao, X. Wang, Z. Hu, Y. Lü, *J. Phys. Chem. C* **2008**, *112*, 17076–17080.
- [68] S. Brunauer, P. H. Emmett, E. Teller, *J. Am. Chem. Soc.* **1938**, *60*, 309–319.
- [69] C. Hess, *J. Catal.* **2007**, *248*, 120–123.
- [70] C. T. Nottbohm, C. Hess, *Catal. Commun.* **2012**, *22*, 39–42.
- [71] P. S. Waleska, C. Hess, *J. Phys. Chem. C* **2016**, *120*, 18510–18519.
- [72] D. Nitsche, C. Hess, *J. Raman Spectrosc.* **2013**, *44*, 1733–1738.
- [73] Z. Cai, Y. Ou, B. Zhang, J. Wang, L. Fu, M. Wan, G. Li, W. Wang, L. Wang, J. Jiang, Z. W. Seh, E. Hu, X.-Q. Yang, Y. Cui, Y. Sun, *J. Am. Chem. Soc.* **2021**, *143*, 3143–3152.
- [74] A. Cao, Z. Wang, H. Li, J. K. Nørskov, *ACS Catal.* **2021**, *11*, 1780–1786.
- [75] W. J. Kim, D. Pradhan, Y. Sohn, *J. Mater. Chem. A* **2013**, *1*, 10193.
- [76] F. Lei, Y. Sun, K. Liu, S. Gao, L. Liang, B. Pan, Y. Xie, *J. Am. Chem. Soc.* **2014**, *136*, 6826–6829.
- [77] W. Wang, Y. Zhang, Z. Wang, J. mao Yan, Q. Ge, C. jun Liu, *Catal. Today* **2016**, *259*, 402–408.
- [78] N. Rui, F. Zhang, K. Sun, Z. Liu, W. Xu, E. Stavitski, S. D. Senanayake, J. A. Rodriguez, C.-J. Liu, *ACS Catal.* **2020**, *10*, 11307–11317.

Abkürzungsverzeichnis

Abkürzung	Beschreibung	Einheit
ΔH_f^0	Standardbildungsenthalpie	kJ mol^{-1}
ν	Schwingungsquantenzahl	
λ_{ex}	Anregungswellenlänge	nm
ρ	Elektronendichte	
T_e	Kinetische Energie der Elektronen	
E_{eK}	Energie der Elektron-Kern-Anziehung	
E_{ee}	Energie der Elektron-Elektron-Wechselwirkung	
J	Coulombenergie	
E_X	Austauschenergie	
\vec{r}	Ortsvektor	
Z	Kernladung	e
R	Kernabstand	
E_{TFD}	Energie nach THOMAS-FERMI-DIRAC	
T_{TF}	Kinetische Energie nach THOMAS-FERMI	
E_C	Energie für die Elektronenkorrelation	
T_S	Kinetische Energie	
φ_i	KOHN SHAM Orbital	
∇	Nablaoperator	
ε_i	Lagrange-Multiplikator	
$V_{\text{eff}}[\rho]$	Effektives Potential	
$V_{\text{XC}}[\rho]$	Austausch-Korrelations Potential	
$E_{\text{XC}}[\rho]$	Austausch-Korrelations Energie	
U_{eff}	Effektiver Hubbard Parameter	eV
E_{cutoff}	Cutoff-Energie	eV
ν	Frequenz	Hz
Ω_{cell}	Zellvolumen	\AA^3
ν_S	Frequenz des gestreuten Lichts	Hz
h	Plancksches Wirkungsquantum	J s
n_i^b	BOSE-EINSTEIN Faktor	
I^{Raman}	Raman-Streuaktivität	
$\tilde{\alpha}$	Polarisierbarkeitstensor	
β	Anisotropie des Polarisierbarkeitstensors	
ϵ_{ij}^∞	Dielektrischer Tensor	
E^{el}	Elektronische Energie	
N_{atom}	Anzahl der Atome	
Ω	Raumwinkel	
δ_{ij}	Kronecker Delta	

Abkürzung	Beschreibung	Einheit
ϵ^∞	Dielektrische Matrix	

Abkürzung	Bedeutung
ALD	<i>Atomic layer deposition</i>
TEM	Transmissionselektronenmikroskopie
DFPT	<i>Density functional perturbation theory</i>
DFT	Dichtefunktionaltheorie
KSG	Kohn-Sham Gleichungen
DRIFTS	Diffuse Reflexions-Infrarot-Fourier-Transformations-Spektroskopie
LDA	<i>Local density approximation</i>
GGA	<i>Generalized gradient approximation</i>
FWHM	<i>Full width at half maximum</i>
PAW	<i>Projector augmented wave</i>
WGS	Wassergas-Shift
rWGS	Reverse Wassergas-Shift
XPS	<i>X-ray photoelectron spectroscopy</i>
NAP-XPS	<i>Near ambient pressure X-ray photoelectron spectroscopy</i>
FTIR	Fourier-Transformations-Infrarotspektroskopie
EDX	<i>Energy dispersive X-ray spectroscopy</i>
ICP-OES	<i>Inductively coupled plasma optical emission spectrometry</i>
TAP	Temporäre Analyse von Produkten
XAS	<i>X-ray absorption spectroscopy</i>
EIS	Elektrochemische Impedanzspektroskopie
GEIS	Galvano Elektrochemische Impedanzspektroskopie
PEIS	Potential Elektrochemische Impedanzspektroskopie
UPS	Ultraviolett-Photoelektronenspektroskopie
VASP	<i>Vienna Ab initio Simulation Package</i>
ESCA	<i>Electron spectroscopy for chemical analysis</i>
XRD	<i>X-ray diffraction</i>

Erklärung zum Eigenanteil an den Veröffentlichungen

Im Folgenden ist aufgelistet, mit welchem Anteil ich an den Veröffentlichungen beteiligt war.

Mein Anteil an der folgenden Veröffentlichung beträgt 30 %.

1. C. Schilling, M. Ziemba, C. Hess, M.V. Ganduglia-Pirovano, Identification of single-atom active sites in CO oxidation over oxide-supported Au catalysts, *J. Catal.* 383 (2020) 264–272.

Mein Anteil an der folgenden Veröffentlichung beträgt 70 %.

2. M. Ziemba, M.V. Ganduglia-Pirovano, C. Hess, Insight into the mechanism of the water–gas shift reaction over Au/CeO₂ catalysts using combined *operando* spectroscopies, *Faraday Discuss.* 229 (2021) 232–250.

Mein Anteil an der folgenden Veröffentlichung beträgt 80 %.

3. M. Ziemba, C. Hess, Influence of gold on the reactivity behaviour of ceria nanorods in CO oxidation: combining *operando* spectroscopies and DFT calculations, *Catal. Sci. Technol.* 10 (2020) 3720–3730.

Mein Anteil an der folgenden Veröffentlichung beträgt 70 %.

4. M. Ziemba, M.V. Ganduglia-Pirovano, C. Hess, Elucidating the Oxygen Storage-Release Dynamics in Ceria Nanorods by Combined Multi-Wavelength Raman Spectroscopy and DFT, *J. Phys. Chem. Lett.* 11 (2020) 8554–8559.

Mein Anteil an der folgenden Veröffentlichung beträgt 60 %.

5. M. Ziemba, D. Stark, C. Hess, Combined DFT and *operando* Spectroscopic Study of the Water-Gas Shift Reaction over Ceria based Catalysts: The Role of the Noble Metal and Ceria Faceting, *Chem. Proc.* 2 (2020) 23.

Mein Anteil an der folgenden Veröffentlichung beträgt 70 %.

6. M. Ziemba, L. Schumacher, C. Hess, Reduction Behavior of Cubic In₂O₃ Nanoparticles by Combined Multiple *In Situ* Spectroscopy and DFT, *J. Phys. Chem. Lett.* 12 (2021) 3749–3754.

Mein Anteil an der folgenden Veröffentlichung beträgt 40 %.

7. M. Ziemba, C. Schilling, M.V. Ganduglia-Pirovano, C. Hess, Toward an Atomic-Level Understanding of Ceria-Based Catalysts: When Experiment and Theory Go Hand in Hand, *Acc. Chem. Res.* 54 (2021) 2884–2893.

Mein Anteil an der folgenden Veröffentlichung beträgt 45 %.

8. M. Ziemba, J. Weyel, C. Hess, Elucidating the mechanism of the reverse water–gas shift reaction over Au/CeO₂ catalysts using *operando* and transient spectroscopies, *Appl. Catal. B Environ.* 301 (2022) 120825.

Mein Anteil an der folgenden Veröffentlichung beträgt 35 %.

9. J. Weyel, M. Ziemba, C. Hess, Elucidating Active CO–Au Species on Au/CeO₂(111): A Combined Modulation Excitation DRIFTS and Density Functional Theory Study, *Top. Catal.* 65 (2022) 779–787.

Mein Anteil an der folgenden Veröffentlichung beträgt 45 %.

-
10. M. Ziemba, M. Radtke, L. Schumacher, C. Hess, Elucidating CO₂ Hydrogenation over In₂O₃ Nanoparticles using Operando UV-vis and Impedance Spectroscopies, *Angew. Chem. Int. Ed.* 61 (2022) e202209388.

Mein Anteil an der folgenden Veröffentlichung beträgt 50 %.

11. M. Ziemba, J. Weyel, C. Hess, Approaching C1 Reaction Mechanisms Using Combined *Operando* and Transient Analysis: A Case Study on Cu/CeO₂ Catalysts during the LT-Water–Gas Shift Reaction, *ACS Catal.* 12 (2022) 9503-9514.

Ort, Datum

M. Ziemba

Erklärung zur Begutachtung der Veröffentlichungen

Weder Referent (Prof. Dr. Christian Hess) noch Korreferent (Prof. Dr. Rolf Schäfer) der vorliegenden kumulativen Doktorarbeit waren an der Begutachtung der nachfolgenden Veröffentlichungen beteiligt:

Datum _____

Referent: Prof. Dr. Christian Hess

Korreferent: Prof. Dr. Rolf Schäfer

1. C. Schilling, M. Ziemba, C. Hess, M.V. Ganduglia-Pirovano, Identification of single-atom active sites in CO oxidation over oxide-supported Au catalysts, *J. Catal.* 383 (2020) 264–272.
2. M. Ziemba, M.V. Ganduglia-Pirovano, C. Hess, Insight into the mechanism of the water–gas shift reaction over Au/CeO₂ catalysts using combined *operando* spectroscopies, *Faraday Discuss.* 229 (2021) 232–250.
3. M. Ziemba, C. Hess, Influence of gold on the reactivity behaviour of ceria nanorods in CO oxidation: combining *operando* spectroscopies and DFT calculations, *Catal. Sci. Technol.* 10 (2020) 3720–3730.
4. M. Ziemba, M.V. Ganduglia-Pirovano, C. Hess, Elucidating the Oxygen Storage-Release Dynamics in Ceria Nanorods by Combined Multi-Wavelength Raman Spectroscopy and DFT, *J. Phys. Chem. Lett.* 11 (2020) 8554–8559.
5. M. Ziemba, D. Stark, C. Hess, Combined DFT and *operando* Spectroscopic Study of the Water-Gas Shift Reaction over Ceria based Catalysts: The Role of the Noble Metal and Ceria Faceting, *Chem. Proc.* 2 (2020) 23.
6. M. Ziemba, C. Schilling, M.V. Ganduglia-Pirovano, C. Hess, Toward an Atomic-Level Understanding of Ceria-Based Catalysts: When Experiment and Theory Go Hand in Hand, *Acc. Chem. Res.* 54 (2021) 2884–2893.
7. M. Ziemba, J. Weyel, C. Hess, Elucidating the mechanism of the reverse water–gas shift reaction over Au/CeO₂ catalysts using *operando* and transient spectroscopies, *Appl. Catal. B Environ.* 301 (2022) 120825.
8. M. Ziemba, L. Schumacher, C. Hess, Reduction Behavior of Cubic In₂O₃ Nanoparticles by Combined Multiple *In Situ* Spectroscopy and DFT, *J. Phys. Chem. Lett.* 12 (2021) 3749–3754.
9. J. Weyel, M. Ziemba, C. Hess, Elucidating Active CO–Au Species on Au/CeO₂(111): A Combined Modulation Excitation DRIFTS and Density Functional Theory Study, *Top. Catal.* 65 (2022) 779–787.
10. M. Ziemba, M. Radtke, L. Schumacher, C. Hess, Elucidating CO₂ Hydrogenation over In₂O₃ Nanoparticles using Operando UV-vis and Impedance Spectroscopies, *Angew. Chem. Int. Ed.* 61 (2022) e202209388.
11. M. Ziemba, J. Weyel, C. Hess, Approaching C1 Reaction Mechanisms Using Combined *Operando* and Transient Analysis: A Case Study on Cu/CeO₂ Catalysts during the LT-Water–Gas Shift Reaction, *ACS. Catal.* 12 (2022) 9503-9514.

Referent
(Prof. Dr. Christian Hess)

Korreferent
(Prof. Dr. Rolf Schäfer)